NMR SPECTROSCOPY IN THE PRESENCE OF ULTRASOUND AND OTHER PERTURBATIONS

STEVEN ANDREW REYNOLDS

Doctor of Philosophy

THE UNIVERSITY OF ASTON IN BIRMINGHAM

JANUARY 1997

The University of Aston in Birmingham

NMR SPECTROSCOPY IN THE PRESENCE OF ULTRASOUND AND OTHER PERTURBATIONS

STEVEN ANDREW REYNOLDS

Doctor of Philosophy

1997

The work described in this thesis has been concerned with exploring the potential uses of ultrasound in Nuclear Magnetic Resonance (NMR) spectroscopy.

The NMR spectra of liquids provide detailed structural information that may be deduced from the chemical shifts and spin-spin coupling, that are evident in the narrow resonances, arising from some of the nuclear broadening interactions being reduced to zero. In the solid state, all of the nuclear broadening interactions are present and broad lines in the NMR spectrum are observed. Current techniques employed to reduce the line widths in solids are based on coherent averaging techniques such as MAS NMR[1, 2] which can remove first order interactions. Recently DOR[3] and DAS[4] have become available to remove higher order interactions. SINNMR (Sonically Induced Narrowing of the NMR spectra of solids) has been reported by Homer et al[5] and developed by Homer and Howard[6] to reduce the line widths of solids. The basis of their work is the proposal that a colloidal suspension of solid particles can be made to move like large molecules by using ultrasonic agitation. The advantage of the technique is that the particles move incoherently removing all of the nuclear interactions responsible for broad lines. This thesis describes work on the extension of SINNMR by showing that the line width of ^{27}Al and ^{11}B for the glass $Na_2O/B_2O_3/Al_2O_3$ can be reduced by placing solid particles in a colloidal suspension. Further line width reduction is possible by applying ultrasound, at 2 MHz, of sufficient intensity. It is proposed that a cavitation field is responsible for imparting sufficient rotational motion to the solid particles to partially average the nuclear interactions responsible for broad lines. Rapid stirring of the colloidal suspension generates turbulent flow, however, the motion is insufficient to narrow the line widths for ^{27}Al in the glass.

Investigations of sonochemical reactions for in situ rate measurements by NMR have been made. By using the Weissler reaction[7], it has been shown that ultrasonic cavitation is possible up to 10 MHz. Preliminary studies have been carried out into the rate of ultrasonic polymerisation of methylmethacrylate by NMR.

Long range order in liquid crystals can imposed when they are aligned in the presence of a magnetic field. The degree of alignment can be monitored by NMR using, for example a deuterated solute added to the liquid crystal[8]. Ultrasonic streaming can then be employed to deflect the directors of the liquid crystal from their equilibrium position, resulting in a change in the NMR spectrum. The angle of deflection has been found for the thermotropic liquid crystal (I35) to be ca. 35^0 and for the lyotropic (ZLI-1167) to be ca. 20^0. Mechanical stirring can be used to re-orientate the liquid crystal but was found to give a smaller deflection.

In a separate study, that did not use ultrasound, it has been found that the signal to noise ratio of ^{13}C NMR signals can be enhanced by rapidly stirring a liquid. Accelerating the diffusion of nuclei out of the coil region enables M_0 to be re-established more rapidly than the normal relaxation process. This allows the pulse repetition rate to be reduced without saturating the spin system. The influence of varying the relaxation delay, acquisition time and inter-pulse delay have been studied and parameters optimised. By studying cholesterol the technique was found to be most effective for nuclei with long relaxation times, such as quaternary carbon sites.

Key Words: NMR, Ultrasound, Liquid crystals, Sonochemistry, Enhanced signals.

DEDICATION

This thesis is dedicated to my family and friends. All of them have been completely supportive in everything I've wanted to do and are always there for me when I need them.

"Will it come down to the fact
that I'm now different from the past,
demanding all my ideals its just
trying to make them last,
and some of the things that you say
they ring home so true"
"Get away", © Ocean Colour Scene, 1996.

ACKNOWLEDGEMENTS

My thanks go to Dr. J. Homer for his advice, support and assistance as my supervisor throughout the three years of my Ph.D.

I am grateful to Dr. M. Beevers for his additional support and assistance. I would like to show my appreciation to Dr. M. Perry for providing the MAS spectra and allowing me to borrow all of his equipment and books. My appreciation also goes to the technical staff, in particular Mr. I. Murkett and Mr. R. Wheeler for their tuition on lathe operation which made the production of the transducer holders possible.

I am grateful to Dr. Christian Jäger for providing the SINNMR glass samples used in chapter 7 and his hospitality during my stay in Germany.

My thanks are also extended to Prof. J. Emsley for his collaboration on the effect of ultrasound on liquid crystals and suggesting the experiments, and to Dr. M Edgar for his support and advice.

I would like to thank Dr. Homer for suggesting the modification to the experiments conducted with the air driven rotor that led to the development of the SPADES experiment.

Finally, and by no means least, I would like to thank my colleagues in the NMR research group for their help, advice, tolerance and making life in the laboratory interesting: Dr. Mark Howard, Dr. John Robson, Mr. Spencer Davies, Mr. Stuart Palfreyman, Mr. Gavin Tilestone and Miss Anna Weekes (including her collaborative input on the design and manufacture of all of the transducer holders).

TABLE OF CONTENTS

CHAPTER TWO

CHAPTER THREE

CHAPTER FOUR

CHAPTER FIVE

CHAPTER SIX

CHAPTER SEVEN

CHAPTER EIGHT

CHAPTER NINE

CHAPTER TEN

APPENDIX ONE

APPENDIX TWO

APPENDIX THREE

APPENDIX FOUR

LIST OF FIGURES

CHAPTER ONE

CHAPTER TWO

CHAPTER THREE

CHAPTER FOUR

CHAPTER FIVE

CHAPTER SEVEN

CHAPTER EIGHT

CHAPTER NINE

APPENDIX ONE

APPENDIX FOUR

LIST OF TABLES

CHAPTER FOUR

CHAPTER FIVE

CHAPTER SIX

CHAPTER SEVEN

CHAPTER EIGHT

CHAPTER NINE

APPENDIX TWO

CHAPTER 1

INTRODUCTION

PART ONE: INTRODUCTION TO THE THESIS

1.0: INTRODUCTION

Nuclear magnetic resonance, NMR, measures the frequency at which nuclei in a static magnetic field absorb energy. With a few exceptions most of the elements possess at least one NMR active nuclide. The wide range of NMR 'active' nuclei make it a very powerful technique in the elucidation of the chemical structure of many compounds, and in particular organic molecules. Nuclear interactions such as spin-spin coupling and the nuclear Overhauser effect have made it possible to determine the stereochemistry of large molecules and proteins.

The existence of nuclear moments was first demonstrated by Stern and Gerlach[9]. These workers passed a beam of atoms with a magnetic moment through an inhomogeneous magnetic field. It was found that the beam split into two distinct components which was attributed to the nucleus of the atom possessing quantum mechanical spin angular momentum. Electron paramagnetic resonance spectra are complicated by hyperfine splitting[10] where the number of lines obtained would be dependent on the atom in which the paramagnetic electron was present. Pauli suggested[11] that hyperfine splitting was due to certain nuclei possessing a spin angular momentum and therefore a magnetic moment. When placed in static magnetic field the nuclear magnetic moment orientates itself with the magnetic field so as to reduce the torque acting on it. The orientation of the magnetic moment creates energy states dependent on whether the moment is aligned with or against the magnetic field. The NMR experiment measures the energy required

(in terms of energy h.ν) to cause a nuclear moment to 'flip' from a lower energy state to a higher one. The first experiments, in bulk matter, to measure the transition frequency of the nucleus were conducted, independently, by Bloch et al[12] and Purcell et al[13] in 1945 on the resonance of protons (^{1}H) in water and paraffin wax respectively. Detection of the nuclear moment was made by observing the additional load on the resonant circuitry of the excitation field when the spins came to resonance.

During its first 25 years (1945-70) NMR relied on the use of continuous wave (CW) instruments. Slow passage of either the static magnetic field or the r.f. frequency was required to collect information: a weak r.f. field was employed to prevent saturation of the spin system: which causes distortions in the signal. The nuclear transition energies in NMR are very small, making the technique relatively insensitive. Signal averaging, using CAT (computer-averaged transient)[14] was often necessary to increase signal-to-noise (S/N). The multiple acquisition of the signal reduced its sensitivity to variations in the magnetic field strength.

The majority of modern spectrometers are now based on pulsed Fourier Transform spectroscopy[15]. The various nuclear transitions are excited simultaneously and the response from all of the nuclei are observed: this permits rapid acquisition and thus multiple measurements to improve signal-to-noise. Selective use of pulse techniques and phase cycling allows the manipulation of the spin system to excite coherences between nuclei.

Random motion in liquids reduces some of the effects of nuclear interactions to zero, resulting in detailed spectra containing narrow resonances from which chemical shift and spin-spin coupling information can be obtained. In solids no motional averaging occurs and the effects of all of the nuclear interactions are present, resulting in broad featureless spectra. Many techniques have been devised to reduce the magnitude of some of the nuclear interactions. The most popular technique is 'Magic' Angle Spinning (MAS), invented by Andrew[1] and Lowe[2], to remove dipolar coupling and chemical shift anisotropy. Other techniques such as double angle (DOR[3]) and dynamic angle spinning (DAS[4]) have been used to remove higher orders nuclear interactions. The techniques work by imposing a new time averaged orientation on the sample which, by the correct choice of angle with respect to the field, coherently averages certain interactions. However, none can remove all of the interactions simultaneously.

The SINNMR (Sonically Induced Narrowing NMR) technique[5,6] proposes that solid particles can be made to behave like liquid molecules if they are agitated. By using ultrasonic energy to supply the agitation it was hypothesised that solid particles, supported in a liquid medium, can be driven into motional behaviour similar to that of large molecules. The advantage of the technique over other methods of line width narrowing is that the particles will have incoherent rotational and translational motion. This type of motion should reduce all of the angular dependent interactions, unlike the coherent spinning techniques which only remove particular interactions.

Ultrasonic agitation can be applied to other media, for example, liquid crystals. Liquid crystals are a viscous transition state between the solid and liquid phase. They possess some short range order but remain randomly orientated within the bulk sample. Macroscopic long range order can be imposed on a liquid crystal sample by placing it in a static magnetic (or electric) field that causes aggregates of the mesophase to be aligned. NMR can be used to study the orientational order of the liquid crystal. The appearance of the NMR spectra is dependent on the orientation of the liquid crystal with respect to the magnetic field. Disruption of the liquid crystal by ultrasonic agitation can be observed by changes in the NMR spectrum.

The wider application of ultrasound in NMR has also been studied. During the development of SINNMR devices capable of delivering ultrasound to samples, while in a NMR magnet, where designed and produced. The possibility exists of using these ultrasonic devices to induce sonochemical reactions. The sonochemical reactions could then be studied using NMR and may give an insight into reaction mechanisms and rates.

A secondary method for the agitation of solid particles was proposed to reduce NMR line widths. It hypothesised that rapid mechanical stirring will impart turbulent motion on the solid particles causing line width narrowing. A side effect of stirring is the accelerated diffusion of the liquid molecules from active coil region of the NMR probe. Such an action may allow the rate of acquisition to be

increased as the repetition time would no longer be directly dependent on the longitudinal relaxation time.

PART TWO: INTRODUCTION TO NMR

1.1: SPIN ANGULAR MOMENTUM

For a nucleus to be observable by NMR it must possess quantised spin angular momentum, $\mathbf{I}$, due to a nucleus containing an unpaired nucleon. The value of I is dependent on the number of protons and neutrons present[16]. If the mass number, A, and the proton number, Z, are even then I =0, when A is odd and Z is odd or even then I is a half integral. If A is even and Z is odd then I is some integer value $\leq$ six. Spin 1/2 nuclei have spherical distribution of charge, whilst quadrupolar nuclei, I>1/2, have an elliptical distribution of charge in which the nuclei are effected by electric field gradients.

The quantisation of spin generates 2I+1 components with discreet values, m, varying between I and -I by $\Delta m=1$. The magnitude of $\mathbf{I}$ is given by $\hbar\left[I(I+1)\right]^{\frac{1}{2}}$, where $\hbar$ is the reduced Planck's constant, $h/2\pi$.

The charge on the nucleus and its associated spin combine to give a magnetic moment, μ, figure 1.0.

Figure 1.0: Magnetic dipole generated by spin, $\mathbf{I}$.

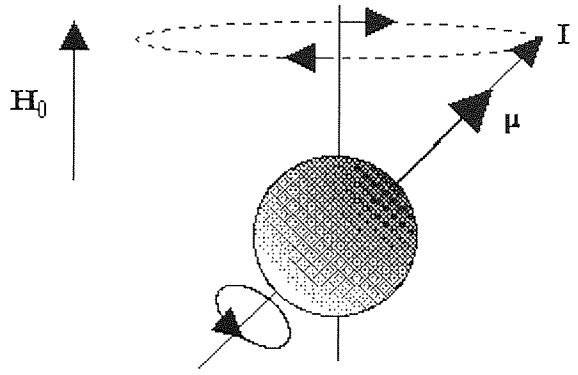

The magnetic moment is related to its spin by equation (1.1),

$$\mu = \gamma.\hbar.\mathbf{I} \qquad (1.1)$$

where, γ is the magnetogyric ratio and is a characteristic constant for a particular nucleus. The magnetogyric ratio is calculated for each nucleus from $\hbar.\gamma = g_I.\mu_n$ (g_I is the nuclear g-factor and μ_n is the nuclear magneton). The sign of the magnetogyric ratio specifies whether the vectors $\mathbf{I}$ and μ lie parallel or antiparallel to each other. The majority of NMR active nuclei possess positive values of γ although notable exceptions are ^{15}N, ^{17}O and ^{29}Si.

When a nucleus is placed in an external magnetic field arbitrarily directed parallel to the z-axis of the laboratory frame, the magnetic moment will align with or against the field in states of differing energy. The quantised energy levels that exist for the nucleus arise from the 2I+1 orientations the nucleus may take with respect to the field. The energy is defined by the Zeeman Hamiltonian, $\mathcal{H}_Z$,

$$\mathcal{H}_z = -\mu.\mathbf{H}_0 \qquad (1.2)$$

The separation of the energy levels, ΔE, is proportional to H_0 as given by equation (1.3), depicted in figure 1.1.

$$\Delta E = \gamma . \hbar . H_0 \qquad (1.3)$$

Figure 1.1: Energy level separation for a spin, I=3/2, with increasing magnetic field strength

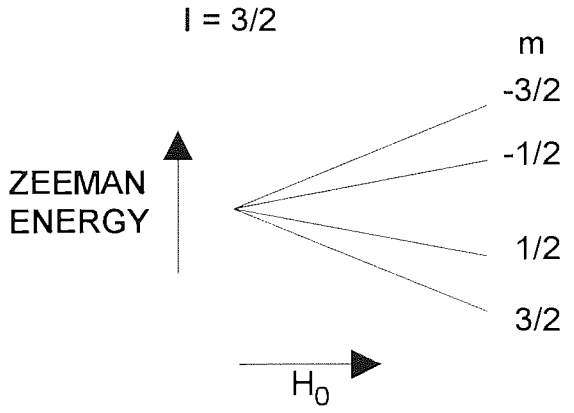

Quantum mechanical selection rules dictate that only $\Delta m \pm 1$ transitions are observable in the NMR spectra. Forbidden transitions, $\Delta m \neq 1$, are not directly observable, but are important in relaxation processes and coherence pathways.

The coupling of the external field to the magnetic moment causes it to precess about H_o. The frequency of the precession is given by,

$$\omega_o = -\gamma . H_o \qquad (1.4)$$

where ω_0 is the Larmor processional frequency. By applying energy of frequency ,ω_o, the nucleus can be made to 'flip' from the lower to the upper energy state, resulting in the resonance phenomenon that allows the detection of NMR.

1.2: ENERGY LEVEL POPULATIONS

For a given system the number of nuclei that exist in a particular state is defined by a partition function or, sum of the states, given by:-

$$Z = \sum_{n} M_n \exp\left(-\frac{\Delta E}{kT}\right) \qquad (1.5)$$

where, ΔE is the energy difference for a particular transition at an equilibrium temperature, T, M_n is the degeneracy of the spin and k is the Boltzmann constant. For a given spin system, say I=1/2, it can be seen from equation (1.5) that the spins will occupy two energy levels of separation $\Delta E = \gamma.\hbar.H_0$ with a Boltzmann distribution between them. Each has an equilibrium number of spins in the upper, N_u, and lower, N_l, level. The ratio of spins in the two levels is given by,

$$\frac{N_u}{N_l} = \exp\left(-\frac{2.\mu.H_0}{k.T}\right) \qquad (1.6)$$

The magnitude of ΔE is extremely small at ambient temperatures and only a few extra nuclei exist in the upper energy state compared to the lower state. Therefore, N_u/N_l is approximately equal to unity and equation 1.6 can be re-written as,

$$\frac{N_u}{N_l} = 1 - \frac{2.\mu.H_0}{k.T} \qquad (1.7)$$

The difference between the energy levels has led to the concept of spin temperature which can behave as in the thermodynamic analogy. In an isolated system the interacting spins come to an internal equilibrium condition given by a Boltzmann distribution ($\exp\{-\Delta E/kT_s\}$ where the ratio of the populations can now be described by the magnitude of the spin temperature, T_s. Using spin temperature it is possible to explain the flow of energy from the spin system to the

lattice or vice versa by a "heat" flow between two spin temperatures, caused by a difference in the two spin populations.

The probability of up (absorption) or down (emission) transitions are equal. However, the lower energy state is thermodynamically more favourable, thus, there is a slightly larger number of spins in the lower state than the upper state and, therefore, there is a net absorption of energy. A NMR signal is only observable when a population difference exists between two energy levels, which can induce an e.m.f in the receiver coil. If transitions are induced then eventually the populations will be equalised (saturated). In order for the signal to be re-examined relaxation must occur for the system to return back to equilibrium.

NMR is a quantitative technique where the line intensity is proportional to the number of nuclei giving rise to it. The magnitude of the population difference, M_0, is given by equation (1.8),

$$\mathbf{M_0} = \frac{\mathbf{N}.\gamma^2.\hbar^2.\mathbf{I}.(\mathbf{I}+1)}{3.k.T}.\mathbf{H_0} = \chi_0.\mathbf{H_0} \qquad (1.8)$$

where **N** is the number of observable nuclei, k is the Boltzmann constant , T (K) is the temperature and χ_0 is referred to as the static magnetic susceptibility. It can be seen from equation 1.8 that $\mathbf{M_0}$ is dependent on $\gamma^2.\hbar^2.\mathbf{I}.(\mathbf{I}+1)$ and thus its magnitude is very small, however $\mathbf{M_0}$ can be observed because of the large number of spins, **N**, involved. Equation 1.8 also shows that the magnitude of M_0 can be enhanced by lowering the temperature.

1.3: BULK MAGNETISATION

In section 1.0 the spin of a nucleus was described in quantum mechanical terms. Quantum mechanics dictates that if the state of a nucleus is measured for a particular spin, say I=1/2, then it would be found that the spin exists in either the +1/2 or -1/2 state. If the measurement was repeated then the result may not give the same spin state for the nucleus. If a large number of measurements were made it would be possible to predict the spin state by an expectation value for a nucleus to exist in a preferred state. Similarly, for a large number of spins then an expectation value can be used to predict the number of nuclei in upper and lower states and thus the population as described by section 1.1. At equilibrium there are more spins in the lower state than the upper. Therefore, an overall magnetisation vector exists which by convention is aligned along the z-axis with respect to the magnetic field. Bulk magnetisation, M_Z, is established when an unmagnetised sample is placed in a field and its approach to an equilibrium value, M_O, is characterised by the equation,

$$\frac{dM_Z}{dt} = \frac{M_O - M_Z}{T_1} \qquad (1.9)$$

where T_1 is the longitudinal relaxation time and describes the rate at which M_0 is established by lattice absorption of the spin energy. The large number of spins involved allows M_0 (and M_z) to be treated as a vector in a co-ordinate frame. The angle M_0 makes with the z-axis corresponds to the relative occupation of the energy levels. If M_0 is parallel to z then the system has a Boltzmann distribution in

the lower state, conversely when M_z is antiparallel the population is inverted. When M_Z equals zero, i.e. the vector is at 90^0, then the energy levels are equally populated.

1.4: THE ROTATING FRAME AND RESONANCE EFFECT

The magnetisation vector, $\mathbf{M}$, experiences a torque, generated by the external field, causing it to precess about $\mathbf{H}$ in the laboratory frame, described by:-

$$\frac{\delta \mathbf{M}}{\delta t} = \gamma . \mathbf{M} \times \mathbf{H} \qquad (1.10)$$

If a second frame is now introduced which rotates with angular velocity, ω. The equation for the motion of $\mathbf{M}$ in the second frame is then defined by equation (1.11).

$$\frac{\delta \mathbf{M}}{\delta t} = \gamma . \mathbf{M} \times \left(\mathbf{H} + \frac{\omega}{\gamma} \right) \qquad (1.11)$$

There are now two components to the magnetic field consisting of the fixed static field, $\mathbf{H_0}$, and a second variable field $+\omega/\gamma$. If a rotating frame is chosen such that $\omega = -\gamma.\mathbf{H_0}$ then it can be seen from equation 1.11 that the torque acting on $\mathbf{M}$ becomes zero and the vector remains stationary in this frame.

The rotating frame can be referenced to a second field $\mathbf{H_1}$, applied orthogonal to $\mathbf{H_0}$, which rotates at a frequency, ω_0. A rotating field generated by an oscillating field of magnitude $2\mathbf{H_1}\cos \omega_{rf} t$ can be resolved into two counter rotating vectors. One of the vector components rotates with the correct Larmor frequency and

sense as the magnetisation vector (the other component can be ignored as it rotates with a frequency twice that of ω_o and has no effect on M_z). As ω_{rf} approaches ω_0 then the pressional rate of $\mathbf{M}$ slows. The magnetisation vector now possesses a Larmor frequency consistent with a field less than $\mathbf{H_0}$: $\mathbf{M}$ is said to be in a reduced field $\mathbf{H_r}$ given by equation 1.12.

$$\mathbf{H_r} = \frac{(\omega - \omega_0)}{\gamma} \qquad (1.12)$$

In the rotating frame M_z will precess about a new effective field $\mathbf{H_{eff}}$ which is the superposition of $\mathbf{H_1}$ and $\mathbf{H_r}$, see figure 1.2 (H_r is much greater than H_1 and H_{eff} is essentially aligned with the z' axis). It is only when $(\omega - \omega_0)$ is comparable with ω_1 that the system comes to resonance and $\mathbf{M_Z}$ freely precesses about $\mathbf{H_1}$.

Figure 1.2: Effective field in the rotating frame.

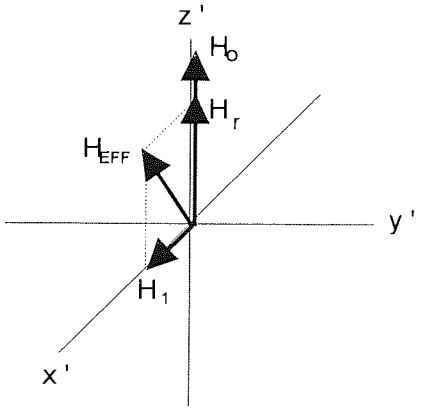

1.5: THE BLOCH EQUATIONS

As first proposed by Felix Bloch[17] the following equations describe, classically, the behaviour of magnetisation during the NMR experiment. The Bloch equations

accurately match the behaviour of the magnetisation vector in liquids. The bulk magnetisation at equilibrium, M_o, can be described in the laboratory frame as having three orthogonal components, M_x, M_y and M_z (figure 1.3).

Figure 1.3: Magnetisation in the laboratory frame.

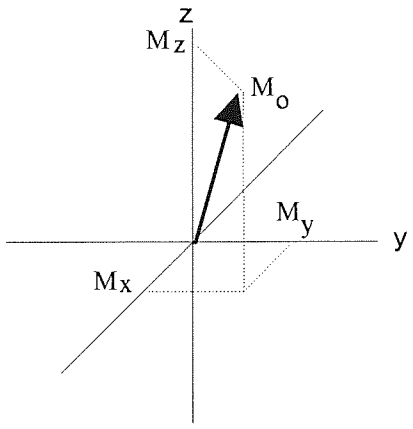

At equilibrium, in the absence of an exciting (r.f.) H_1 field, M_z will not change with time. The motion of the remaining components M_x and M_y can be characterised by,

$$\frac{dM_x}{dt} = \gamma . H_o . M_y \qquad (1.13)$$

$$\frac{dM_y}{dt} = -\gamma . H_o . M_x \qquad (1.14)$$

If an exciting r.f. H_1 field is now applied at a frequency such that one of its components is equal to ω_o, where the x-, y- components are given by,

$$H_{1x} = H_1 \cos(\omega t) \qquad (1.15)$$

$$H_{1y} = -H_1 \sin(\omega t) \qquad (1.16)$$

then the x-axis will contain components of M_y precessing about H_o and a component of M_z rotating about H_1. The time dependent changes in M_x, M_y, and M_z then become,

$$\frac{dM_x}{dt} = \gamma.[M_y.H_o - M_z.H_{1y}] \tag{1.17}$$

$$\frac{dM_y}{dt} = -\gamma.[M_x.H_o + M_z.H_{1x}] \tag{1.18}$$

$$\frac{dM_z}{dt} = -\gamma.[M_x.H_{1y} - M_y.H_{1x}] \tag{1.19}$$

The full Bloch equations also contains terms to describe the relaxation of the system back to equilibrium, equations 1.20-1.22. These take the form of time constants, T_1 and T_2 which are known respectively as the longitudinal (z) and transverse (x,y) relaxation times.

$$\frac{dM_x}{dt} = \gamma.[M_y.H_o + M_z.H_1.\sin(\omega t)] - \frac{M_x}{T_2} \tag{1.20}$$

$$\frac{dM_y}{dt} = -\gamma.[M_x.H_o + M_z.H_1.\cos(\omega t)] - \frac{M_y}{T_2} \tag{1.21}$$

$$\frac{dM_z}{dt} = -\gamma.[M_x.H_1\sin(\omega t) - M_y.H_1.\cos(\omega t)] - \frac{M_z - M_o}{T_1} \tag{1.22}$$

In the rotating frame co-ordinate system, where the H_1 field is usually applied along the x-axis, equations 1.20-1.22 can be simplified to give,

$$\frac{dM_{x'}}{dt} = (\omega_o - \omega).M_{y'} - \frac{M_{x'}}{T_2} \tag{1.23}$$

$$\frac{dM_{y'}}{dt} = -(\omega_o - \omega).M_{x'} - \frac{M_{y'}}{T_2} + \gamma.H_1.M_z \tag{1.24}$$

$$\frac{dM_{z'}}{dt} = -\gamma.H_1.M_{y'} - \frac{(M_{z'} - M_o)}{T_1} \qquad (1.25)$$

If it is assumed that the r.f. power is sufficiently low to prevent saturation, $(\gamma.H_1^2.T_1.T_2 << 1)$, then the solutions for equations 1.23-1.25 are given by,

$$M_{x'} = M_o \frac{\gamma.H_1.T_2^2.(\omega_o - \omega)}{1+4.\pi^2.T_2^2(\omega_o - \omega)^2} \qquad (1.26)$$

$$M_{y'} = M_o \frac{\gamma.H_1.T_2}{1+4.\pi^2.T_2^2(\omega_o - \omega)^2} \qquad (1.27)$$

$$M_{z'} = M_o \frac{1+4.\pi^2.T_2^2(\omega_o - \omega)}{1+4.\pi^2.T_2^2(\omega_o - \omega)^2} \qquad (1.28)$$

Equations (1.26) and (1.27) predict the existence of two magnetisation components in the transverse plane and these can be detected either as a dispersion mode ($M_{x'}$) signal or an absorption mode ($M_{y'}$) signal (see section 2.4).

1.6: RELAXATION

1.6.1: MECHANISMS FOR RELAXATION

The Bloch equations of section 1.5 describe the behaviour of the magnetisation vector with time. These equations contain the longitudinal time constant (T_1) which characterises the relaxation of the population dependent magnetisation back to its equilibrium state. An additional relaxation mechanism exists which describes the loss of magnetisation from the x,y plane and is denoted by the transverse relaxation time, T_2.

Longitudinal relaxation takes place by an energy transfer between the spin system and a thermal reservoir (also known as the lattice). A spin in the upper energy state will return to the lower state emitting energy which is absorbed by the degrees of freedom of the lattice. The process returns magnetisation to the z-axis to re-establish M_0 back to equilibrium. The time constant, T_1, governs the rate of relaxation defined by equation (1.29).

$$M_Z = M_0.(1-e^{\frac{-t}{T_1}}) \qquad (1.29)$$

Relaxation can only be induced by random fluctuating magnetic fields, occurring at the nucleus, of the order of the transition frequency for the spin. The rate of relaxation is dependent on the magnetic field strength for a particular frequency, ω, present at the nucleus.

A magnetic field of the correct frequency can be produced by the random motion of molecules. Molecular motion is characterised by a correlation time, τ_c, which can be defined as the mean time that a molecule spends in a particular orientation, i.e. if a molecule exist in a particular state for τ_c seconds then it will generate frequencies centred around τ_c^{-1} Hz. The strength of the random magnetic fields can be represented by a spectral density function, $J(\omega)$, which gives the field strength in the frequency domain and is defined by the function.

$$J(\omega) = \frac{2.\tau_C}{1+\omega^2.\tau_C^2} \qquad (1.30)$$

Figure 1.4 shows a spectral density function for three values of τ_c. The linear region of the function is valid for $\omega.\tau_c >> 1$ and is referred to as the extreme narrowing condition. The total magnetic field produced at a nucleus by another nucleus is constant if the internuclear separation is fixed. Therefore, as τ_c increases the area under the function must be kept constant and the magnitude of $J(\omega)$ increases for the extreme narrowing region.

Figure 1.4: Spectral density function.

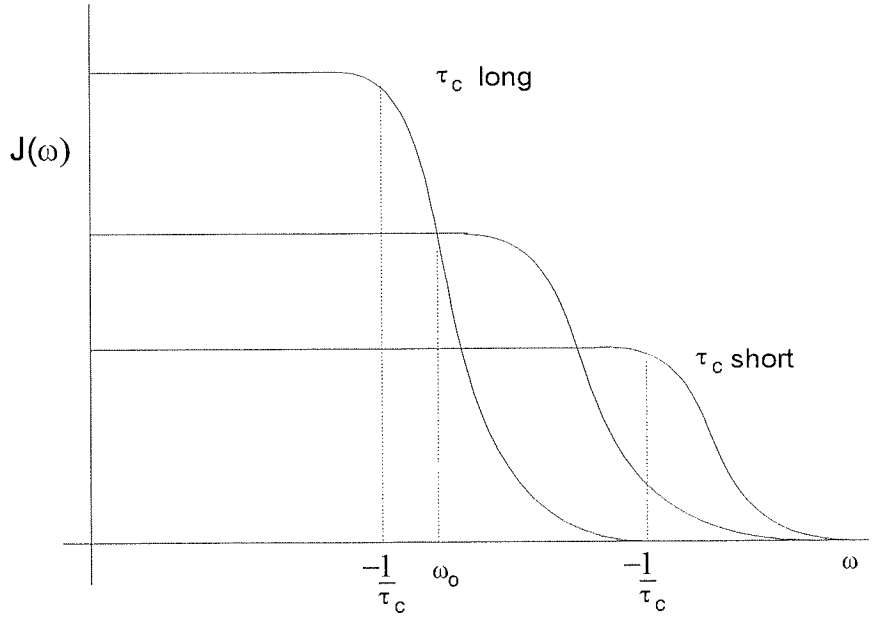

The effect of the correlation time on relaxation can be seen in figures 1.5. Increasing τ_c will cause T_1 (and T_2) to decrease because the nucleus will experience an larger spectral density. At $\omega.\tau_c=1$, the longitudinal relaxation time is minimised because $\omega=\tau_c^{-1}$ and the resonance condition for the spin is met. Beyond the extreme narrowing condition the spectral density function rapidly decays and the longitudinal relaxation time will increase.

Figure 1.5: Relaxation time verses correlation time for a fixed field

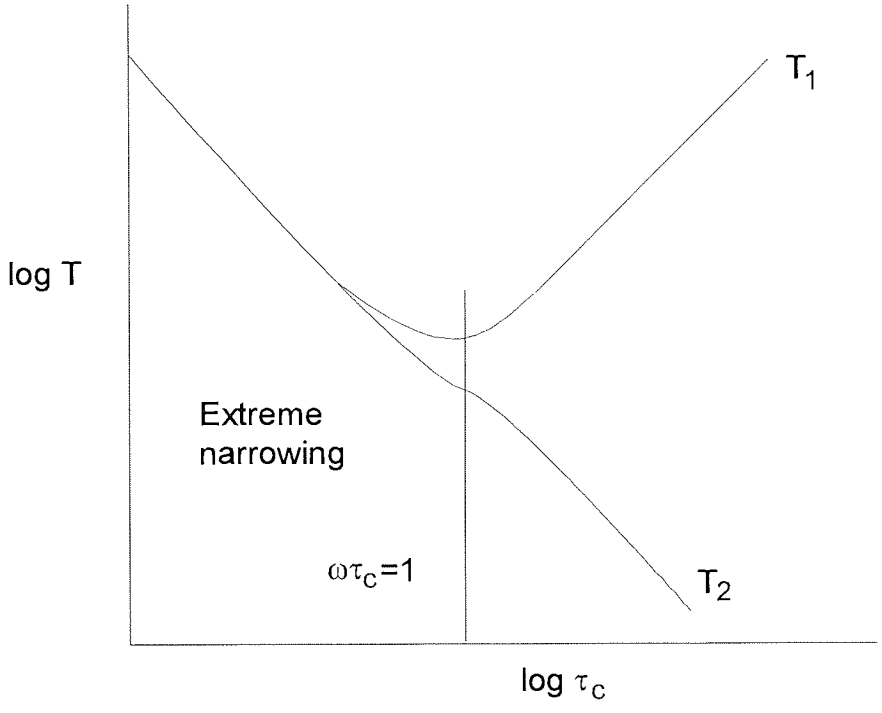

Nuclear transition between the energy levels are induced by fluctuating fields with an x,y component (with respect to the static field) in the same manner as if excited by the H_1 field. The value of T_1 may be calculated for a simple case in which an ensemble of isolated spins experiences a random time dependent isotropic field, $H_{x,yLoc}$. The relaxation rate is given as,

$$\frac{1}{T_1} = \frac{1}{2}.\gamma^2.\left[H_{x,yLoc}\right].J(\omega_0) \qquad (1.31)$$

The theory for longitudinal relaxation is usually complicated by differing relaxation pathways (see section 1.6.2) and the value of T_1 is normally determined experimentally (section 1.6.4).

Transverse (spin-spin) relaxation describes the decay of magnetisation in the x,y-plane. It does not involve an overall reduction in energy or a change in the

population of the levels of the spin system, but occurs through a mutual exchange of energy between two spins, in a flip-flop mechanism. Spins within a static magnetic field precess with differing rates (see section 1.7), spin-spin relaxation transfers energy between them and can be represented in the rotating frame as a loss of phase coherence and a 'fanning' out of the magnetisation vector in the x,y plane. As T_2 becomes smaller the life time of the spin state before it under goes transverse relaxation reduces and there is an uncertainty in the frequency of the spin. Therefore, the value of T_2 can be found from line widths of the resonance produced by the spin. In practice the experimental value of T_2 is shortened by the loss of phase coherence due to inhomogeneitity of the static field and is represented by a new time, T_2^*. Thus the experimental line width at half maximum is given by;

$$\Delta\nu_{1/2} = \frac{1}{\pi . T_2^*} \qquad (1.32)$$

The transverse relaxation rate is also dependent on the correlation time for the molecule. However, there is also a zero frequency component, J(0), in the spectral density function. In figure 1.5 the zero frequency component is responsible for a further decrease in T_2 as the correlation time increases. For most liquids the spin system is in the extreme narrowing region of figure 1.4 and T_1=T_2.

1.6.2: RELAXATION PATHWAYS

Random magnetic fields can be generated by six different mechanisms; dipolar, paramagnetic, scalar, spin rotation, chemical shift anisotropy and quadrupolar[18,

[19]. The total relaxation rate is a linear combination of the rates for each relaxation pathway.

i) Dipole-dipole:

The most important mode of relaxation occurs via a dipolar mechanism. A nuclear dipole generates a magnetic field that can be experienced by other nuclei. The magnitude of the field is dependent on the internuclear separation and the orientation of the internuclear vector with respect to the external field. Molecular motion randomly modulates the dipolar field strength by varying the angle between the magnetic field and the dipolar vector.

ii) Paramagnetic:

This relaxation mechanism is similar to that of the dipolar. However, electron dipoles are closer to the nucleus and their magnetic moments are ca. 2000 times larger than those of nuclear dipoles. Therefore, the field intensity generated at the nucleus is greater and thus relaxation with this source is more rapid.

iii) Quadrupolar:

Quadrupolar relaxation occurs in nuclei where $I>1/2$. A quadrupolar nucleus has a non-spherical distribution of charge and the presence of an electric field gradient (EFG) at the nucleus will perturb the spin energy levels from the Zeeman separation. The EFG arises from asymmetry in the chemical environment of a molecule and thus the interaction is intramolecular. Molecular motion modulates the magnitude of the EFG which, if it occurs at the appropriate frequency, will

induce relaxation. Quadrupolar relaxation is the dominant mechanism for spins>1/2, however the nucleus must exist in an asymmetric molecule for an EFG to be present.

iv) Spin-rotation:

Molecules can possess magnetic moment's of their own. Fluctuating magnetic fields can be generated at a nucleus by the molecules angular momentum. The change in angular momentum is characterised by a different correlation time, τ_J, the angular momentum correlation time: which differs from the orientational correlation time, τ_c. For angular momentum to be maintained τ_J must be long and this therefore requires rapid re-orientation of the molecule, i.e. a short τ_c. The two correlation times are related by $\tau_c.\tau_J=1/kT$. The mechanism becomes more effective at higher temperatures because as the temperature is increased τ_c becomes shorter, while τ_J increases so that T_1 is decreased.

v) Chemical shift anisotropy:

The mechanism is dependent on there being an anisotropic distribution of electrons around the nucleus which gives rise to its chemical shift (section 1.7). As the molecule tumbles the nucleus will experience a time dependent chemical shift and, therefore, local field. The mechanism is most significant when the nucleus possesses a large chemical shift range or when the frequency shift range is large as obtained in high field magnets.

vi) Scalar:

Scalar coupling, J, (section 1.8) generates a field at a nucleus due to the presence of another nucleus. A time dependent field can occur if J is also time dependent, i.e. by relaxation of the coupled nucleus or by chemical exchange. If the relaxation time of one nucleus, I_i, is short in comparison to 1/J then relaxation of I_i will alter the field experienced by the coupled spin, I_k, fluctuating at the rate $1/T_{1i}$. A second mechanism occurs by a break in the scalar coupling due to chemical exchange. If the exchange rate of nucleus, I_k, is faster than J or $1/T_{1i}$ then I_i will experience a fluctuating field, due to its being coupled and uncoupled from the other spin, with a rate equal to that of the chemical exchange.

1.6.3: QUANTITATIVE RESULTS

Quantitative results can be obtained from NMR because the intensity of a resonance is proportional to the number of nuclei giving rise to it. For the intensities to be meaningful the magnetisation must always return to equilibrium before it is re-examined. Therefore, it is necessary to wait $5.3T_1$ between repetitions ($M_z=0.99M_0$) (see equation 1.29 (section 1.6.1)). In order for intensities to be directly comparable the signal must be exactly on resonance to remove off resonance effects (section 2.2).

1.6.4: T_1 MEASUREMENT

In order for quantitative results to be made the maximum magnetisation, M_0, must be attained. This requires a knowledge of the T_1 for the nucleus being observed

for a particular chemical environment. If the NMR signal is examined at a rate greater than $1/(5.3T_1)$ then the magnetisation will not have attained equilibrium and the population difference will be gradually saturated. The length of T_1 is normally based on the intuitive knowledge of the operator, however, many techniques do exist to measure its value[20, 21, 22, 23, 24, 25, 26]. The inversion-recovery sequence[20] is the most common and accurate method for the measurement of T_1, although it is time consuming. The basic sequence, see figure 1.6, shows that after the application of a 180^0 pulse M_0 lies along the -z axis. The spins now relax back towards equilibrium along the z-axis. The length of time before the application of the 90^0(+x) pulse dictates whether M_z has +y or -y phase. By acquiring spectra with a variation in time, τ, the intensity of each peak will pass through a null point. T_1 has an exponential decay described by:-

$$\mathbf{M_z}(\tau) = \mathbf{M_0}.[1 - 2.\exp(-\tau / T_1)] \qquad (1.33)$$

If A is the intensity of the resonance. A plot of $\ln(A_\infty - A_\tau)$ verses τ gives a linear plot where the gradient is equal to $-1/T_1$. For accurate values to be obtained at least one of the τ values must be equal to infinity (usually $5.3T_1$) and each sequence must start with M_0. Problems can occur with imperfections in the pulse length and phase but can usually be removed with phase cycling (see section 2.4).

Figure 1.6: Inversion-recovery sequence.

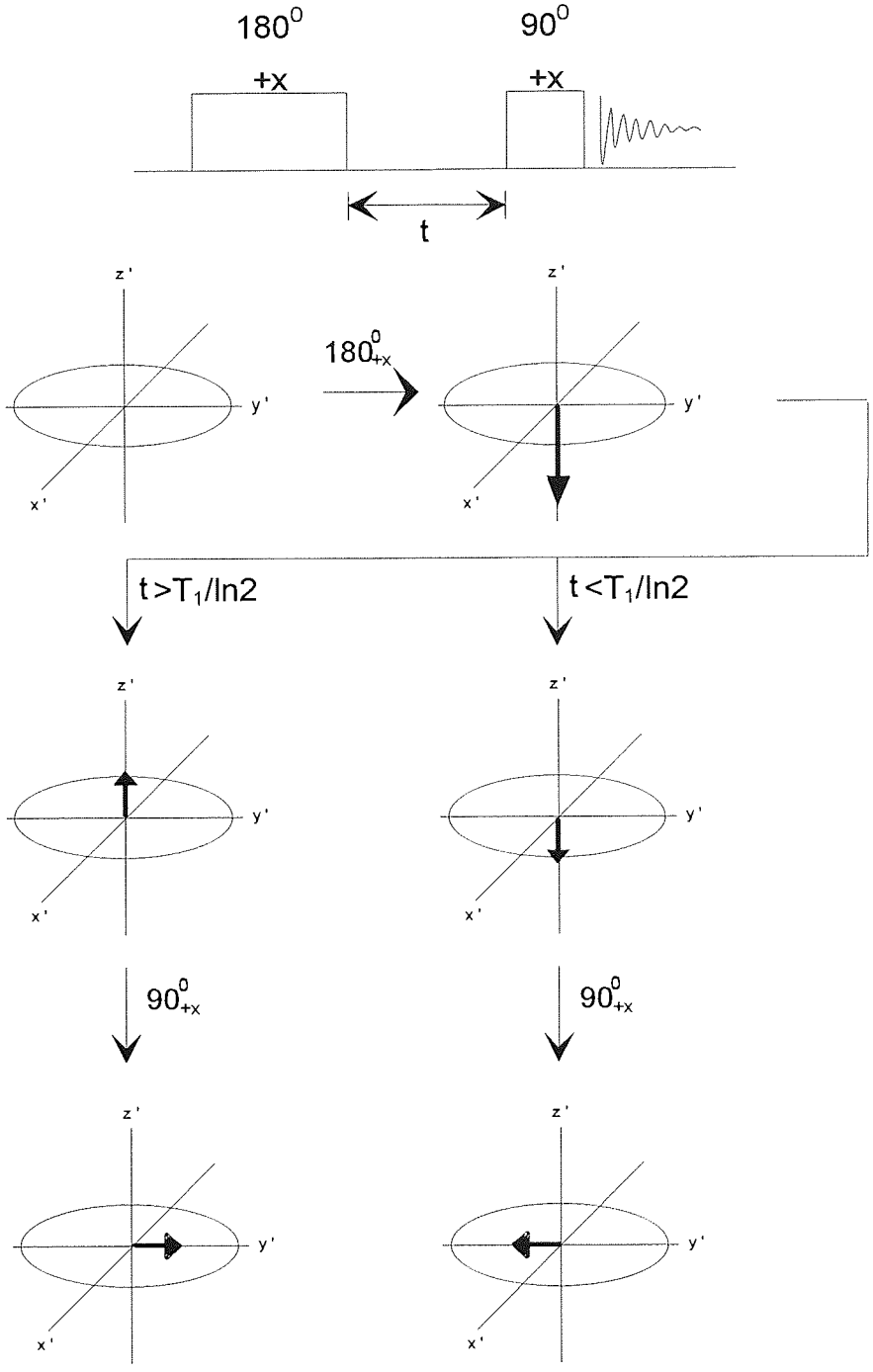

1.6.5: SPIN LOCKING

Spin locking[27] is a useful technique for the measurement of rotating frame relaxation[28], $T_{1\rho}$, and for the creation of coherences between spins necessary for cross polarisation in solids[29] (see section 3.5.3 for further implications of spin

locking). If a 90^0 pulse is applied with x-phase then the magnetisation is aligned along the y-axis. If a second pulse is applied with y-phase the magnetisation vector is locked along the axis and the precessional motion is removed, see figure 1.7.

Figure 1.7: Spin locking pulse sequence.

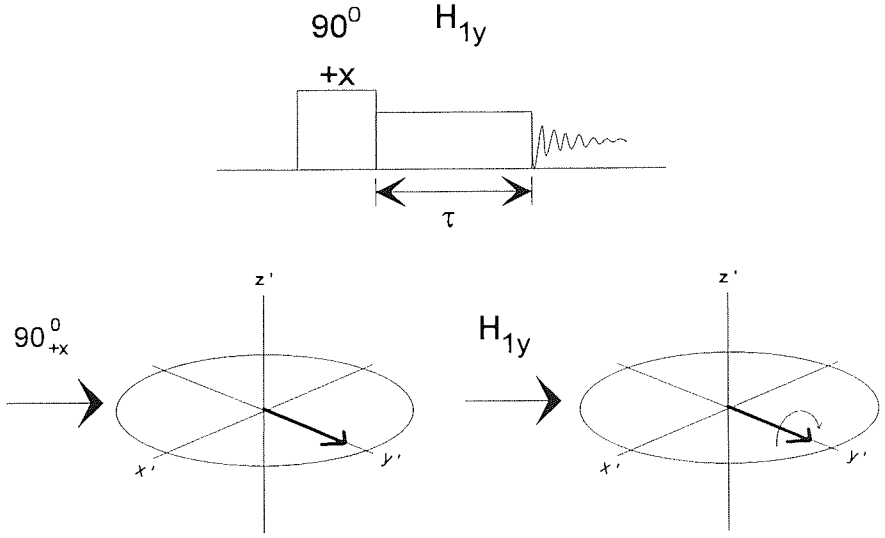

M can be locked in the y-axis and the H_1 field behaves as a static magnetic field, however, H_0 is still present and much larger than H_1 and therefore the magnetisation will relax back to the z-axis. Such relaxation, along the y-axis is analogous to spin-lattice relaxation, however, because relaxation in the x,y plane is described by T_2 a new relaxation time is introduced, $T_{1\rho}$. For liquids in the extreme narrowing region $T_2=T_{1\rho}$, but in solids T_2 is very short and the values are very different.

1.7: THE CHEMICAL SHIFT

The ability of NMR to determine chemical structure arises from the large variations in the resonant frequency of nuclei which are governed by their chemical environment. The range of frequencies, for a particular nucleus, can be as small as 10 ppm (part per million) for ^1H or the order of several thousand ppm for metals.

Each spin within a system experiences a particular magnetic field strength, the intensity of which depends, essentially, upon the level of shielding provided by the electrons surrounding the nucleus. The frequency at which a nucleus resonates is related to the external field by a shielding constant, σ, given by,

$$\omega = \gamma.H_0.(1-\sigma) \qquad (1.34)$$

The shielding experienced at a nucleus can be resolved into two distinct components; those arising intramolecularly and those intermolecular. These terms can be expanded further to encompass various molecular effects by equations (1.35) and (1.36).

$$\sigma_{intra} = \sigma_d+\sigma_p+\sigma_{en}+\sigma_{ef}+\sigma_{aniso}+\sigma_{deloc}, \qquad (1.35)$$

$$\sigma_{inter} = \sigma_b+\sigma_{vdw}+\sigma_{na}+\sigma_{ef}+\sigma_s. \qquad (1.36)$$

(σ_d: diamagnetic, σ_p: paramagnetic, σ_{en}: electronegativity, σ_{ef}: electric fields, σ_{aniso}: anisotropic electron density, σ_{deloc}: delocalised electrons, σ_b: bulk magnetic susceptibility, σ_{vdw}: van der Waals, σ_{na}: neighbouring anisotropy, σ_{ef}: electric fields, σ_s: specific effects, e.g. hydrogen bonding).

For intramolecular shielding, σ_{intra}, the two principal shielding terms are the diamagnetic, σ_d, and paramagnetic, σ_p, screening. The diamagnetic screening term is always positive and shields the nucleus from the applied field, the paramagnetic shielding term opposes the diamagnetic shielding and is opposite in sign to σ_d. The first theoretical treatment of the chemical shift was by Ramsey[30], although, detailed accounts of the chemical shift can be found in the articles by O'Reilly[31] and Musher[32] and in the texts by Pople, Schneider and Bernstein[33] or Emsley, Feeney and Sutcliffe[34].

A nucleus will also experience an intermolecular shielding, σ_{inter}, dependent on the bulk environment in which it exists, i.e. the chemical shift of a solute varies with the solvent used. See Emsley and Philips[35] for further details on the contributions to σ_{inter}.

The electron density surrounding a nucleus can be described by a tensor (see appendix 1) for each of the components of equations 1.35 and 1.36. Off diagonal elements of the tensor represent an anisotropic distribution of electron density around the nucleus. Rapid molecular tumbling in the liquid or gaseous phase causes spatial averaging of the tensor. The chemical shift is then reduced to an isotropic value given by one third of the trace (sum of the diagonal elements) of the matrix.

Chemical shifts are usually defined in terms of the separation of two particular resonances and are measured on the δ scale (in numbers of parts per million, ppm), given by:-

$$\delta = \frac{\nu - \nu_{ref}}{\nu_{ref}}.10^6 \qquad (1.37)$$

where, ν is measured in hertz from ν_{ref}. A standard chemical, for a particular nucleus, is used to define ν_{ref}, e.g. for ^1H, ^{13}C and ^{29}Si the standard is tetramethylsilane (TMS) at 0 ppm. The scale is defined as increasing shielding from left to right, and thus, from equation (1.37), resonant frequencies occurring to the left of δ=0 ppm are given a positive value. Figure 1.8 shows the δ scale, here it can be seen that as σ increases from left to right then the field or frequency necessary to bring the nucleus to resonance also increases.

Figure 1.8: Direction of field/frequency with shielding.

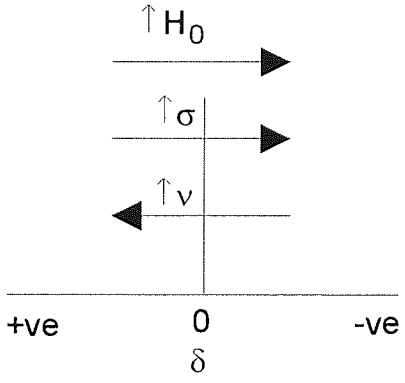

A review of the expected chemical shifts for all NMR nuclei can be found in Brevard and Granger[36].

1.8: SPIN-SPIN COUPLING

Spin coupling in liquids is defined in terms of a coupling constant, J. Its magnitude is independent of the external field strength. The coupling of two spins is caused by each having a knowledge of the others spin state through the bonding electrons between them. If two spins A and X are considered (I=1/2) then the X spin may be coupled to the A in either its +1/2 or -1/2 state, this results in the A spin experiencing two different magnetic fields giving a doublet in its spectrum. By the reverse argument the X spin is also split into a doublet. The number of lines generated by spin coupling can, in general, be predicted as 2In+1, where n is the number of nuclei of spin, I, that the observed spin is coupled to, see figure 1.9.

Figure 1.9: Line splitting for a proton coupled to three near neighbours.

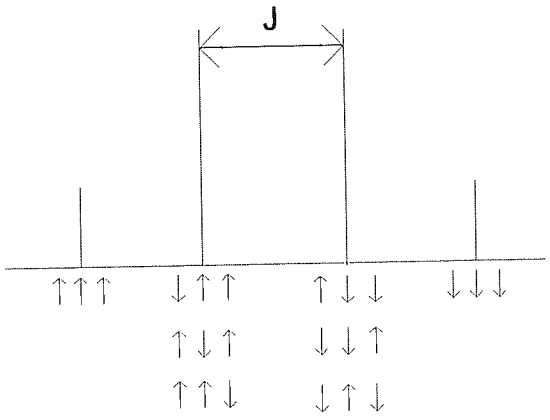

It can be seen in figure 1.11 that the relative intensities of the lines depends on the number of neighbouring spins and can be determined using Pascal's triangle, see figure 1.10.

Figure 1.10: Pascal's triangle.

n									
1				1		1			
2			1		2		1		
3		1		3		3		1	
4	1		4		6		4		1

Coupling information is transferred between nuclei via bonding electrons. If an electrons is in contact with a nucleus then the most stable arrangement is for the two spins to be anti-parallel, i.e. for a positive value of γ_{nuc} then the nuclear and electron magnetic moments are parallel. In the Dirac vector model coupling, if the coupling is across one bond then the Pauli exclusion principle dictates that the two bonding electrons must have opposing spin states, therefore, the two nuclear spins are anti-parallel. For coupling over two bonds then Hund's rule applies and the electronic spins are parallel, resulting in parallel nuclear spins, see figure 1.11.

Figure 1.11: Spin orientations for coupled nuclei over: One (H-D) bond and Two (H-O-D) bonds.

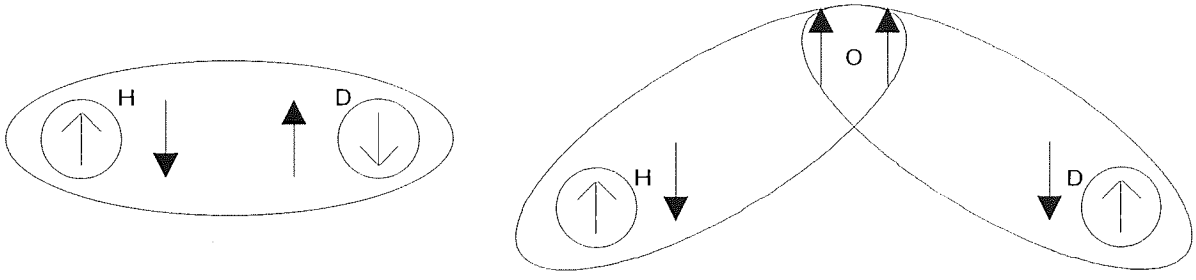

The sign of J is usually defined to be positive for anti-parallel nuclear spins and negative for parallel spins. From this model it can be seen that positive values of J will be obtained for coupling over an odd number bonds and negative over an even number of bonds (the nomenclature, ^{x}J, is used to specify the number of bonds, x, over which the coupling occurs).

For geminal protons, ^{2}J, is approximately -9 to -21 Hz: the magnitude of J is attenuated over an increasing the number of bonds becoming negligible for $^{4}J_{HH}$. For vicinal protons, ^{3}J, Karplus[37, 38] has shown a variation in J with the dihedral angle between the protons. The magnitude of J becomes large for angles zero (gauche) and π (trans) radians where the p-orbital overlap is at its greatest. Coupling is enhanced in unsaturated molecules and can extend over many bonds.

When coupling occurs between nuclei other than protons then the magnitude and sign of J depends on the product of the two magnetogyric ratios. The coupling constants for differing elements can be compared by using the reduced coupling constant, K given by,

$$K = \frac{4.\pi^2.J}{\hbar.\gamma_A.\gamma_B} \qquad (1.38)$$

Spin-spin coupling can cause the spectrum of large molecules to become very complex and contain many over-lapping lines. The effect of spin-spin coupling can be removed by the technique known as spin decoupling. If the spin A transition, where A causes a splitting in X, is irradiated continuously with a rotating field, H_2, then, because the probability of up and down transitions are equal, the spin is saturated. Spin X experiences an average field due to A and the spin splitting is removed. By selective irradiation of A one or more resonant lines of X will collapse, showing the connectivities of neighbouring spins. Complete decoupling of all the X spins can be obtained by the application of non selective broadband, high power, irradiation to cause all of the A transitions to saturate.

Irradiation of A can cause a shift in the resonant frequency of X if $\gamma.H_2 > |\omega_A - \omega_X|$, and is known as the Bloch-Siegert shift[39, 40]. The presence of H_2 introduces an additional field component, dependent on the resonance offset, ΔH, from H_1, causing a change in the precessional frequency of X. The magnitude of the shift, $\Delta\nu$, may be calculated as,

$$\Delta\nu = \frac{1}{2}.\left(\frac{\gamma.H_2}{2.\pi}\right)^2.\left(\frac{2.\pi}{\gamma.\Delta H}\right) \qquad (1.39)$$

Much greater use of spin-spin coupling can be made in 2D experiments that were first suggested by Jeener[41]. It allows the connection between nuclei of differing chemical shifts, through their coupling constant, to be established. The spectrum is displayed in two dimensions relating to the spectra of the two nuclei, the appearance a peak at a frequency in both dimensions shows a correlation between the nuclei. Since the invention of COSY[42], (correlated spectroscopy), many other techniques have been published, a review of two dimensional techniques can be found in the text by Kessler et al[43] and Traficante[44].

1.9: NUCLEAR OVERHAUSER EFFECT

The spin decoupling by the irradiation of one nucleus coupled to another causes a modification in the intensity of the observed spin, due to a mechanism known as the Nuclear Overhauser Effect (NOE)[45, 46, 47]. The NOE effect can be seen for two homonuclear dipolar coupled spins, I and S, in the absence of J coupling. The system contains four energy levels $\alpha\alpha$, $\alpha\beta$, $\beta\alpha$, $\beta\beta$, the levels $\alpha\beta$ and $\beta\alpha$ can be

considered to be degenerate because the chemical shifts the two spins are small in comparison to the Larmor frequency. Transitions between the energy levels are governed by rate constants, and the observable single quantum transition rates (quantum mechanical selection rule $\Delta M=+1$)are denoted W_1^I, W_1^S for the two I and two S transitions respectively. In addition to these there are non-observable zero quantum and a double quantum transition rates denoted W_0 and W_2 respectively, see figure 1.12.

Figure 1.12: Transition rates for a dipolar coupled IS system.

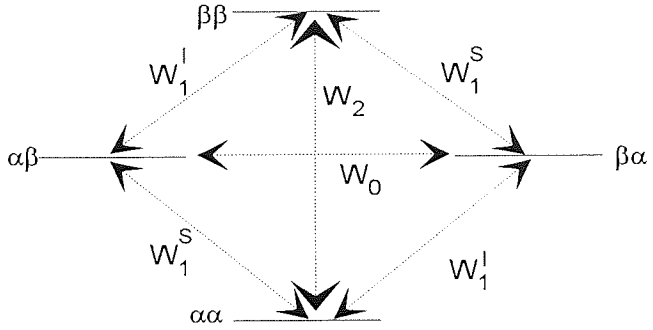

At equilibrium the population is governed by a Boltzmann distribution such that for a total population 4p there will be an excess, Δ, between the levels given by:

$$P_{\alpha\beta}^{eqm} = P_{\beta\alpha}^{eqm} = p,\ P_{\alpha\alpha}^{eqm} = p + \Delta \text{ and } P_{\beta\beta}^{eqm} = p - \Delta \qquad (1.40)$$

The intensity can then be calculated for each transition, from the population difference, as;

I transitions: $$(P_{\alpha\alpha}^{eqm} - P_{\beta\alpha}^{eqm}) + (P_{\alpha\beta}^{eqm} - P_{\beta\beta}^{eqm}) = 2\Delta \qquad (1.41)$$

S transitions: $$(P_{\alpha\alpha}^{eqm} - P_{\alpha\beta}^{eqm}) + (P_{\beta\alpha}^{eqm} - P_{\beta\beta}^{eqm}) = 2\Delta \qquad (1.42)$$

Applying an r.f. saturation field equalises the populations across the S transitions ($P_{\alpha\alpha}^{Sat} = P_{\alpha\beta}^{Sat} = p + 1/2\Delta$ and $P_{\beta\alpha}^{Sat} = P_{\beta\beta}^{Sat} = p - 1/2\Delta$) and the new intensities of the spin system are given by:

I transitions: $$(P_{\alpha\alpha}^{Sat} - P_{\beta\alpha}^{Sat}) + (P_{\alpha\beta}^{Sat} - P_{\beta\beta}^{Sat}) = 2\Delta \quad (1.43)$$

S transitions: $$(P_{\alpha\alpha}^{Sat} - P_{\alpha\beta}^{Sat}) + (P_{\beta\alpha}^{Sat} - P_{\beta\beta}^{Sat}) = 0 \quad (1.44)$$

The above shows that saturation of the S spin has caused no net change in the intensity of the I transitions for single quantum transition mechanism only.

However, examining the population difference across the zero quantum (ΔM=0) and double quantum (ΔM=2) transitions, for equilibrium and S saturated conditions, it can be seen that:

W_0 transition: $$(P_{\alpha\beta}^{eqm} - P_{\beta\alpha}^{eqm}) = 0 \quad \rightarrow \quad (P_{\alpha\beta}^{Sat} - P_{\beta\alpha}^{Sat}) = \Delta \quad (1.45)$$

W_2 transition: $$(P_{\alpha\alpha}^{eqm} - P_{\beta\beta}^{eqm}) = 2\Delta \quad \rightarrow \quad (P_{\alpha\alpha}^{Sat} - P_{\beta\beta}^{Sat}) = \Delta \quad (1.46)$$

Therefore, under saturation conditions the W_0 transition has gained a population difference of Δ and the W_2 transitions has lost a population difference of Δ. The system has now been perturbed from equilibrium and therefore transitions will occur to re-establish the populations, i.e. W_0 to zero and W_2 to 2Δ. Both W_1^S transitions have been saturated by an excitation field and cannot return to equilibrium.

The W_0 mechanism will attempt to regain equilibrium by transferring population from $\alpha\beta$ to the $\beta\alpha$ state to decrease the population difference across the I

transitions, whilst the W_2 mechanism returns spins from $\beta\beta$ to $\alpha\alpha$ so increasing the population difference across the I transitions. The transfer of spin population by the W_0 and W_2 mechanisms perturbs the I spins from equilibrium, therefore, both W_1^I transitions will act to maintain a population difference of 2Δ.

The NOE effect is then based upon three interacting mechanisms on spin I, the zero quantum transition decreases the signal intensity of spin I, the double quantum transition increases the signal intensity and the W_1^I transitions will attempt to oppose both mechanisms in order to maintain the signal intensity.

The enhancement attained from the NOE effect depends on which of the forbidden mechanisms is dominant. For two spin 1/2 nuclei, such as protons, which are relaxed by the dipolar mechanism only, then the maximum NOE enhancement, η, possible is given by,

$$\eta = \frac{\gamma_S}{\gamma_I} \cdot \frac{(W_2 - W_0)}{(2W_1^I + W_2 + W_0)} \qquad (1.47)$$

If the nuclei are in the extreme narrowing limit ($\omega^2\tau_c^2 << 1$) then the relative transition rate for each mechanism becomes; $W_0:W_1:W_2 = 2:3:12$ and η is equal to 0.5. Conversely for slow tumbling, $\omega^2\tau_c^2 >> 1$, the W_0 mechanism is the most effective and negative NOE's are observed. For a heteronuclear system the NOE sign and enhancement are dependent on the magnetogyric ratios of the two nuclei, e.g. for $^{13}C/^{1}H$ the ratio is ≈ 4 giving an enhancement of 2.

The NOE enhancement can be measured experimentally from the line intensities for the equilibrium, I_0, and non equilibrium (decoupled), I_z, condition. The NOE enhancement for the I spin by saturating S is defined as;

$$\eta_I(S) = \frac{(I_z - I_0)}{I_0} \tag{1.48}$$

CHAPTER 2

EXPERIMENTAL NMR

2.0: FOURIER TRANSFORM NMR

During continuous wave (CW) NMR either the frequency or the field is swept to excite individual nuclear transitions to give the NMR spectrum. In Fourier Transform NMR all the transitions are excited simultaneously by a pulse of radio frequency (r.f.) radiation and the response of the spin system is observed. The advantage of this method is that multiple acquisitions can be made in a shorter time period and accumulated to improve the signal to noise.

2.1: PULSE EXCITATION

Excitation of all the spin transitions is achieved by the application of a pulse of frequency, ω_0. The Heisenberg's uncertainty principle[48] implies that a pulse of duration, t_p, will also contain a bandwidth of frequencies t_p^{-1} centred about the carrier frequency, $\omega_{r.f.}$. By increasing the length of the pulse the uncertainty in the frequency is reduced and, therefore, the bandwidth of frequencies. A Fourier Transform ($\mathcal{FT}$) (section 2.6) of a pulse shows the frequency bandwidth it contains, figure 2.0.

Figure 2.0: Fourier transform of a square wave pulse.

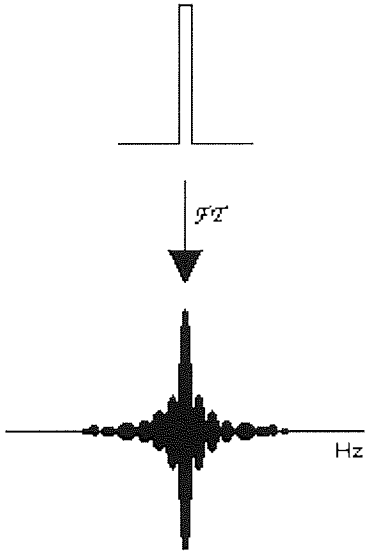

At equilibrium the bulk magnetisation is aligned along H_0. Application of a pulse along the x'-axis of; frequency ω_o, strength H_1 and duration t_p, will impose a torque on M_0 causing it to rotate through some angle, θ, into the y-z plane, figure 2.1. The angle of rotation can be calculated using equation (2.1) where t_p is the pulse length and is usually the order of a few μs,

$$\theta = \gamma . H_1 . t_p \qquad (2.1)$$

Figure 2.1: Tip angle in the rotating frame.

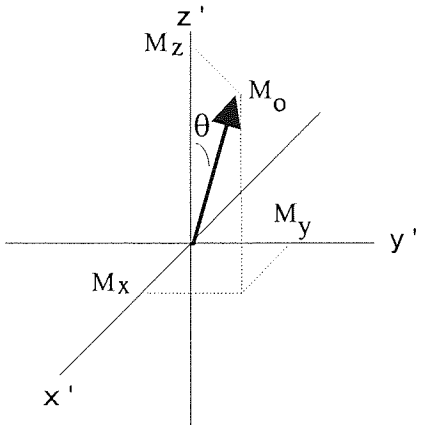

The tip angle that M_o makes with z-axis determines the component of magnetisation remaining in the z-axis, M_z, and therefore, the distribution of the spins between their energy levels. When θ is equal to zero then $M_z=M_0$ and the spins have a Boltzmann distribution with the lower energy state more populated. Conversely at $\theta=180^0$ the inverse Boltzmann distribution exists. At $\theta=90^0$ then $M_z=0$ and there is an equal number of spins in each of the energy states. This situation is analogous to continuous wave saturation, however, the pulse has the effect of creating a phase coherence between all of the spins, giving a transverse magnetisation vector, saturation in the rotating frame is equivalent to $M_x=M_y=M_z=0$.

After a pulse has been applied the magnetisation vector will precess in the x-y plane. With time the magnetisation vector will relax back to equilibrium with a rate governed by T_1 for M_z and T_2 for M_x and M_y, see figure 2.2.

Figure 2.2: Movement of magnetisation components.

$$\text{Equilibrium} \xrightarrow{\gamma.H_1.t_p} \text{Resonance} \xrightarrow{\text{relaxation}} \text{Equilibrium}$$

$$\sum_i \mu_{zi} = M_0 \qquad M_z \xrightarrow{e^{-\frac{t}{T_1}}} M_0$$

$$\sum_i \mu_{yi} = 0 \qquad M_y \xrightarrow{e^{-\frac{t}{T_2}}} 0$$

$$\sum_i \mu_{xi} = 0 \qquad M_x \xrightarrow{e^{-\frac{t}{T_2}}} 0$$

Experimental values for the transverse relaxation time, T_2, are usually a lot shorter than the time predicted for spin-spin relaxation mechanism acting alone. This is because transverse magnetisation also decays by a loss of phase coherence of the spins due to magnetic field inhomogeneitity. Consequently T_2 is replaced with a new time, T_2^*, which measures the actual decay of transverse magnetisation.

2.2: OFF RESONANCE EFFECTS

It is usually assumed that the amplitude of the r.f. pulse is large enough to excite equally all the spin transitions within the chemical shift range of interest, i.e. $|\gamma.H_1| >> |\omega - \omega_{r.f.}|$. Sometime this requirement does not hold and off-resonance effects occur. As seen in section 1.4 when the precessional frequency of a nucleus, ω_0, moves away from the rotating frame frequency, $\omega_{r.f.}$, then it will experience an effective field,

$$H_{eff} = \left\{ H_1^2 + \left(\frac{(\omega_{r.f.} - \omega_0)}{\gamma} \right)^2 \right\}^{\frac{1}{2}} \qquad (2.2)$$

which makes an angle α to the z-axis given by,

$$\tan\alpha = \frac{\gamma.H_1}{(\omega_{r.f} - \omega_0)} \qquad (2.3)$$

The application of a pulse will nutate M_z about H_{eff} by an angle β_{eff},

$$\beta_{eff} = \gamma.H_{eff}.\tau_p \qquad (2.4)$$

The consequence of equation 2.4 is that M_z is nutated by a reduced angle dependent on the magnitude of H_{eff}. Thus, M_z is not nutated by the full angle as for

the on resonance case but by some other angle giving magnetisation components,

$$M_x = M_0.\sin\beta_{eff}.\sin\alpha \tag{2.5}$$

$$M_y = M_0.(1-\cos\beta_{eff}).\sin\alpha.\cos\alpha \tag{2.6}$$

$$M_z = M_0.(\cos^2\alpha + \cos\beta_{eff}.\sin^2\alpha) \tag{2.7}$$

A 90^0 pulse applied along the x-axis will nutate on resonance magnetisation to lie along the y-axis. Any off resonance magnetisation will give transverse components with a phase shift, ϕ, from the y-axis depending on the tip angle and the magnitude of H_{eff} that the spin experiences,

$$\tan\phi = \frac{(1-\cos\beta_{eff})\sin\alpha}{\sin\beta_{eff}}.\frac{|\omega-\omega_0|}{-\gamma.H_1} \tag{2.8}$$

Consequently, it is not possible to invert the spin population of off resonance magnetisation, an important requirement in the measurement of pulse widths. Off resonance effects can be minimised by using composite pulse sequences such as DANTE[49].

2.3: DETECTION AND DATA ACQUISITION

The NMR signal is detected by a receiver coil, which is usually treated as having its axis aligned with the y-axis of the rotating frame so that it is initially in phase with the magnetisation component, M_y. The time dependent magnetisation components M_x and M_y induce an e.m.f in the coil which is amplified to give a free induction decay, figure 2.3.

Figure 2.3: Free induction decay during acquisition.

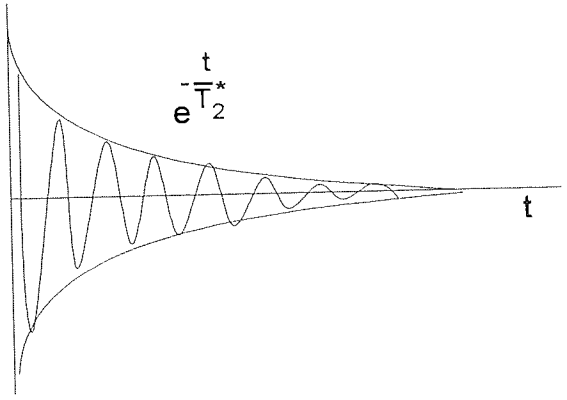

The FID decays exponentially with a rate governed by T_2^*, if the magnetisation is exactly on resonance then the FID will take the form of a single exponential line. However, as the magnetisation moves away from resonance then the FID will vary sinusoidally with a frequency dependent on its shift from resonance.

The e.m.f induced in the receiver coil of a probe is an analogue response of the spin system to a pulse, the intensity of which is very low and must be amplified. Signals emerging from the NMR probe are at the Larmor frequency plus or minus the chemical shift frequency, and a phase sensitive detector simplifies the signal by subtracting the carrier frequency, $\omega_{r.f.}$, to leave the low frequency chemical shift components.

In order for the NMR signal to be processed and interpreted by the spectrometer it must be converted by an analogue to digital converter (ADC) into a digital data set. The dynamic range of the ADC is the weakest signal that can be digitised in the presence of a strong signal. For a 16 bit ADC the largest integer that can be stored is 65535 (2^{16}-1). If the ratio of the strongest signal to the weakest is larger

than 65535:1 then the dynamic range is exceeded and the weaker signal will not be digitised correctly. Dynamic range is important in liquid state NMR where solvent resonances may dominate the spectrum and the solute resonance of interest can not be observed. Solvent suppression can be achieved, for example, by irradiating the solvent peak, before beginning the experiment, to partially saturate its resonance therefore reducing its magnitude.

2.4: QUADRATURE DETECTION AND PHASE CYCLING

Magnetisation in the x-y plane can have a frequency of $\omega_0 \pm \Delta\omega$. In the rotating frame transverse magnetisation would precess clockwise or anticlockwise depending on the sign of $\Delta\omega$. A single detector placed on the x' axis would be insensitive to the sense of rotation and on Fourier transformation (section 2.6) the resulting spectrum would give two peaks centred about the carrier frequency. The sense of rotation can be determined by using a second receiver placed on the y'-axis, however, this arrangement is not physically practical in the confines of a NMR probe.

In practice a single detector coil is used and the signal is split and delivered to two phase sensitive detectors, which are being supplied with reference signal having a 90^0 phase shift. The two components of the signal, due to the phase shift, consist of a cosine and sine wave. Figure 2.4 shows the Fourier transform of the two components. A Fourier transform of the even cosine function produces two positive peaks whereas the odd sine function produces one positive and one

negative peak. Combining the two spectra will eliminate one of the peaks depending on the sense of rotation of the original signal.

Figure 2.4: Fourier transform components of sine and cosine functions.

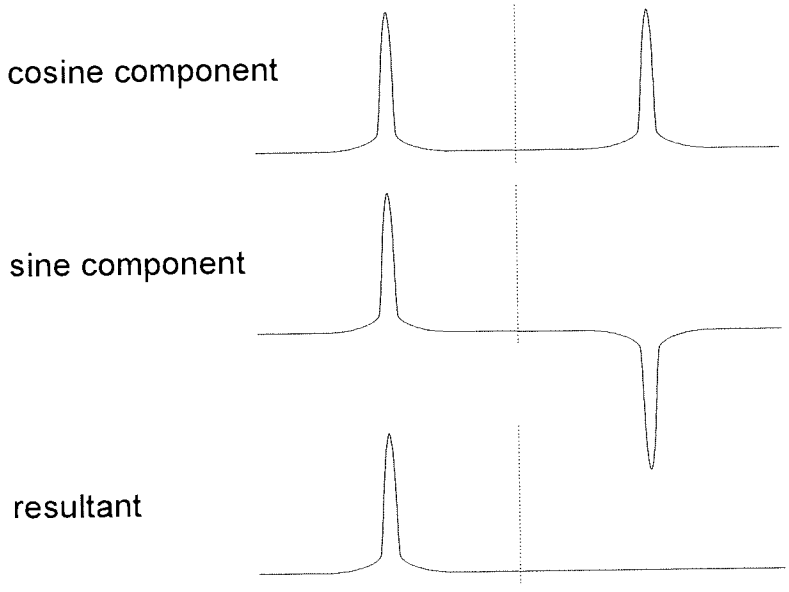

Further information on quadrature detection can be found in the article by Hoult[50].

If the phase of the pulse and the detector are not orthogonal then ghost images from the resonance peak appear symmetrically, about the carrier centre. This is caused by the failure of the quadrature detection system to perfectly cancel the resonance components. The result is the appearance of a mirror image of the peak about the carrier frequency. To remove artifacts in the spectrum the phase of the pulser and detector channels can be cycled in 90^0 steps along the x, y, -x and -y axes. The phase rotation sequence known as CYCLOPS (cylindrically ordered phase cycle)[50] is used to suppress any undesired peaks and to remove any d.c. offset artifacts.

Phase cycling of pulses becomes important in the selection of coherence pathways in many pulse sequences. Use of the correct phase cycle will select or remove particular multiple quantum coherences.

2.5: SAMPLING THEOREM

The analogue signal entering the ADC is sampled for a finite time. Sampling theorem dictates that if features of separation $\Delta\nu$ are to be resolved then the signal must be sampled for $1/\Delta\nu$ seconds. The sampling time is usually referred to as the acquisition time, A_t, and for protons in the liquid state it is the order of 2-3 seconds.

An analogue frequency can be digitally characterised by measuring the amplitude of the waveform at discrete points. In order for a frequency, $\mathcal{N}$, to be characterised correctly by the ADC then the sampling rate must be $2\mathcal{N}$. The Nyquist frequency, $\mathcal{N}$, defines the maximum frequency or spectral width that the sampling rate of the ADC can handle, i.e. if a frequency of up to $\mathcal{N}$ Hz is presented to the ADC then the signal must be sampled every $1/2\mathcal{N}$ s.

The effect of an insufficiently fast sampling rate is shown for two wave forms of differing frequency in figure 2.5. Each of the two frequencies are digitised at the points marked "X". The solid line has a frequency less than the rate of digitisation and is sampled correctly. The dotted line has a higher frequency and contains an

extra cycle before being sampled. However, the ADC is unaware of the extra cycle and will characterises it as having a lower frequency.

Figure 2.5: Effect of insufficient data points required to characterise a signal.

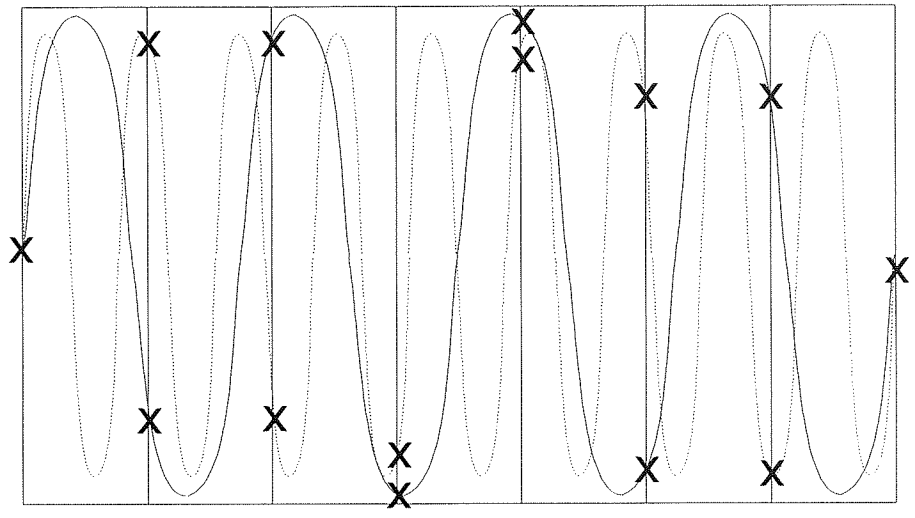

The resulting spectrum will contain one peak of the correct frequency and a second peak, often out of phase, 'folded' to the edge of the spectrum. Folded peaks are easily determined by moving the carrier frequency. If the peak moves in the opposite direction to that of the carrier frequency then it is genuine, however, if it moves in an unpredictable manner or disappears then its folded.

To resolve features on a peak then a sufficient number of data points must lie on it. The digital resolution, $\mathcal{R}_d$, required to characterise a feature, is equal to the inverse of the acquisition time or,

$$\mathcal{R}_d = \frac{2.SW}{N} \tag{2.9}$$

where SW is the spectral width, in Hz, of the spectrum and N is the size of the data set. Digital resolution can be improved by a technique known as zero filling. For the technique to be possible then the acquisition time must be set such that the FID has sufficiently decayed into the baseline. The size of the time domain data set, N, can be increased by the addition of zero amplitude data points to the end of the FID. Zero filling is a cosmetic effect to increase the digital resolution of a feature in a spectrum, improving its appearance.

2.6: FOURIER TRANSFORM

Conversion of the FID from the time domain data to the frequency domain is achieved by a mathematical process known as Fourier transform[51]. Time and frequency are related by the Fourier relationship,

$$F(\omega) = \int_0^{\infty} f(t).e^{-i\omega t}dt \qquad (2.10)$$

given that $e^{i\omega t} = \cos\omega t + i\sin\omega t$,

$$Re[f(\omega)] = \int_{-\infty}^{\infty} f(t)\cos(\omega t)dt \qquad (2.11)$$

$$Im[f(\omega)] = \int_{-\infty}^{\infty} f(t).\sin(\omega t)dt \qquad (2.12)$$

Equations 2.11 and 2.12 correspond to the real and imaginary parts of the line shape, see figure 2.6. The peak obtained now not only contains information about its frequency and amplitude but also the relative mixture of the real and imaginary components gives information about the phase of the peak.

Figure 2.6: Absorption (real) and dispersion (imaginary) components of the acquired signal.

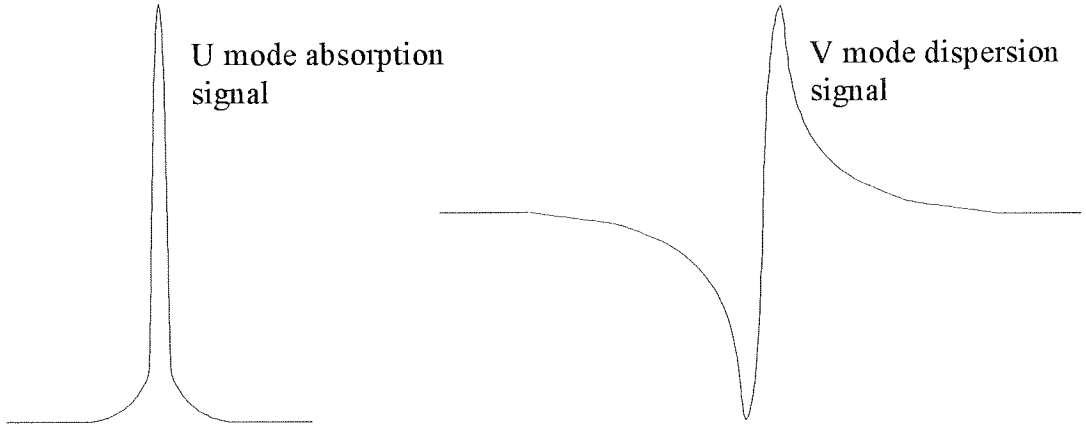

The NMR spectrum is usually plotted for the absorption lineshape, where the peak amplitude is governed by the intensity of the first data point of the FID and the full (line) width at half maximum (FWHM), of the absorption mode, is equal to $1/\pi T_2^*$.

The intensity of the dispersion mode signal is zero at the center of its resonance, any change in line width is reflected in a change in the spread of its wings. A dispersion mode signal is detected in the frequency locking of the field. When the magnetic field is of the correct strength then the dispersion signal is exactly on resonance and the signal intensity is zero. Any shift in the magnetic field strength will cause the detected intensity of a dispersion mode signal to become positive or negative. A feedback circuit detects the sign of the signal and applies the appropriate field strength correction to return the intensity to zero. The deuterium resonance is commonly used for frequency locking because its resonant frequency is very different from common nuclei of interest such ^{1}H or ^{13}C.

2.7: TRUNCATION AND SATURATION

The exponential decay of the FID is dependent on the relaxation time T_2^*. If the acquisition time is shorter than the time required for the FID to decay into the baseline then the FID is truncated. The FID now has partial exponential character and partial step function (sinc x≡(sin x)/x) character. The result can be seen in figure 2.7 as a super-position of the two functions.

Figure 2.7: Effect of terminating the FID before it has fully decayed.

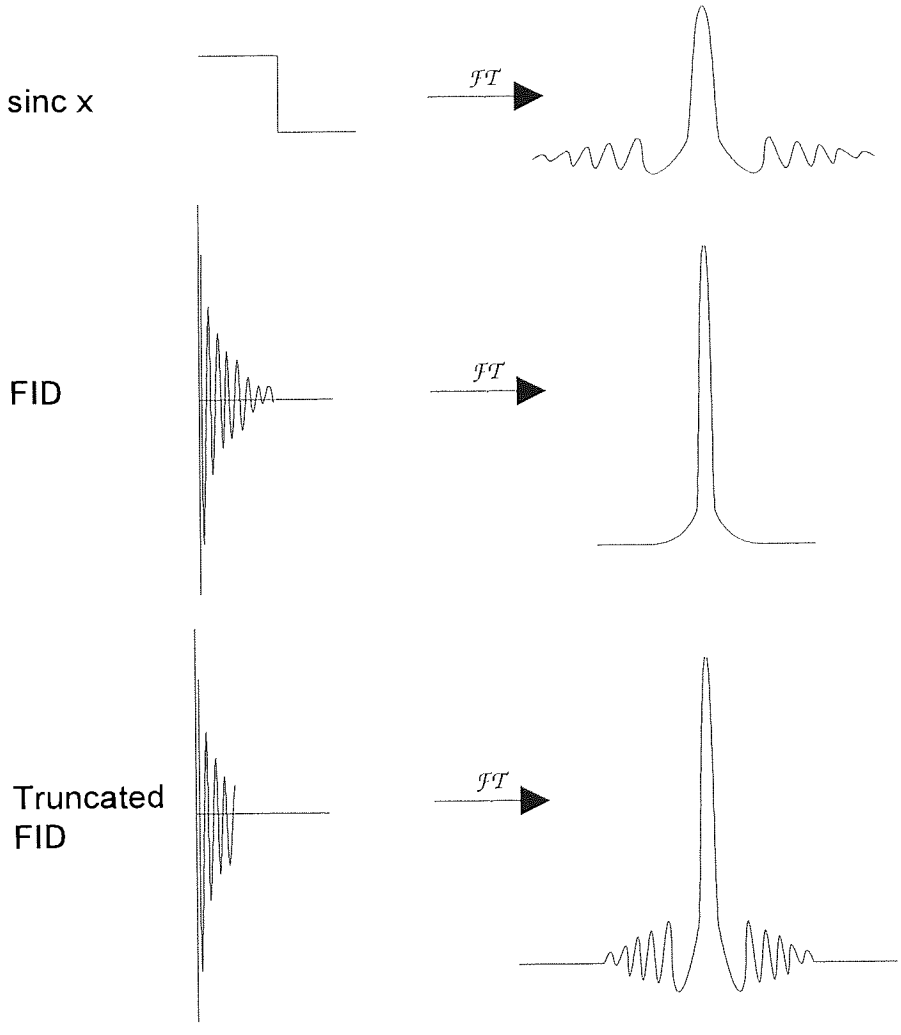

Electronic saturation of the ADC occurs when the spectrometer receiver gain has been set too high. If the signals over load the ADC then they are all represented

by the same maximum binary number. The FID is clipped with flat regions top and bottom until the signal has sufficiently decayed to be represented by a lower binary number. The resulting transform of a clipped FID contains distortions in the baseline.

2.8: SIGNAL TO NOISE AND ERNST ANGLES

In order to improve the S/N ratio then it is necessary to accumulate multiple acquisitions of the NMR signal. Each acquisition also contains a certain degree of noise which is accumulated along with the NMR signal. If n scans are accumulated the signal to noise (S/N) is increased by $\sqrt{n}$, i.e. to obtain a ten-fold increase in the signal to noise then a hundred times the number of scans is required.

When considering equal numbers of nuclei the signal intensity is determined by the tip angle of the magnetisation vector, and the maximum signal is achieved with a 90^0 pulse. However, to prevent saturation of the resonance the experiment can only be repeated after the signal has fully relaxed ($5.3T_1$). Thus, the time required to wait between pulses is a function of the tip angle, i.e. how much z magnetisation already exists.

Steady state magnetisation can be achieved by selecting a repetition rate and tip angle where the magnetisation, M_z, relaxes back to its previous value before being pulsed again. Such a relationship exists through what is known as the Ernst angle[52], which is given by:

$$\cos\theta_E = e^{-\frac{t}{T_1}} \qquad (2.13)$$

For protons $T_2^* \approx T_2 \approx T_1$ and provided that the transverse magnetisation decays completely between pulses then the optimum repetition time, t_r, is equal to the acquisition time, A_t, where small angles are used to given quantitative results. However, for heteronuclei $T_1 > T_2 > T_2^*$ and small angles are necessary to achieve steady state.

CHAPTER 3

AN INTRODUCTION TO SOLID STATE NMR

3.0: SOLID STATE NMR

NMR line widths obtained from solids are inherently broad by comparison with liquid or solution spectra. In liquids rotational motion, which is fast compared to the NMR time scale, causes spatial averaging of the tensors (see appendix 1) of each Hamiltonian operator to reduce it down to its trace value. This eliminates all interactions except for chemical shift and scalar coupling, resulting in high resolution spectra. In the solid state the lattice is essentially static and therefore, in the absence of motional averaging, all the Hamiltonian operators are non-zero and thus contribute to the line shape. For a given spin system the total Hamiltonian is composed of the following Hamiltonians (some of which have been discussed in the previous chapter),

$$\mathcal{H} = \mathcal{H}_Z + \mathcal{H}_{R.F.} + \mathcal{H}_{CS} + \mathcal{H}_Q + \mathcal{H}_{SR} + \mathcal{H}_D + \mathcal{H}_J \qquad (3.1)$$

where, $\mathcal{H}_Z$: Zeeman interaction, $\mathcal{H}_{RF}$: Spin interaction with the external r.f. field, $\mathcal{H}_{CS}$: Chemical shift, $\mathcal{H}_Q$: Quadrupolar interaction, $\mathcal{H}_{sr}$: Spin rotation, $\mathcal{H}_D$: Dipolar coupling, $\mathcal{H}_J$: J-coupling.

The dominant operators in solid state NMR that are responsible for line broadening are $\mathcal{H}_D$, $\mathcal{H}_{CS}$, $\mathcal{H}_Q$. The relevant Hamiltonians are discussed in a review by Smith et al[53].

3.1: DIPOLAR INTERACTION

In solids the principal broadening mechanism is dipolar coupling which is caused by the interaction of two (or more) nuclear dipoles. The magnetic moment of each spin generates a local field that can be experienced, through space, by other nuclei. The energy for two interacting dipoles is dependent on their separation, r, given by

$$E_D = \left\{ \frac{\mu_j . \mu_k}{r_{jk}^3} - \frac{3.(\mu_j . r_{jk}).(\mu_k . r_{jk})}{r_{jk}^5} \right\} \qquad (3.2)$$

where $\mu_{j,k}$ are the dipole moments for the two nuclear spins (or an electron). For multiple, N, spins, the Hamiltonian can be expressed by the summation,

$$\mathcal{H}_D = \frac{1}{2} \sum_{j=1}^{N} \sum_{k=1}^{N} \left\{ \frac{\mu_j . \mu_k}{r_{jk}^3} - \frac{3.(\mu_j . r_{jk}).(\mu_k . r_{jk})}{r_{jk}^5} \right\} \qquad (3.3)$$

(the energy is halved so that each spin interaction is not counted twice and $j \neq k$).

Figure 3.0 shows the situation for two spins in the laboratory frame where H_0 is parallel to the z-axis: the orientation of the internuclear vector with respect to the magnetic field is characterised by polar coordinates.

Figure 3.0: Dipole-dipole interaction.

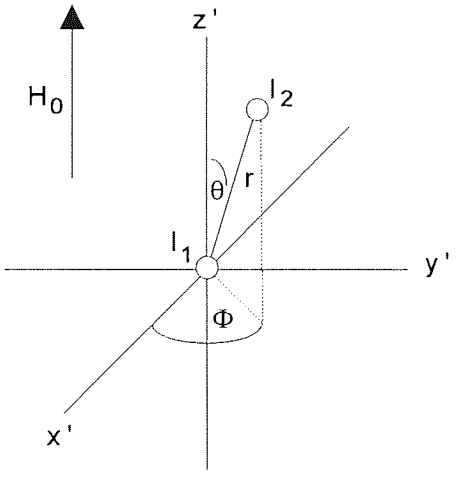

Given that; $\mu = \gamma.\hbar.\mathbf{I}$ and $\mathbf{I} = I_x x + I_y y + I_z z$, equation 3.3 can be expanded, in terms of polar coordinates. The result is the dipole alphabet (the terms $I^{\pm} = I_x \pm i I_y$ are the raising and lowering operators and have the effect of causing a change up or down in the quantum number, m, of a spin),

$$\mathcal{H}_D = \left(\frac{\gamma_1.\gamma_2.\hbar^2}{r_{12}^3}\right).(A+B+C+D+E+F) \tag{3.4}$$

$$A = I_{1z}.I_{2z}(3.\cos^2\theta - 1) \tag{3.5}$$

$$B = -\frac{1}{4}.(I_1^+.I_2^- + I_1^-.I_2^+).(1-3\cos^2\theta) \tag{3.6}$$

$$C = -\frac{3}{2}.(I_1^+.I_{2z} + I_{1z}.I_2^+).\sin\theta.\cos\theta.e^{-i\phi} \tag{3.7}$$

$$D = -\frac{3}{2}.(I_1^-.I_{2z} + I_{1z}.I_2^-)\sin\theta.\cos\theta.e^{i\phi} \tag{3.8}$$

$$E = -\frac{3}{4}.I_1^+.I_2^-.\sin^2\theta.e^{-2i\phi} \tag{3.9}$$

$$F = -\frac{3}{4}.I_1^-.I_2^-.\sin^2\theta.e^{2i\phi} \tag{3.10}$$

The first term on the RHS of equation 3.4 is the dipolar coupling constant (not to be confused with the term D of the alphabet expansion).

$$\mathcal{D} = \frac{\gamma_1.\gamma_2.\hbar^2}{r_{12}^3} \tag{3.11}$$

The spin interaction of each term in the dipole alphabet can be seen for a two spin system in figure 3.1.

Figure 3.1: Spin interaction for two dipoles in a IS system.

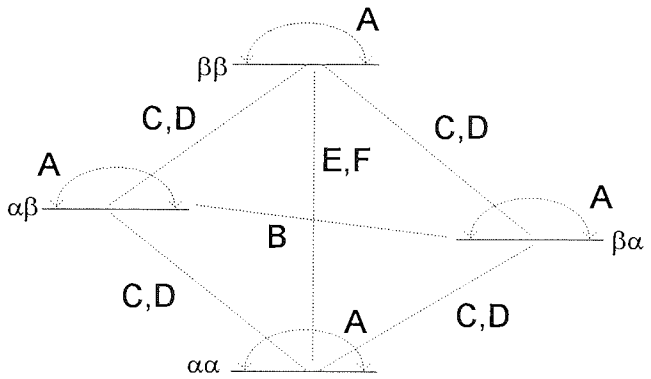

The A term describes the static dipolar field produced at one spin due to the z-component of a magnetic moment of another nucleus. The precessional motion of a magnetic moment, μ_j, at the Larmor frequency, due to the presence of H_0, results in time dependent x and y components of the dipolar field occurring at another nucleus, I_k. Therefore, the terms B-F describe coherences between the spin states caused by oscillating dipolar fields. In the heteronuclear AX case and for $\mathcal{H}_z >> \mathcal{H}_D$ only the A term is secular and contributes to a reduced Hamiltonian,

$$\mathcal{H}_D = -h(\nu_A . I_{Az} + \nu_X . I_{Xz}) + \mathcal{D} . I_{Az} . I_{Xz} . (1 - 3.\cos^2\theta) \qquad (3.12)$$

(ν is the resonant frequency for the spin).

The consequence of equation 3.12 is that, the spectrum of spin A will consist of two lines, each having a frequency given by.

$$\nu = \nu_A \pm \frac{1}{2} . \mathcal{D} . (1 - 3.\cos^2\theta) \qquad (3.13)$$

For a pair of isolated spins in a single crystal the spectrum of A (or X) will appear as two single lines with a separation of $\mathcal{D} . (3.\cos^2\theta - 1)$ depending on the crystal orientation with respect to the external field. When the crystal is at an angle of $54^0 44'$ to the external field then $\mathcal{D} . (3.\cos^2\theta - 1)$ becomes zero and a single line is

observed. In the case of a powder all orientations are possible and the spectrum becomes the Pake doublet[54], where the separation of the horns is equal to $\mathcal{D}$, see figure 3.2.

Figure 3.2: Powder pattern for two dipoles.

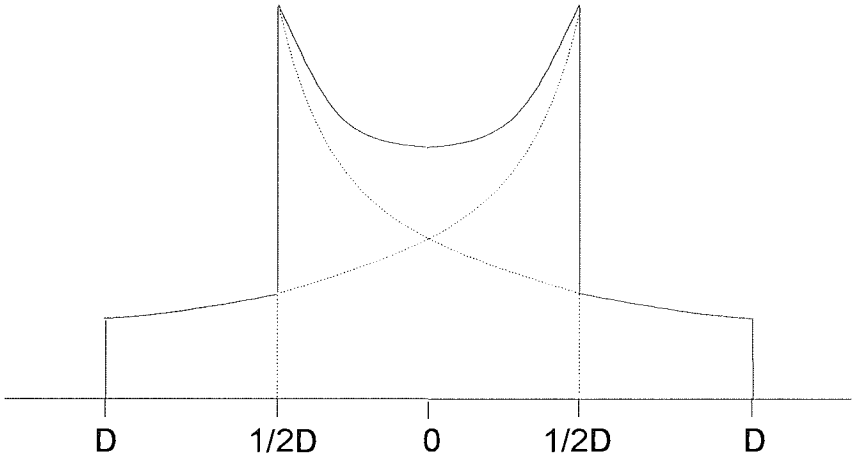

For homonuclear dipolar coupling, for $\mathcal{H}_z >> \mathcal{H}_D$, the $\alpha\beta$ and $\beta\alpha$ states are degenerate. The flip-flop (B) term is now secular and thus contributes to the dipolar Hamiltonian.

$$\mathcal{H}_{D,Homo} = \mathcal{D}.(3.\cos^2\theta - 1).\left[I_{1z}.I_{2z} - \frac{1}{4}.(I_1^+.I_2^- + I_1^-.I_2^+)\right] \qquad (3.14)$$

where $\left[I_{1z}.I_{2z} - \frac{1}{4}.(I_1^+.I_2^- + I_1^-.I_2^+)\right]$ can be re-written as $\frac{1}{2}.(3.I_{1z}.I_{2z} - I_1.I_2)$. Thus, for a homonuclear two spin system, the spin transitions will occur at,

$$\nu = \nu_0 \pm \frac{3}{4}.\mathcal{D}.(1 - 3.\cos^2\theta) \qquad (3.15)$$

giving a doublet separation of $\frac{3}{2}.\mathcal{D}.(1 - 3.\cos^2\theta)$.

As the dipolar coupling constant, $\mathcal{D}$, contains an internuclear separation term, r_{12}^{-3}, the magnitude of dipolar broadening will also depend on the whether the nuclear spins are abundant or dilute. An organic solid consists largely of C-H bonds, the close proximity and abundance of protons causes the ^{13}C resonance to be dominated by heteronuclear dipolar coupling. A ^{13}C-^{13}C homonuclear coupling will also be present but since the coupled nuclei are likely to be in different molecules (r_{12} is large) the interaction is much weaker.

3.2: CHEMICAL SHIFT ANISOTROPY

Chemical shift anisotropy (CSA) arises from the non-spherical distribution of electrons around a nucleus. The variation in shielding can be described by a 2nd rank tensor (see appendix 1) where the value of the shielding constant for a particular direction, $\sigma_{nn'}$, defines the electron density surrounding the nucleus with respect to the static field. A rigorous treatment of the shielding tensor can be found in the article by Anet and O'Leary[55].

In the liquid state the shielding experienced by the nucleus is described by a shielding constant, σ_{iso}. The value of σ_{iso} is derived from the time averaging of the shielding tensor, due to rapid molecular reorientation, and is given by:

$$\sigma_{iso} = 1/3(\sigma_{xx} + \sigma_{yy} + \sigma_{zz}) \qquad (3.16)$$

For the solid state no such averaging occurs and the full shielding Hamiltonian is given by,

$$\mathcal{H}_{CS} = \gamma.\hbar.\begin{pmatrix} H_x & H_y & H_z \end{pmatrix}.\begin{pmatrix} \sigma_{xx} & \sigma_{xy} & \sigma_{xz} \\ \sigma_{yx} & \sigma_{yy} & \sigma_{yz} \\ \sigma_{zx} & \sigma_{zy} & \sigma_{zz} \end{pmatrix}.\begin{pmatrix} I_x \\ I_y \\ I_z \end{pmatrix} \qquad (3.17)$$

By the careful choice of the molecular axis the tensor can be rotated into a new coordinate frame known as the principal axis system (see, for example, Haeberlen[56] for details). In this new frame off diagonal components are zero, leaving only the diagonal components $\sigma_{zz} \geq \sigma_{yy} \geq \sigma_{xx}$. The general form for the z-component of the shielding in a molecule of less than axially symmetry is given by,

$$\sigma_{zz} = \sigma_{iso} + \frac{1}{3}.\sum_{j=x,y,z}(3\cos^2\theta - 1)\sigma_{jj} \qquad (3.18)$$

Equation (3.18) shows that there is a $(3.\cos^2\theta\text{-}1)$ dependence in shielding experienced by the nucleus, where θ is the angle between the molecular axis and the external field. A similar angular dependence can be seen for the simplified case of an axially symmetric molecule ($\sigma_{zz}=\sigma_{//}$, $\sigma_{xx}=\sigma_{yy}=\sigma_{\perp}$):

$$\sigma_{zz} = \frac{1}{3}.(\sigma_{//} + 2.\sigma_{\perp}) + \frac{1}{3}.(3.\cos^2\theta - 1).(\sigma_{//} - \sigma_{\perp}) \qquad (3.19)$$

The first term on the RHS of equation 3.19 is the isotropic shift value and the second term ($\sigma_{//}$-$\sigma_{\perp}$) is the degree of anisotropy $\Delta\sigma$.

The theoretical powder patterns for; cubic, axially symmetric and non symmetric molecules are shown in figure 3.3.

Figure 3.3: Powder pattern for a; cubic (top), axially symmetric (middle) and non-axially symmetric (bottom) molecule.

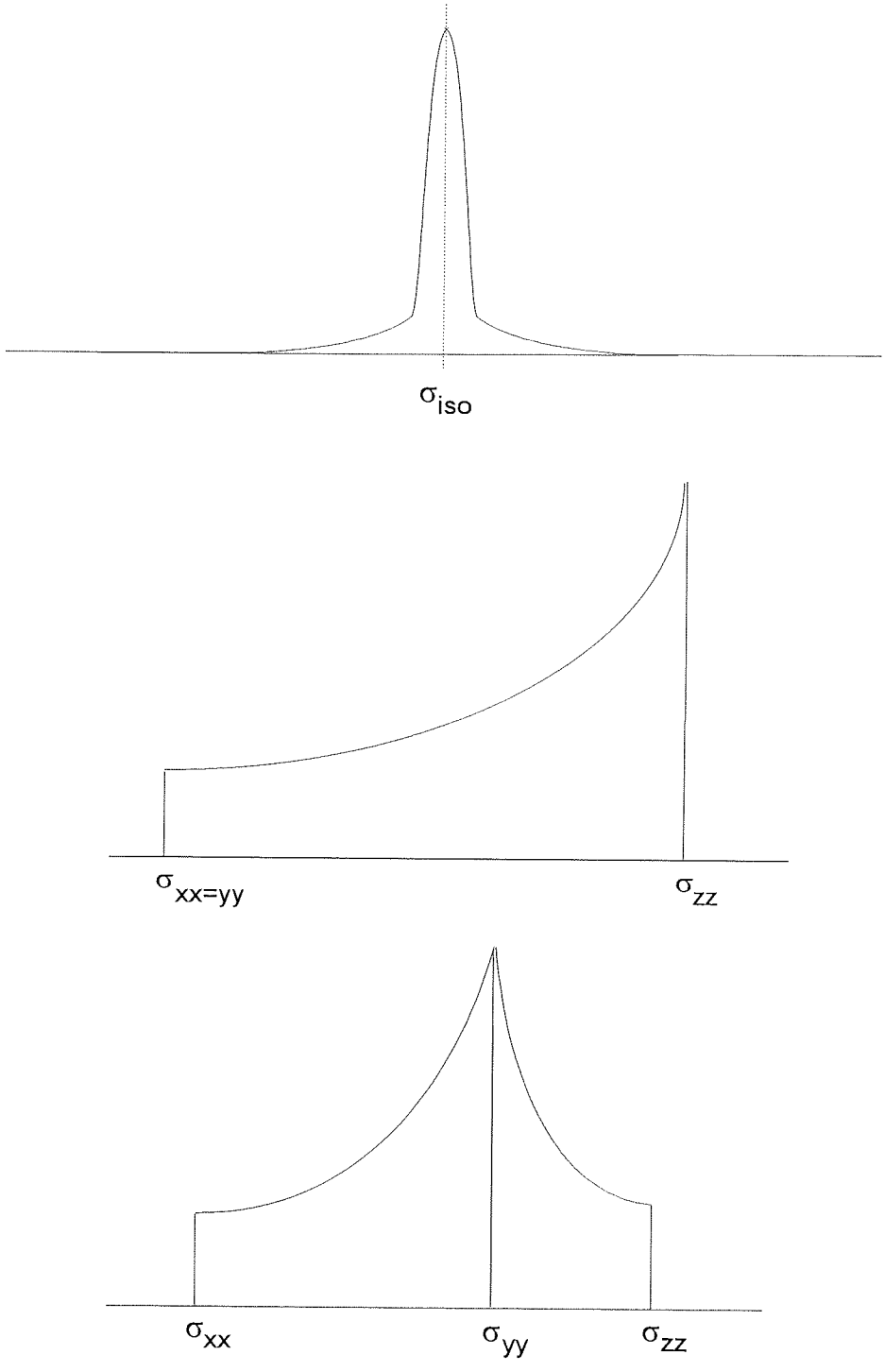

The point of greatest intensity, of figure 3.3, can occur at high or low resonance relative to σ_{iso} depending on whether $\sigma_{//}>\sigma_{\perp}$ or $\sigma_{\perp}>\sigma_{//}$ and is a measure of the preferred molecular orientation. The maximum intensity in the powder pattern is

not the isotropic shift and identical line shapes can be obtained for a variety of differing values of σ_{xx}, σ_{yy}, σ_{zz}, figure 3.4.

Figure 3.4: Change in pattern shape for identical isotropic shift.

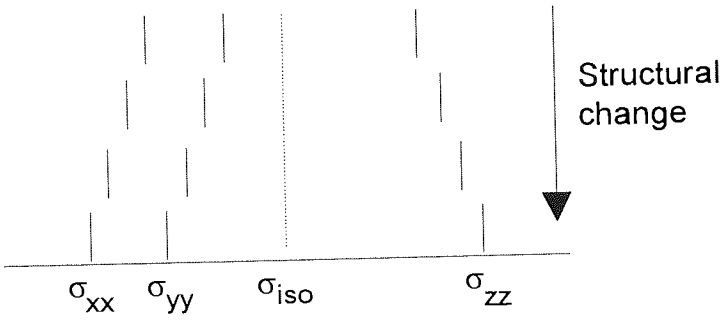

3.3: QUADRUPOLAR INTERACTION

For nuclei with spin>1/2 the quadrupolar effect dominates the nuclear interactions and the total spin Hamiltonian can be largely described by:

$$\mathcal{H} = \mathcal{H}_Z + \mathcal{H}_Q \tag{3.20}$$

The charge distribution for spin, 1/2, nuclei is spherical, however, for spin>1/2 nuclei the charge distribution is spheroidal. The nucleus now possess a quadrupolar moment , Q, the sign of which is dependent on whether the spheroid is prolate (positive Q) or oblate (negative Q) with respect to the axis of the nuclear spin. The quadrupolar Hamiltonian for a spin, I, is described by

$$\mathcal{H}_Q = \mathbf{I}.\hat{Q}.\mathbf{I} \tag{3.21}$$

$\hat{Q}$ is a tensor quantity arising from the interaction of the quadrupolar moment, Q, with the electric field gradient tensor, $\hat{V}$, present at the nucleus, given by,

$$\hat{Q} = \frac{eQ}{2I.(2I-1).h}.\hat{V} \tag{3.22}$$

If the molecule has cubic symmetry then there is no EFG axis present at the nucleus and the spin behaves in the normal Zeeman manner giving 2I+1 energy levels of equal separation.

For a molecule with axial symmetry there is a single EFG present at the nucleus. In the principal axis system the molecule can be orientated in such a way so that the EFG is characterised by the z-component of the electric field gradient component, V_{zz} (or by the charge, eq_{zz}). For the first order interaction, where $\mathcal{H}_z >> \mathcal{H}_Q$, the EFG perturbs the energy levels from their Zeeman splitting, ν_0, to give a shift in the frequency for the transition, $m \leftrightarrow m-1$, given by,

$$\nu_Q = \frac{3.(2m-1)}{8I.(2I+1)}.\chi.(3.\cos^2\theta - 1) \qquad (3.23)$$

where θ is the angle of the EFG vector with respect to H_0 and χ is the quadrupolar coupling constant:

$$\chi = \frac{e^2.q_{zz}.Q}{h} \qquad (3.24)$$

It can seen from equation (3.23) that the quadrupolar contribution for the centre band $(1/2 \leftrightarrow -1/2)$ transition is zero for all values of θ. However, when $\mathcal{H}_z \approx \mathcal{H}_Q$ then second order quadrupolar effects become important and the centre band transition is perturbed from the Larmor frequency, ν_0, by:

$$\nu''_{1/2,-1/2} = \left(\frac{\nu_Q}{16.\nu_0}\right).\left[I.(I+1) - \frac{3}{4}\right]\left(1-\cos^2\theta\right).\left(1-9.\cos^2\theta\right) \qquad (3.25)$$

If χ is large then the satellite transitions (e.g. $3/2 \leftrightarrow 1/2$ and $-1/2 \leftrightarrow -3/2$) are usually too weak to be observed in the NMR spectrum due to the influence of

$(3.\cos^2\theta\text{-}1)$. The influence of the first and second order quadrupolar interaction on the energy levels can be seen in figure 3.5 and the resulting first order powder pattern for an axially symmetric molecule in figure 3.6.

Figure 3.5: Spin 3/2 nucleus in EFG showing the first and second order quadrupolar interaction.

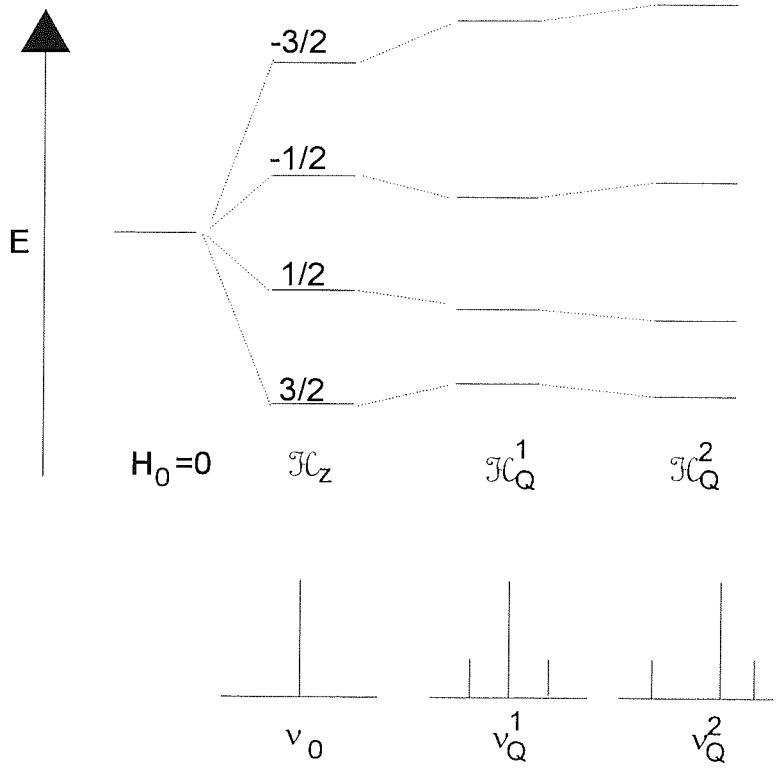

Figure 3.6: First order quadrupolar splitting powder pattern for a spin 3/2 nucleus in an axially symmetric molecule..

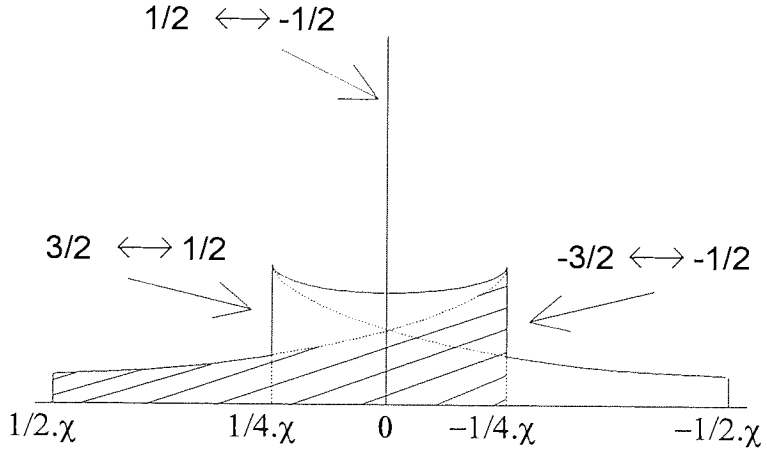

For a molecule of less than axial symmetry then more than one EFG will be present at the nucleus. Asymmetry in the molecular environment is defined by the parameter, η. In the principal axis system only the field gradient components, $q_{zz}>q_{xx}>q_{yy}$, are non zero giving,

$$\eta = \left(\frac{q_{xx} - q_{yy}}{q_{zz}} \right) \qquad (0 \leq \eta \leq 1) \tag{3.26}$$

The appearance of the quadrupolar powder pattern changes profoundly with increasing η and its effect on powder patterns has been simulated by Amoureux et al[57]. The quadrupolar shift from the Larmor frequency, ν_o, for the general symmetry case can be calculated for each transition, m$\leftrightarrow$m-1, through equation 3.21.

$$\nu'_{m,m-1} = \left(\frac{\nu_Q}{4} \right).(1-2.m).\left[(3.\cos^2\theta - 1) + (\eta.\sin^2\theta.\cos 2\phi) \right] \tag{3.27}$$

The angles θ and ϕ are defined in an analogous manner to figure 3.0 for the orientation of H_0 in the principal axis system of the EFG.

A more rigorous treatment of the quadrupolar effect can be found in the article by Taulelle[58].

3.4: RELAXATION IN SOLIDS

The effect of restricted motion in the solid state has a quite marked effect on the nuclear relaxation times. Spin-spin relaxation tends to be very rapid due to large correlation times for the nucleus. The inverse effect is true for spin-lattice

relaxation as the lack of molecular motion reduces the spread and intensity of the random magnetic fields necessary to induce transitions.

3.5: METHODS OF LINE NARROWING

3.5.1: MAGIC ANGLE SPINNING

Magic-angle spinning (MAS) was developed by Andrew[1] and Lowe[2] as a method for suppressing the dipole-dipole interaction in solids. It is based on rotating a sample at the so called magic angle of $54^o44'$ for which the solution of $(3.\cos^2\theta\text{-}1)$ (present in many of the above equations) is zero. Figure 3.7 shows the internuclear vector being rotated about the magic angle. By rotating at high speed the average direction of the vector, r_{jk}, becomes the magic angle, removing the appropriate interactions.

Figure 3.7: Inter nuclear vector rotating about the magic angle.

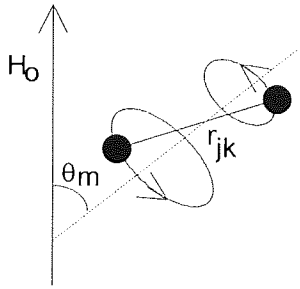

When a sample is spun at the magic angle the resonance will collapse to the isotropic shift value for the spin. However, if the spinning speed is less than the line width of the static solid resonance all the interactions are not completely removed and satellite transitions, know as spinning side bands, appear at multiples of the rotor speed.

It can be seen from equations (3.12) and (3.18) that MAS can be used to remove the dipolar interaction and chemical shift anisotropy. The first order quadrupolar interaction also has $(3.\cos^2\theta-1)$ dependence for an axially symmetric molecule, and can thus be removed by MAS. However, if the site symmetry for the nucleus is less than axially symmetric then the centre band transition, broadened by the term $(\eta.\sin^2\theta.\cos2\phi)$, will only be partially averaged by MAS. The second order quadrupolar effect contains no $(3.\cos^2\theta-1)$ terms and thus even for axially symmetric molecules (equation 3.25) MAS will have only a small effect on the line width.

3.5.2: DOUBLE ROTATION AND DYNAMIC ANGLE SPINNING

Higher order interactions of quadrupolar nuclei do not have a $3.\cos^2\theta-1$ dependence in their Hamiltonian, thus, spinning at the dipolar magic angle only partially removes their interactions. A technique to remove second order quadrupolar effects has been developed by Samosen and Pines[3]. This is known as double rotation. The double rotor (DOR) NMR makes use of two rotors, one inside the other, with individual rotational frequencies and relative angles to H_0 (and each other), see figure 3.8.

Pines et al[3] and Llor and Virlet[4] calculated the first and second order quadrupolar interaction from the angular dependence of the 2^{nd} and 4^{th} order Legendre polynomials

$$P_2 = \frac{1}{2}.(3.\cos^2\theta - 1) \quad (3.28)$$

$$P_4 = \frac{1}{8}.\left(35.\cos^4\theta - 30.\cos^2\theta + 3\right) \quad (3.29)$$

The rotor is constructed such that the angles θ_1 and θ_2 satisfy the condition $P_2(\cos\theta)=P_4(\cos\theta)=0$ of equations 3.28 and 3.29, i.e. $\theta_1=54.7^0$ and $\theta_2=30.56^0$ or 70.12^0. Further details of the solutions to DOR can be found in the article by Samoson et al[59].

Figure 3.8: Schematic of DOR probe operation.

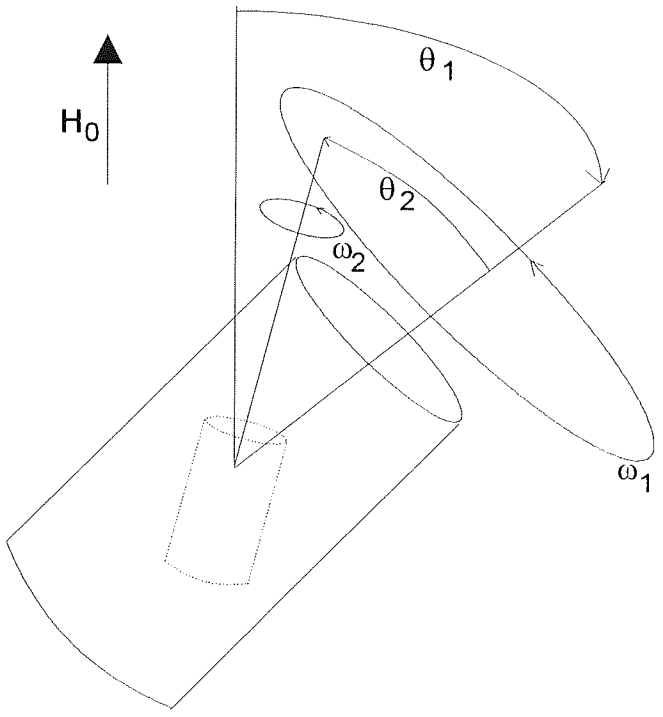

Dynamic angle spinning (DAS), which can achieve the same effect as DOR, was developed by Llor and Virlet[4], figure 3.9. A single rotor is placed at N discrete angles for a fraction of time , κ_i, such that:

$$\sum_{i}^{N} P_2(\cos\theta).\kappa_i = \sum_{i}^{N} P_4(\cos\theta).\kappa_i = 0 \qquad (3.30)$$

An infinite number of complementary angles satisfy the conditions of equation (3.30) and have been calculated by Mueller et al[60]. The simplest solution of equation (3.30) is for two angles, where $\kappa_1=\kappa_2$, such that $\theta_1=37.38^0$ and $\theta_2=79.19^0$.

Figure 3.9: Principle of DAS operation.

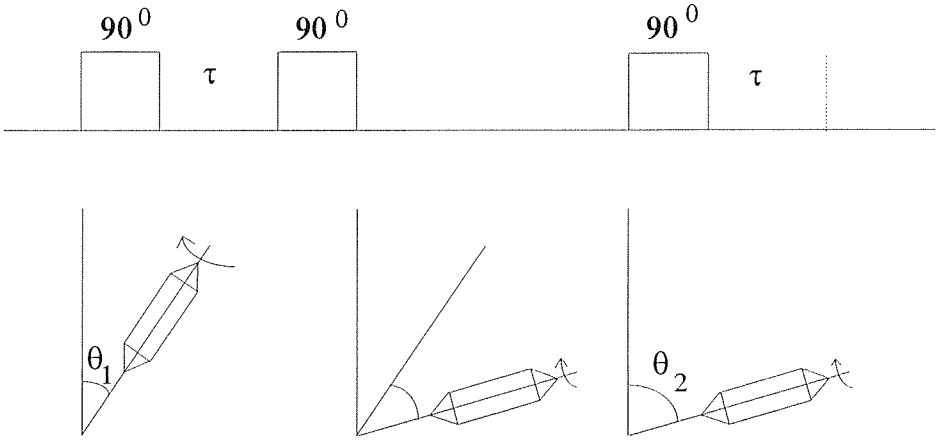

The pulse sequence of figure 3.9 first places the magnetisation vector in the xy plane, the Hamiltonians are then allowed to develop at angle θ_1 for τ_1 seconds. To prevent the Hamiltonians developing during switching between angles, the magnetisation is temporarily placed along the z-axis. When the rotor is at the new angle θ_2 the magnetisation is nutated back into the xy plane, allowed to develop. An FID is acquired during the evolution time, τ, of the magnetisation for each discreet angle. The DAS spectrum is formed by combining the FIDs obtained for each of the two angles to give a spectrum containing only the isotropic shift information.

3.5.3: DIPOLAR DECOUPLING AND CROSS POLARISATION

If the nucleus of interest is contained within a molecule where there is an abundance of a second spin, then a strong dipolar coupling will exist between them causing a large broadening of the line width. An example of this is the very large ^{13}C line widths (c.a. 5000 Hz) obtained in organic solids from ^{13}C-^{1}H coupling. The removal of heteronuclear dipolar coupling was first achieved by Pines et al[61] for the proton decoupled ^{13}C spectra of adamantane. By applying irradiation at the proton resonance frequency the dipolar (and scalar) coupling is removed. For all the proton transitions to be saturated, it is necessary to use a very high power decoupler of short pulse width. When used in combination with MAS the line widths obtained can be compared with those of liquids. Due to the long T_1 characteristics of solids and the insensitivity of the ^{13}C nucleus the experiment must have a long relaxation delay and a high number of acquisitions: this can cause the decoupler coils to overheat.

The poor signal to noise and long relaxation times of nuclei such as ^{13}C can be circumvented by using cross polarization in which the S/N of the rare spin, S, is enhanced by the abundant spin, I. The experiment, originally achieved in liquids by experiments such as INEPT[62, 63], was applied to solids by Hartmann and Hahn[64]. Polarisation transfer occurs through the abundant spin (with a lower spin temperature) being placed in contact with rare spin (of higher spin temperature). The pulse sequence used can be seen in figure 3.10,

Figure 3.10: Cross polarisation sequence.

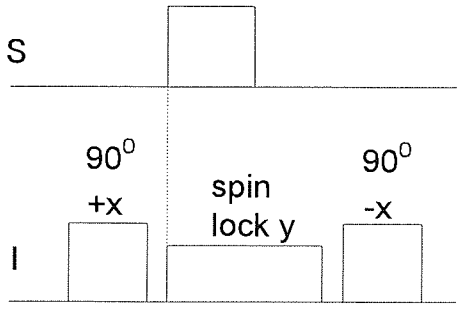

At equilibrium the magnitudes of the magnetisation for spins I and S are given by equation 1.8 as M_0^I and M_0^S for a lattice temperature, T_L. If a spin locking field is applied to the I spin then its magnetisation is held in a static H_1 field. Since $H_1 <<< H_0$ then the magnitude of M_0^I in H_1 is equivalent to it having been polarised in H_0 at a much lower temperature, T_{SL}, given by,

$$T_{SL} = \left(\frac{H_1^I}{H_0}\right).T_L \qquad (3.31)$$

where H_1^I is the r.f. field experienced by spin I.

During spin locking the energies of both I and S spins are matched to meet the Hartmann-Hahn condition[64] $\gamma^I.H_1^I = \gamma^S.H_1^S$ and rapid polarisation transfer occurs by the flip-flop (B) term of the dipolar alphabet. The two spins are now in contact with each other and since the spin temperature of spin I is much lower that the spin temperature of spin S then 'heat' energy flows to equilibrate the system. Heat transfer takes the form of a transfer of spin polarisation from the I spin to the S resulting in a new S magnetisation of;

$$M^S = \left(\frac{\gamma_I}{\gamma_S}\right).M_0^S \qquad (3.32)$$

For dipolar coupled proton(I) and carbon(S) spins the ratio of the two magnetogyric ratios results in a gain in ^{13}C magnetisation of $4M_0^S$.

When the maximum transfer has occurred the H_{1s} field is switched off. The H_{1I} field is maintained during acquisition so that dipolar coupling does not broaden the S spin line width. After spin locking and acquisition a 90^0 (-x) pulse is applied to return any M_{yI} magnetisation to the z-axis. The pulse sequence of figure 3.10 does not completely destroy the polarisation of spin I and multiple cross-polarisations (contacts) with spin S can be made. Thus, the S spin can be continually re-polarised by the I spins until the M^I has decayed to zero, either by magnetisation transfer or relaxation governed by $T_{1\rho}$. In the case of ^{13}C spectra, the repetition rate is dependent on the proton relaxation time, $T_{1\rho}$. Cross polarisation is normally combined with mechanical narrowing techniques (CPMAS[65, 66], CPDOR[67])to give very narrow lines.

3.5.4: MULTI-PULSE LINE NARROWING

For nuclei with strong dipolar coupling, such as ^1H-^1H homonuclear coupling, then their interaction can only be removed through ultra-fast MAS (>20 kHz). An alternative method for the removal of homonuclear dipolar coupling is by pulse sequence manipulation of the magnetisation vector to average the dipolar Hamiltonian,

$$\mathcal{H}_{D,\alpha\alpha} = \sum_{j<k} \mathcal{D}_{jk}.(3.I_{\alpha j}.I_{\alpha k} + \mathbf{I_j}.\mathbf{I_k}) \qquad (3.33)$$

where $\mathcal{D}$ is the dipolar coupling constant and α=x, y, z.

The first pulse sequence to achieve this was WAHUHA[68] (developed by WAugh, HUber and HAeberlen), see figure 3.11. The notation X represents a 90^0 pulse of phase +x and similarly Y indicates a 90^0 pulse of phase +y: a dash above the symbol denotes a 180^0 shift in phase, i.e. -x or -y.

Figure 3.11: WAHUHA pulse sequence, above; the pulse sequence, below; the phase of the magnetisation vector.

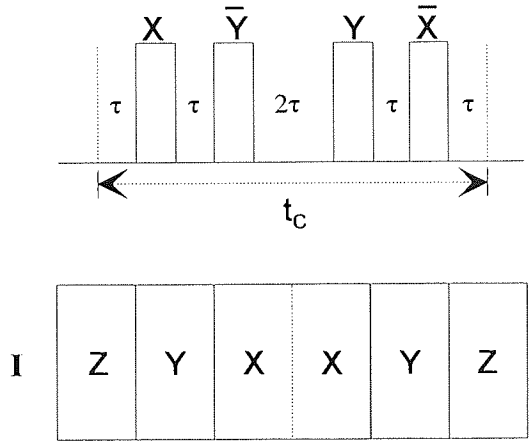

The WAHUHA sequence uses pulses and time delays to arrange for the magnetisation vector to spend equal time periods, τ, along the x, y and z axes of the rotating frame. A full description of the sequence requires the use of coherent averaging theory to derive the average dipolar Hamiltonian as being equal to zero. However, the sequence can also be explained classically. If $\mathbf{M}$ is taken to be a unit vector then its orientation along each axis of the rotating frame can be described by the coordinates; +x (1,0,0), +y (0,1,0) and +z (0,0,1). The resultant vector under influence of WAHUHA is a time dependent summation each

orientation and $\mathbf{M}$ appears to be aligned with the vector (1,1,1): which makes an angle of $54^0 44'$ to the z-axis. By acquiring one data point in each τ window the average FID is constructed.

A secondary consequence of coherent averaging of $\mathcal{H}_D$ is that any other interactions with a I_z dependence, e.g. chemical shift anisotropy and heteronuclear dipolar coupling, will be scaled by a factor of $1/\sqrt{3}$.

To prevent dephasing of the magnetisation vector, it is important for the sequence cycle time to be less than T_2^*. Therefore, the pulses must be an order of magnitude less the sequence time, with accurate timing and phase. Further sequences have been developed to account for inaccuracies in the pulse-timing and phase (MREV-8[69-73], BR-24, BR-52[74-78]) but they are still based on the WAHUHA building block.

3.5.5: CRAMPS

MAS is limited in that it requires very high spinning speeds and is unable to remove second order interactions. Multi-pulse sequences can overcome strong homonuclear dipolar coupling but will not remove chemical shift anisotropy. The combination of these two techniques (proposed by Haeberlen and Waugh[79], developed by Gerstein[80-84]) gives CRAMPS (Combined Rotation And Multiple Pulse Spectroscopy). The sample is spun at the magic angle whilst a BR-24 sequence is used for high resolution. CRAMPS is a very difficult experiment to perform and requires an accurate set up by an experienced operator.

CHAPTER 4

BASIC ULTRASOUND THEORY

4.0: ULTRASOUND

Ultrasound is usually taken to mean sound waves with vibration frequencies that are inaudible to the human ear (approximately >20 kHz), although the study of ultrasound sometimes encompasses frequencies within the bounds of human hearing. The use of ultrasound may be split into two main fields of high and low intensity applications. At low intensity, ultrasound can be used as an analytical probe. Typically, high frequencies are used to provide greater accuracy in measurements or higher resolution in flaw detection. High intensity applications have a greater effect on the medium shock waves and cavitation fields can occur. These can be used in forming emulsions, cleaning, ultrasonic soldering, etc. The purpose of this chapter is to give the reader some insight into the behaviour of ultrasound and its effect on the systems studied in this thesis. More detailed accounts of ultrasonic theory can be found in the texts by Blitz[85], Gooberman[86], or in the series edited by W. P. Mason[87].

4.1: WAVE MOTION

If a medium is considered as a series of adjacent layers, then the passage of ultrasound is concerned with the time dependent disturbance of these layers from their equilibrium position. If a source of vibration is placed at one end of a medium its motion will be transmitted to its neighbour, energy is then passed from one layer to the next until a boundary is reached. Energy transfer takes a small but finite time, thus, a phase difference exists between the layers. The characteristic time for the wave to travel through the layers gives a wave velocity, c. Two main

types of ultrasonic wave that can exist within a medium are longitudinal and shear, see figure 4.0.

Figure 4.0: Longitudinal and transverse ultrasonic modes.

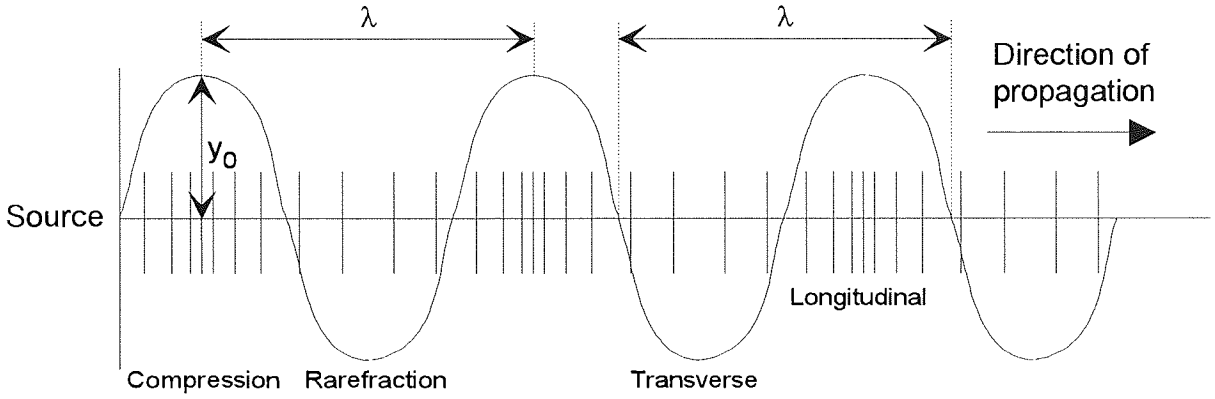

A longitudinal wave consists of regions of the medium being under compression or tensile stress (rarefaction), the motion of the layers occurs in the direction of propagation. For shear waves, the motion of the layers occurs at right angles to the direction of propagation. Shear waves usually only exist in solids as gases and liquids cannot support shear stresses, unless they are highly viscous. The shape of the sine wave can be defined in terms of the displacement of the layers or particles, y, during a time period, t, given by,

$$y = y_0 . \sin\omega . t \qquad (4.1)$$

where y_0 is the maximum displacement amplitude from equilibrium and ω is the angular frequency. It is more convenient to express particle displacement in terms of the particle velocity, u,

$$u = u_0 . \sin\omega . \left(t - \frac{x}{c} \right) \qquad (4.2)$$

and the pressure experienced, p,

$$p = p_0 . \sin\omega . \left(t - \frac{x}{c} \right) \qquad (4.3)$$

where x is the distance of the particles from the source and u_0 and p_0 are the maximum particle velocity and acoustic pressure amplitudes respectively.

4.2: IMPEDANCE

An ultrasonic wave passing through a medium experiences a resistance opposing its motion, known as the specific acoustic impedance, Z_a. The value of Z_a is the ratio of acoustic pressure, p, to particle velocity, u, and is independent of the nature of the wave and its frequency. The value is normally complex, but, for a plane progressive wave with infinite boundaries the term becomes real and is equal to the product of the density and wave velocity, giving the characteristic impedance,

$$R_a = \rho.c \qquad (4.4)$$

Some values of for R_a are given in table 4.1.

Table 4.1: Ultrasonic impedance's for some common media[88].

Material	Velocity, ms^{-1}		Density kgm^{-3}	Characteristic impedance, $kgm^{-2}s.10^6$
	Longitudinal	Shear		
Aluminium	6400	3130	2700	17.3
Brass	4370	2100	8500	37
Titanium	5990	3120	4500	27
PTFE	1350	-	2200	3
Glass	5660	3420	2500	14
Water	1480	-	1	1.48
Benzene	1320	-	0.88	1.16
Air	330	-	0.13	0.00043

For an unattenuated plane progressive wave the intensity, I, at any point may be calculated, in Wm^{-2}, as the energy passing through a plane of unit area, given by,

$$I = \frac{u_0 . p_0}{2} = \frac{p_0^2}{2.\rho.c} \qquad (4.5)$$

The intensity of a spherical wave propagating in all directions will be inversely proportional to the square of its distance from the source ($I \propto 1/4.\pi.r^2$).

The intensity may be expressed in terms of the decibel scale compared to a reference, I_0, which may be the incident intensity,

$$\text{Intensity level (dB)} = 10.\log\frac{I}{I_0} = 20.\log\frac{A_2}{A_1} \qquad (4.6)$$

where A is the wave amplitude.

4.3: TRANSMISSION AND REFLECTION

The characteristic impedance becomes important when considering the behaviour of a wave when it comes into contact with a boundary. If a wave propagating through a medium, of impedance R_1, comes into contact with a second medium, of impedance R_2 ($R_1 \neq R_2$) then the beam will be partially reflected and partially refracted. At the boundary the wave is split into transverse and longitudinal components, in a process know as mode conversion. Mode conversion occurs because the incident wave at a boundary can be resolved into parallel and perpendicular components. Parallel and perpendicular stress components act on the boundary causing it to oscillate, generating longitudinal and transverses waves (assuming the medium can support a transverse wave) which are reflected and refracted., see figure 4.1.

Figure 4.1: Transmission/reflection and mode conversion at a boundary.

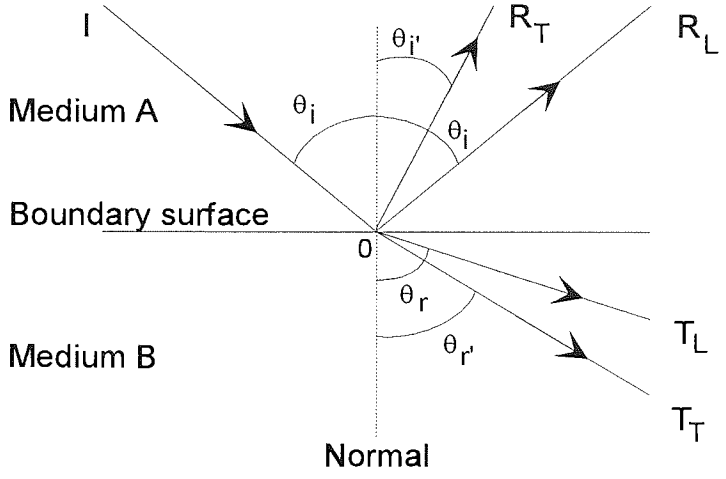

The transmission, a_t, and reflection coefficient, a_r, for a wave in the absence of mode conversion are given as,

$$a_t = \frac{4.R_A.R_B.\cos\theta_i.\cos\theta_r}{(R_B.\cos\theta_i.+R_A.\cos\theta_r)^2} \tag{4.7}$$

$$a_r = \left(\frac{R_B.\cos\theta_i.-R_A.\cos\theta_r}{R_B.\cos\theta_i.+R_A.\cos\theta_r}\right)^2 \tag{4.8}$$

Multiple reflections occur if the wave encounters a large number of particles distributed uniformly. The beam will reflect off the particle(s) surfaces and the wave is scattered in all directions. Rayleigh scattering occurs when the particle size is less than the wavelength, usually 0.1λ, and the acoustic wave is scattered uniformly[89]. The absorption coefficient due to presence of solid particles in a sound field can be deduced for a medium from the equation,

$$\alpha = K.f^4.D^3 \tag{4.9}$$

where K is a constant for the medium, f is the frequency and D is the particle diameter. Scattering can occur in aerosol, emulsions and polycrystalline metals.

4.4: ATTENUATION OF SOUND WAVES

The propagation of a wave through a medium will experience attenuation, causing its energy to be dissipated. Provided there are no losses by reflection the main causes of the attenuation are scattering (see section 4.3), diffraction and absorption.

i: Diffraction

A point source emits energy in all direction resulting in a spherical wavefront emanating in all directions. A circular face of finite dimensions can be described by a series of adjacent point sources. If the motion of the circular face is piston like then a plane progressive wave will be generated. The beam will remain parallel for a distance dependent on the diameter of the source after which it will begin to diverge as if the wave had been generated by a point source at the center of the disc, figure 4.2.

Figure 4.2: Diffraction from a piston source.

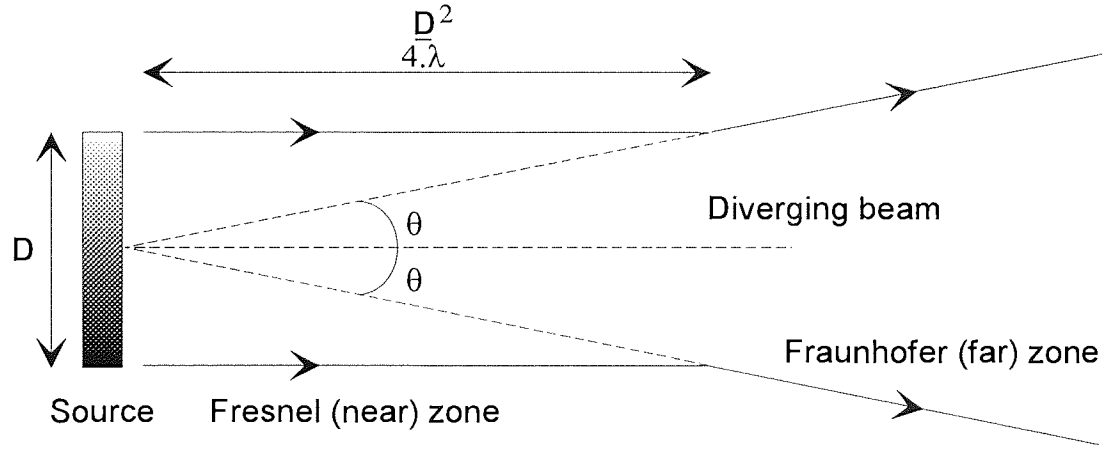

Thus the intensity of the ultrasonic beam in the far zone will be given by the inverse square law.

ii: Absorption

Classical absorption is the result of the combined absorptions due to viscous damping and thermal conduction of the acoustic energy. An acoustic wave passes through a medium by the transfer of energy from one particle/layer to another. Viscous drag will damp the motion of each particle/layer resulting in the loss of acoustic energy. Thermal conduction arises from the adiabatic compression and rarefaction of the medium. This generates large pressure gradients between the neighbouring compression and rarefaction phases of the wave. Heat will flow down each temperature gradient to reduce the energy of the wave. The absorption coefficient is proportional to the acoustic frequency, however in gases it does not become significant until >100 kHz. For liquids absorption due to thermal conductivity is negligible although absorption due to viscosity can still be large.

The finite time required for wave energy to be transferred to the medium results in hysteresis. If a periodic adiabatic stress is applied to the medium the resultant strain does not vary linearly. The stress/strain curve is a hysteresis loop, see figure 4.3, where the area of the loop is the energy lost per cycle. Therefore, as the frequency (cycles per second) increases the total energy lost increases.

Figure 4.3: Ideal and real hysteresis loop for energy lost during a cycle.

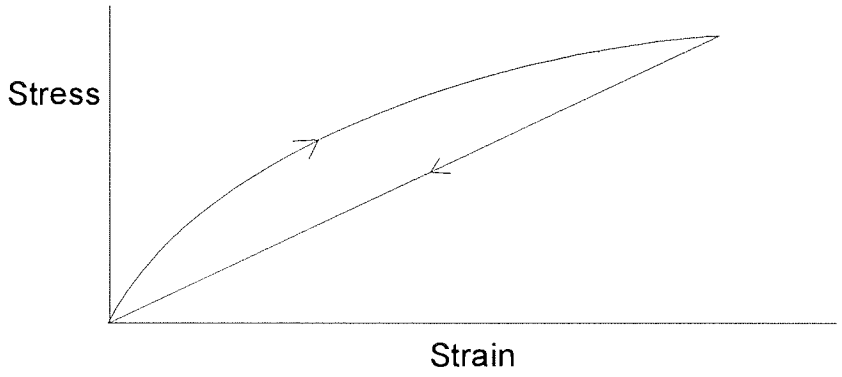

When ultrasound passes through a medium containing polyatomic molecules some of its energy is given up to internal degrees of freedom. Energy is absorbed to excite vibrational/rotational transitions or cause conformational change.

In solids, losses are due to many factors such as grain boundaries, dislocations and imperfections in the crystal lattice, which will absorb or reflect the wave. When the frequency approaches the high MHz region (>100 MHz) the wave will interact with the lattice vibrations and a very strong absorption will occur. By analogy to the photon, an ultrasonic wave can be considered to consist of phonons where their energy is equal to $h\nu$. If the phonons have energy comparable to the energy difference between two modes of lattice vibration then absorption occurs causing vibrational transitions.

Ultrasonic attenuation is the greatest for gases followed by liquids and is the least in solids. Therefore, the pathlength that the wave can travel is shortest in gas. If ultrasound is irradiated into liquids or a solid then care must be taken to ensure that no air gaps are present in front of the ultrasonic source. Solid surfaces are

optically ground to provide the best coupling surface (wetting the surface with a coupling liquid will also help transmission).

The wave amplitude can be described at any point from the source by an absorption coefficient, α, in nepers/cm, (1 neper=8.686 dB), and the initial amplitude, A_0, by equation (4.10).

$$A = A_0.e^{-\alpha x} \qquad (4.10)$$

4.5: STANDING WAVES

When a wave transmitted from a source comes into contact with a boundary, perpendicular to its direction of propagation (and of infinite impedance), it will be completely reflected back along its direction of propagation. The wave amplitude at a particular point may be calculated as the sum of the individual waves for that point. The superposition of multiple amplitudes may result in constructive (antinodes) or destructive (nodes) interference, see figure 4.4.

Figure 4.4: Superposition of reflected waves to produce a standing wave.

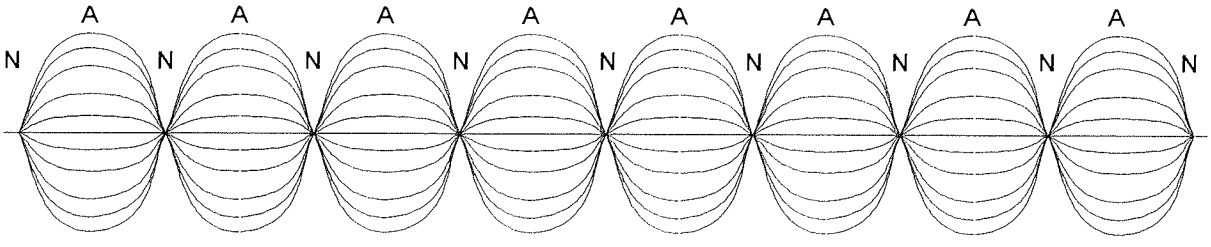

The position of the nodes and antinodes occur at half wavelength integers.

4.6: SONIC GENERATION

Acoustic wave motion is generated by a vibrational source. Devices that can transform electrical energy into mechanical oscillation are known as transducers. The choice of transducer for a particular application depends on the frequency range that it is capable of operating at and its power output. Also, the transducer may be required to act as a receiver to convert mechanical energy back to an electrical signal.

4.6.1: PIEZOELECTRIC TRANSDUCERS

The piezoelectric effect was discovered by Jacques and Pierre Currie[90] in 1880 for naturally occurring materials such as quartz, tourmaline and lithium sulphate. For an undeformed unit cell, within a crystal lattice, the position of the positively and negatively charges atoms are such that their centres of gravity are identical and the charges cancel completely. When a deformation is applied the centers of symmetry no longer coincide and a dipole is formed with electrical charges appearing at the surfaces. Similarly the reverse affect can be used. If a thin film electrode is coated on the material and a voltage is applied across the crystal it will deform accordingly. The crystal can then be made to vibrate by using an AC current. Since the crystal oscillates only when there is a net dipole at the surface, only the odd harmonics can resonate, see figure 4.5.

Figure 4.5: Harmonic frequency modes generated by an electric field

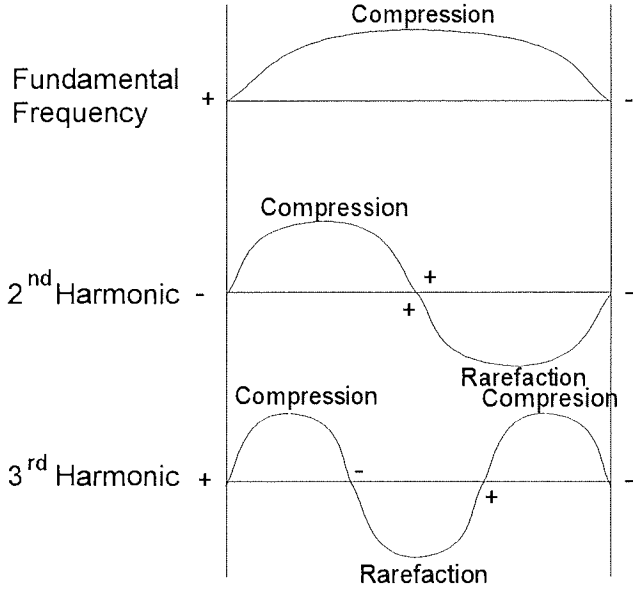

Figure 4.6 shows a section through a quartz crystal, it is represented in a coordinate frame where the z-axis is non-polar and exhibits no piezoelectric effect,

Figure 4.6: Piezoelectric axes for a single quartz crystal.

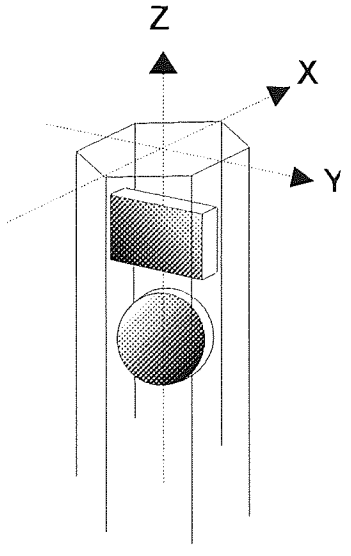

Lying perpendicular to the z-axis are the polar axes. There are three x-axes connecting the opposite points of the six vertices of the hexagonal face, and three y-axes perpendicular to the x-axes, i.e. connecting the opposing edges. The

direction in which the crystal deforms when an electric field is applied depends on which of the six polar axes is normal to the crystal face. The crystal is said to be X-cut for compresional mode and Y-cut for shear mode, see figure 4.7.

Figure 4.7: Longitudinal (X) and shear (Y) modes with polar axis.

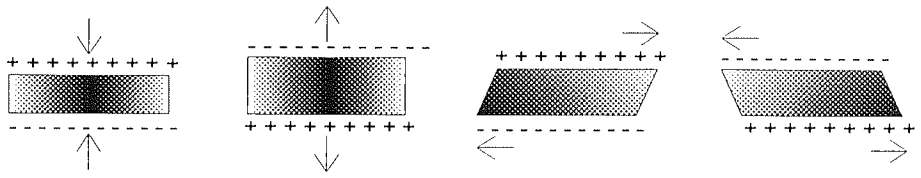

The piezoelectric effect can be obtained for ferroelectric materials which exhibit the electrostrictive effect i.e. materials that will produce a strain when placed in the presence of an electric field. The deformation is proportional to the square of the applied field but is insensitive to its direction. For the material to produce a sinusoidal vibration it must be polarised with a particular axis. Heating the material to above its Curie temperature, T_c, (the point above which the piezoelectric effect disappears) in the presence of a strong polarising field, will impose a polar axis on the material when it is cooled. The transducer will now be capable of sinusoidal motion in the direction of the exciting field provided that its magnitude does not approach that of the initial polarising field. Barium titanate, lead meta-niobate and lead zirconate titanate are examples of this type of transducer. These transducers generally have a polycrystalline structure that can be molded into a variety of shapes and then polarised. The advantage of ceramic transducers over quartz is that they have a higher efficiency in the conversion of

electrical energy to mechanical energy, although they are more brittle than quartz crystals.

The variety of piezoelectric materials that are available means that it is important to define a number of parameters that characterise a transducer. One is the electromechanical coupling coefficient, k, which characterises the conversion of electrical energy into mechanical and is a measure of the losses in the transducer.

$$k^2 = \frac{\text{electrical energy converted into mechancal energy}}{\text{electrical energy put into the crystal}} \qquad (4.11)$$

There are two other piezoelectric coefficients, d and g, which define the mechanical and electrical properties of a transducer. The constant, d, is the mechanical strain, S, for an applied voltage, V,

$$d = \frac{V}{S}\ Vm^{-1} \qquad (4.12)$$

and the constant, g, is the electric field, q, produced in a piezoelectric crystal for an applied stress, F.

$$g = \frac{q}{F}\ CN^{-1} \qquad (4.13)$$

The two constants are related by the dielectric constant, K, and permittivity in a vacuum, ε_0, by equation 4.14.

$$g = \frac{d}{K.\varepsilon_0} \qquad (4.14)$$

For example, quartz is found to have a small value of d, but a high value of g, due to its low dielectric constant.

The type of transducer required depends on the application it is used for. If it is intended for ultrasonic processing, e.g. cavitation effects, then a large deformation in the crystal is necessary, i.e. a high d. For sensitive detection, e.g. pulse-echo flaw detection, a high value of g is necessary along with a high dielectric constant to prevent signal loss due to the capacitance of the connecting electrodes.

Some values of d and k are given in table 4.2. By varying the chemical composition of the material[91] the properties necessary for the application can be obtained.

Table 4.2: Electromechanical properties for some piezoelectric materials.

Material	d	g	k	K	T_c
Quartz (x-cut)	2.3	58	0.1	4.5	575
Lead zirconate titanate (PZT)-4	285	26.1	0.64	1300	320
PZT-5	374	24.8	0.67	1700	365
Lead meta-niobate	85	42.5	0.42	225	550
Barium titanate, type B	149	14.0	0.48	1700	115

4.6.2: RESONANCE CONDITION

The importance of standing waves can be seen for transducers when their thickness becomes comparable with the ultrasonic wavelength. For a particular frequency there will be a boundary path length where there will exist a node or antinode at the boundary. If the pathlength of the ultrasonic wave is equal to an multiple of a quarter of the wavelength, then, superposition of the waves will result in maximum constructive interference, see figure 4.8. Transducer thicknesses are usually found to be equal to half the wavelength for the material. The forward

transmission of an ultrasonic wave can be greatly enhanced if the transducer is backed by an air gap of n.λ/4.

Figure 4.8: Pathlengths necessary for standing wave resonance.

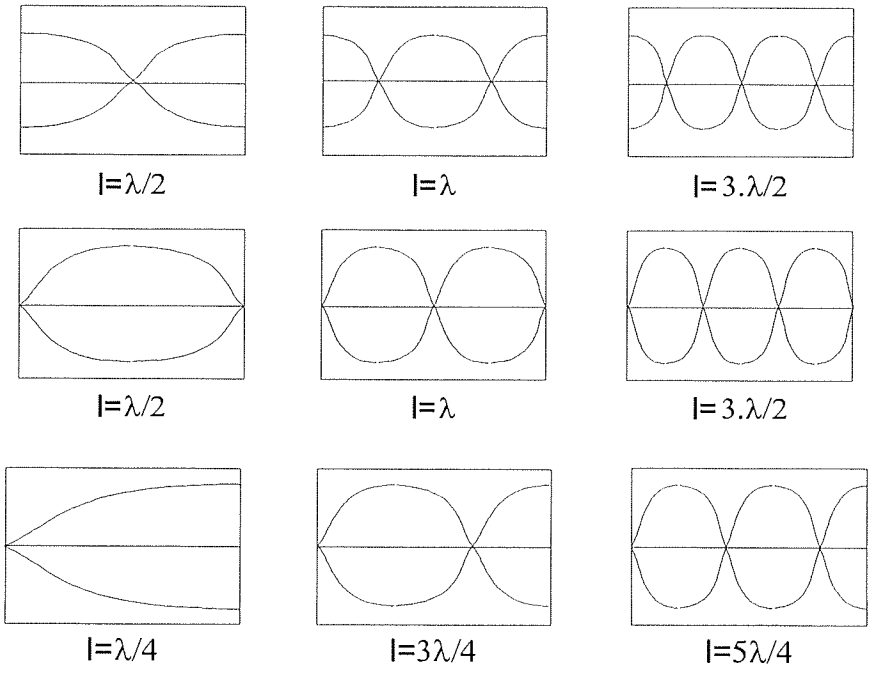

The quality of the resonance is defined by a dimensionless Q factor for a resonating material and is usually quoted for ultrasonic generating materials. Figure 4.9 shows the variation in vibrational amplitude with frequency for an oscillating transducer. As the driving frequency of a generator approaches the resonant frequency of the transducer its vibrational amplitude builds to a maximum.

Figure 4.9: Frequency response curve for high and low Q conditions.

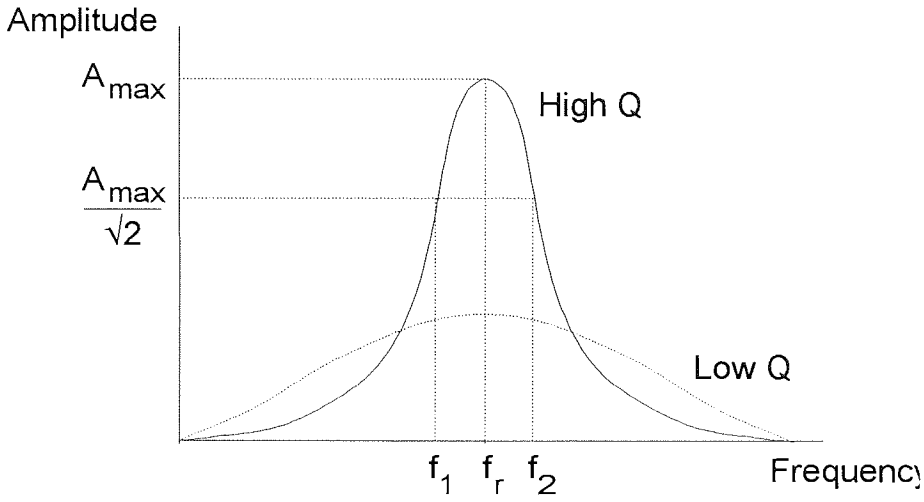

The frequency bandwidth of a transducer can be determined by its Q value, obtained from figure 4.9 and given by equation 4.15 (provided Q>3) as,

$$Q = \frac{f_r}{f_2 - f_1} \tag{4.15}$$

Thus a transducer with a high value of Q will provide a sharp bandwidth of frequencies and will typically be used in ultrasonic processing. Conversely, a transducer with a low value of Q will resonate at larger bandwidth of frequencies and thus is used in detection systems.

The value of Q is also dependent on the medium to which the transducer is coupled. It will be greatly enhanced if it has a backing of high impedance and a light load e.g. an air backing irradiating into water.

4.7: LOW INTENSITY PASSAGE

At low intensities, ultrasound can be used as an analytical tool. By measuring constants of propagation, i.e. velocity and absorption, the properties of gases, liquids and solids may be determined. Examples of the measurements that can be made are flaw detection[92, 93] and thickness gauging[94] using a pulse-echo/detection technique. Knowledge of the velocity of the wave in a particular medium allows the path length to be determined, if the wave encounters a flaw or grain boundary it will either be reflected or scattered resulting in an attenuated signal or early echo. The speed of a wave through a solid is influenced by the elastic modulus of the material. Provided that the solid is isotropic, then velocity measurements can be used to produce a stress map[95].

The principal use of ultrasound, at low power, is medical imaging[96]. Variations in the impedance and absorption of the body can be detected by reflection and attenuation giving an image. Frequencies of 1-10 MHz are usually employed, increasing the frequency increases the resolution of the image but causes a reduction in the depth of the scan due to attenuation. Powers are kept sufficiently low to prevent any harm to the body.

4.8: HIGH INTENSITY PASSAGE

At high intensities the resulting strain for an applied stress is no longer linear. The passage of a wave can have a profound effect on the medium, resulting in acoustic streaming, shock waves and cavitation.

4.8.1: ACOUSTIC STREAMING

Acoustic streaming generates a turbulent flow of liquid in a medium through which ultrasound propagates. An ultrasonic beam passing through a fluid element will experience some attenuation in its energy. The energy difference on either side of the element causes a pressure gradient, resulting in a net force acting on the element. This will cause the fluid element to translate in the direction of the wave, see figure 4.10.

Figure 4.10: Streaming flow in an open tube.

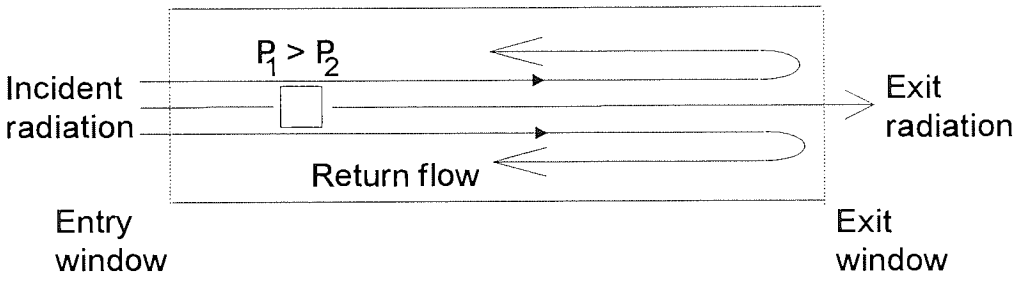

The rate of streaming is dependent on the ultrasonic intensity, the viscosity of the liquid and its absorption coefficient. A more detailed account of acoustic streaming by Nyborg can be found in the series edited by Mason[97].

4.8.2: SHOCK WAVES

At infinitesimally small acoustic intensities the pressure at a point on a wave will vary sinusoidally. As the acoustic intensity increases then the sine wave will be distorted, becoming a saw tooth wave, resulting in large instantaneous pressures. Wave distortion occurs at high powers because of the dependence of wave velocity on pressure. The wave velocity is given by:

$$c = \sqrt{\frac{\text{elastic modulus}}{\text{density}}} \qquad (4.16)$$

When acoustic pressure is applied, then the rate of increase in the elastic modulus is greater than for the density. Therefore, the velocity is greater at the pressure maxima than the minima. The higher velocity of the pressure peaks will cause them to "catch up" with the pressure troughs. Although a peak cannot overtake a trough it does lead to very steep pressure gradients on the leading edge to the wave, see figure 4.11.

Figure 4.11: Wave distortion with distance in gases leading to shock wave formation.

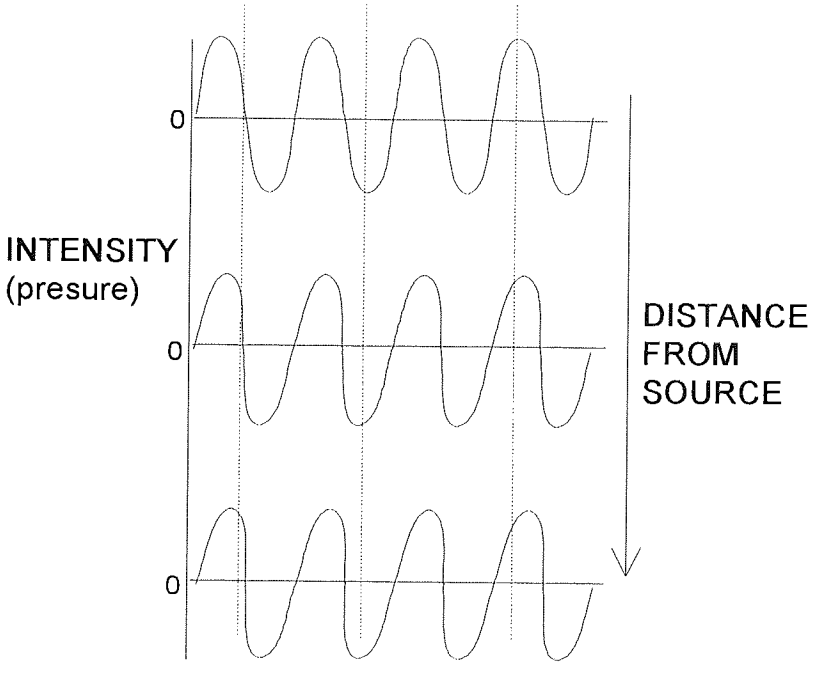

As the wave front becomes steeper then the pressure gradient tends to infinity and a shock wave is generated. For a gas the distance, L, required for shock wave formation is related to the ratio of its specific heats ($\gamma=C_p/C_v$) and the static gas pressure, P_0, by,

$$L = \frac{\gamma.P_0}{\gamma+1}.\frac{\lambda}{\pi.P} \qquad (4.17)$$

where P is the acoustic pressure of the wave of wavelength λ. The leading edge gives large temperature and pressure gradients which are absorbed by the medium. In a gas increasing the ultrasonic intensity will lead to an earlier appearance of a shock wave and therefore further increases in the energy absorption limiting the overall ultrasonic intensity. In liquids shock wave formation is prevented by the onset of cavitation.

4.8.3: CAVITATION

The term cavitation is used to describe the sudden and violent collapse of bubbles. Cavitation creates conditions of very high localised temperatures and pressures. The effects of these conditions have been seen in the pitting of the surfaces of ship propellers. A detailed theoretical account of ultrasonic cavitation can be found in the text by H. G. Flynn[98].

Within the bulk of a pure liquid there will be microscopic bubbles containing a mixture of gas and vapour. The lifetime of a bubble is a function of its size. Small bubbles will rapidly dissolve as the gas within them is forced out due to the surface tension. Larger bubbles will tend to rise to the surface of the liquid.

A number of theories[99, 100, 101] have been proposed as mechanisms by which gas/vapour bubbles can be stabilised in a liquid. The most popular and successful theory for the stabilisation of bubbles is the solid crevice model, proposed by Harvey et al[101] and developed by a number of workers[102-106]. Tiny gas/vapour bubbles are trapped in the crevices of solid particles present in the liquid. The

stability of the bubble is dependent on the affinity of the liquid to the solid, see figure 4.12.

Figure 4.12: Gas stabilisation in a solid crevice.

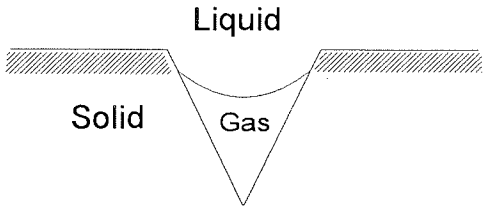

If the bubble interface is concave with respect to the crevice apex then gas pressure within the bubble, p_g, is higher than the pressure of the gas dissolved in the liquid, p_{gL}, and gas diffuses out of the bubble, destroying it. Conversely, if the bubble interface is convex with respect to the crevice apex then $p_g<p_{gL}$ and gas diffuses into the bubble.

Despite the problems of bubble stability within liquids, most of the theory modeling the behaviour of bubble is based on a free spherical bubble.

A bubble having an internal pressure p_g+p_v (p_v is the vapour pressure within the bubble) will exist in equilibrium with a liquid of ambient pressure, p_{L0}, and temperature, T. The radius of the bubble, R_0, will be given by,

$$p_{Lo} + \frac{2\sigma}{R} = p_g + p_v \qquad (4.18)$$

where σ is the gas/liquid surface tension. If the liquid pressure is reduced to p_L the bubble will expand to a new radius, R_n, (assuming isothermal expansion) to maintain the equilibrium, such that,

$$p_{g'}\left(\frac{R_o}{R_n}\right)^3 + p_V = p_L + \frac{2\sigma}{R_n} \qquad (4.19)$$

where $p_{g'}$ is the gas pressure in the bubble at radius, R_n. Equation 4.19 predicts the stable equilibrium radius of a bubble for values of $p_L > p_v$. However, if $p_L < p_v$ the bubble is only stable against spontaneous growth if its radius is less than a critical radius, R_c, defined as,

$$R_C = \frac{4\sigma}{3(p_V - p_L)} \qquad (4.20)$$

when $p_L < p_v$, a bubble will be in stable equilibrium with the liquid when $R_n < R_c$, bubbles having a radius $\geq R_c$ will grow spontaneously in an uncontrollable manner until they can no longer sustain themselves and collapse.

Bubbles that possess radii below the critical radius can be made to grow in size by a process of rectified diffusion. As governed by equation (4.19), applying a pressure wave of sufficient magnitude a bubble can be made to expand and contract. As the bubble pulsates, gas diffuses across its interface due to variations in p_g. The net effect of this process is to increase the overall gas content of the bubble. Increasing the gas pressure inside the bubble will cause it to grow in size until $R=R_c$ where it will grow rapidly.

A free bubble within a liquid will oscillate at a natural frequency, ω_b, dependent on its radius, R, and may be calculated, using equation 4.21, as,

$$\omega_b^2 = \frac{1}{\rho.R_0^2}.\left[b.\left(p_{L0} + \frac{2\sigma}{R} - p_V\right) - \frac{2\sigma}{R}\right] \qquad (4.21)$$

b is a damping term and equals 3 for isothermal compression and 3γ for adiabatic compression (where γ is the ratio of the specific heats for the gas). A plot of resonant frequency verses bubble radius can be found in figure 3 of the text by Flynn[98].

A liquid can be made to undergo cavitation if an acoustic field is introduced of pressure amplitude, P_A, and frequency, ω_A. For small values of P_A ($\approx$0.333 bar), where $R>R_c$ and $\omega_b<\omega_A$, the bubble will have a small amplitude oscillation about an equilibrium radius. The liquid is said to undergoing stable cavitation when the motion of the bubble is non-linear with respect to the pressure wave. The bubble will pulsate over many acoustic cycles before it dissolves, drifts out of the sound field, or is converted into a transient cavity.

A transient cavity is formed by increasing the acoustic pressure amplitude to a threshold value or by satisfying the bubble resonance condition $\omega_b=\omega_A$. Under these conditions a bubble will expand rapidly to a much larger radius ca. $R/R_0>2$. The bubble will then collapse, violently, during the positive acoustic pressure cycle. As the acoustic pressure is increased the bubble will grow to a larger maximum radius, R_m, before collapsing. The initial collapse speed is proportional to R_m and the bubble is said to undergoing transient cavitation when its collapse

speed exceeds the speed of sound in the liquid. Increasing the collapse speed of the bubble reduces the probability of the bubble maintaining its integrity and it may shatter into smaller bubbles; these can act as nuclei for further cavitation.

If $\omega_b < \omega_A$ the growth is rate of the bubble is too slow for it to reach an unstable radius and collapse as a transient cavity. The limit for transient cavitation has been calculated by Noltingk and Neppiras[107] as ω_A=10 MHz. At this frequency the resonant bubble radius, R_r, equals the critical radius. Bubbles with radii $>R_{c,r}$ will grow too slowly to become transient, while bubble with radii $<R_{c,r}$ are in stable equilibrium with the liquid.

A bubble tends to collapse adiabatically with a force dependent on the ratio of initial size to maximum size. Any gas/vapour within the bubble will oppose the rate of collapse by cushioning its force. A volume of liquid containing collapsing bubbles is referred to as a cavitation field. Increasing the number of cavitating bubbles in the volume will increase the intensity of the cavitation field. However, the increase is limited by presence of a large number of bubbles causing the acoustic wave to be scattered and attenuated, thus requiring a much higher acoustic intensity to generate them.

The adiabatic compression of the gas during collapse generates very high temperatures and pressure at the cavity centre. Lord Rayleigh produced a model for conditions within the bubble predicting pressures and temperatures of 10000 atm and 10000^{0}C on collapse[108]. More conservative calculations have been

made[109] estimating a temperature of 4200 K and pressure of 975 bar. Experiments into conditions on collapse performed by Suslick et al[110] report temperatures of 5200 K within the bubble and 1900 K in the immediate area of a bubble. The accompanying large releases of energy can result in a weak emission of light known as sonoluminescence[111]. A discussion of sonoluminescence and its applications by Verrall and Sehgal can be found in the text edited by Suslick[112]

Cavitation erosion has been attributed to shock waves and microjets close to a solid surface[113]. When the collapse speed of the bubble exceeds the speed of sound in the liquid a shock wave is formed which can damage solid surfaces. Cavities which are close to a solid surface experience an asymmetric acoustic field. This will cause a bubble to collapse asymmetrically from the surface furthest from the solid creating a microjet that will impact on the solid surface[114], see figure 4.13

Figure 4.13 Microjetting action at a solid surface.

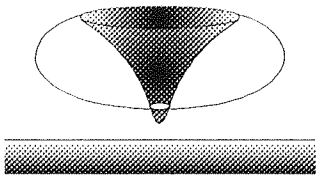

Calculations made by Plesset and Chapman[115] showed that for the liquid jet to have an effect on the solid surface then the separation of the centre of the bubble from the solid, x, must be $<1.5R_m$ (where R_m is the bubble collapse radius). These calculations also estimated the velocity of the liquid jet to be 130 ms^{-1} with an impact pressure of 2 kbar.

Microjetting may be a possible mechanism in SINNMR for creating particle motion close to collapsing bubbles. If the particle is struck by an impacting microjet then momentum will be transferred to it. The particle will posses mostly transitional motion if the impact lies on an axis of rotation or towards the centre of mass. However, if the particle is struck off axis it will also have a rotational component. The probability of a particle being struck off axis is reduced if the diameter of the microjet is greater than or equal to the diameter of the particle, thus, the bubble size should be less than the particle diameter if it is to cause particle rotation. For this reason particle sizes in the low micrometer range should be used when applying ultrasound in the MHz frequency range.

4.9: EFFECT OF ULTRASOUND ON SOLID PARTICLES

The idea of SINNMR is to cause linewidth narrowing in the NMR spectra of solids by making them act more like liquid molecules i.e. by induced incoherent motion. When an ultrasonic wave passes through a colloidal suspension of a solid then the particles will tend to follow the motion of the wave. The effectiveness of this will be dependent on the size of the particles. Large particles will move slowly and will be out of phase with the wave. Smaller particles will translate more readily with the direction of the fluid. The mismatch in particle velocities means that collisions will be more likely when there exists a large range of particle sizes.

The Bernoulli attraction[116] causes two particles to move towards each other when in a flowing liquid. Bernoulli's theorem states that the fluid velocity between two

objects, due to the constricted cross-section between them, must be greater than that of the bulk liquid. Consider two particles placed in an acoustic wave (where the vector linking the centre of mass of the two particles is perpendicular to the direction of wave propagation). Provided that the particles have a mass large enough to remain stationary with respect to the acoustic wave, then the fluid will flow between the particles during the compression and rarefaction phases. The increase in velocity between two particles relates to a drop in pressure causing them to move toward each other, allowing the particles to aggregate.

The dynamics of particles suspended in a standing wave have been characterised by Dysthe[117]. The orientation of a rigid particle, whose dimensions are small compared to the wavelength, will depend on its shape. The shape of a particle may be characterised by a mass tensor, M. A sphere will possess mass components $M_{xx}=M_{yy}=M_{zz}$, therefore, it will have no preferred orientation in the acoustic wave. For a spheroid, $M_{zz}>M_{yy}=M_{xx}$, the most stable orientation is when M_{zz} is parallel to the direction of ultrasonic propagation. If the spheroid lies away from its most stable orientation then the acoustic wave acts to rotate the particle back to its position of greatest stability. The strength of the orientational stability for a spheroid depends on the relative magnitudes of M_{zz}, M_{xx} and M_{yy}. As the shape of the spheroid approaches that of a sphere then the particles stability in a particular orientation is reduced. Any small perturbation in the acoustic wave or fluid will rotate the particle away from its most stable axis.

A rigid sphere will be subject to an overall radiation force, F_u, causing it to translate with the direction of propagation. In addition to F_u a sphere will also experience gravity and a buoyancy force, F_b, due to the density difference between the sphere and the medium, ρ_m-ρ_s. Attenuation of the acoustic wave increases from the source, thus, the magnitude of F_u decreases with distance. A particle within a sound field will come to rest at a position where all the forces balance, see figure 4.14

Figure 4.14: The equilibrium position of a solid particle due to buoyancy and radiation pressure.

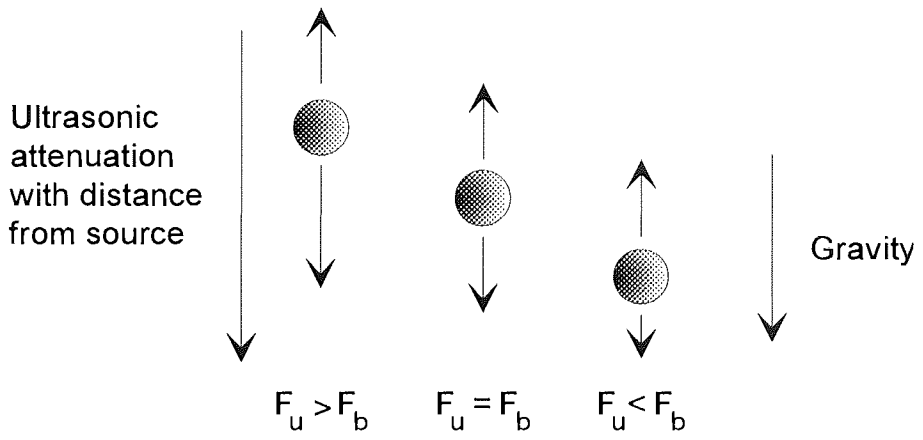

During the SINNMR experiment a colloidal suspension of solid particles can be brought into the coil region of the NMR probe by adjusting the magnitude of the acoustic intensity and the density of the medium.

4.10: CHEMICAL EFFECTS

The high temperatures and pressures produced during cavitation have lead to the use of ultrasound as a means of carrying out chemical reactions. It has been proposed that high temperature and pressure[118], electrical discharge[119] and sonoluminescence/photoinitiation[120, 121] are all possible mechanisms for the

initiation of chemical reactions. Most of the sonochemistry is based on radical reactions. Cavitation in water has been studied by Lindström and Lamm[122] for the production of H$^{\bullet}$ and OH$^{\bullet}$ radicals and they have proposed the following reactions to describe the process;

$$H^{\bullet} + OH^{\bullet} \rightarrow H_2O \qquad (4.22)$$

$$H^{\bullet} + H^{\bullet} \rightarrow H_2 \qquad (4.23)$$

$$H_2 + OH^{\bullet} \rightarrow H_2O + H^{\bullet} \qquad (4.24)$$

$$OH^{\bullet} + OH^{\bullet} \rightarrow H_2O_2 \qquad (4.25)$$

$$H^{\bullet} + H_2O_2 \rightarrow H_2O + OH^{\bullet} \qquad (4.26)$$

These reaction are the basis for further oxidation reactions such as the liberation of I_2 from potassium iodide in the Weissler reaction[7]. Radicals can be used as initiators in polymerisation reactions[123] or in chain cleaving for depolymerisation[124]. Ultrasonic emulsification can act as a phase transfer catalyst for some reactions[125].

CHAPTER 5

EXPERIMENTAL APPARATUS AND CONDITIONS

5.0: NMR SPECTROMETERS

5.0.1: JEOL FX 90-Q

SINNMR experiments were performed using a JEOL FX 90Q FT spectrometer. The spectrometer is based around a water cooled iron core magnet operating at 90 MHz (2.11 T) for ^{1}H. The axis of the probe is orientated perpendicular to the field direction and is capable of observing all nuclei except for ^{3}H. The resonant frequencies for some typical nuclei are given in table 5.1.

Table 5.1: Resonant frequencies for a 90 MHz spectrometer.

Nuclei	Nuclear spin	Sensitivity to ^{1}H =1.00	Frequency, MHz
^{1}H	1/2	1.00	89.60
^{13}C	1/2	$1.76*10^{-4}$	22.53
^{2}D	1	$1.45*10^{-6}$	13.75
^{23}Na	3/2	$9.25*10^{-2}$	23.7
^{11}B	3/2	$1.3*10^{-1}$	28.70
^{27}Al	5/2	$2.1*10^{-1}$	23.34
^{31}P	1/2	0.0663	36.28

The probe has a 10 mm internal diameter and 2 copper coils, 14 mm in length, for pulsing, observation and decoupling. Field stability is maintained by field/frequency locking, for which two nuclei can be utilised with an internal (^{2}D) or external (^{7}Li) lock nuclei.

The air temperature surrounding the probe can be set using a NM-VTS2 variable temperature controller. The desired experimental temperature is produced by the evapouration of liquid nitrogen or by heating the air flow to the probe and is

capable of operating between -100^{0}c and +180^{0}C, with an accuracy of ±2^{0}C. A copper/constantin thermocouple is employed to monitor the probe temperature.

5.0.2: BRUKER WM 250

Other experiments were performed on a Bruker WM 250 FT spectrometer, linked to a super conducting magnet at 250 MHz (5.8 T). Two probes, with axes in line with the magnetic field direction are used. One is a triple resonance probe capable of observing ^{13}C, ^{1}H and ^{31}P, and a broadband probe capable of observing nuclei up to ^{31}P. A list of the resonant frequencies for the nuclei observed is given in table 5.2.

Table 5.2: Resonant frequencies for nuclei in a 250 MHz spectrometer.

Nuclei	Nuclear spin	Sensitivity to ^1H =1.00	Frequency, MHz
^1H	1/2	1.00	250.130
^{13}C	1/2	$1.76*10^{-4}$	62.860
^2D	1	$1.45*10^{-6}$	38.376
^{23}Na	3/2	$9.25*10^{-2}$	66.128
^{11}B	3/2	$1.3*10^{-1}$	80.209
^{27}Al	5/2	$2.1*10^{-1}$	65.143
^{31}P	1/2	0.0663	101.202

The probes used were all 10 mm internal diameter with an excitation/detection coil and decoupler/lock coil (^2D internal only), both of length 20 mm. The spectrometer is controlled by an Aspect 3000 computer fitted with a pulse programmer.

Probe temperature is maintained by a B-VT1000 variable temperature unit capable of operating between 64K-574K (-209-301^{0}C), and the experimental temperature is monitored by a copper/constantin thermocouple. The temperature

of the probe can be set, by the operator, using a pulse program for variable temperature work.

MAS spectra were provided by Dr. M. Perry using a AC300 spectrometer. All spectra obtained on the Bruker spectrometer were transferred to a PC computer using a "NMRLINK" and processed on "WINNMR".

5.1: PULSE PROGRAMS AND CALCULATIONS

Experiments requiring pulse programs were performed on the Bruker spectrometer. T_1 measurements were made using the inversion-recovery sequence[1.12], outlined in section 1.5.2, using a standard microprogram installed on all Bruker spectrometers. Calculations for the value of T_1 were made using the Aspect 3000 software. NOE difference experiments were performed using an inverse-gated decoupling microprogram also preinstalled.

5.2: SAMPLE PREPARATION

Samples required for the SINNMR experiments were first ground under acetone, using a pestle and mortar, to give a fine powder. The powder was then graded using sieves obtained from Endecotts Ltd, manufactured to standard BS419/1986, to give the desired particle range. In order for the particles to remain in the NMR probe detector coil region the conditions were manipulated to give the particles zero buoyancy: this was achieved by density matching them in a support medium of chloroform and bromoform (obtained from Aldrich Chemical Company, stock

numbers: $CHCl_3$-31,998-8, $CHBr_3$-13,294-2). These chemicals have densities of 1.49 and 2.89 g/cm respectively and when combined in varying proportions the mixture can be arranged to have a density similar to that of the solid particles. It was found that the density of the liquid mixture should be slightly higher than that of the particles to allow for a possible reduction in density due to heating. The sample was then placed in a Goss 10 mm NMR sample tube (type 1005-P). If the glass tube contained the nucleus that was under observation then a 10 mm PTFE tube was used. In order to maintain the particles in the desired size range a few drops of octanol (Aldrich-29,324) were added as a surfactant to prevent particle aggregation. Any deuterium lock solvent was usually omitted due to the large amounts required effecting the density of the mixture.

5.3: SPECTRAL ACQUISITION

As discussed in section 3.4 the value of T_2 can be very small for solids and the NMR signal decays rapidly. In order to maximise the potential signal the delay between pulsing and acquisition was made short. The time was of the order of 100-150 μs for the JEOL and 15-20 μs for the Bruker. If the delay time is too short then the spectrum will contain baseline roll. Baseline roll is due to the probe electronics 'ringing' after the application of a pulse, if the detection period is started too soon, i.e. a short delay time, then the effect of ringing will be recorded in the FID and the transformed spectrum will have a sinusoidal baseline. The SINNMR technique is quite insensitive and a large number of scans are required to give sufficient signal to noise for detection purposes. The time required to perform the experiment can result in sample heating due to ultrasonic losses and particularly around the transducer face.

5.4: ULTRASOUND EQUIPMENT

5.4.1: TRANSDUCER MOUNTING

Ultrasound was applied to the liquid medium by a piezoelectric transducer, with connections of low electrical resistance, driven by a generator of suitable frequency. It must be able to oscillate freely and be resistant to chemical attack. A transducer holder was designed and built with these attributes that is capable of being inserted into the 10 mm NMR tube used. Various holders were developed and manufactured by the author and Weekes, the latest version of the transducer holder design is shown in figure 5.0.

Figure 5.0: Design for mounting of 5 mm transducers.

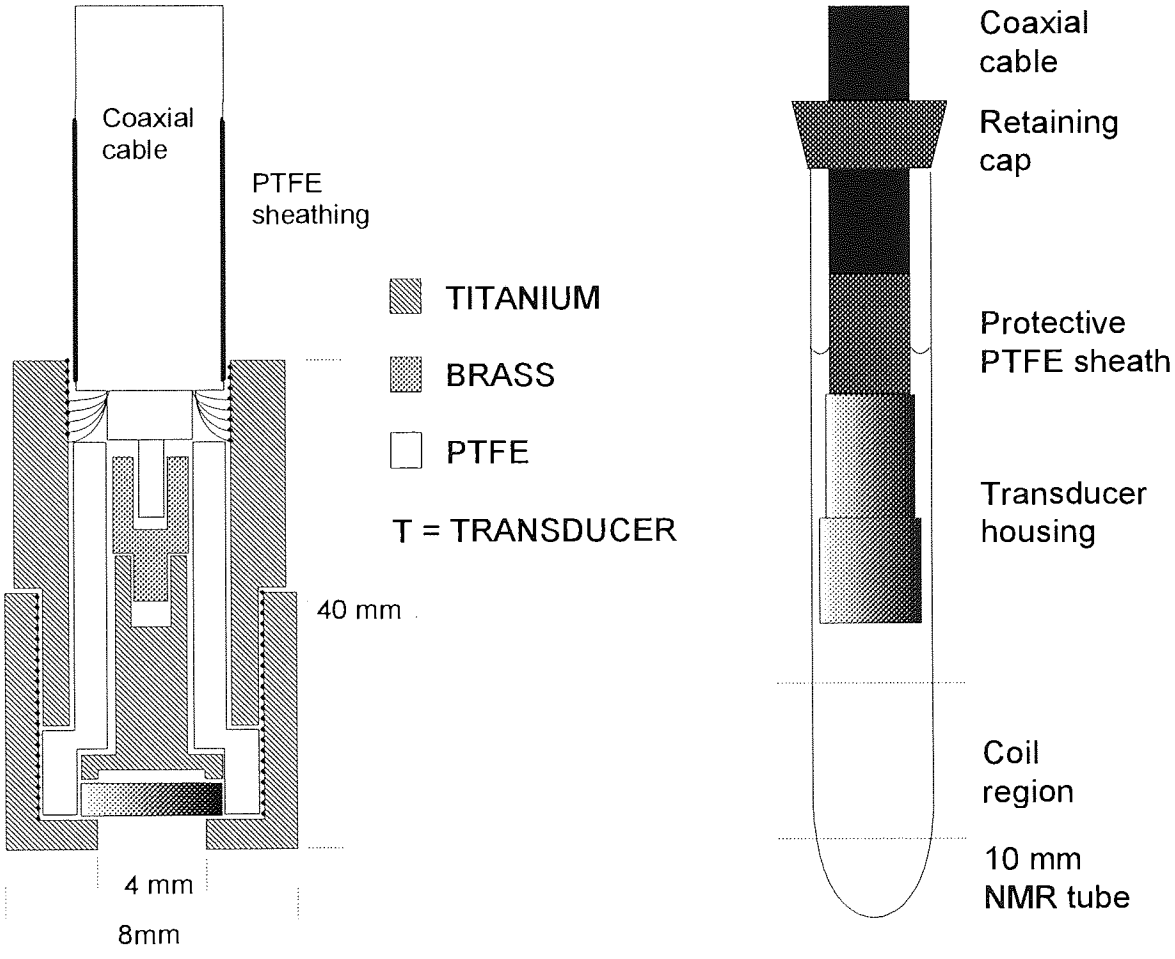

The holder was placed in the sample tube where there was sufficient liquid volume to cover the holder and act as a coolant. Care was taken to ensure that no air bubbles were present in front of the transducer face which could attenuate the ultrasound.

When use of a transducer housing was not practical a freely oscillating transducer was used. Copper electrodes were soldered to each face and attached to a glass rod by PTFE tape, see figure 5.1.

Figure 5.1: Mounting arrangement for transducer to a glass rod.

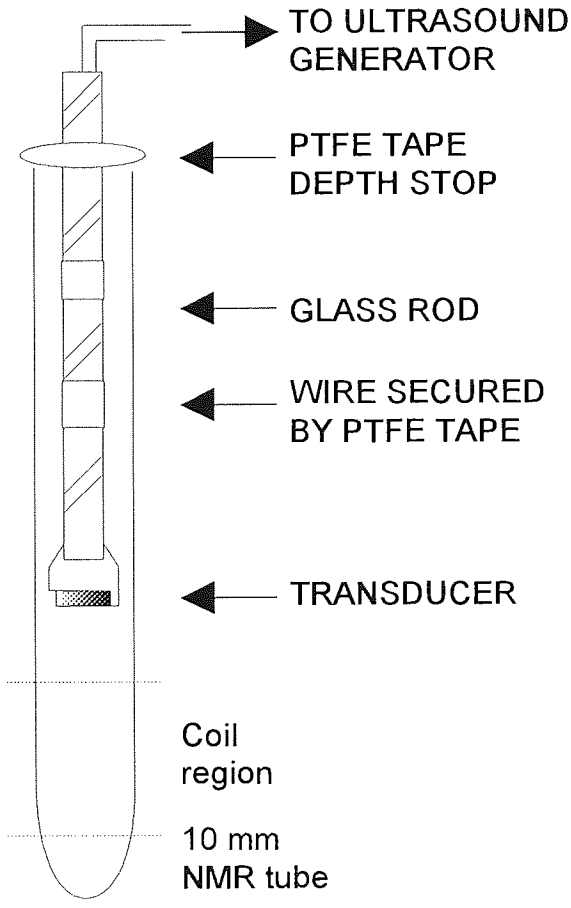

To prevent the interference of ultrasonic frequencies in the FID, from the r.f. power supplied to the transducer, a distance of at least 10 mm was maintained

between the transducer holder and the NMR probe coil, failure to do so resulted in a sinusoidal base line on the transformed spectrum at the frequency of the ultrasound. Variable temperature equipment was used to prevent overheating of the sample.

5.4.2: FREQUENCY GENERATION

All the ultrasonic frequencies used were in the MHz region and are synthesized using a radio frequency generator. The equipment, capable of generating frequencies in the range of 0.1-30 MHz with a maximum power delivery of 100 W, is show schematically in figure 5.2.

Figure 5.2: Schematic of the system used for the generation of radio frequencies.

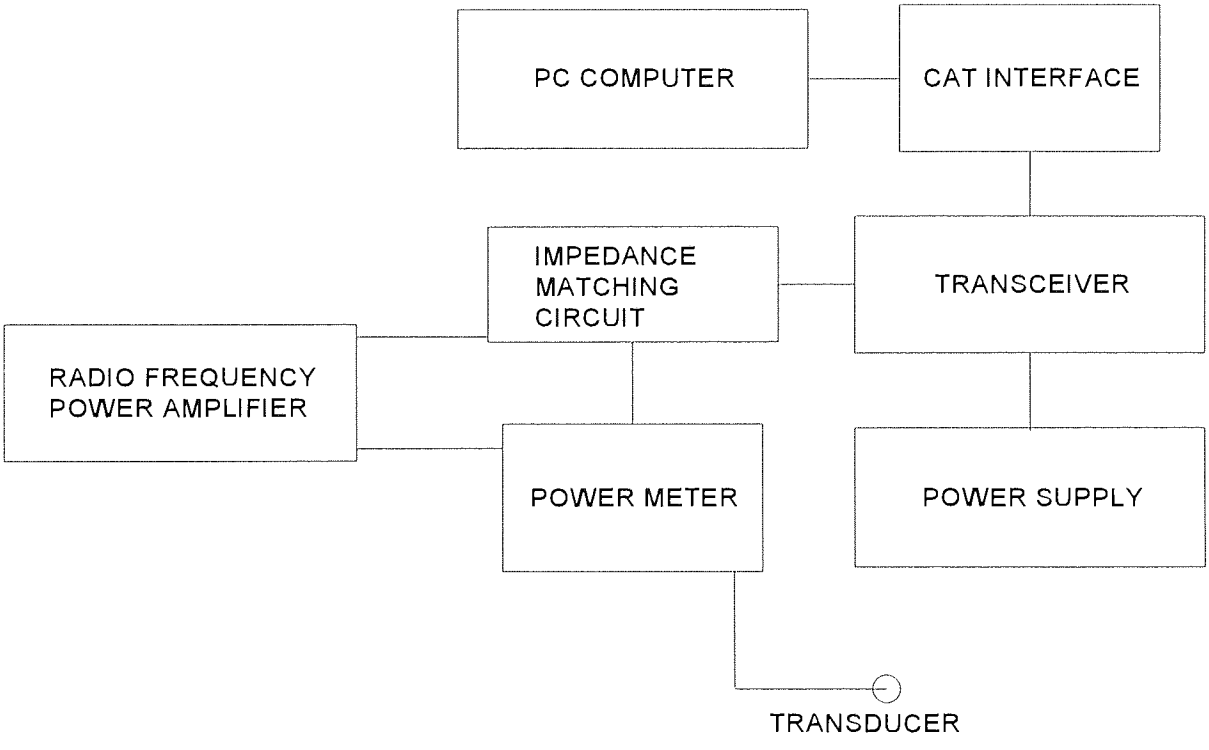

The system is based around a Yaesu FT840 transceiver driven by a suitable 13.5 V DC power supply of up to 20 A. Power delivery was maintained at a maximum by impedance matching of the circuit to the transducer. This was achieved by using a manual tuner, MJF-949E or an automatic antenna tuner, Yaesu FC-800. Additional power amplification was possible with a BNOS radio frequency $\times 10$ power amplifier: the maximum power that could be delivered to the transducer was a 150 W, as above this the transducer material breaks down.

The transceiver was computer controlled by an Amstrad PC 1512 SD (see appendix 3 for control program), via a Yaesu FIF-232 CAT (Computer Aided Transceiver) interface. This allowed the ultrasound to be delivered in continuous wave, pulsed, frequency sweep and random frequency modes.

5.4.3: TRANSDUCERS

The ultrasound was generated by piezoelectric crystals manufactured by Morgan Matroc Ltd. The crystals used were lead zirconium titinate (PZT) 5 mm diameter discs, silvered on both faces. The two types used in the experiments are PZT-4 and PZT-5A. PZT-4 has a high quality of resonance, Q_m=500, and is designed for use in high power applications: its Currie temperature is 325^0C. PZT-5A transducers have a larger bandwidth, Q_m=75, and find application in sensing equipment: its Currie temperature is 365^0C. The crystals used for the experiments resonate at fundamental frequencies of 2.0, 3.0, 5.0 and 10.0 MHz.

5.5: AIR DRIVEN ROTOR

All signal enhancement experiments (detailed in chapter 9) were carried out on the Bruker instrument because the field alignment does not affect the rotation speed. The device used is outlined in figure 5.3 and is designed to fit in a 10 mm NMR tube. PTFE was used in its construction because of its low friction qualities. As few metallic parts as possible were used to avoid circulating eddy currents, which would couple with the magnetic field. As with the transducer mountings a distance of 10 mm was maintained from the coil region to avoid interference. Sufficient sample volume (typically 5 ml) was used to prevent centrifugal forces and vortexing from reducing the coupling of the rotor with the liquid. The rotor that contacts the liquid was designed to provide a translation component to the liquid as well as a rotational one. A light operated frequency counter measured the spinning speed (minimum: 300 Hz).

Figure 5.3: Schematic design of the Air Driven Rotor.

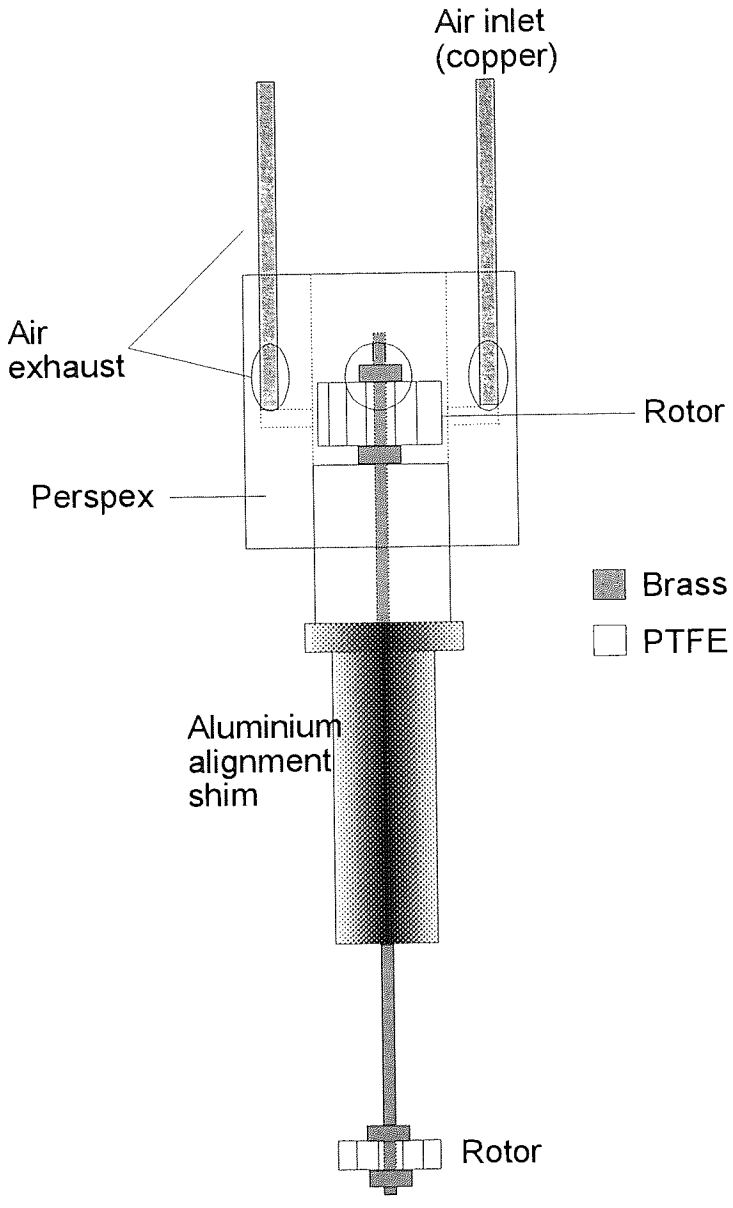

CHAPTER 6

SONOCHEMISTRY AND NMR

6.0: INTRODUCTION

In studying the use of ultrasound in NMR it is important to understand how the input of ultrasonic energy affects the medium. Cavitation occurs at high powers in liquids and may be important in SINNMR experiments. Cavitation is also used in sonochemical reactions and the possibility exists for using NMR to study rates of sonochemical reactions in situ. It has been stated[126] that the practical limit for cavitation in water is 2 MHz above which power requirements become to high. It is for this reason that medical ultrasonic imaging usually operates above 3 MHz[96]. Consequently, experiments were conducted to determine the conditions under which cavitation could be stimulated.

6.1: EXPERIMENTAL

The power required to generate a cavitation field within a liquid can be studied using the Weissler reaction[7]. The reaction is based on the oxidation of potassium iodide by free radicals to form iodine. The mechanism proceeds by radical formation in water, as described in section 4.10, which then activates oxygen dissolved in the aqueous medium. The yield of the reaction can be increased by the addition of a small quantity of carbon tetrachloride[127] which reacts with activated oxygen to produce free chlorine,

$$CCl_4 + H_2O \rightarrow Cl_2 + CO + 2HCl \qquad (6.1)$$

$$2HCl + O^{\bullet} \rightarrow Cl_2 + H_2O \qquad (6.2)$$

Chlorine then proceeds to liberate iodine,

$$2KI + Cl_2 \rightarrow 2KCl + I_2 \qquad (6.3)$$

which can be detected using starch solution to give blue/black colouration.

The reaction cell was set up as described for the SINNMR experiment (section 5.2). The quantities required for the experiment are not critical, however, the approximate quantities usually employed were; 1 g of potassium iodide in 5 ml of water with a 0.5 ml carbon tetrachloride and 2 ml of 2% starch solution was used as an indicator.

6.2: RESULTS

The Weissler reaction was performed at 2, 3, 5 and 10 MHz and the minimum input power, to initiate the release of I_2 (detected by the appearance of a blue/black colour) was noted. Table 6.1 shows the input power required to initiate the reaction based on an irradiating area of 0.125 cm^2.

Table 6.1: Power levels required for initiation of Weissler reaction.

	Frequency, MHz					
Power	2	2	3	3	5	10
Absolute, W	3	20	8	25	30	35
Intensity, Wcm^{-2}	23.8	159	63.6	198.9	238.7	278.5

The lower values of the intensity required for oxidation at 2 MHz and 3 MHz show that cavitation is possible at relatively low intensities at the lower frequencies. However, the experiments took several minutes to yield a colour change. All the other values resulted in colour changes after a few seconds.

The reaction was also performed in the presence of a magnetic field in order to determine whether the field would inhibit transducer oscillation. The results showed that there was no significant difference in the required input power to cause cavitation. An attempt was made to initiate the reaction by heating. The reaction sample was placed in a water bath and the temperature was increased until boiling of the sample occurred; no colouration was observed.

Work performed in conjunction with Weekes enabled the harmonic and sub-harmonic components of the transducer's frequency to be investigated using a spectrum analyser. It was found that the sub-harmonic components for each frequency was negligible and, therefore, not responsible for cavitation in the reaction.

Other sonochemical reactions based on the generation of radicals have been studied as a possibility of monitoring reaction, in situ, with NMR. The polymerisation of methylmethacrylate by ultrasound[123] was studied in conjunction with a final year project student[128]. However, no success with the reaction has so far been achieved.

6.3: CONCLUSION

The above results prove that is possible to achieve cavitation at frequencies up to the theoretical limit of 10 MHz. At lower powers, for 2 and 3 MHz, several minutes are required to observe a colour change. However, the reaction rate can be increased to give almost instantaneous colour changes at higher power levels.

The rate of colouration is proportional to the rate of liberation of iodine (from Beer's law). Therefore, increasing the ultrasonic power increases the intensity of the cavitation field and thus the rate of radical formation.

The lack of success in performing other sonochemical reactions at high frequencies is most likely due to incorrect experimental procedure. The polymerisation of methylmethacrylate does require the rigorous removal of oxygen. Attempts were made to remove the oxygen, but with the currently available apparatus this may not have been achieved sufficiently.

CHAPTER 7

SINNMR STUDY OF GLASSES

7.0: INTRODUCTION

All of the previous techniques concerned with the narrowing of the line width of solids are based on coherent averaging techniques, i.e. the motion is based on rotation about one or two axes. Molecular behaviour in liquids is random and it is the motional averaging of the internal Hamiltonians which is responsible for the narrow line widths observed. A colloidal suspension of solid particles will be subject to Brownian motion. Perin[129] has shown that particles may posses Brownian motion for sizes up to 130 μm. The spacial averaging of internal NMR Hamiltonians by Brownian motion has been studied by Yesinowski[130] and Satoh and Kimura[131, 132]. Both used techniques based on creating a colloidal suspension of ultra fine particles (UFP) such that the Brownian induced rotational correlation time meets the extreme narrowing condition ($\omega_0\tau_c<<1$). Yesinowski has shown[130] that chemical shift information can be obtain for the narrowed ^{31}P resonance in hydroxyappatite when the particle size is <5 μm. Satoh and Kimura have created UFPs of 1-100 nm and have produced narrowed ^{27}Al resonances from AlF_3 in colloidal suspension[131, 132].

Possible mechanisms responsible for the SINNMR effect are; ultrasonic cavitation (shock waves and microjetting), interparticle collisions, and turbulent streaming. During ultrasonic cavitation a collapsing bubble can generate shock waves or, if close to a solid surface, microjets. If a shock wave, or microjet, strikes a solid particle then its translational and rotational momentum may be increased. Further transfer of momentum between particles can occur via collisions. Turbulent motion of colloidal suspensions may be rapid enough for particles to experience spatial

averaging. A possible alternative method to ultrasound, to achieve the same motional averaging, was the use of an air driven rotor in contact with a colloidal suspension. Rapid stirring may be able to generate sufficient turbulent motion to cause a reduction in the NMR line widths of solids.

7.1: SINNMR STUDY OF GLASS

The samples under investigation, and their chemical data, were provided by Dr. Christian Jäger at the Mainz institute of Jena Physics department. The glass is composed of units of $Na_2O/B_2O_3/Al_2O_3$ in the molar ratio 20/70/10%. For the ^{27}Al nucleus there exists 4-, 5- and a few 6- co-ordination sites. For the ^{11}B nucleus there are BO_3 sites and a smaller number of BO_4 sites in the ratio 80:20. The boron units are soluble in water and the glass will completely dissolve in a strong acid. For this reason and to avoid solvation the sample was placed in a inert mixture of chloroform/bromoform, density matched to give the particles zero buoyancy. In order to reduce the heating of the sample by ultrasonic attenuation the samples were run with an air stream, provided by the spinner air, flowing over the sample tube. A list of spectrum parameters can be found in appendix 2.

7.1.1: ^{27}AL RESONANCE OF GLASS POWDER

The static ^{27}Al line width obtained for a powdered sample of the glass, with a large particle size distribution, is shown in figure 7.0 (reference: $Al_2(SO_4)_3$= 0 ppm). The full width at half maximum (FWHM), of the sample was 175 ppm (11400 Hz). The MAS spectrum (rotor speed: 7000 Hz), figure 7.1, shows mainly the presence of

the 4-co-ordination site with some 5-, while the 6- site is obscured by spinning side bands.

Figure 7.0: ^{27}Al static powder pattern, obtained from mixed particle range, using a non-spinning MAS probe. FWHM=175 ppm.

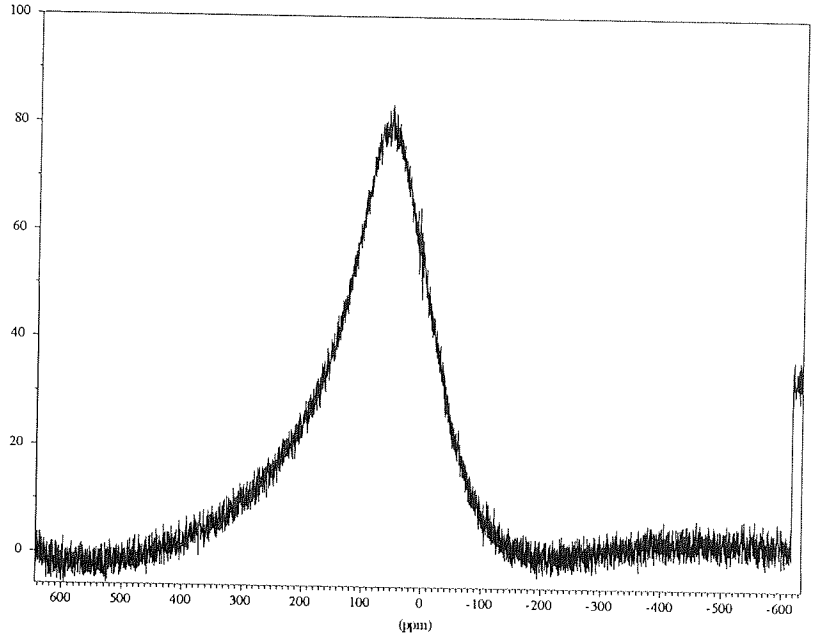

Figure 7.1: ^{27}Al MAS spectrum (rotor speed: 7000 Hz) of glass, $Na_2O/B_2O_3/Al_2O_3$. FWHM=27.8 ppm

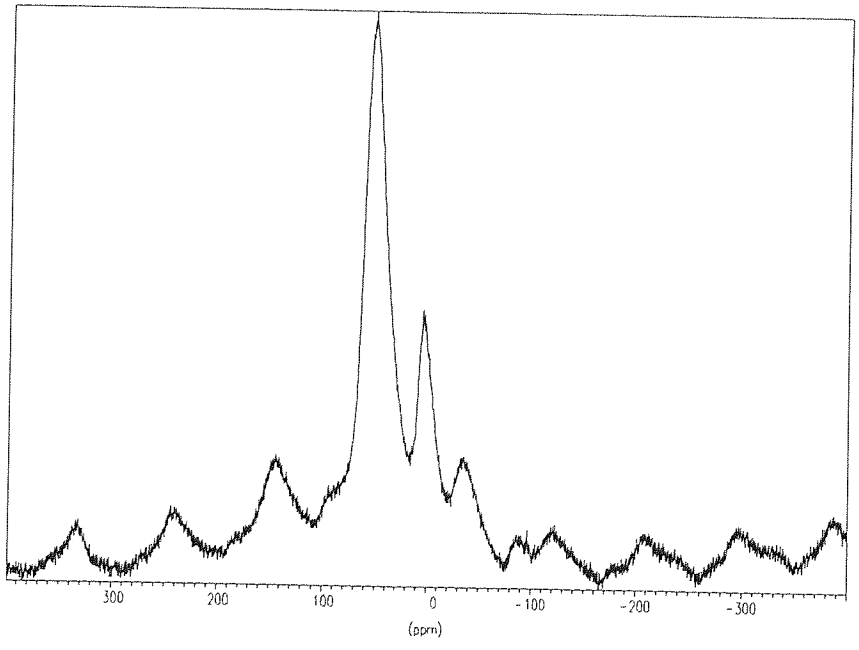

7.1.2: ^{27}Al RESONANCE OF COLLOIDAL SUSPENSION

A powdered sample of the glass with particle sizes less than 38 μm was suspended in water. A few drops of a surfactant 1-hydroxyethane1,1-diphosphonic acid (ADPA) was added to prevent the particles from aggregating or settling on the tube wall. The concentration of the acid used was insufficient to dissolve the glass as there was no change in the line shape on its addition. In suspension the particles are subject to rotational Brownian motion which results in partial averaging of the spins. Figure 7.2 shows the resulting spectrum for the suspension that has a line width (FWHM) of 38.5 ppm (900 Hz).

Figure 7.2: ^{27}Al spectrum of glass colloid, <38 μm, suspended in water/ADPA. FWHM=38.5 ppm.

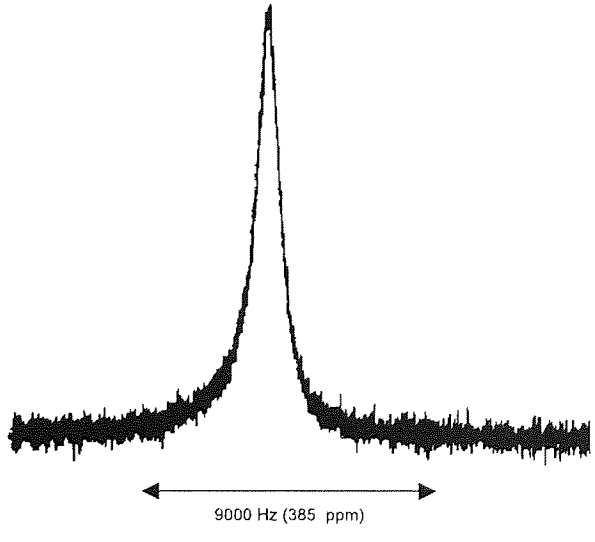

Ultrasound was then applied using a PZT-5A transducer, mounted on glass rod, operating at 2 MHz and 15 W. The resulting spectrum, figure 7.3, is extremely

noisy as a result of r.f. noise emitted from the transducer being picked up by the receiver coil during acquisition (the r.f. noise problem does not arise to such an extent for the housing mounted transducer as they are largely shielded). The S/N of the spectrum can be improved by multiplying the FID with an exponential weighting function, expressed in terms of additional line broadening, in Hz (see appendix 2 for value). The line width of the resonance is approximately half that in the previous spectrum at 18.9 ppm (440 Hz). Indications of any temperature effects can be determined by acquiring a spectrum immediately after the ultrasound has been switched off, see figure 7.4: each spectrum required 189 seconds to acquire. The line width for the spectrum in figure 7.4 is 31.7 ppm (740 Hz). Whilst figure 7.4 shows a partial return to the original line width it is not identical and thus indicates that some of the line width narrowing obtained in figure 7.3 is due to temperature induced Brownian motion.

Figure 7.3: ^{27}Al spectrum of <38 μm glass particle suspended in water/ADPA. Irradiate with ultrasound at 2 MHz and 15 W. FWHM=18.9 ppm.

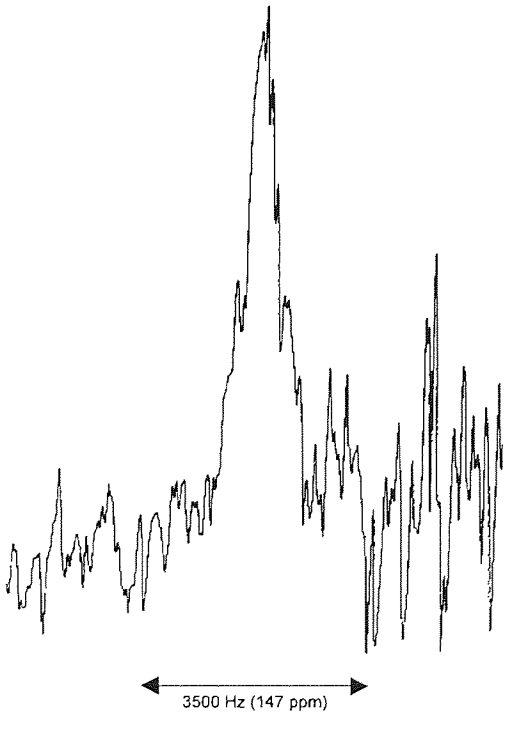

Figure 7.4: ^{27}Al spectrum of <38 μm glass particle suspended in water/ADPA, with no ultrasound and taken immediately after the acquisition of figure 7.3. FWHM=31.7 ppm.

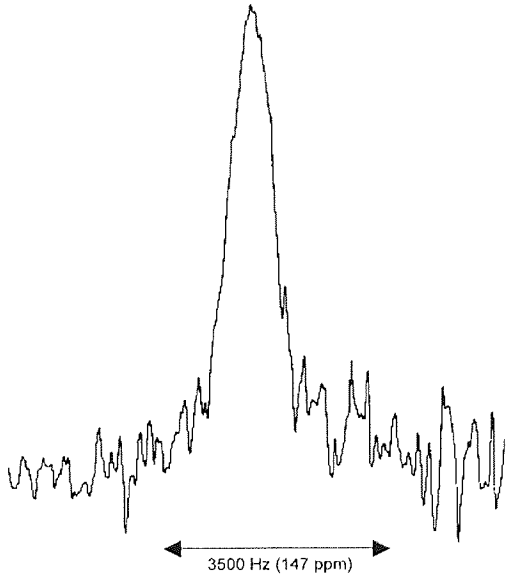

7.1.3: ^{11}B RESONANCE OF GLASS POWDER

Similar results can be obtained for the ^{11}B resonance in the glass sample. Figure 7.5 shows the ^{11}B static solid resonance for the glass powder, of mixed particle size, and this has a line width of 139.9 ppm (11200 Hz). The MAS spectrum (rotor speed: 5000 Hz) for the sample shows the two sites for BO_4 and BO_3, see figure 7.6.

Figure 7.5: ^{11}B static solid powder pattern for a mixed particle range using a non-spinning MAS probe. FWHM=139.9 ppm.

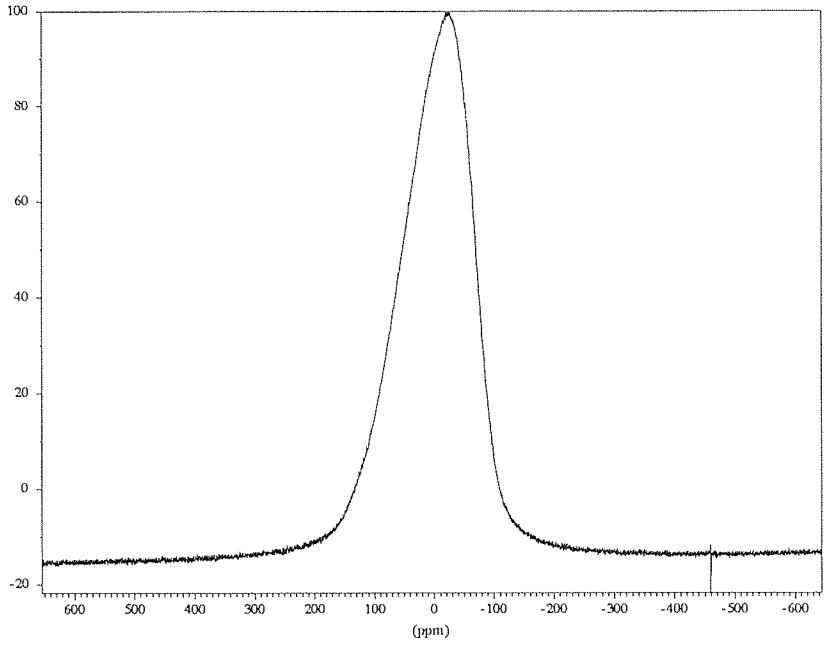

Figure 7.6: ^{11}B MAS spectrum (rotor speed: 5000 Hz) for $Na_2O/B_2O_3/Al_2O_3$. FWHM=6.18 ppm.

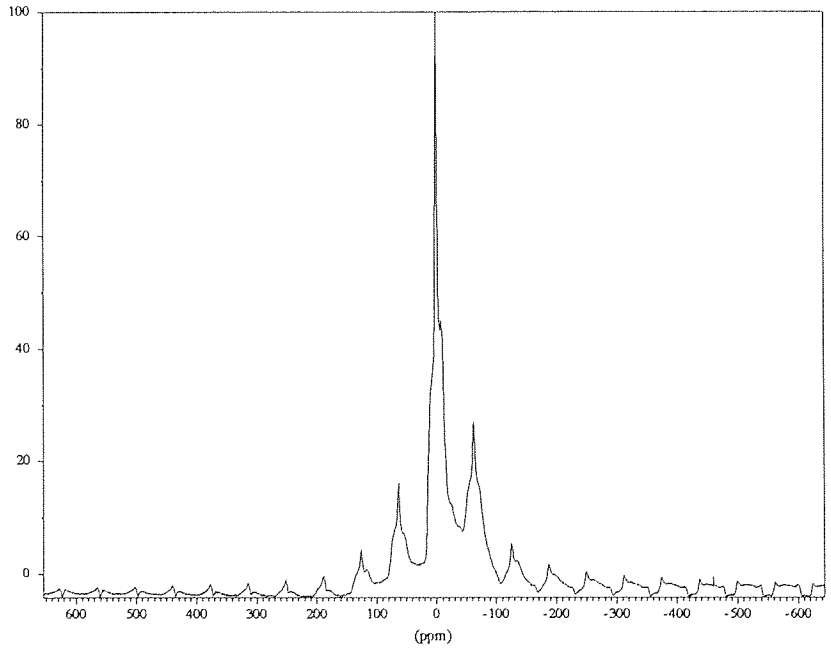

7.1.4: ^{11}B RESONANCE OF COLLOIDAL SUSPENSION

The sample was graded to give a particle size range of 75-104 μm and was density matched using a chloroform/bromoform mixture for zero buoyancy. The ultrasound was delivered by a 2 MHz PZT-4 transducer mounted on a glass rod. The broader resonance in figure 7.7, 41 ppm up field from the main peak, is due to boron present in the glass NMR tube. The spectrum obtained for the non-irradiated sample, figure 7.7, had a line width of 12.0 ppm (347 Hz). Ultrasound applied at 2 MHz and 20 W, figure 7.8, caused the line width to be reduced to 6.47 ppm (186 Hz). To investigate the effect of temperature the ultrasound was turned off and a spectrum was then acquired (each spectrum requires a 189 seconds), figure 7.9, and a line width of 7.96 ppm (229 Hz) was observed. Ultrasound was then re-applied at 50 W, figure 7.10, and yielded a line width of 4.22 ppm (122 Hz).

Figure 7.7: ^{11}B resonance for glass, of particle range 75-104 μm, suspended in a chloroform/bromoform mixture no ultrasound. FWHM=12.0 ppm.

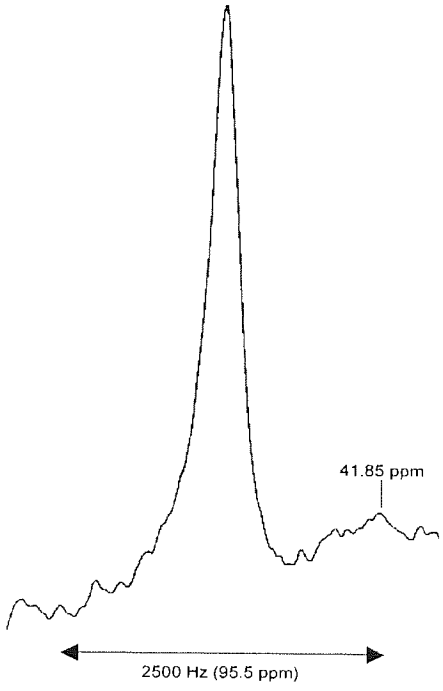

Figure 7.8: ^{11}B resonance for glass, of particle range 75-104 μm, suspended in a chloroform/bromoform mixture with 2 MHz ultrasound at 20 W. FWHM=6.47 ppm.

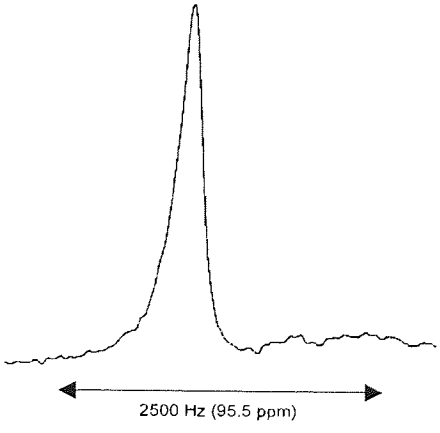

Figure 7.9: ^{11}B resonance for glass, of particle range 75-104 μm, suspended in a chloroform/bromoform mixture no ultrasound. Acquired immediately after figure 7.8. FWHM=7.96 ppm.

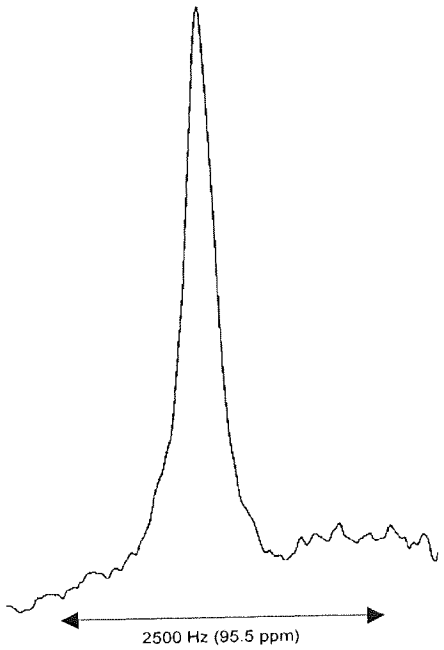

Figure 7.10: ^{11}B resonance for glass, of particle range 75-104 μm, suspended in a chloroform/bromoform mixture, with 2 MHz ultrasound at 50 W. FWHM=4.22 ppm.

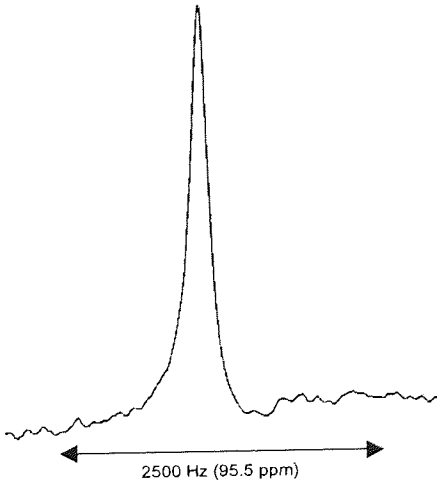

The experiment was then repeated using PTFE tubes to prevent any of the ^{11}B resonance being obscured by the boron resonance present in the glass tubes. The sample was graded to give a particle size range of 75-104 μm and density matched in a chloroform/bromoform mixture. The spectrum for the non-irradiated sample was acquired, figure 7.11, and gave a line width of 8.33 ppm (240 Hz). Ultrasound was then applied at 2 MHz and 50 W, figure 7.12, and had a line width of 4.59 ppm (132 Hz).

Figure 7.11: ^{11}B resonance for glass, of particle range 75-104 μm, suspended in a chloroform/bromoform mixture, no ultrasound. FWHM=8.33 ppm.

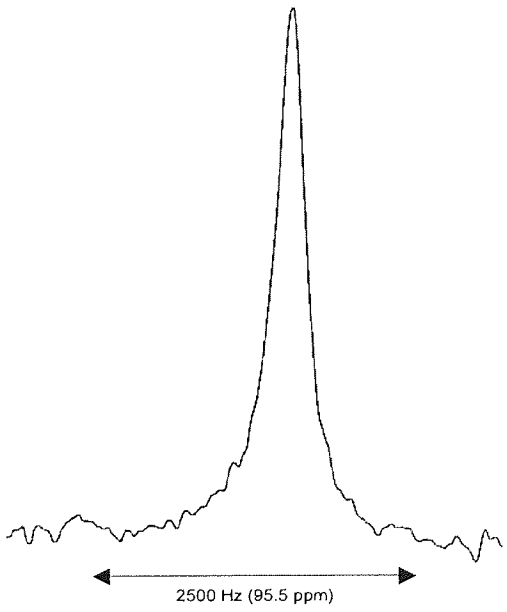

Figure 7.12: ^{11}B resonance for glass, of particle range 75-104 μm, suspended in a chloroform/bromoform mixture with 2 MHz ultrasound at 50 W. FWHM=4.59 ppm.

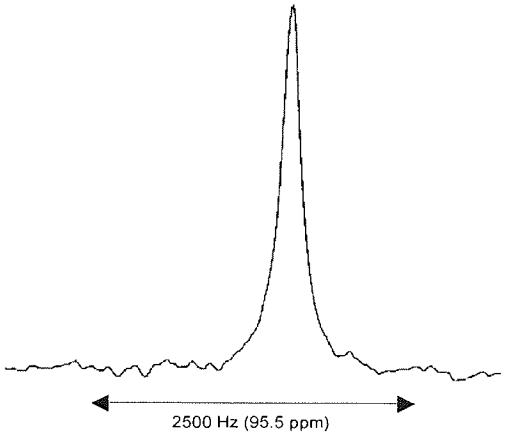

7.1.5: ^{27}Al RESONANCE FOR A RAPIDLY STIRRED SUSPENSION

The sample was graded to give a particle size range of <38 μm and suspended in water with a few drops of the surfactant ADPA. The experiment was performed on a Bruker WM 250 spectrometer, as the rotor would only operate when it was aligned with the magnetic field. The broadband probe used had self-supporting coils because the glass present in most Bruker probes contains ^{27}Al nuclei. The air driven rotor was fitted to a PTFE tube and the assembly placed in the probe. Acquisition parameters can be found in appendix 2.

The ^{27}Al spectra obtained showed no difference in the line width for stirring and non-stirring conditions. The experiment was repeated for the particle size range <38 μm in density matched chloroform and bromoform. Again, the line width was independent of stirring. The above experiment was repeated for a sample having

a particle size range of 75-104 μm and again no difference in the line width between stirred and non-stirred conditions was found.

7.2: CONCLUSION

Results have been obtained for the line widths for colloidal suspension with and without ultrasonic irradiation, for both the ^{27}Al and ^{11}B resonance of the glass $Na_2O/B_2O_3/Al_2O_3$. A summary of the line widths can be found in tables 7.1 and 7.2.

Table 7.1: SINNMR line widths for ^{27}Al resonance in $Na_2O/B_2O_3/Al_2O_3$.

SINNMR status	FWHM, ppm (Hz)
Static powder, mixed range	175 (11400)
MAS spectrum, mixed range	28.7 (2247)
Colloidal suspension, <38 μm	38.5 (900)
2 MHz ultrasound @ 15 W	18.9 (440)
Post-ultrasound	31.7 (740)

Table 7.2: SINNMR line widths for ^{11}B resonance in $Na_2O/B_2O_3/Al_2O_3$.

SINNMR status	FWHM, ppm (Hz)
Static powder, mixed range	139.9 (11200)
MAS spectrum, mixed range	6.18 (596)
Colloidal suspension, 75-104 μm	12.0 (347)
2 MHz ultrasound @ 20 W	6.47 (186)
Post-ultrasound	7.96 (229)
2 MHz ultrasound @ 50 W	4.22 (122)
Colloidal suspension, 75-104 μm	8.33 (240)
2 MHz ultrasound @ 50 W	4.59 (132)

The ^{27}Al resonance results show that by placing a solid powder in a colloidal suspension, significant line width narrowing can be achieved relative to that of the

solid state, figures 7.0 and 7.2. This is supported by the ^{11}B resonance, which when placed in colloidal suspension experiences a similar reduction in the line width, figure 7.5 and 7.7. The reduction in the line width is due to the partial averaging of the NMR Hamiltonians. For this to occur the solid particles must possess rotational Brownian motion, as stated by Perin[129], and supports the work of Yesinowski[130] and Satoh and Kimura[131, 132].

By irradiating the colloidal suspension with ultrasound further line width narrowing was achieved for both the ^{27}Al, figure 7.4, and ^{11}B, figures: 7.8, 7.10 and 7.12. Since the line width narrowing was obtained for both nuclei then it is likely that the mechanism is additional particle motion rather than solvation of a particular nucleus: the line widths are too broad for the solution state. Various ultrasonic power levels have been used but successful line width narrowing has only been achieved with power levels in excess of 15 W. The results of chapter six imply that a cavitation field is the mechanism responsible for additional Brownian motion. Given that power levels of >15 W are required, then a significant cavitation field intensity is necessary for the solid particles to possess rotational motion rapid enough to cause spatial averaging of the spins.

As shown in section 7.1.5, rapid stirring of a colloidal suspension generates turbulent motion imparting translational and rotational motion to the solid particles. However, this type of motion is not rapid enough to result in line width narrowing.

Each spectra obtained for the colloidal suspension requires 189 seconds to acquire. During this time period the sample will experience some heating, due to the ultrasonic losses, and will cool when the ultrasound is removed. Spectra that were taken immediately after the application of ultrasound, figure 7.4 and 7.9, show an increase in the measured line width. However, the line width is not identical to the original line widths obtained before the irradiation with ultrasound. The Brownian motion of particles suspended in the liquid is proportional to the temperature of the liquid, the implication is that the narrowing was partially due to temperature induced Brownian of the solid particles. Temperature effects cannot be discounted as a mechanism toward the achievement of narrow line widths in the SINNMR experiment. However, similar line widths were obtained on separate occasions for a 50 W power input, indicating a similar cavitation field is responsible for the line width rather than a similar heating rate. Also, the irreproducibility of the technique means that temperature is unlikely to be the sole mechanism, as otherwise line width narrowing would be more readily obtained. A study of the line width of the ^{27}Al and ^{11}B resonances with temperature would give clearer evidence of the role of temperature in SINNMR, unfortunately there was insufficient glass sample remaining to perform this experiment.

The SINNMR experiment has been performed for various particle size ranges, ultrasonic frequencies and power level have been investigated but no one set of parameters gives consistent line width narrowing on sonic irradiation. This suggests that other factors are important in the SINNMR technique, which has proved difficult to reproduce. Given that cavitation appears so important in

narrowing, these factors must impinge on the cavitational field intensity. The mass of solid particles suspended in the liquid will scatter sonic waves reducing the cavitational field intensity.

The SINNMR technique has been performed also by gating the ultrasonic power. This method prevents the collection of solid particles at standing wave nodes which may form within the tube. Pulsing also prevents streaming and the use of higher instantaneous power levels without incurring excessive heating. Sweeping of the ultrasonic frequency has also been investigated to induce particle motion. As yet, none of the above ultrasonic modes has achieved line width narrowing.

CHAPTER 8

SONIC IRRADIATION OF LIQUID CRYSTALS

8.0: INTRODUCTION

The work in this chapter was carried out in collaboration with Professor J. Emsley and Dr. M. Edgar of the University of Southampton.

A liquid crystal in the presence of a static magnetic field will align itself in an equilibrium position either parallel or perpendicular to the direction of the field[8, 133, 134]. It was proposed that liquid crystals can be deflected from their field aligned direction by the influence of ultrasonic radiation pressure. The work in this chapter is concerned with observing the changes in the ^{2}H NMR spectrum of a solute probe aligned with the liquid crystals when they are deflected from equilibrium by using ultrasound. The motion of liquid crystals under sonic irradiation might be used as an indication of the motional behaviour of a sample in the SINNMR experiment, i.e. whether the motion of the sample, under the influence of acoustic streaming, is random, and thus, if it is capable of imparting incoherent motion to solid particles.

8.1: LIQUID CRYSTALS

Liquid crystals were first characterised towards the end of the last century by Reinitzer[135] and Lehman[136]. These workers noticed that on raising the temperature of certain solids an opaque liquid was formed which became colourless at a higher temperature. The transition state was described as a mesophase.

A solid has a long range regular crystal structure extending in three dimensions, whereas a liquid possesses some short range order but is mobile and chaotic at long range. For a liquid crystal there is a degree of long range orientational order arising from strong interactions between neighbouring molecules caused by preferential stacking. Most liquid crystals are rod like and tend to align themselves in parallel, however, the liquid crystal molecules are still mobile and their direction of alignment varies continuously from point to point within the bulk sample. The liquid crystals can form a number of mesophases, with differing degrees of order, which have been characterised by Friedel[137]. Those that possess specific phases with temperature changes are designated as thermotropic. The lowest form of ordering is the nematic phase where molecules posses only parallel alignment. The nematic phase is the last mesophase before the clearing temperature, where they have sufficient energy to overcome their intermolecular interactions, and the system becomes isotropic. Higher modes of ordering are the smectic phases where the molecules are arranged in a parallel and lateral array, see figure 8.0.

Figure 8.0: Ordering of liquid crystals in their mesophase.

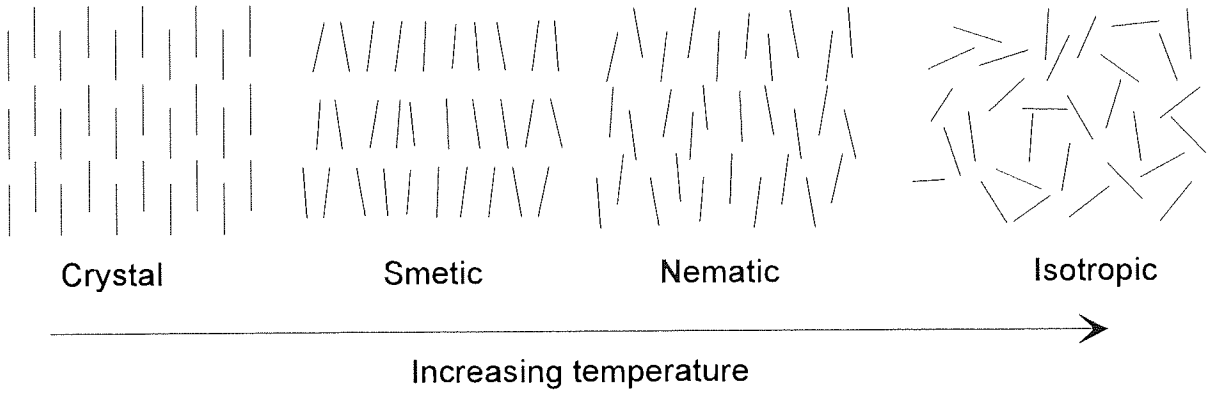

A mixture of detergent molecules and solvent can be used to form liquid crystals known as lyotropics. A detergent molecule consists of a hydrophilic polar head with a hydrophobic long hydrocarbon chain. The detergent can form differing mesophases depending on the solvent in which they exist. Packing of the phases, see figure 8.1, can be, (a) lamellar; amphipiles are arranged adjacently in sheets with the solvent sandwiched in-between, (b) cubic; micelles with the polar heads on the exterior arrange themselves in a body centred cubic formation, (c) middle or hexagonal phase which consists of cylindrical units, where the polar heads lie on the surface of a tube, arranging themselves in a hexagonal array.

Figure 8.1: Phase formation for lyotropic liquid crystal.

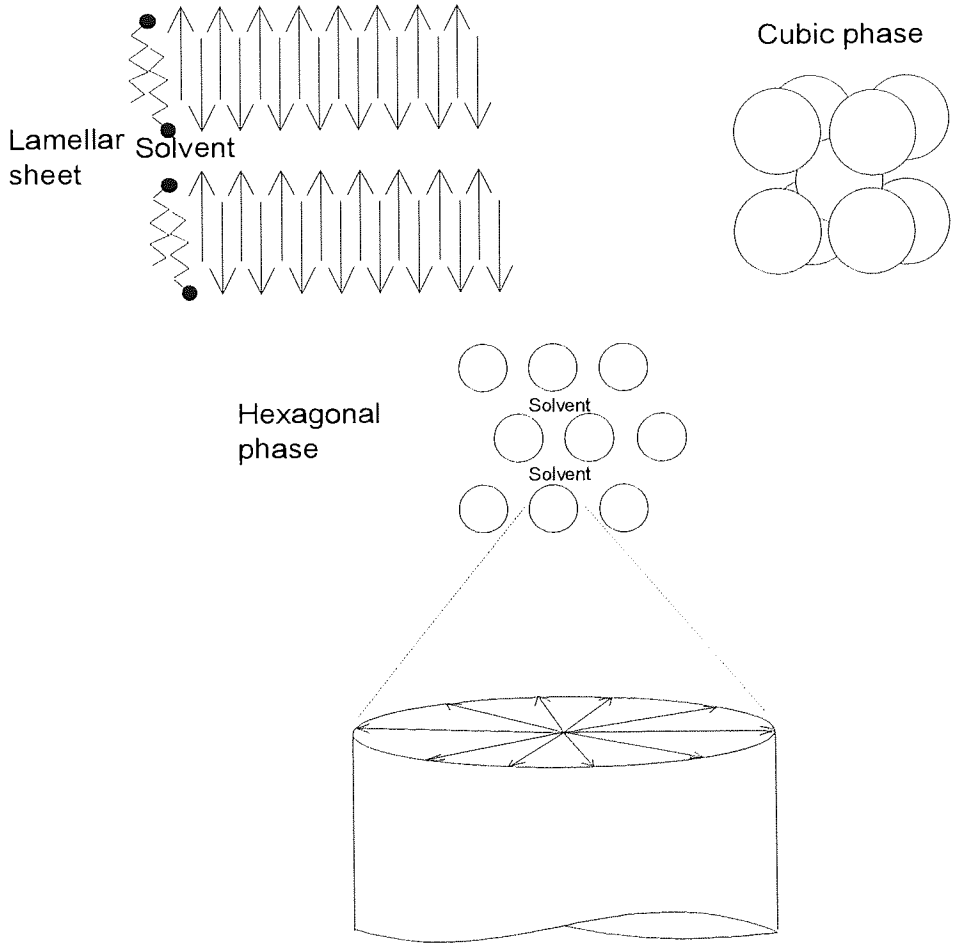

For a further account on the theory of liquid crystals see the text by Chandrasekhar[138].

8.2: LIQUID CRYSTALS IN MAGNETIC FIELDS

The orientation of the nematic phase is governed by a director for the molecule. In the absence of other influences this will be parallel with the major molecular axis. When placed in a magnetic field most liquid molecules will experience a torque tending to align themselves with the minimum free energy. Normally the free energy of a molecule is much smaller than the thermal energy, thus the molecules randomly orientate themselves. However, for liquid crystals this is not the case when in the presence of a static magnetic field. The liquid crystal aggregates experience a larger torque, due to intermolecular interactions, and therefore, the free energy is larger than the thermal energy. The liquid crystal now possesses long range ordering with a free energy, G, dependent on the angle, α, between the director and the magnetic field, given by,

$$G = -\Delta\chi.H_0^2.\frac{\left(3.\cos^2\alpha - 1\right)}{6} \qquad (8.1)$$

$\Delta\chi=\chi_{\parallel}-\chi_{\perp}$ is the anisotropy in the bulk diamagnetic susceptibility, where the parallel component is aligned with the director. For a thermotropic liquid crystal $\Delta\chi$ is positive and the minimum energy is for parallel alignment to the magnetic field. A lyotropic liquid crystal has a negative $\Delta\chi$ and G is minimum for perpendicular alignment.

8.3: NMR OF LIQUID CRYSTALS

Pure liquid crystals give very broad proton spectra because of the lack of averaging of the nuclear interactions. Solvating a liquid crystal averages many of the non-equivalent nuclei and a complexed resolved spectrum can be seen. If a

small amount of solute is added it need not disrupt the mesophase and can be used as a probe for the orientation of the liquid crystal within a magnetic field.

The appearance of the NMR spectrum of the solute probe will depend on the orientation of the liquid crystal within the magnetic field. Deuterated solvents are usually employ as probes to prevent the resonance observed being obscured by peaks arising from the liquid crystal. For a random 3D distribution of the liquid crystal directors the powder pattern is typical for a quadrupolar nucleus (c.f. figure 3.6). The spectrum changes as the degree of alignment increases, becoming a pair of single lines when completely aligned, see figure 8.2.

Figure 8.2: Line shape of a ^{2}H molecular probe with liquid crystal alignment.

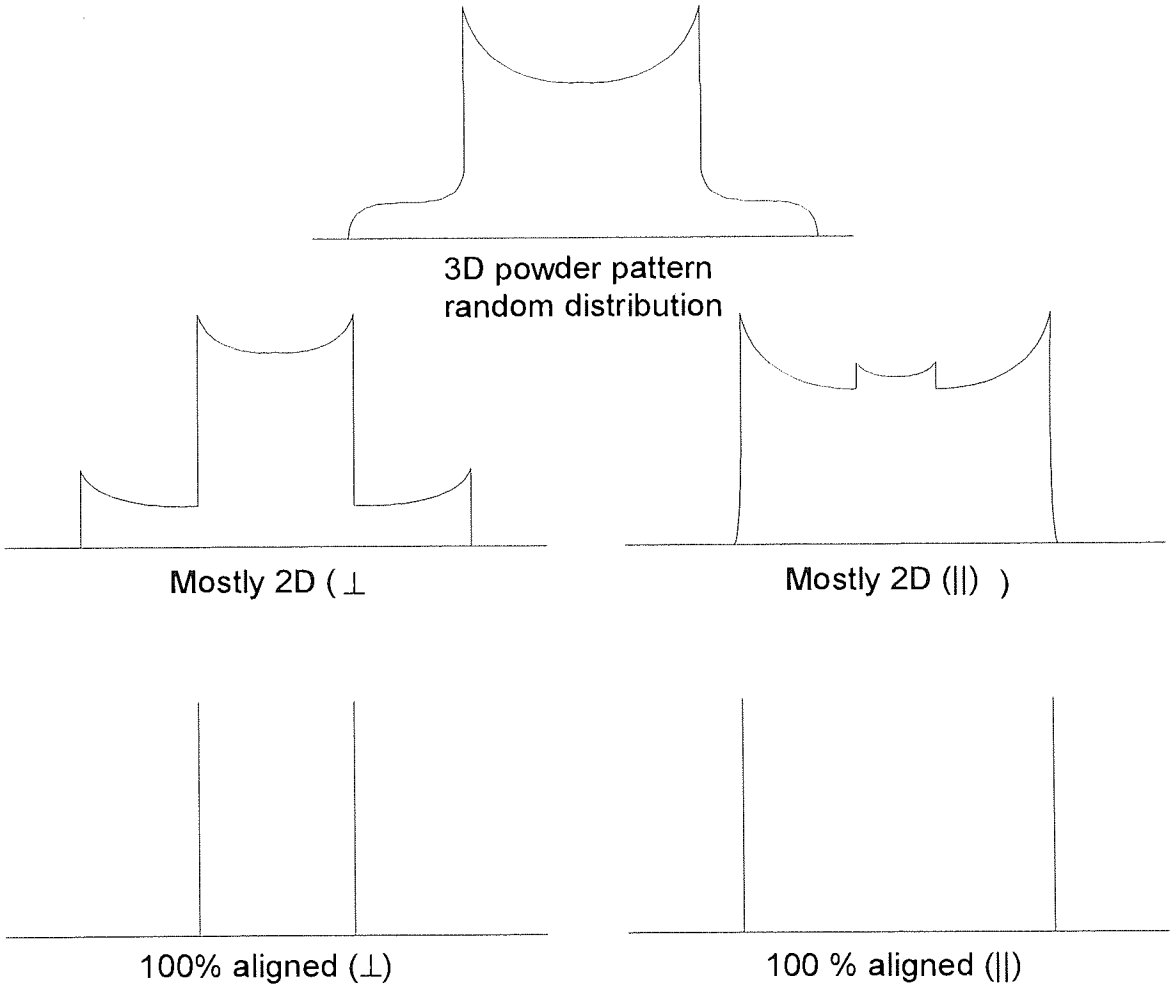

The degree of deviation of the director orientation from its equilibrium position can be calculated from the ratio of the original, Q_0, and perturbed, Q_p, quadrupolar splittings. The angle between the director and the magnetic field can be related to the quadrupolar splitting by equation (3.23). Assuming that the ordering parameter of the benzene molecule to the liquid crystal molecule does not change and the rise in the temperature of the sample is small, the angle of the director with respect to the magnetic field may be calculated as,

$$\frac{Q_p}{Q_0} = \frac{\chi.(3.\cos^2\theta_p - 1)}{\chi.(3.\cos^2\theta_0 - 1)} \tag{8.2}$$

Thus, for a thermotropic liquid crystal, where $\theta_0=0^0$, the angle of deflection, θ_p, may be determined from,

$$Q_p = \frac{Q_0.(3.\cos^2\theta - 1)}{2} \tag{8.3}$$

For a lyotropic liquid crystal, $\theta_0=90^0$, and the director angle with respect to H_0 is given by,

$$Q_P = Q_0.(1 - 3.\cos^2\theta) \tag{8.4}$$

and the angle of deflection equals $(90\text{-}\theta_p)$, see figure 8.5.

Figure 8.3: Angle change of a lyotropic liquid crystal director due to ultrasound.

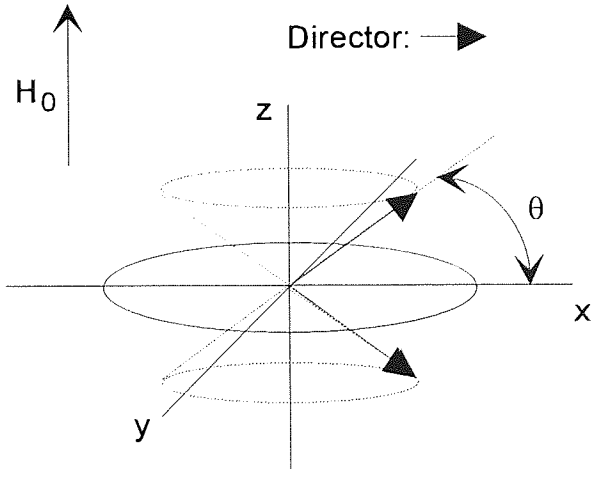

8.4: EXPERIMENTAL

The object of the experiment is to perturb the director orientation within a magnetic field by using ultrasonic radiation pressure to deflect the directors from their equilibrium position. The effect is likely to depend on the relative orientation of the acoustic and magnetic fields and the nature of the liquid crystal used. For example, if the liquid crystal is aligned parallel to H_0 then the ultrasonic radiation pressure will be most effective when it propagates perpendicular to H_0. Radiation pressure can be generated by ultrasonic streaming causing the directors to be aligned with the direction of flow, as described by Dysthe[4.12] (section 4.9).

Due to the highly viscous nature of liquid crystals, ultrasound is strongly attenuated and the ultrasonic wave cannot penetrate completely through the sample. In all of the liquid crystal experiments performed a region of ultrasonic influence was observed in which streaming occurred, see figure 8.4.

Figure 8.4: Streaming effect in a viscous liquid crystal.

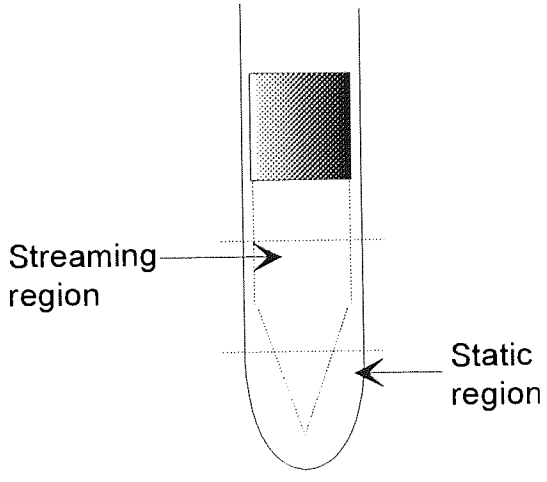

High attenuation means that a large power requirement is necessary to generate streaming within the coil region and the absorption will manifest itself as heating

within the sample. The NMR of liquid crystals are highly temperature dependent and the ^{2}H quadrupolar splitting of the NMR spectrum will reduce with increasing temperature to form a singlet at the clearing temperature. The effect of ultrasonic heating can be minimised using VT equipment to maintain the probe temperature, but a temperature gradient will always be present to some degree. A list of spectrum parameters used can be found in appendix 2.

Ultrasound is attenuated as it moves away from the source, therefore the liquid crystals will experience a decreasing radiation pressure and the directors will be deflected through a range of orientations. Each angle results in a particular quadrupolar splitting and therefore a broadening of the doublet will occur for the range of orientations. As observed during the liquid crystal experiments, and shown in figure 8.4, a large proportion of the sample is under the influence of ultrasound, with a small volume left unperturbed. If director reorientation was the dominant effect then it was found that the NMR spectrum would be similar to spectrum on the left hand side of figure 8.5. The position of maximum intensity represents a large proportion of the liquid crystal directors being reorientated through a maximum angle. The 'tail off' in the intensity of the line is attributed to the attenuation in ultrasound perturbing the directors through smaller angles, until a maximum quadrupolar splitting is obtained for unperturbed liquid crystal molecules.

A typical line shape was observed for the effect of ultrasonic heating. At ambient temperature the quadrupolar splitting will have some value, Q_T. The ultrasound

sound can be considered as a source of heating which generates a temperature gradient through the sample. The variation in temperature will result in a range of quadrupolar splittings and a lineshape similar to that on the right hand side of figure 8.5 will be observed, where the decay in the intensity of the lineshape is related to the rate of heating. For a small rate of heating there will be a small range of splittings, giving a sharp tail off in the lineshape. Increasing the rate of heating will reduce the decay in the line shape and the line width will increase. The heating effect is limited by the clearing temperature, which results in the rapid appearance of the isotropic shift if the heating rate is too high.

The effect on lineshape for director orientation and temperature gradient can be seen in figure 8.5

Figure 8.5: Pattern shape for liquid crystal due to reorientation or temperature gradient.

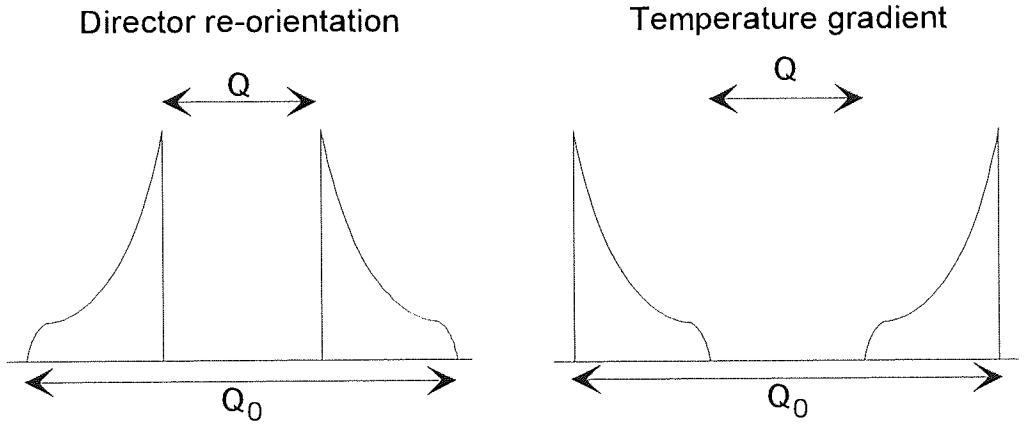

8.5: RESULTS

8.5.1: EFFECT ON LIQUID CRYSTAL I35

The liquid crystal I35 is thermotropic and aligns itself parallel to the magnetic field (see appendix 4 for molecular structure). Dysthe theory[4.12] states that the most stable orientation is when the long axis of the molecule is parallel to the direction of sonic propagation. In order for the ultrasonic radiation pressure to re-orientate the liquid crystal director it must be applied from a perpendicular direction with respect to the director. The iron core magnet system of a JEOL FX 90Q spectrometer is arranged such that the magnetic field direction, H_0, is perpendicular to its probe axis and, therefore, the direction of ultrasonic propagation.

The liquid crystal contained 10 $\%^{w}/_{w}$ benzene d-6, and a clearing temperature of 92^{0}C (365 K) was measured. A plot of the quadrupolar splitting with temperature is shown in figure 8.6 (table 8.1).

Table 8.1: ^{2}H quadrupolar splitting with temperature for benzene-d6 in I35.

Temperature, K	Splitting, Hz (ppm)
303	27326(2023)
307	26181(1903)
320	24487(1780)
325	22716(1651)
340	20216(1469)

Figure 8.6: Doublet splitting with temperature for I35.

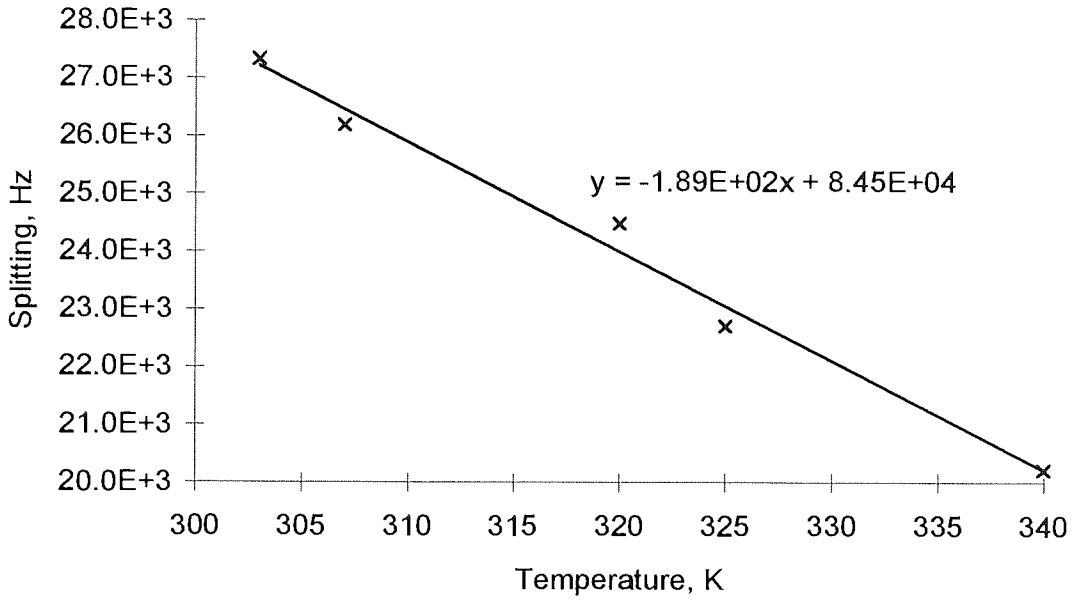

A ^{2}H spectrum was obtained for the liquid crystal under ambient magnet conditions ($T=28^{0}C$) and the peak separation was measured as 27155 Hz (1965.6 ppm), see figure 8.7. Ultrasound was then applied to the liquid crystal (2 MHz @ 9W), see figure 8.8. The spectrum contains an outer pair of lines from unperturbed liquid crystal separated by 26984 Hz (1953 ppm), which is equivalent to a temperature of 304 K. Asymmetry in the line shape is due to a temperature gradient existing within the sample. The inner pair of lines, separated by 14157 Hz (1024.7 ppm), arise from the liquid crystal being re-orientated within the field, their broad nature is due to a range of orientations. Assuming both Q_0 and Q_p are for the same temperature, the angle of deflection of the director can be calculated from equation 8.3 as,

$$\frac{Q_p}{Q_0} = \frac{14157}{26984} = \frac{\left(3.\cos^2\theta - 1\right)}{2} = 34.26^{\circ} \qquad (8.5).$$

The quadrupolar splitting of the inner lines was compared to the temperature plot of figure 8.6, and the separation was found to be equivalent to a temperature of 372 K which is greater than the clearing temperature. Consequently, this pair of lines must be due to the effect of ultrasound on the director orientation. The central line is the isotropic shift caused by a hot spot close to the transducer face.

Figure 8.7: Normal ^{2}D spectrum of benzene-d6 in liquid crystal I35.

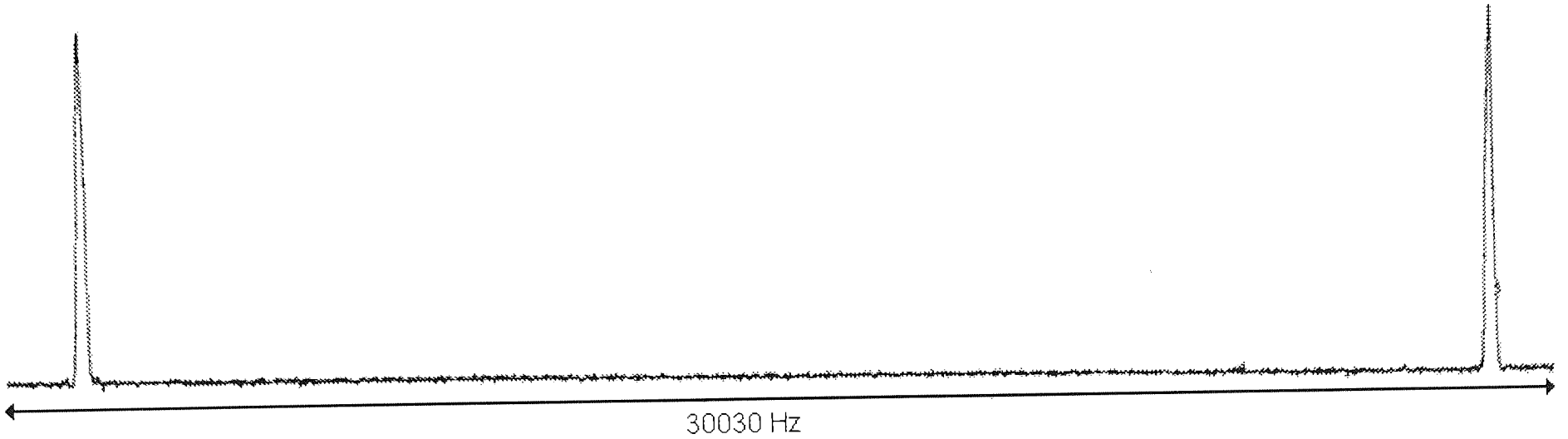

Figure 8.8: ^{2}D spectrum of benzene-d6 in liquid crystal I35, irradiated with ultrasound (2 MHz @ 9W).

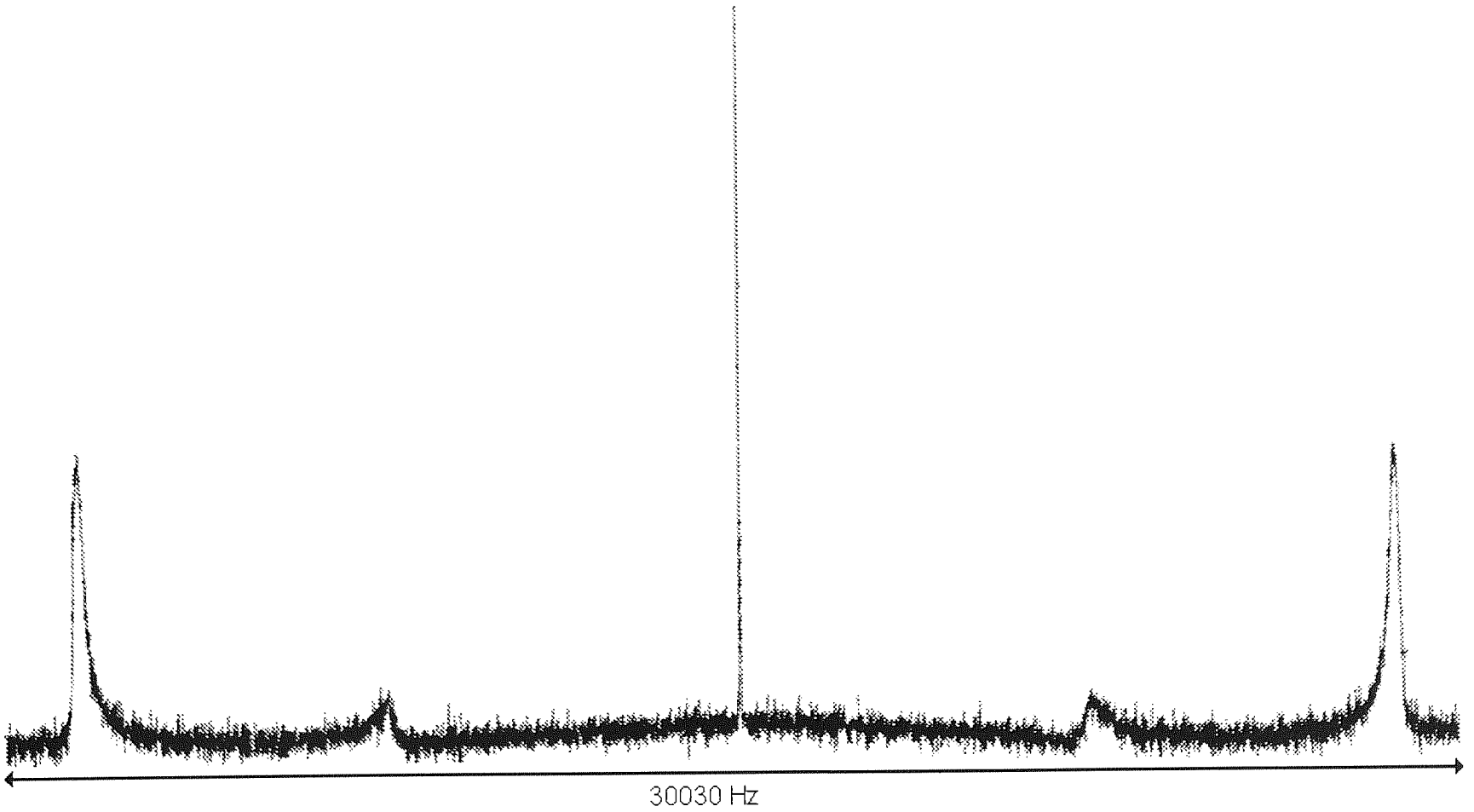

8.5.2: EFFECT ON LIQUID CRYSTAL ZLI-1167

The liquid crystal ZLI-1167 is thermotropic mixture in which the directors align perpendicular to the direction of the magnetic field (see appendix 4 for molecular structure). As discussed in section 8.5.1 (and section 4.9), the maximum ultrasonic effect on the liquid crystal directors will be when the ultrasound is applied from a perpendicular direction with respect to the liquid crystal director. Therefore, all ZLI-1167 experiments were conducted in the super conducting magnet of a Bruker WM 250 spectrometer, where the probe axis lies parallel to the field direction.

The sample contained 10 $\%^{w}/_{w}$ of benzene-d6 and a clearing temperature of $51^{0}C$ (324 K) was measured. A plot of quadrupolar splitting with temperature is shown in figure 8.9 (table 8.2).

Table 8.2: Quadrupolar splitting with temperature for ZLI-1167.

Temperature, K	Splitting, Hz
273.0	16235.4
283.0	16246.7
293.0	16250.8
303.0	15559.4
313.0	14840.7
316.0	13452.2
319.0	12793.0
323.0	13145.5
323.0	11743.2
326.0	10791.0
329.0	9570.3
332.0	7860.8

Figure 8.9: Quadrupolar splitting with temperature for ZLI-1167.

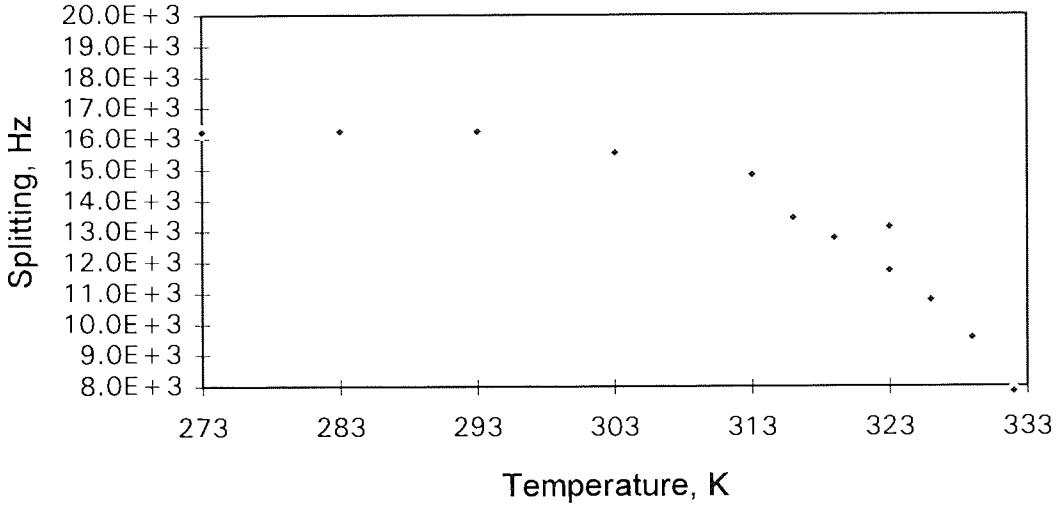

A deuterium spectrum of benzene-d6 for the unperturbed liquid crystal at ambient temperature, 293K, is shown in figure 8.10 and has separation of 16456 Hz (428.7 ppm).

Figure 8.10: ^{2}D spectrum of benzene-d6 in ZLI-1167 at 293 K.

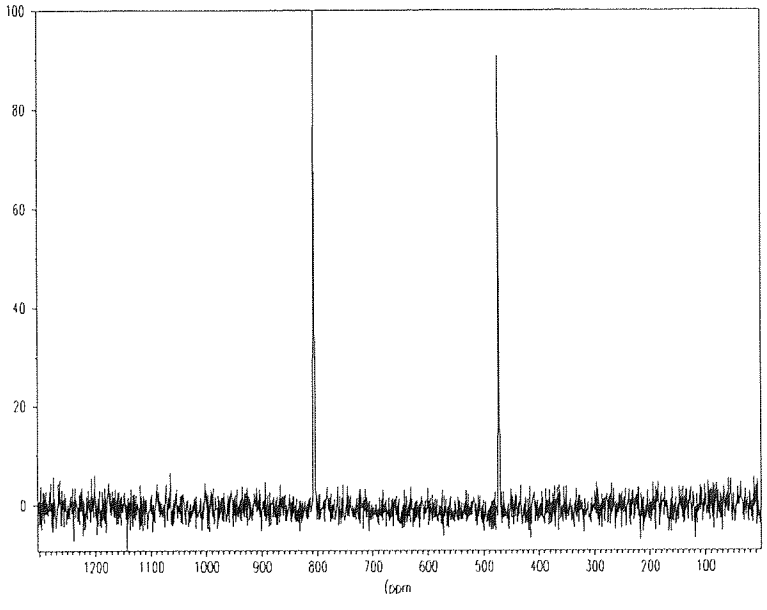

Ultrasound was then applied at 2 MHz @ 4 W, see figure 8.11 (VT equipment was employed to prevent over heating, and was set at 273 K). The quadrupolar splitting for the unperturbed liquid crystal can be found from the separation of the

outer wings of the two lines (marked Q_0), and was found to be equal to 18521 Hz. The effect of the ultrasound was to cause a broadening of the line widths. This arose from a range of new director orientations caused by a distribution of reordering effects due to attenuation in the streaming volume.

Figure 8.11: ^{2}D spectrum of liquid crystal ZLI-1167 irradiated with 2 MHz ultrasound at 4W.

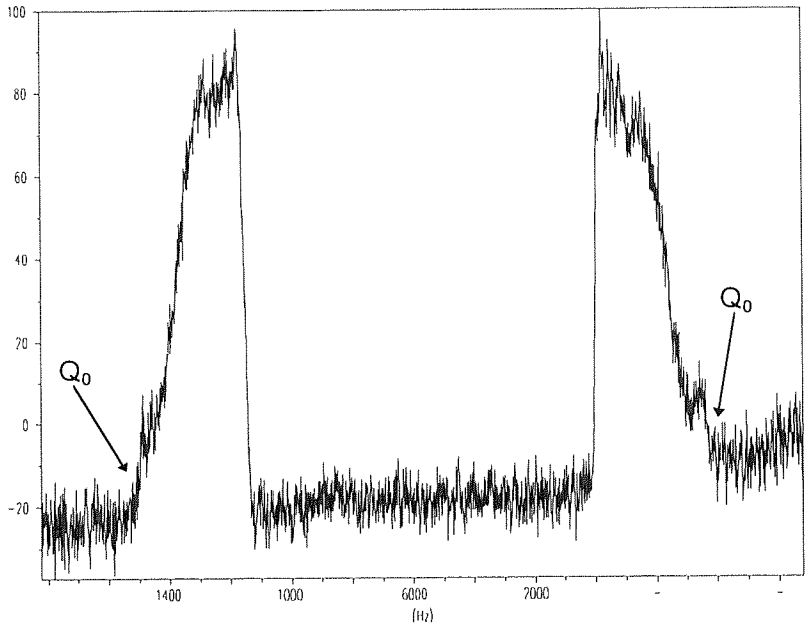

The maximum angle that the director has been rotated through, by the application of ultrasound, was determined by measuring the minimum quadrupolar splitting between the two lines. The minimum quadrupolar splitting was measured as 11582 Hz, which, by using equation 8.4, corresponds to an angle of,

$$\frac{Q_p}{Q_o} = \frac{11582}{18521} = 0.6253 = (1 - 3.\cos^2\theta) = 69.3^\circ \text{ w.r.t. } H_0 \qquad (8.6)$$

and thus corresponds to a deflection of (90-69.3) 20.7^0 from the perpendicular. The separation of the peaks can be read from the graph (figure 8.9) to give a

temperature 330 K which is approximately the clearing temperature, although, no isotropic resonance was observed.

The experiment was then repeated by applying ultrasound at 2.3 MHz and 4 W (this frequency was selected because it reduced the reflected power from the transducer). Figure 8.12 shows the appearance of a second pair of lines for a distinct director orientation with an angle of,

$$\frac{Q_p}{Q_o} = \frac{7922}{13550} = 0.585 = (1 - 3.\cos^2\theta) = 68.15^\circ \text{ w.r.t } H_0 \qquad (8.7)$$

and thus corresponds to a deflection of 21.8^0 from the perpendicular. Some heating has occurred in figure 8.12 as indicated by the presence of the isotropic shift.

Figure 8.12: ^{2}D spectrum of liquid crystal ZLI-1167 irradiated with 2.3 MHz ultrasound at 4W.

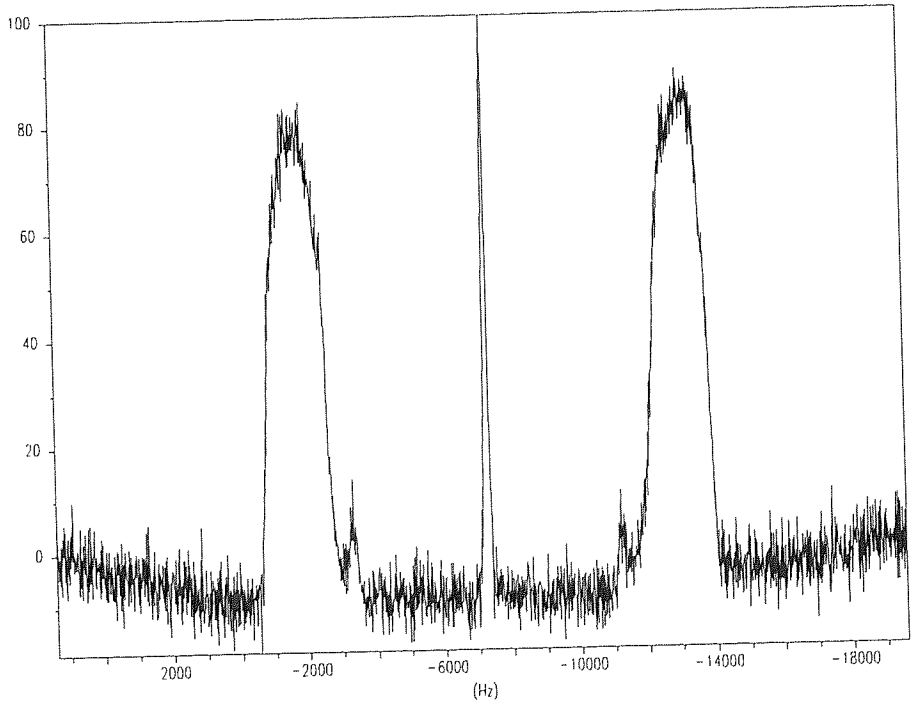

The degree of sample heating can be found by acquiring spectra during the cooling period after the application of ultrasound. Figure 8.13 shows the appearance of the liquid crystal line shape during cooling. In the foreground of figure 8.13 is the spectrum of figure 8.12, the ultrasound was then switched of and successive spectra taken with an interval of 75 seconds. The line shape after 75 seconds has returned to its original shape, as displayed in figure 8.10, showing that the heating effect was minimal. The spectra taken after this show a slight narrowing of their line widths as the sample cools.

Figure 8.13:Variation in line width for ^{2}D in benzene-d6 on cooling (separated by 75 s) after the application of ultrasound in figure 8.12.

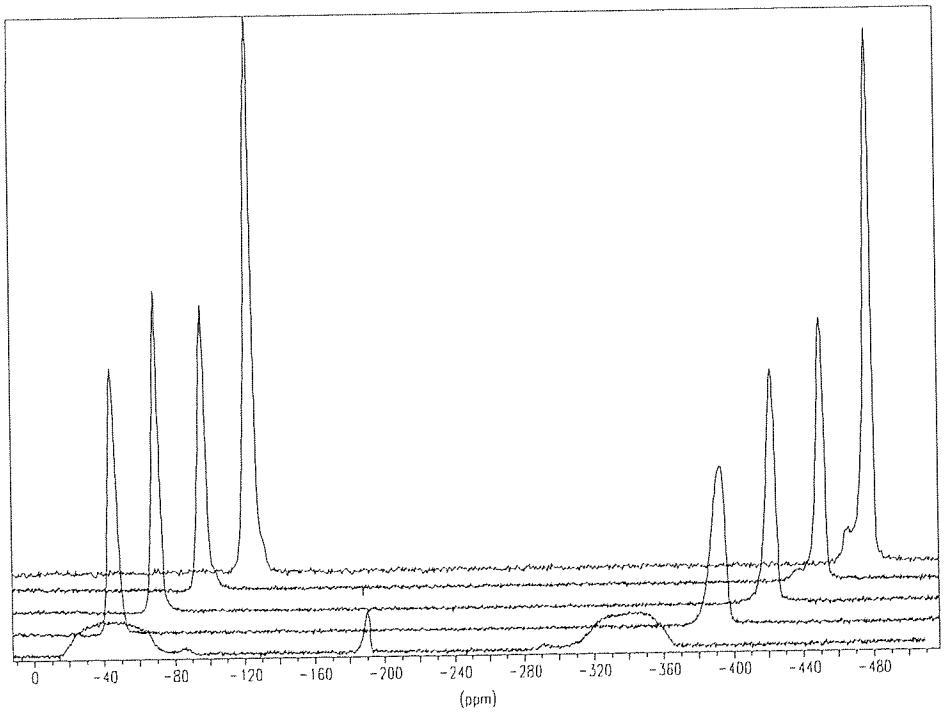

Increasing the acoustic power will increase the acoustic streaming within the sample and should decrease the quadrupolar splitting. The input power will also affect the heating rate of the sample and a change in the line shape of the doublet will be observed. The perturbation of the liquid crystal with increasing ultrasonic

power was studied, to observe the influence of these two mechanisms on the ^{2}H spectrum. The input power levels vary (back to front) as 1, 2, 3, 4, 5, 6, 7, 8 ,9 15, 20 W and the ^{2}H spectrum was acquired, see figure 8.14. Up to 3 W input there is no effect on the line shape (apart from a slight heating effect) because the ultrasonic power is insufficient to generate streaming. Up to 6 W each line splits into two, one line is due to heating effects and the other line is due to director reorientation (see figure 8.5 for line shapes). Above 6 W, heating effects become dominant and a typical line shape is observed.

Figure 8.14: Variation in line shape with increasing input power at 2 MHz. Back to front as 1, 2, 3, 4, 5, 6, 7, 8 ,9 15, 20 W.

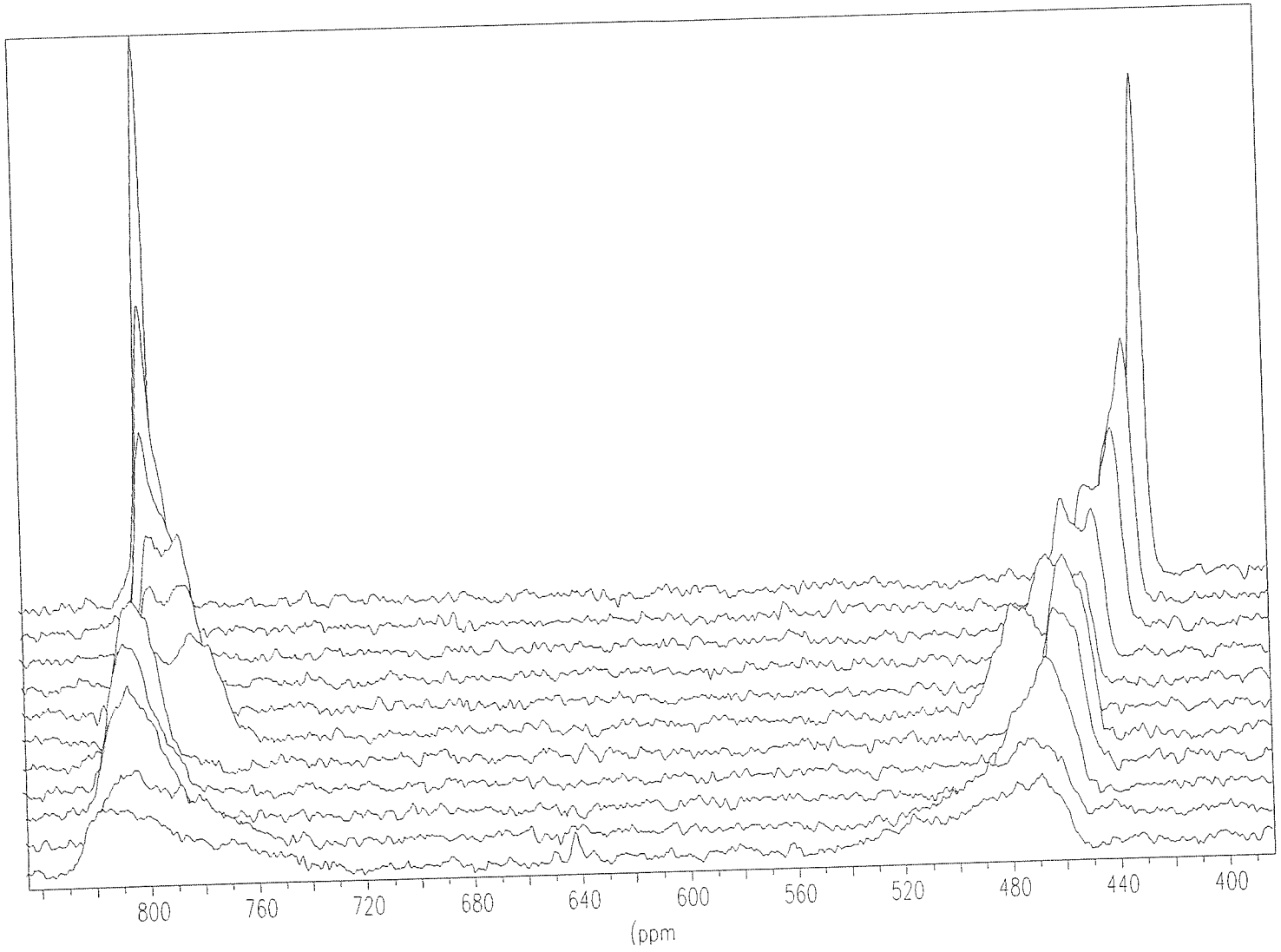

8.5.3: EFFECT OF AIR DRIVEN ROTOR ON ZLI-1167

It was proposed that director re-orientation could also be achieved by the use of mechanical stirring to impose shear stresses on the liquid crystal. As in the case of ultrasonic streaming the viscous nature of the medium results in a region of liquid crystal where the stirring motion is not experienced, see figure 8.15.

Figure 8.15: Stirring motion of ZLI-1167 by AIR DRIVEN ROTOR.

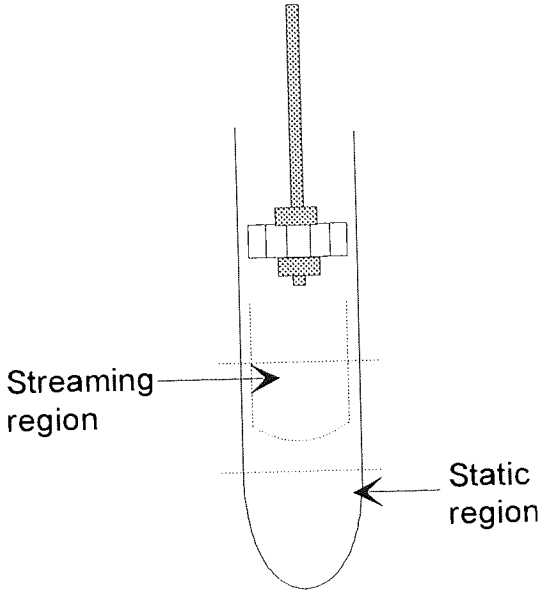

Figure 8.16 shows the ^{2}D spectrum of benzene-d6 in ZLI-1167 under the influence of stirring. It can be seen that two distinct director orientations have been achieved for the region that is stirred and for that which is unperturbed.

Figure 8.16: ^{2}D spectrum of liquid crystal ZLI-1167 under the influence of stirring.

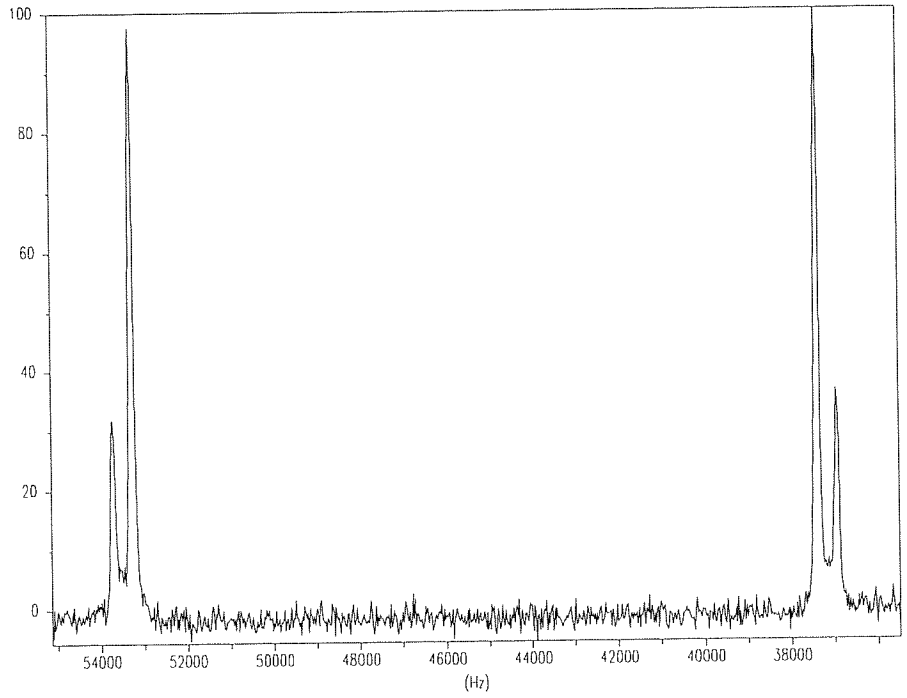

The outer pair of lines, in figure 8.16, have a separation of 16772 Hz and the inner pair have a separation of 15893 Hz. The maximum deflection of the directors can be calculated (using equation 8.4) to give,

$$\frac{Q_p}{Q_o} = \frac{15893}{16772} = 0.947 = (1 - 3.\cos^2\theta) = 82.4^\circ \text{ w.r.t. } H_0 \qquad (8.8)$$

corresponding to a deflection of 7.6^0. The intensities of the lines show that a high proportion of the liquid crystal has been deflected and the narrow nature of the line width indicates that the range of director orientations is small. Measurement of the probe temperature during the experiment showed that there was no heating effect. Therefore, the NMR spectrum obtained in figure 8.16 can only be due to director re-orientation.

8.6: CONCLUSION

Experiments have been carried out into the forced reorientation of liquid crystals in a magnetic field. Benzene-d6 was used as the probe for determining the orientation of the liquid crystal director.

The ^{2}H NMR spectrum of benzene-d6 in the liquid crystal, I35, has been obtained for ultrasonic irradiated and non-irradiated conditions. When ultrasound is applied from a perpendicular direction with respect to the liquid crystal director two distinct liquid crystal regions are formed, figure 8.8. The outer pair of lines arise from non-perturbed liquid crystal, and have a line shape that is asymmetric due to a temperature gradient within the sample. An inner pair of lines was observed during ultrasonic irradiation with a quadrupolar splitting of 14157 Hz. From the ultrasound induced change to the quadrupolar splitting the maximum angle of deflection was calculated to be 34.26^{0}. The asymmetry in the inner pair of lines was caused by a range of director orientations forming broad lines. The appearance of the inner lines can only be due to director re-orientation because their quadrupolar splitting corresponds to a temperature of 372 K, which is above the clearing temperature (365 K) for I35.

Results were obtained for the director re-orientation of the lyotropic liquid crystal, ZLI-1167. The quadrupolar splittings measured from the spectra of figures 8.11/12 show that a deflection angle of ca 20^{0} is possible using ultrasound. However, due to the low clearing temperature, 324 K, heating had a more pronounced effect on the line shape. The effect of heating was investigated in figure 8.13 and showed

that the spectra return to the original line shape, c.f. figure 8.10, after 75 seconds, indicating that the degree of heating is small. In order to reduce the heating influence on the line shape, input powers were restricted to below 6 W. Figure 8.14 showed that below 6 W, heating and re-orientation compete to give a pair of doublets with distinct line shapes. Above 6 W heating dominates and a typical line shape was observed, see figure 8.5.

Director re-orientation is also possible with mechanical stirring of the liquid crystal ZLI-1167 within a super conducting magnet. The air driven rotor produced a very specific deflection, as shown in figure 8.16, by the appearance of distinct doublets. This can only be attributed to the stirring action as there was no heating effect. The liquid crystal directors lie in the same plane as the direction of rotation and therefore only small changes in the angle to the field occurred, 7.6^{0}.

The results show that ultrasonic streaming is a more effective technique for the perturbation of directors than mechanical stirring. Larger angles of deflection can be achieved by using ultrasonic radiation force, although due to the nature of streaming a range of orientations occurs. Higher ultrasonic powers can be used but this tends to result in an increase in the attenuation of ultrasound within the sample and therefore an increase in heating. Heating effects have been seen to obscure the change in line shape due to the directors. It may be possible to over come the heating problem with more effective cooling or by moving to a lower acoustic frequency where attenuation is less acute.

CHAPTER 9

INVESTIGATION INTO SATURATION PREVENTION BY ACCELERATED DIFFUSION TO ENHANCE SIGNALS

9.0: INTRODUCTION

In the previous chapters mechanical stirring of the samples used in SINNMR and also of liquid crystals was investigated. This approach lead to the hypothesis that fast stirring could be used to enhance the NMR spectra of liquids. The principle underlying the idea is that by effectively accelerating the diffusion in samples, the pulse provided by the NMR probe can be made to act only on 'fresh' sample, i.e. a polarised sample that has not been previously irradiated by the H_1 field, making it unnecessary to wait for normal relaxation to occur. The flow of liquid through the NMR coil region reduces the rate of spin saturation that is caused by pulsing more rapidly than $5.3.T_1$. Therefore, the experiment has been given the acronym SPADES (Saturation Prevention by Accelerated Diffusion to Enhance Signals).

It was also hypothesised that by agitating the liquid it will experience an average of the field inhomogeneity, within the sample, and therefore a reduction in the line width will occur.

Rotating metallic components in the presence of a magnetic field generate eddy currents which can couple to the static magnetic field. For this reason the present version of the rotor can only be utilised in the in-line probe of a superconducting magnet, where the rotational motion of the rotor is largely unaffected by the magnetic field. All of the initial experiments were conducted using ethylbenzene, which contains a number of ^{13}C sites with differing T_1 times. This allows the study of the relative enhancements achieved from spinning the rotor (see section 5.5 for

description). The terms non-spinning/spinning will be used to describe the action of the air driven rotor. A list of acquisition parameters can be found in appendix 2.

9.1: RESULTS

The effect of the SPADES experiment can be demonstrated for the ^{13}C NMR spectrum of ethylbenzene. Figure 9.0 shows the effect on S/N of spinning the rotor in the liquid for identical acquisition parameters.

Figure 9.0: ^{13}C spectrum of ethylbenzene for non-spinning (top) and spinning (bottom) conditions.

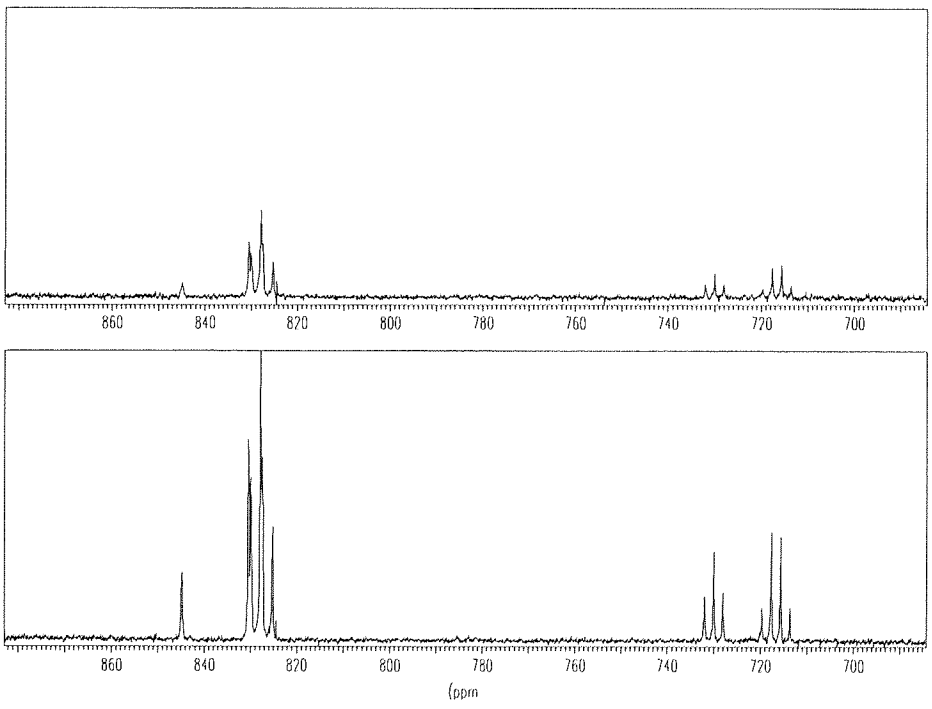

As can be seen in figure 9.0, there is a significant increase in the S/N of the spectrum when the air driven rotor is spinning.

It is important to ascertain whether the increase in signal to noise is due to the flow of liquid or the presence of rotating metallic components close to the coil

region. Figure 9.1 shows the effect the rotor has on the NMR spectra of ethylbenzene with varying conditions.

Figure 9.1: Effect of the SPADES experiment on ^{13}C in ethylbenzene with: A: no rotor present, B: rotating tube (30 Hz), C: rotor present in contact with the liquid but not spinning, D: rotor present in contact with the liquid and spinning, E: rotor present but not in contact with the liquid and not spinning, F: rotor present but not in contact with the liquid and spinning.

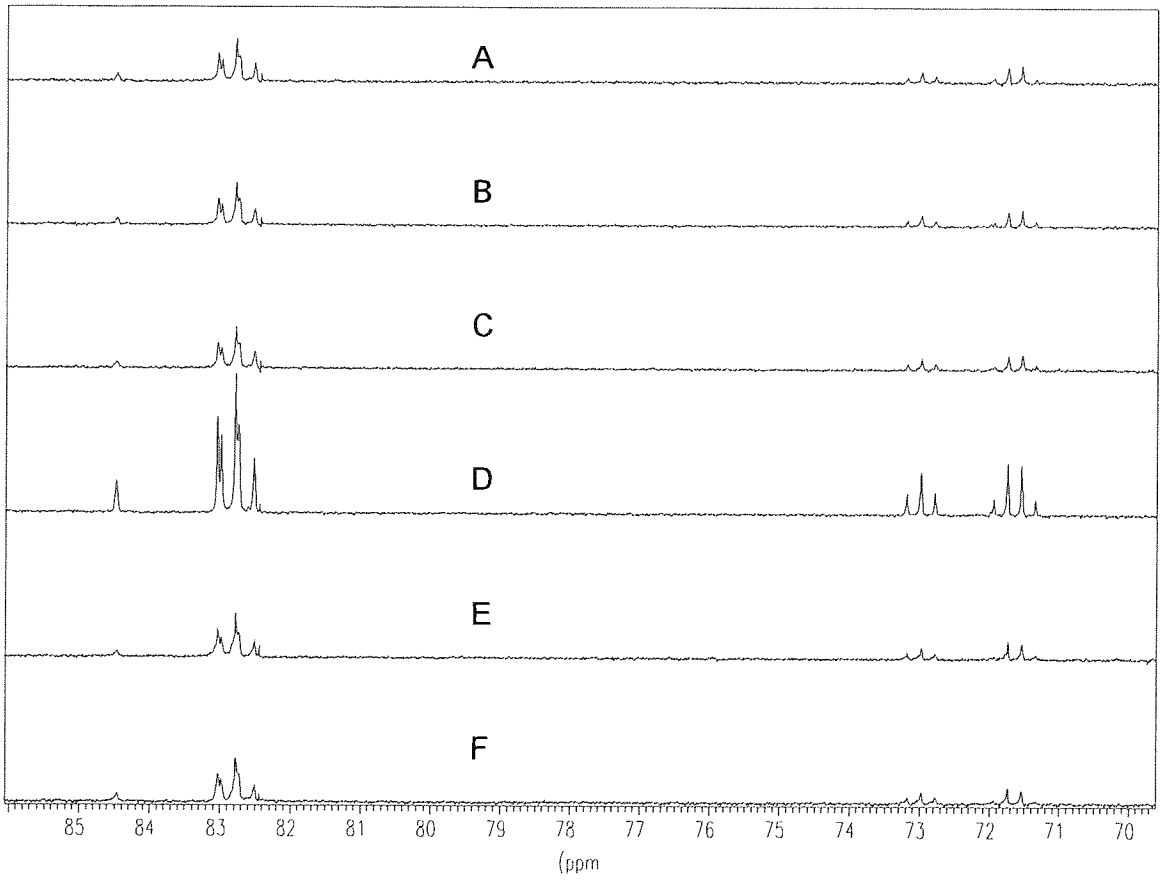

It can be seen from figure 9.1 that there is only a change in the signal to noise for the spectrum of ethylbenzene for condition D, i.e. when rotor is in contact with the liquid and spinning. In all other cases the S/N remains constant and, therefore, the increase must be due to the motion of the liquid.

9.2: EVALUATION OF CONDITIONS

In the following sections all the experiments were performed on ^{13}C in ethyl benzene. Each of the spectra are for single 90^0 pulse-detection with an identical number of scans. All other parameters, except the one which is under investigation, are kept constant throughout all of the experiments.

9.2.1: EFFECT OF RELAXATION DELAY ON SPADES

By replacing the excited nuclei with those unaffected by the H_1 field the rate of saturation, due to pulsing more rapidly than $5.3.T_1$, is reduced. The variation in signal intensity with relaxation delay time was studied under spinning and non-spinning conditions, see figures 9.2 and 9.3.

Figure 9.2: ^{13}C spectra of ethylbenzene with relaxation delay, non-spinning. RD values (s): A=10, B=5, C=1, D=0.5, E=0.25, F=0.1.

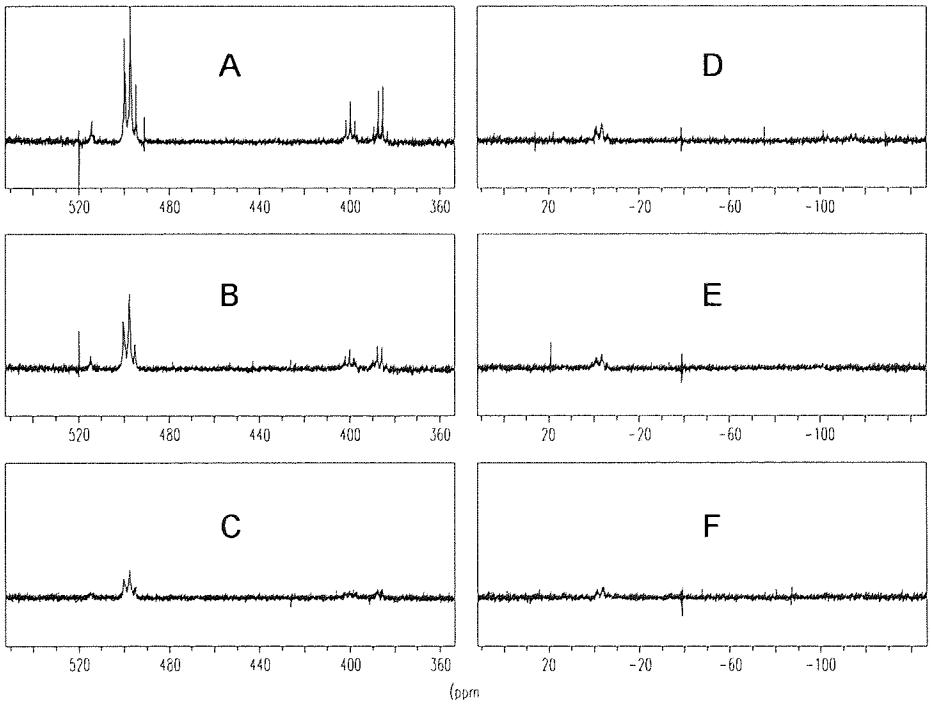

Figure 9.3: ^{13}C spectra of ethylbenzene with relaxation delay, spinning. RD values (s): A=10, B=5, C=1, D=0.5, E=0.25, F=0.1.

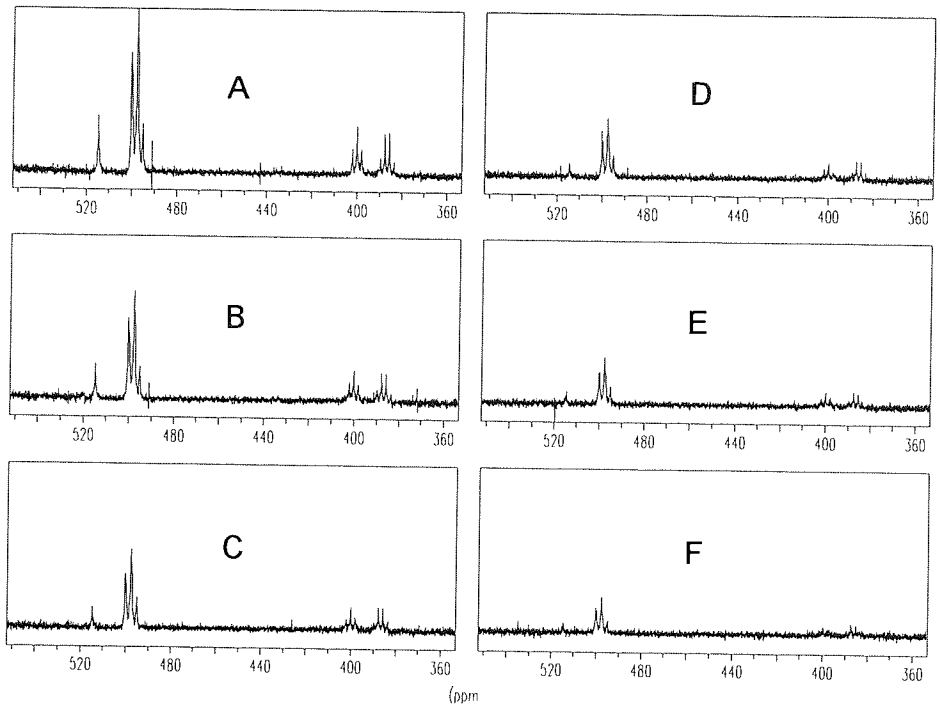

By reducing the inter sequence delay the NMR signal becomes increasingly saturated for the non spinning sample. For the SPADES experiment the sample is less affected than the corresponding one obtained for non-spinning, especially for the quaternary carbon which is visible on all of the 'spinning' spectra. Figures 9.4 and 9.5 (tables 9.1 and 9.2) show the signal intensities (area), for the four differing ^{13}C sites in ethylbenzene, with changing relaxation delay.

Table 9.1: ^{13}C signal intensity with relaxation time for non-spinning.

Relaxation time, s	C	CH	CH_2	CH_3
0.01	1.12E+04	1.06E+05	2.87E+04	3.22E+04
0.25	3.40E+03	1.42E+05	2.40E+04	2.44E+03
0.5	1.07E+04	2.04E+05	4.58E+04	6.00E+04
1	2.40E+04	3.16E+05	7.80E+04	5.94E+04
5	4.58E+04	7.59E+05	1.37E+05	2.15E+05
10	6.09E+04	1.03E+06	1.90E+05	1.86E+05

Table 9.2: ^{13}C signal intensity with relaxation time for spinning.

Relaxation time, s	C	CH	CH_2	CH_3
0.01	1.70E+04	3.11E+05	5.76E+04	6.49E+04
0.25	2.36E+04	4.39E+05	8.50E+04	9.42E+04
0.5	3.29E+04	5.55E+05	1.05E+05	1.17E+05
1	4.45E+04	7.33E+05	1.42E+05	1.58E+05
5	1.10E+05	1.07E+06	2.15E+05	1.50E+05
10	1.72E+05	1.55E+06	2.86E+05	2.43E+05

Figure 9.4: ^{13}C signal intensities verses relaxation delay for ethylbenzene, non spinning.

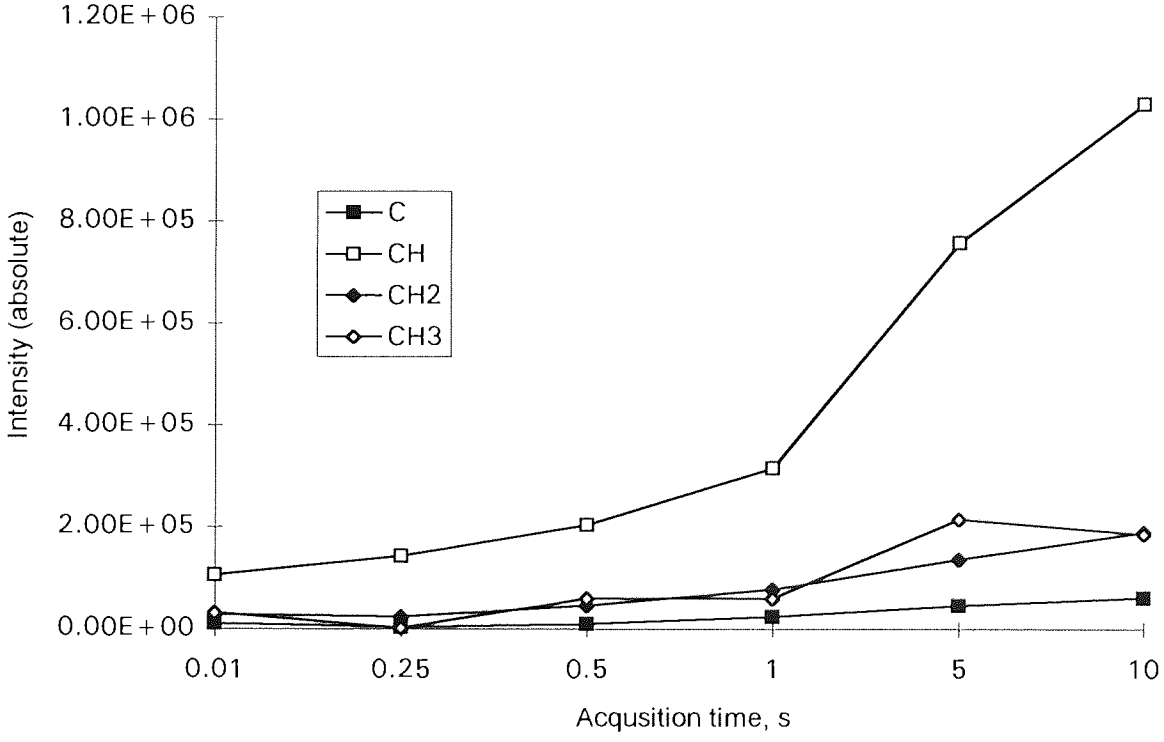

Figure 9.5: ^{13}C signal intensities verses relaxation delay for ethylbenzene, spinning.

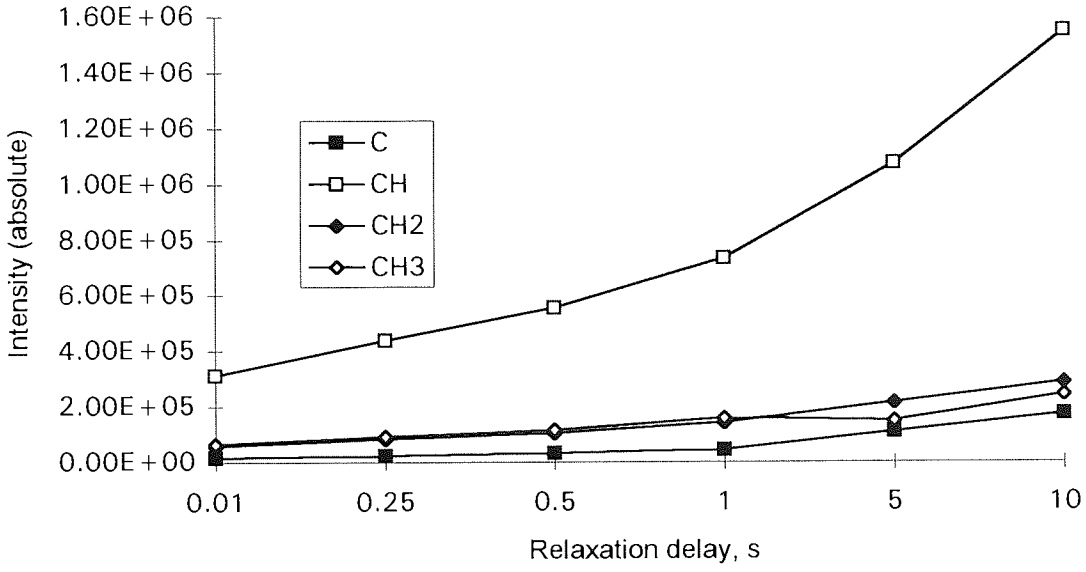

The plots show that the slow relaxing nuclei, such as the quaternary carbon, have a relatively flat response to an increasing relaxation delay. However, the magnitude of the signal is greater for spinning than non spinning. In the faster relaxing cases, i.e. methine carbon, a steady increase in the signal intensity is observed for both cases. Again, the signal intensity is greater for spinning than non spinning. The relative magnitudes are compared in figure 9.6

Figure 9.6: Comparison of ^{13}C signal intensities with relaxation delay, in ethylbenzene, for spinning (S) and non spinning (N) spectra.

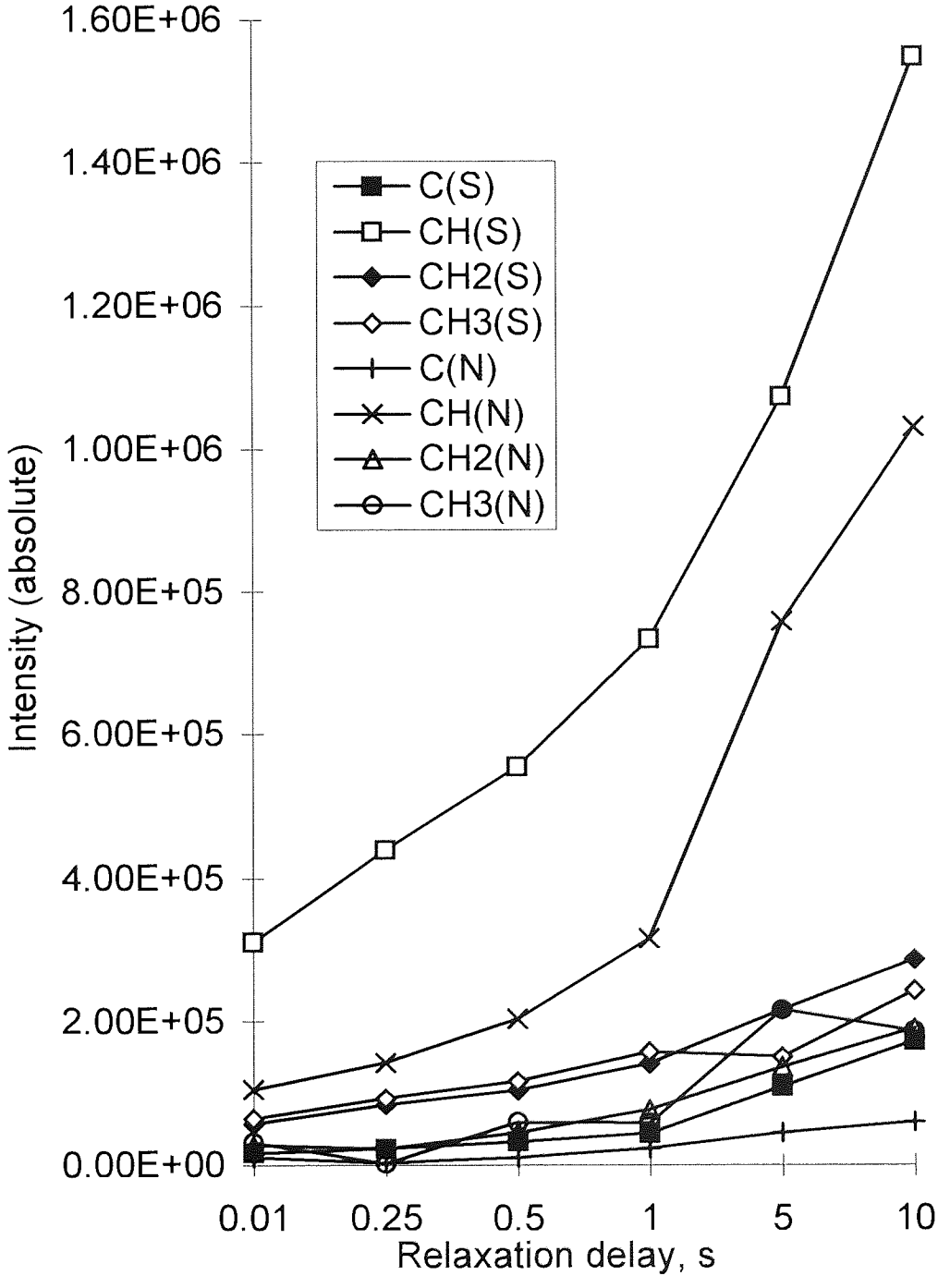

9.2.2: EFFECT OF ACQUISITION TIME ON SPADES

The effect of the motion of liquid through the probe coil on the signal intensity will also be affected by the acquisition time necessary to collect the data. Nuclei that have been excited by the H_1 field may not remain present in the coil during acquisition, being ejected by the rotor. A series of spectra, for non-spinning and spinning conditions, were obtained for differing acquisition times (0.01, 0.025, 0.05, 0.1, 0.25 seconds), see figures 9.7 and 9.8. In order to preserve the digital resolution of the spectra only the time domain memory size was altered to provide the required acquisition times. The FID was then zero filled to give the necessary number of data points. The variation in signal intensities for ethylbenzene with acquisition time were measured, see figures 9.9 and 9.10 and tables 9.3 and 9.4.

Figure 9.7: Non-spinning, ^{13}C spectra of ethylbenzene with acquisition times. AQ values (s): A=0.25, B=0.1, C=0.05, D=0.025, E=0.01.

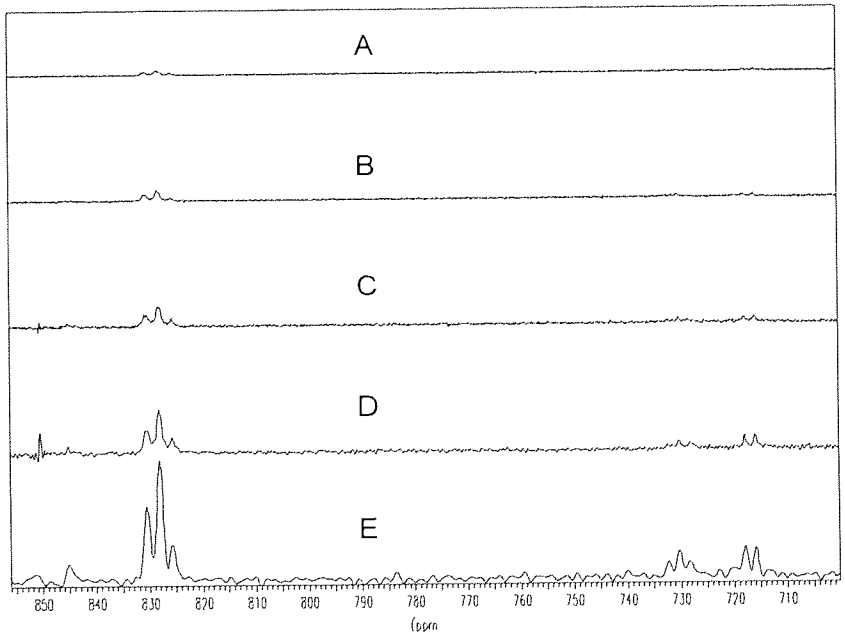

Figure 9.8: Spinning, ^{13}C spectra of ethylbenzene with acquisition times AQ values (s): A=0.25, B=0.1, C=0.05, D=0.025, E=0.01.

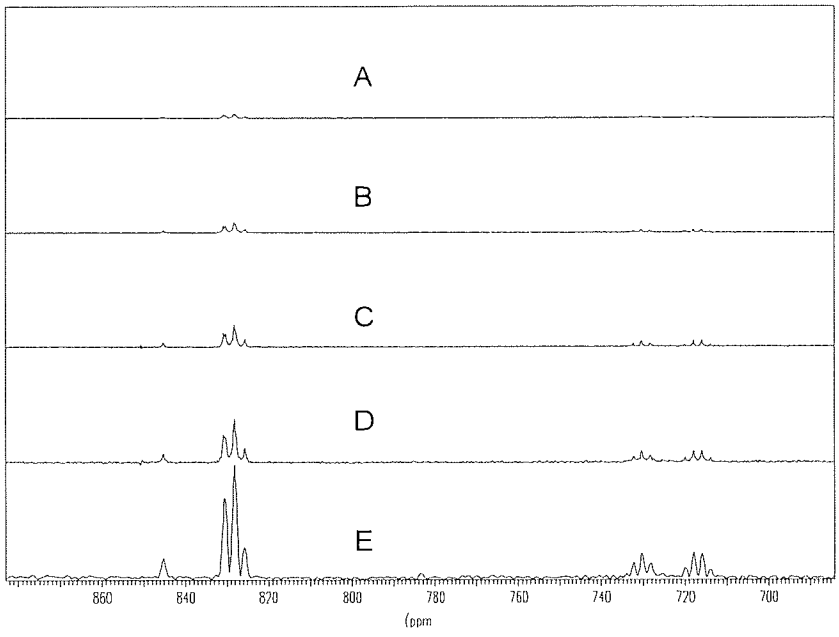

Table 9.3: ^{13}C signal intensity with acquisition time for non-spinning.

Acquisition time, s	C	CH	CH_2	CH_3
0.25	3.73E+04	3.45E+05	7.31E+04	1.06E+05
0.1	5.11E+04	7.88E+05	1.79E+05	1.87E+05
0.05	9.04E+04	1.58E+06	3.28E+05	4.31E+05
0.025	1.82E+05	3.36E+06	7.00E+05	8.79E+05
0.01	5.26E+05	9.79E+06	2.17E+06	2.59E+06

Table 9.4: ^{13}C signal intensity with acquisition time for spinning.

Acquisition time, s	C	CH	CH_2	CH_3
0.25	8.29E+04	9.24E+05	1.92E+05	1.96E+05
0.1	1.50E+05	2.17E+06	4.74E+05	4.20E+05
0.05	2.53E+05	4.36E+06	9.28E+05	8.93E+05
0.025	7.90E+05	8.99E+06	1.71E+06	1.88E+06
0.01	2.03E+06	2.67E+07	5.49E+06	5.61E+06

Figure 9.9: ^{13}C signal intensities for ethylbenzene with acquisition time, non-spinning.

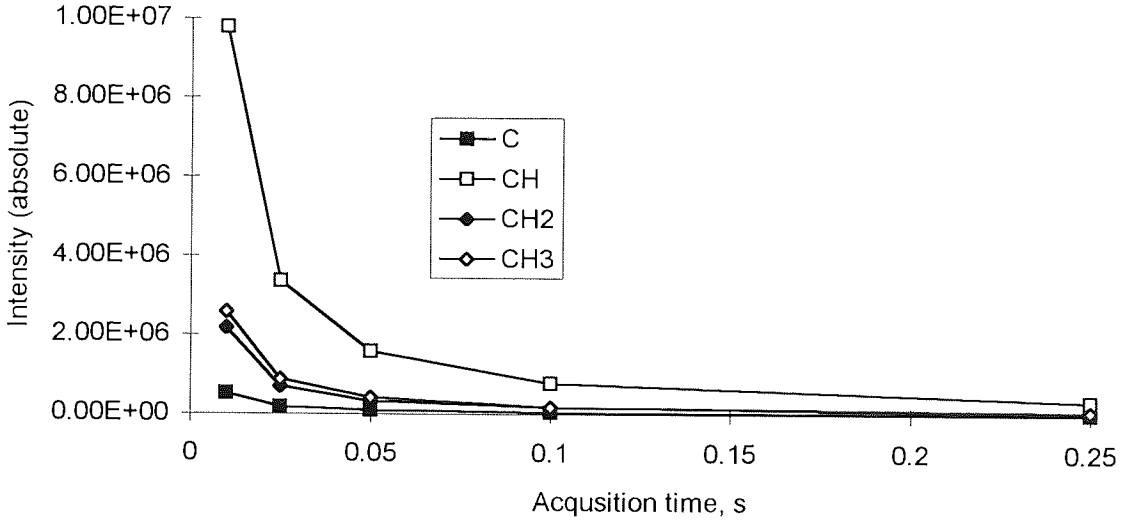

Figure 9.10: ^{13}C signal intensities for ethylbenzene with acquisition time, spinning.

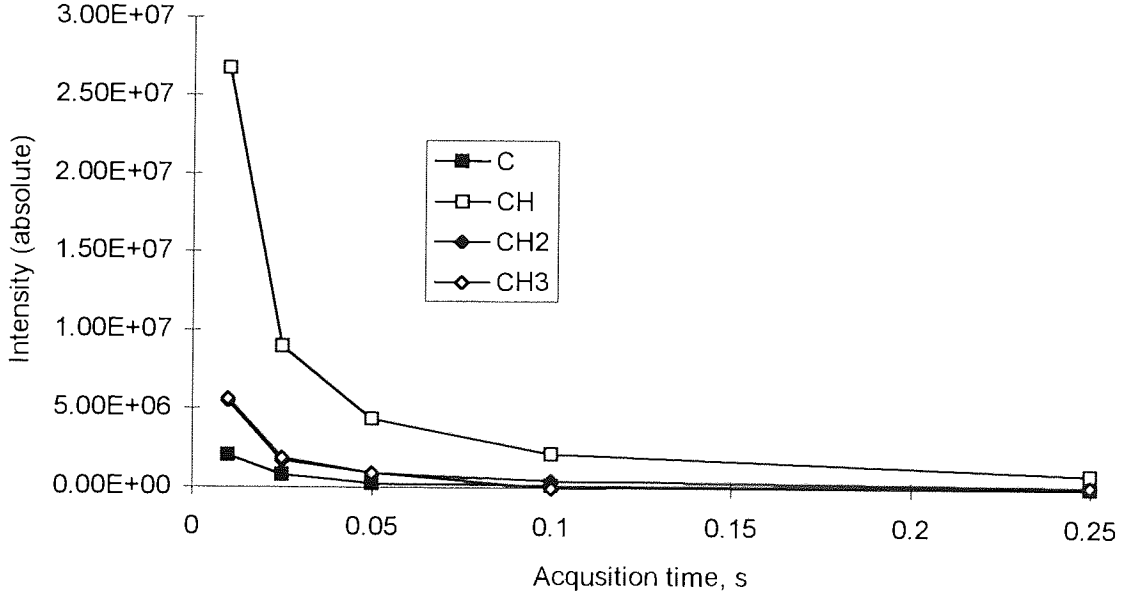

Both figures 9.9 and 9.10 show a similar drop in intensity with increasing acquisition time. The effect is analogous to the application of exponential line broadening, as an examination of the line widths shows a broadening of each line

with decreasing acquisition time. At the start of an FID the ratio of coherent signal strength. S, of the nuclear resonance to the random noise, n, is >>1. As the FID decays the magnitude of S decreases and the NMR signal becomes increasingly obscured by noise. If the NMR signal is truncated then the portion of the FID containing 'noisy' data is removed and after transforming the FID the S/N of the spectrum appears to be improved (this is at the expense of digital resolution which is reduced as the acquisition time is decreased).

By comparing the signal intensities for non-spinning and spinning conditions, figure 9.11, it can be seen that the variation in the acquisition time appears to have an equal influence on the S/N in both spinning and non-spinning cases. It is likely that the variation in the acquisition time is too small to effect the S/N and the differences in intensity for spinning an non-spinning is dominated by the short relaxation delay (1 s).

Figure 9.11: Comparison of ^{13}C signal intensity with acquisition time, in ethylbenzene, for spinning (S) and non-spinning(N).

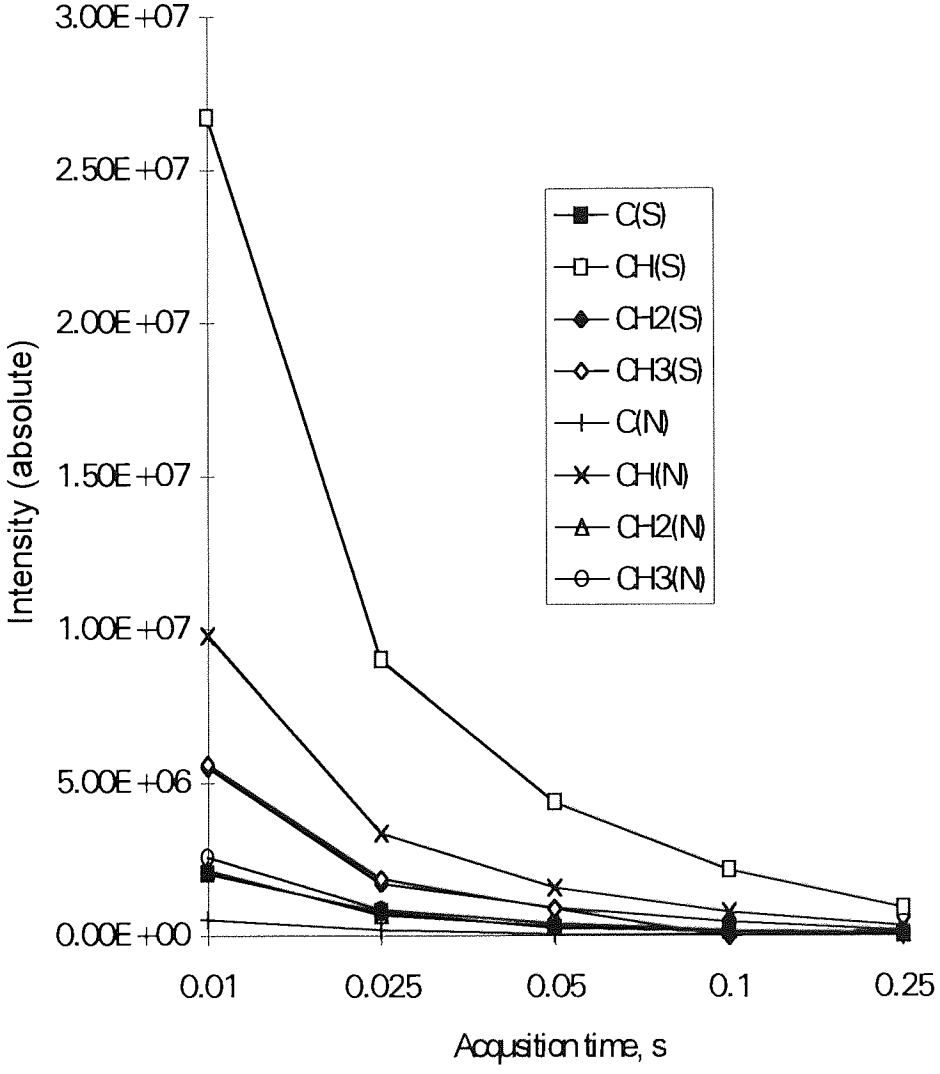

9.2.3: EFFECT OF PULSE/ACQUISITION DELAY TIME ON SPADES

The time between pulsing and receiving, known as the delay time (DE) could dictate the ratio of the number of nuclei remaining in the probe coil to those replaced by diffusion, at the start of the acquisition time. Under spinning conditions the liquid is rapidly moving, thus, the length of DE was studied in order to ascertain if it would influence the NMR signal, see figure 9.12 and 9.13 and tables 9.5 and 9.6. Due to the magnitude of this time delay (μs) there was no discernible change. However, the results serve to show that a general difference in signal intensity between the spinning and non spinning case was observed, figure 9.14.

Table 9.5: ^{13}C signal intensity for ethylbenzene with delay time (DE) for non-spinning.

Delay, μs	C	CH	CH_2	CH_3
5	1.93E+04	3.00E+05	5.31E+04	4.98E+04
10	2.88E+04	2.92E+05	6.05E+04	4.93E+04
25	2.58E+04	2.99E+05	5.26E+04	6.57E+04
50	2.40E+04	3.16E+05	7.80E+04	5.94E+04

Table 9.6: ^{13}C signal intensity for ethylbenzene with delay time (DE) for spinning.

Delay, us	C(S)	CH(S)	CH2(S)	CH3(S)
5	3.12E+04	7.12E+05	1.23E+05	1.00E+05
10	3.20E+04	7.04E+05	1.29E+05	1.38E+05
25	4.10E+04	6.96E+05	1.37E+05	1.19E+05
50	4.45E+04	7.33E+05	1.42E+05	1.58E+05

Figure 9.12: ^{13}C signal intensity verses delay (DE) for ethylbenzene with non-spinning.

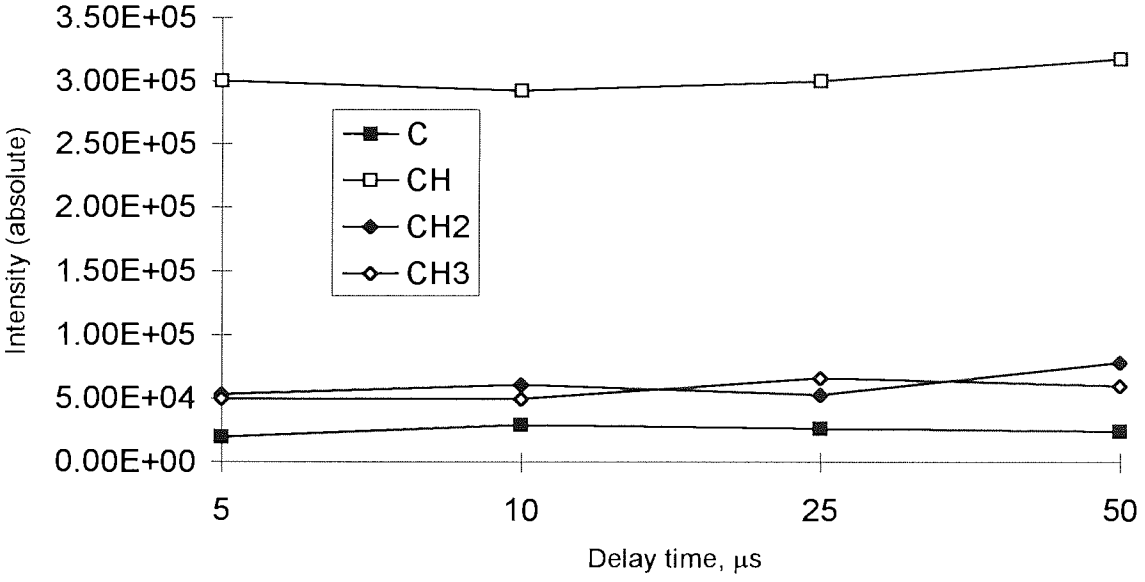

Figure 9.13: ^{13}C signal intensity verses delay (DE) for ethylbenzene with spinning.

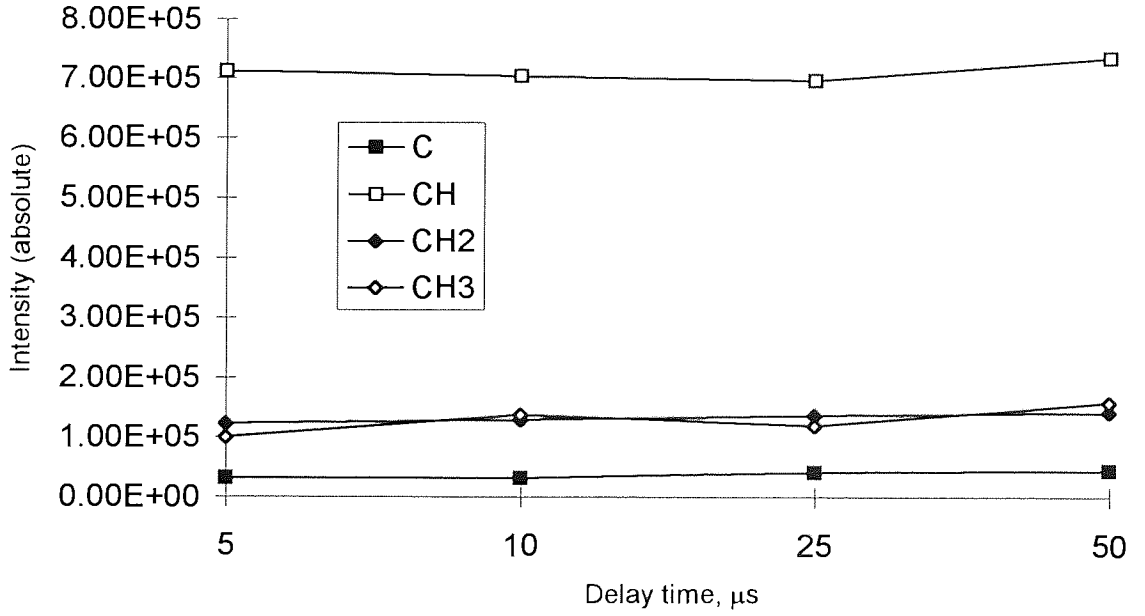

Figure 9.14:Comparison of ^{13}C signal intensity with delay time (DE), in ethylbenzene, for spinning (S) and non-spinning(N).

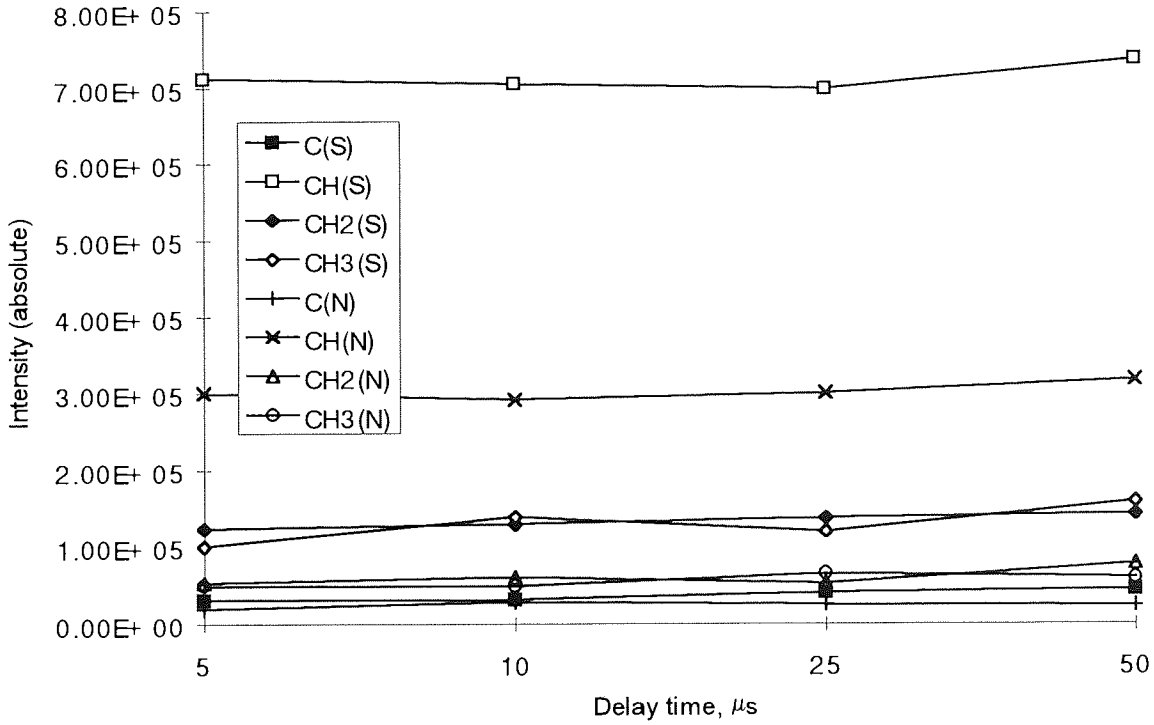

9.2.4: SPECTRUM ENHANCEMENT

The results of section 9.3.1,2,3 can be combined to give the maximum enhancement, for a 90^0 excitation pulse, that can be achieved by the SPADES experiment. Figures 9.15 compares the difference in signal to noise for ethylbenzene with a relaxation delay of 1s, obtained for non-spinning and spinning (distortions in the baseline are the result of a truncated FID).

Figure 9.15: Comparison of intensities for ^{13}C in ethylbenzene, non-spinning (top) and spinning (bottom). PW=90^0, RD=1 s, AQ=0.01 s, DE=5 μs.

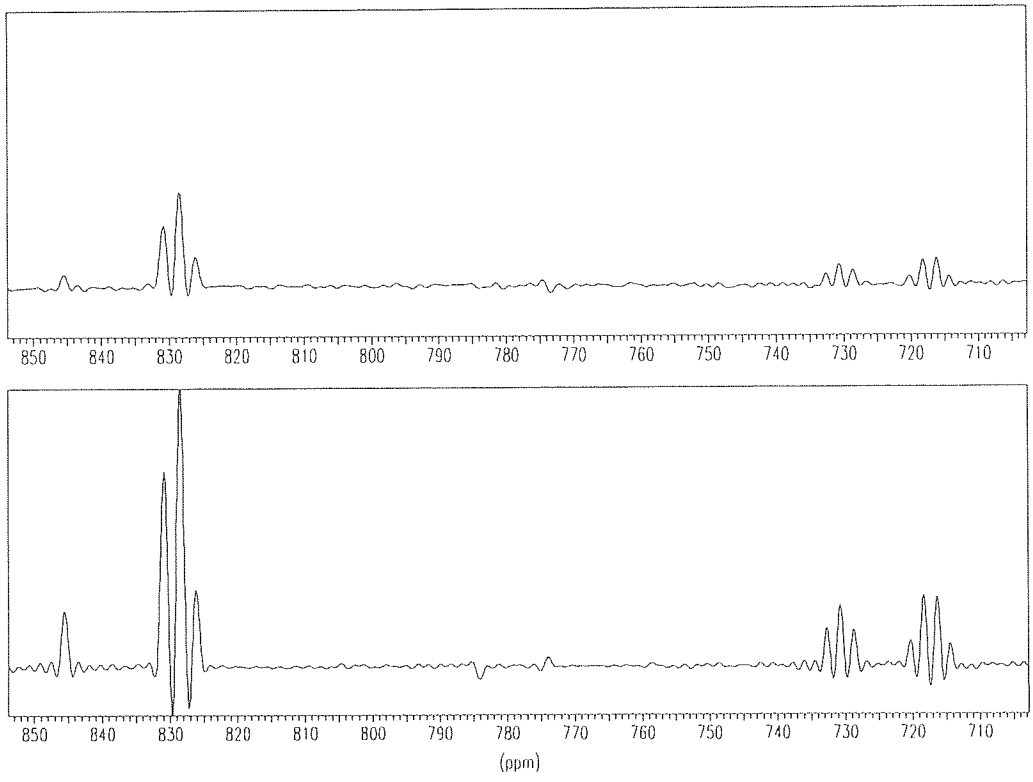

Integrals of each of the four ^{13}C resonance regions were measured and their ratio taken. The ratio gives the possible signal enhancement, see table 9.7. The integrals are for an identical number of scans, with the same repetition rate.

Table 9.7: Ratio of enhancement on spinning for different ^{13}C sites in ethylbenzene.

Site (^{13}C)	Integral(avg.)		Ratio
	Non-spinning	Spinning	
C	$4.56.10^5$	$2.04.10^6$	4.47±1.0
CH	1.0910^7	$2.88.10^7$	2.64 ±0.2
CH2	$2.14.10^6$	$4.45.10^6$	2.08 ±0.5
CH3	$2.74.10^6$	$6.70.10^6$	2.44±0.14

Routine 1D spectra are usually performed by rapid multipulsing using the Ernst angle (section 2.8), in order to save spectrometer time. The SPADES experiment can also save spectrometer time by increasing the available magnetisation, before a pulse, for a short relaxation delay time. An experiment was performed to ascertain if SPADES could still enhance the S/N of ^{13}C in ethylbenzene for rapid multipulsing at the Ernst condition. A spectrum of ethylbenzene was taken, at the Ernst angle, to see if S/N enhancement was possible with the air driven rotor.

Using the T_1 relaxation times obtained in section 9.4.1 the Ernst angle was calculated, for each ^{13}C site, based on T_1 relaxation during the acquisition time, and an average of $\approx 18^0$ was used (see appendix 2 for spectral parameters). Figure 9.16 compares the spectra for non-spinning and spinning conditions.

Figure 9.16: Comparison of intensities for ^{13}C in ethylbenzene at the Ernst angle (18^0); Non spinning (top), Spinning (bottom).

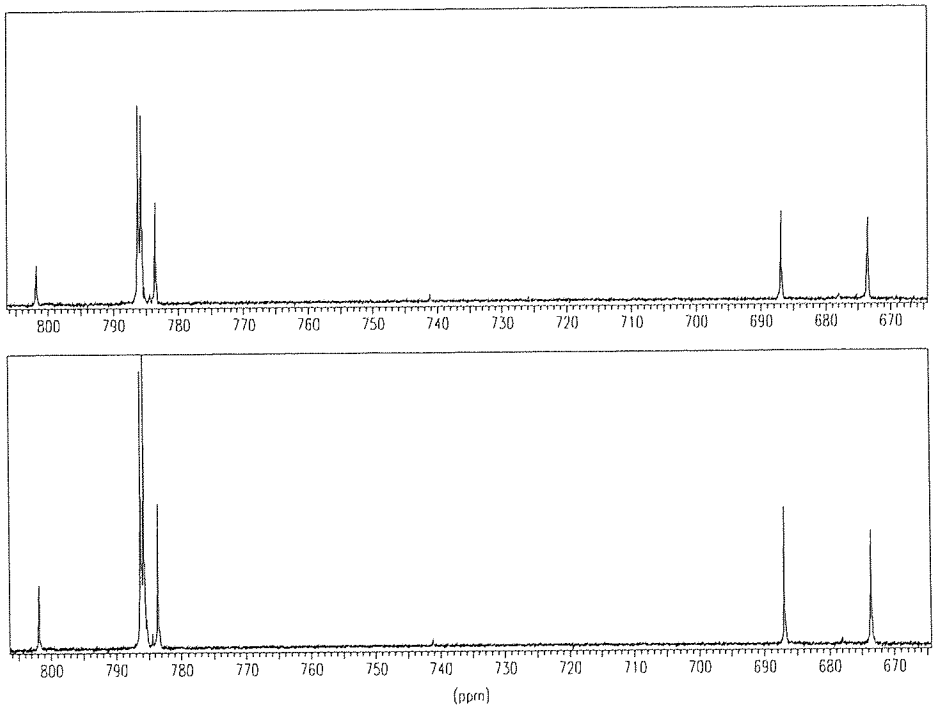

Comparison of the two spectra for non-spinning and spinning conditions, figure 9.16, shows that enhancement is still possible for by spinning. This is because SPADES promote the magnitude of M_z toward M_0 beyond that of the steady state magnetisation of the Ernst condition to increasing the signal to noise of the spectrum. Table 9.8 shows the integrals for each ^{13}C site in ethylbenzene and the ratio of enhancement.

Table 9.8: Ratio of enhancement for different ^{13}C sites in ethylbenzene at the Ernst angle.

Site (^{13}C)	Integral (abs.)		Ratio
	Non-spinning	Spinning	
C	$4.72.10^3$	$9.08.10^3$	1.92
CH	$4.62.10^5$	$5.85.10^5$	1.26
CH2	$7.08.10^4$	$8.28.10^4$	1.17
CH3	$7.29.10^4$	$8.74.10^4$	1.20

The ratios of enhancement are not as large as that for table 9.7 as the 'saturation' of the spin system is not as prominent under the Ernst condition. However, the SPADES experiment can be carried out just as effectively for a 90^0 pulse angle with a similar repetition rate, therefore, the transverse magnetisation component is larger than that for the Ernst angle, further improving the S/N. As SPADES operates with any pulse angle the technique could be used with most pulse sequences (Unlike the Ernst condition) and would benefit multi-dimensional experiments.

9.3: EFFECT OF SPADES EXPERIMENT ON RELAXATION

9.3.1: PSEUDO-RELAXATION TIME WITH SPADES

True relaxation times are only valid for degassed samples that are restricted to the active volume of the probe coil. The relaxation time will decrease if oxygen is present and if diffusion is allowed. The SPADES experiment accelerates diffusion and introduces oxygen into the sample. Therefore, a pseudo-relaxation time is imposed by the action of the rotor and an effective T_1 time can be measured under spinning conditions. An inversion-recovery sequence was used for spinning and non-spinning conditions on a non-restricted aerated sample of ethylbenzene. Figure 9.17 shows the spectra obtained with the inversion-recovery sequence for the non-spinning case.

Figure 9.17: Inversion-recovery sequence on ^{13}C, ethylbenzene, non-spinning. The values of τ are (front to back); 1, 3, 5, 10, 15, 25, 45, 180, 300 seconds.

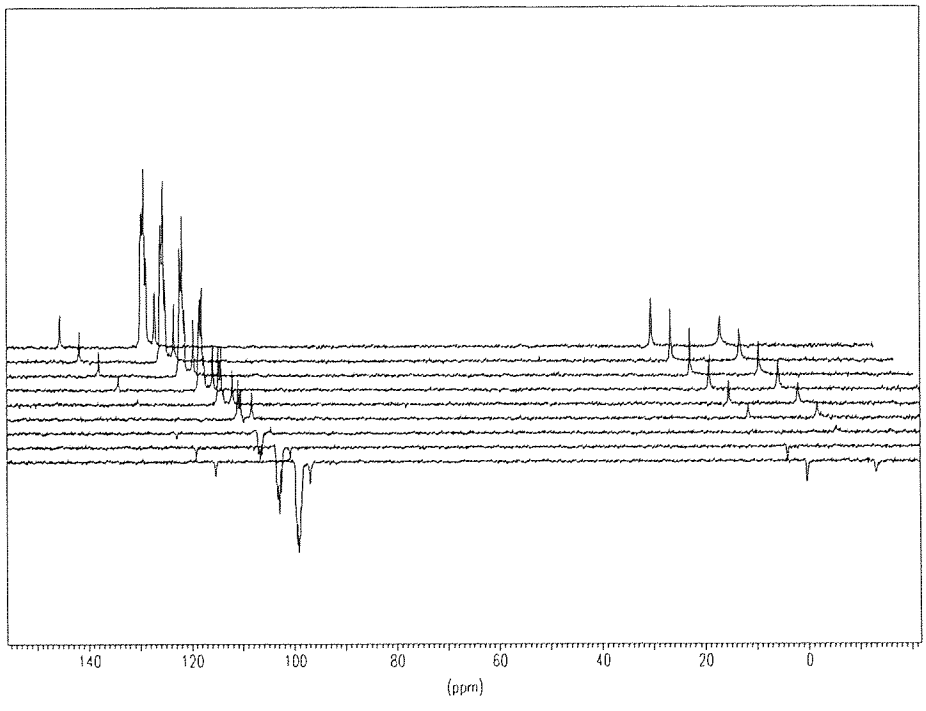

The inversion-recovery sequence was then performed again for the spinning case. The increased liquid motion means much shorter values of τ were required to give a observable change in the NMR signal. Figure 9.18 shows the resulting spectra.

Figure 9.18: Inversion-recovery sequence on ^{13}C, ethylbenzene, spinning. The values of τ are (front to back); 0.01, 0.1, 0.05, 1, 3, 5, 8, 15, 30 seconds.

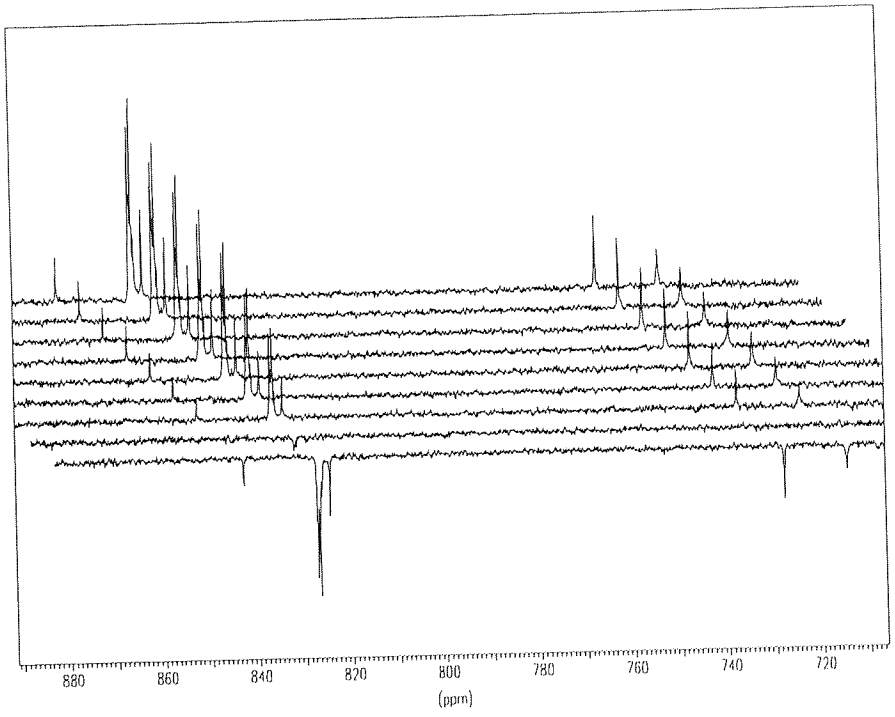

Using the T_1 calculation software installed on the Bruker spectrometers, the values of T_1 can be determined for each ^{13}C site. Table 9.9 gives the T_1 value for each ^{13}C site for the spinning and non-spinning case. The standard deviation refers to the accuracy of the line fit to the points and not to the relaxation time given.

Table 9.9: Calculated T_1s for ^{13}C sites in ethylbenzene under non-spinning and spinning conditions.

Site (^{13}C)	Non-spinning, s		Spinning, s	
	T_1	std	T_1	std
C	14.7	0.02	0.336	0.08
CH	11.34	0.02	0.338	0.07
CH_2	9.68	0.3	0.275	0.06
CH_3	6.6	0.02	0.328	0.05

The values for the T_1 time on spinning give an indication of the recovery time of the system from saturation and the repetition times possible using the technique.

9.3.2: REAL RELAXATION TIMES UNDER SPADES CONDITIONS

As already mentioned (section 9.4.1) the rapid stirring of liquids may introduce a more fundamental change to the relaxation times of the nuclei present. The motion of the rotor will introduce oxygen into the system, impose a new correlation time on the molecules or cause the passage of molecules through regions of magnetic inhomogeneity to provide an relaxation pathway.

Obviously, as demonstrated in the previous section, the effect of SPADES on natural T_1's cannot be measured. However, like T_1's the NOE has both intra and intermolecular contributions. Consequently, it was hypothesised that measurements of NOE's under spinning and non-spinning conditions might provide some insight into the effect of SPADES on the natural relaxation times. If there is a change to the NOE's enhancement, measured under spinning and non-spinning conditions, then the relaxation times must have been altered. Spectra

were obtained for ^{13}C in cyclohexane, under spinning and non-spinning conditions, with broadband (BB) decoupling and inverse-gated decoupling (to suppress the NOE), see figure 9.19. All spectra are acquired with a sixty second relaxation delay to allow full NOE build up.

Figure 9.19: NOE effect in cyclohexane with spinning and non-spinning, 60 s relaxation delay. A: BB decoupled non-spinning, B: BB decoupled spinning, C: inverse-gated decoupling non-spinning, D: inverse-gated decoupling spinning.

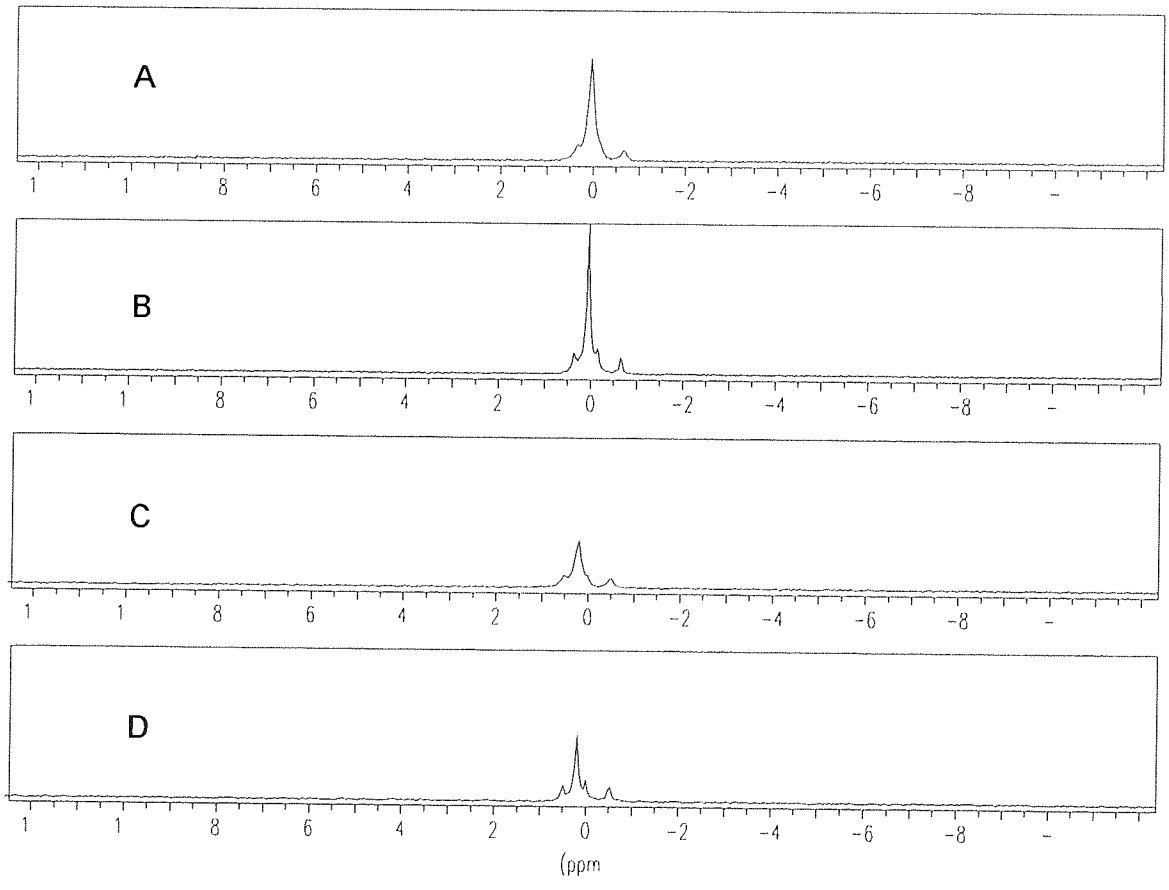

The experiment was repeated with a three second relaxation delay. By reducing the intersequence delay there will be a reduced NOE effect which may result in a larger difference between the spectra, see figure 9.20.

Figure 9.20: NOE effect in cyclohexane with spinning and non-spinning, 3 s relaxation delay. A: BB decoupled non-spinning, B: BB decoupled spinning, C: inverse-gated decoupling non-spinning, D: inverse-gated decoupling spinning.

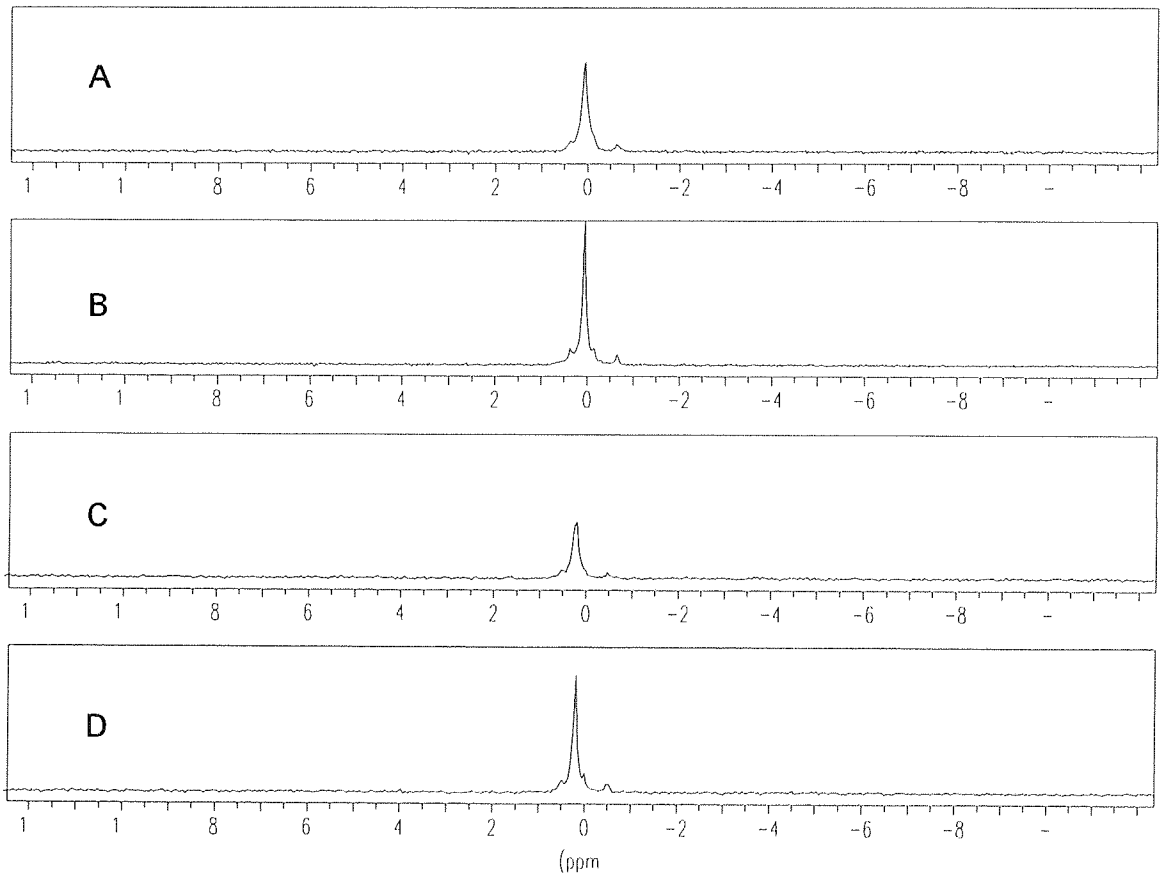

All the ^{13}C spectra were transformed in the absolute intensity mode of the spectrometer (referenced to the spectrum with the largest intensity). In order to calculate the NOE it is necessary to integrate the spectrum. However, due to the presence of artefacts near the base of the peak the values are unreliable. Meaningful intensities can be obtained using a Bruker spectrometer line-fit routine to yield line widths and intensities. Errors are based on the RMS (root mean

square) noise, also calculated from the spectra on the Aspect 3000. The intensities and calculated NOE values are shown in table 9.10.

Table 9.10: Line areas and NOE's for cyclohexane with RD of 3 and 60 seconds.

	BB decoupled		Inverse-gated		NOE, n±0.02	
RD, s	60	3	60	3	60	3
Non-spinning	11.61	5.59	5.26	3.42	1.21	0.63
Spinning	17.19	8.92	7.82	7.26	1.20	0.23

As expected, the results show a larger NOE for a 60 second relaxation delay than for a 3 second relaxation delay. For a 60 s time delay a full NOE is allowed to build up and full relaxation can occur, therefore, the excitation pulse acts on the spins at equilibrium and the NOE enhancement should be similar for spinning and non-spinning and any small change in T_1 will not be observed. On reduction of the relaxation delay the time available for NOE build up is diminished. For a three second relaxation delay the spin system is partially saturated resulting in a change in the signal to noise. More importantly, the NOE's under spinning and non-spinning conditions, with RD=3 s, are significantly different. The difference is interpreted in section 9.6.

9.3.3: EFFECT OF SPADES EXPERIMENT ON LARGE MOLECULES

SPADES was performed on a saturated sample of cholesterol dissolved in chloroform-d. Large molecules have a longer correlation time and greater asymmetry, thus, a shorter relaxation time. Figures 9.21, 9.22 and 9.23 show the ^{13}C spectra for the non-spinning and spinning case. Various relaxation delays were used to give differing levels of enhancement.

Figure 9.21: ^{13}C spectrum of cholesterol under non-spinning (top) and spinning (bottom) conditions, RD=7s.

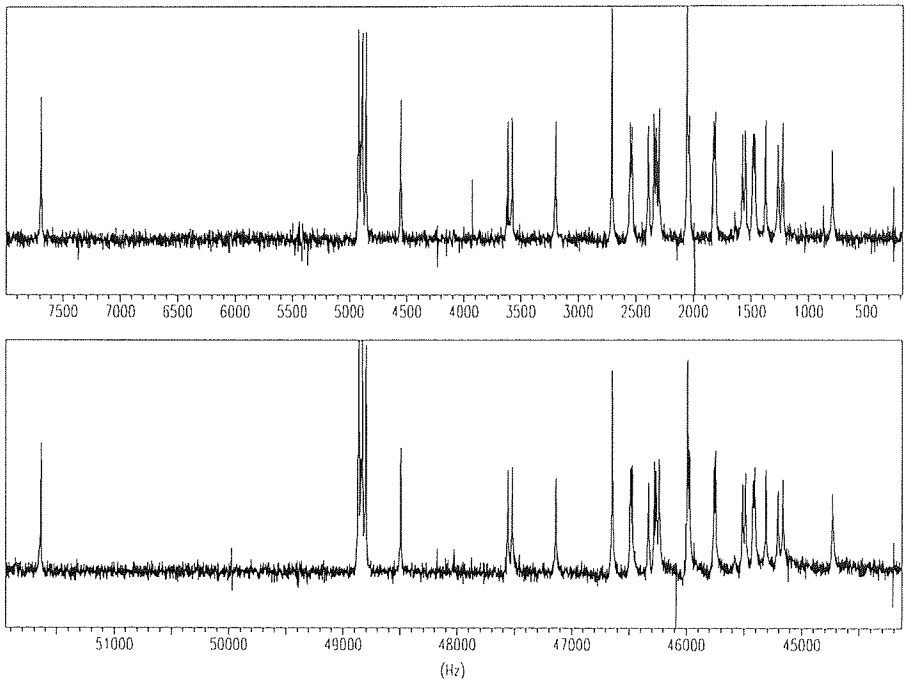

Figure 9.22: ^{13}C spectrum of cholesterol under non-spinning (top) and spinning (bottom) conditions, RD=1s.

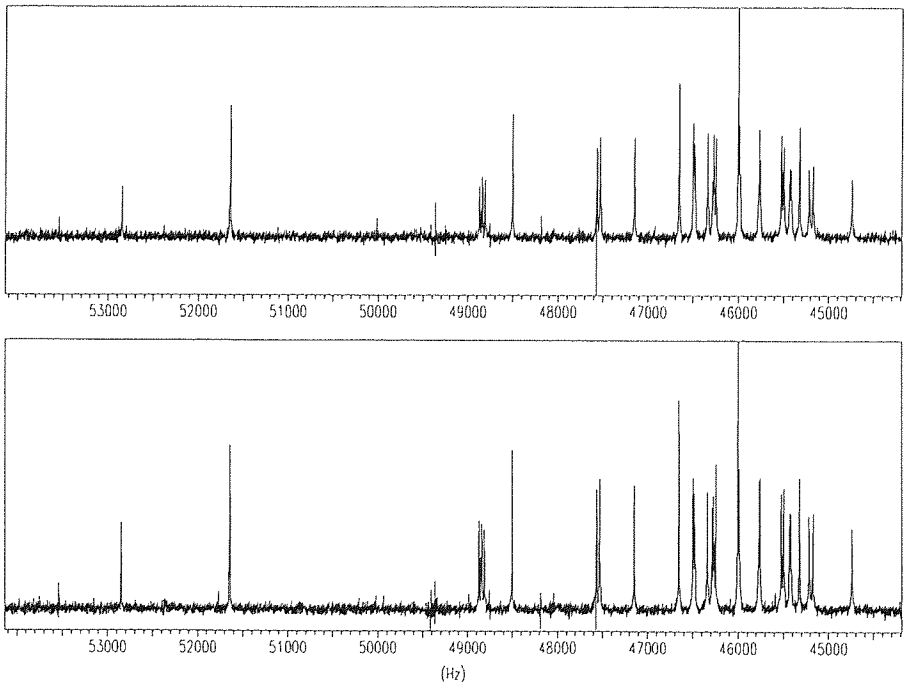

Figure 9.23: ^{13}C spectrum of cholesterol under non-spinning (top) and spinning (bottom) conditions, RD=0.1s.

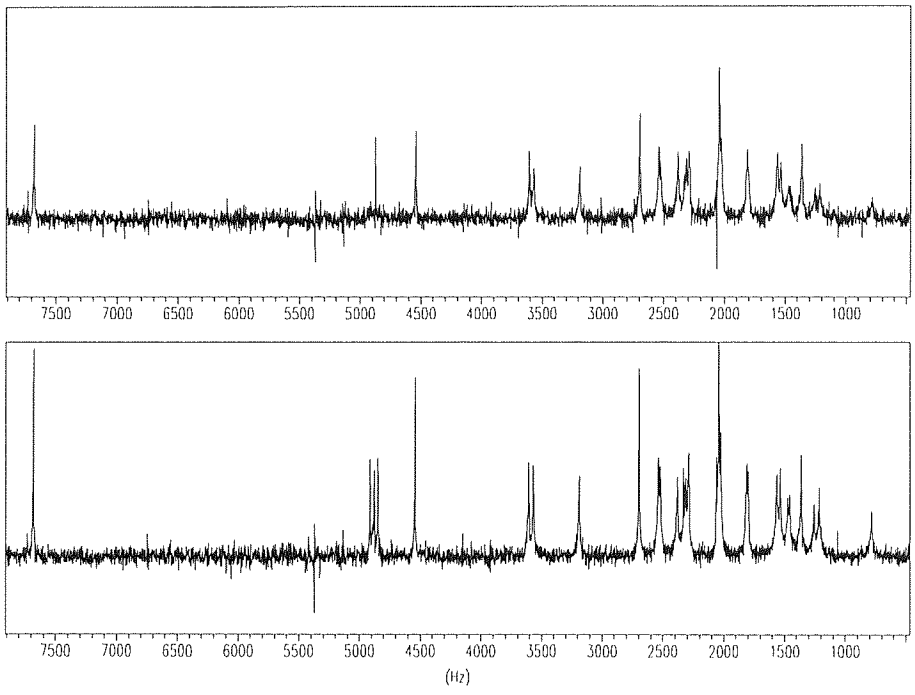

For a 7 second delay there is very little enhancement. The difference in S/N between the spinning and the non-spinning case increases as the relaxation delay time decreases and forces the spin system to be increasingly saturated. Thus, varying degrees of enhancement can be seen throughout each spectrum, as the relaxation delay is reduced, depending on the T_1 for each ^{13}C site. The triplet due to chloroform-d, at 48800 Hz (4800 Hz, figure 9.21) gives a consistent enhancement in each spectra, due to its longer relaxation time.

9.4: EFFECT OF SPADES EXPERIMENT ON LINE WIDTHS

A secondary consequence of accelerated diffusion is that the sample will experience a motionally averaged magnetic field. Line widths measured in the

NMR spectrum are dominated by T_2^* due to magnetic inhomogeneity. By increasing sample diffusion the molecules will all experience the same inhomomgeneitities more rapidly and therefore a more effective averaging will occur. Evidence that this occurs can be seen from the measurement of line widths, reported in section 9.4.2, which show a change in FWHM for the spinning and the non-spinning case, see table 9.11.

Table 9.11: Effect of SPADES experiment on the ^{13}C line widths of cyclohexane.

	Line width (FWHM), Hz				
	BB decoupled		Inverse-gated		Average
RD, s	60	3	60	3	
Non-spinning	9.89	9.41	9.81	8.2	9.33
Spinning	4.94	5.16	4.31	4.79	4.8

SPADES not only provides a method of S/N enhancement but of resolution improvement.

9.5: CONCLUSION

The results displayed in figure 9.0 show that the signal to noise of NMR spectra can be enhanced for nuclei with long relaxation times. In figure 9.1, it can be seen that enhancement was only achieved when the liquid is stirred rapidly, causing an accelerated diffusion of molecules. Increasing sample diffusion results in the nuclei, which have experience excitation by the H_1 field, being removed and replaced with polarised unexcited nuclei. The consequence of this replacement is that the magnitude of M_z before each pulse is larger (tending to M_0) than it would be for normal diffusion and relaxation processes. It has been shown that the rate

of spin saturation is reduced because there is a larger active sample volume, thus allowing the pulse repetition rate to be reduced.

Some of the experimental parameters have been investigated in order to improve the level of enhancement, section 9.2. Results were obtained for the variation in relaxation delay time (figure 9.6), acquisition time (figure 9.11) and delay time (figure 9.14). All of the figures show that the rate of change in S/N for non-spinning and spinning is the same on variation of each parameter. The only difference between the spinning and the non-spinning case is an increase in the magnitude of the signal.

The study of cholesterol dissolved in chloroform-d, figure 9.21, 9.22 and 9.23, indicates that enhancement is possible to varying degrees depending on the T_1 for each ^{13}C site and the repetition rate, e.g. quaternary carbons show the major effect with each spectra showing a large enhancement in the S/N of the deuterated chloroform peak. Only smaller changes are observed for the other sites, again suggesting that it is a reduction in the saturation rate of the spin system which is responsible for the enhanced signal to noise. This finding could be particularly important to the multi-dimensional NMR studies of proteins, where times constraints demand very low values of RD. The implication is that SPADES could facilitate a significant enhancement in S/N, while reducing the experimental time of these type of pulse sequences.

The effect of the motion of the liquid through the probe coil region imposes a new pseudo-relaxation time on the molecules, very much shorter than the real T_1s, due to the accelerated diffusion of the molecules through the probe coil. The measured relaxation time, table 9.8, is an indication of the rate of saturation of excited nuclei, therefore, a new repetition rate for a 90^0 pulse can be deduced from the spinning longitudinal relaxation time, T_1^{SP}. Since a 90^0 pulse can be used, the maximum transverse magnetisation can be generated and a much greater enhancement by SPADES is possible compared to the Ernst condition (in the same time scale). The effect on actual relaxation times can be found by measuring the NOE enhancement for carbon nuclei. Measurement of the NOE for a 60 second relaxation delay, figure 9.19, shows no difference in the NOE's for spinning and non-spinning: for this to occur the nuclei must have been allowed to attain a full NOE and relax completely, whether or not the nuclei, under spinning and non-spinning conditions, have different T_1's. A 3 second repetition time, figure 9.20, prevents a full NOE, and complete relaxation, and the results give a reduced NOE for the non-spinning case and a further reduction for the spinning case. The reduction in NOE for the spinning case are larger than in the non-spinning case. The action of the rotor will impose a new shorter correlation time on the molecules which is dependent on the forced diffusion rate created by spinning. In the extreme narrowing region of the spectral density plot, figure 1.5, shortening the correlation time corresponds to an increase in the T_1 for the molecule.

For liquids, the time dependent magnetisation for a ^{13}C nucleus dipolar coupled to a proton is given by equation 9.1.

$$\frac{dM_Z^C}{dt} = \frac{\left(M_0^C - M_Z^C\right)}{T_{1CC}} + \frac{\left(M_0^H - M_Z^H\right)}{T_{1CH}} \qquad (9.1)$$

(where T_{1CC} and T_{1CH} are the relaxation time for carbon-carbon and carbon-proton interactions respectively).

For steady state conditions, when the proton transition is saturated, M_Z^H and dM_Z^C / dt are equal to zero, and equation 9.1 becomes,

$$M_Z^C = M_0^C + \frac{T_{1CC}.M_0^H}{T_{1CH}} \qquad (9.2)$$

Thus, the magnitude of M_Z^C becomes dependent on the ratio T_{1CC}/T_{1CH}. The total relaxation time for T_{1CC} and T_{1CH} will comprise of inter and intramolecular contributions. The total relaxation rate for the homonuclear interaction is given by,

$$\frac{1}{T_{1CC}} = \frac{1}{T_{1CC}^{Intra}} + \frac{1}{T_{1CC}^{Inter}} \qquad (9.3)$$

and, for the heteronuclear interaction,

$$\frac{1}{T_{1CH}} = \frac{1}{T_{1CH}^{Intra}} + \frac{1}{T_{1CH}^{Inter}} \qquad (9.4)$$

Under the SPADES experimental conditions of forced diffusion, only the translational correlation time will change significantly, while the rotational correlation time will be largely unaffected. The effect of the translational correlation time will be $T_{1CH}^{inter} > T_{1CC}^{inter}$ because the protons are on the exterior of the molecule, allowing them to approach neighbouring molecules more closely than the ^{13}C nuclei. If τ_{trans} decreases then $dT_{1CH}^{inter}/d\tau > dT_{1CC}^{inter}/d\tau$ and, therefore, the ratio

T_{1CC}/T_{1CH} decreases. Thus, from equation 9.2 it can be seen that the magnitude of M_Z^C will be reduced and the NOE enhancement will be smaller.

Line widths are dominated by inhomogeneities present in all magnets, shimming of the field is necessary to reduce the line widths to an acceptable resolution. By accelerating the sample diffusion rate more of the molecules will experience an increased proportion of the coil region and, therefore, average magnetic inhomogeneity. Results indicate, table 9.10, that the line width of the ^{13}C resonance of cyclohexane can be almost halved on spinning.

CHAPTER 10

CONCLUSIONS AND FUTURE WORK

10.0: CONCLUSIONS

The purpose of this thesis was to explore the potential uses of ultrasound within a NMR spectrometer. A study has been carried out into expanding the application of the SINNMR technique, proposed by Homer et al[5] and investigated by Homer and Howard[6], to glass samples. Another area of work has involved assessing the potential of monitoring sonochemical reactions by NMR, as this could create the possibility of measuring reaction rates and the elucidating mechanisms of sonochemical reactions. Ultrasound can be applied to other media, such as liquid crystals and work was carried out in collaboration with Prof. J. Emsley and Dr. M. Edgar (Southampton University) into the effects of ultrasound on the molecular alignment of liquid crystals in magnetic fields. Piezoelectric transducer assemblies, suitable for all of the above investigations, were designed and fabricated by the author.

In a separate study, the enhancement of the S/N ratio of the NMR spectra of samples subject to forced rapid diffusion was investigated.

As acoustic cavitation is believed to be important to the success of SINNMR, studies were undertaken to establish the frequency and intensity threshold for this. Although It has been stated that the theoretical limit for cavitation in liquids is 10 MHz[107], it is commonly believed that the practical upper frequency limit was 2 MHz[126]: it is for this reason that medical ultrasonic imaging commonly operates at above 3 MHz. The Weissler reaction[7], for the liberation of iodine from potassium iodide, was used to determine the cavitation threshold for frequencies of 2, 3, 5,

and 10 MHz. It was shown that the reaction could be initiated at low powers but took several minutes to give a noticeable colour change. The reaction rate was increased with higher input powers, to give a noticeable colour change in only a few seconds. As expected, this is consistent with the intensity of the cavitation field being increased with increasing input power. However, the fact that cavitation occurs at lower powers has important implications in medical imaging.

Having determined the high frequency cavitation criteria, attempts were made to initiate the polymerisation of methylmethacrylate by ultrasonic radiation[123, 128]. The most likely the reason for no initiation is the difficulty in the removal of inhibitor and the degree of oxygen saturation in the liquid, which "mops up" free radicals,

The SINNMR technique was investigated for the glass $Na_2O/B_2O_3/Al_2O_3$ in the molar ratio 20/70/10 %. It was shown that a significant line width reduction, relative to that of the static powder, is possible when the material is simply placed in colloidal suspension. The reason for this observation (also made for other materials in the authors laboratory) is that the particles experience rotational Brownian motion which contributes to spatial averaging of the nuclear interactions. A further reduction in the line width (by about a factor of two) can be attained when the suspension is irradiated with 2 MHz ultrasound. This effect was observed for both the ^{27}Al and ^{11}B resonance which indicates that the narrowing is due to the rotational motion of the solid particles. The SINNMR effect was only possible for input powers of >15 W, suggesting that only a significant cavitation field was capable of generating rotational motion rapid enough to spacially

average the solid particles: this is supported by the results for the turbulent motion of solid particles, by rapid stirring, which was insufficient to cause spatially averaging, and therefore had no influence on the line width. The acoustic narrowing of the resonance was found to be partially due to heating of the sample. This was deduced from the fact that the line width of the narrowed resonance did not return to its original values after the cessation of acoustic irradiation. The implication is that the acoustic irradiation raised the temperature with an accompanying increase in Brownian narrowing of the resonances. Temperature induced line width narrowing is an important effect and cannot be discounted as a mechanism in SINNMR. However, the spectra only required 189 seconds to acquire and, therefore, the temperature change due to heating, or cooling, should be small.

Long range ordering of liquid crystals can be achieved by aligning the molecular aggregates in a magnetic field. The direction of alignment can be found by monitoring the quadrupolar splitting of deuterated solute that is added to the liquid crystal. Thermotropic liquid crystals align themselves parallel to the field, while, lyotropic liquid crystals align themselves perpendicular. Studies were undertaken into the possibility that sonic irradiation of the liquid crystals could deflect the molecules, from their normal field aligned position, by acoustic streaming. According to the Dysthe theory[117], the most stable orientation, under acoustic irradiation, should be when the director axis of the liquid crystal lies parallel to the direction of ultrasonic propagation. It was found that changes in the orientation of the liquid crystal I35 and ZLI-1167 were only possible when the ultrasound was

applied from a perpendicular direction with respect to the director. Attenuation of ultrasonic streaming as it passed through the medium gave rise to a range of director orientations, giving broadened lines in the ^{2}H NMR spectra. The maximum angle of deflection due to ultrasonic streaming was calculated to be ca. 35^{0} for I35 and 20^{0} for ZLI-1167. Ultrasonic heating was also found to influence the appearance of the NMR spectrum. However, this effect was minimised by using power levels below 6 W. It was also found that director reorientation could be achieved by rapid mechanical stirring that simulated acoustic streaming. This gives a narrower range of orientations, indicated by sharp lines in the NMR spectra. Since the alignment of the liquid crystal was in the same plane as the rotational motion of the rotor, the angle of deflection was found to be only the order of 7^{0}.

It has been found that the signal to noise of ^{13}C NMR spectrum of ethylbenzene can be enhanced if the liquid sample is rapidly stirred. These results are due to effectively accelerating the diffusion of nuclei though the NMR coil region so that M_0 can be re-established without being simply dependent on the natural spin-lattice relaxation time of the spins. The consequence of this is that the FID can be acquired more rapidly than the conventional experimental relaxation delay of $5.3T_1$ without saturating the spin system. The technique has been designated Saturation Prevention by Accelerated Diffusion to Enhance Signals, SPADES. Longitudinal relaxation times measured under spinning gave a pseudo-relaxation time, T_1^{SP}, for ^{13}C in ethylbenzene of around 300 ms. The implication of this is that pulse repetition rates can be of the order of milliseconds, without severely

degrading the S/N. An indication of the influence of rapid flow on the real relaxation times of ^{13}C in cyclohexane were deduced from measurements of the NOE parameter, η. As discussed in chapter nine, shorting the translational correlation time influences the carbon-carbon and carbon-proton relaxation mechanisms by differing degrees. This results in the molecule having a different T_1 and therefore a reduced NOE enhancement.

Spectra obtained for the ^{13}C resonance in cholesterol have shown that the degree of enhancement varies, depending on the relaxation time for the nucleus and the repetition rate. The SPADES experiment is most beneficial for nuclei with very long T_1 values, where rapid multi-pulsing with SPADES can be more advantageous than using the Ernst condition because SPADES works well with a 90^0 excitation pulse. The implications are that SPADES should provide particular advantage in reducing the experimental time in multidimensional NMR studies of, for example, proteins.

10.1: FUTURE WORK

Initial results obtained for the glasses show that the line widths can be narrowed using ultrasound. Future work must involve of trying to improve the reproducibility of the technique. The results suggest that cavitation is the mechanism responsible for narrowing, although some effect of temperature enhanced Brownian motion cannot be discounted. The generation of a cavitation field in a liquid is not difficult, but, the presence of solid particles must disrupt the ultrasonic wave. The

influence of the 'concentration' of solid particle present, in the liquid, should be investigated using ultrasound in the MHz region in order to assess its effect on the cavitation field The cavitation field intensity can be monitored using the Weissler reaction. By varying the mass of solid particles in the presence of the reaction and monitoring the rate of colouration, possibly by UV spectroscopy, then the cavitation experienced by the particles could be found. By varying the particle size with respect to the ultrasonic wavelength, the Weissler reaction rate could be used to give an indication of ultrasonic scattering by the solid. If cavitation effects are responsible for the narrowed lines observed, and shock waves and microjetting are the mechanisms by which particle Brownian motion is enhanced, then, it is possible that these mechanisms have sufficient force to erode the particles. Small particles have been shown to give narrow NMR line widths[130, 131, 132] and the effect of ultrasound on particle size should be investigated (as well as the rate of particle aggregation after the cessation of acoustic irradiation) to determine if this is the explanation for narrowing of the lines. Temperature effects must be removed if a genuine study of the effect of ultrasound is to be made. More efficient piezoelectric crystals and better mounting will reduce some of the liquid heating. The total input power during accumulation of the signal could be reduced if the ultrasound is timed to coincide with the acquisition time.

Results show that liquid crystal can be re-oriented, in a magnetic field, by applying ultrasound. Further experiments should concentrate on the degree of re-orientation attainable with ultrasonic streaming. Larger angles of deflection are possible by increasing the input power levels, but this is usually accompanied with

heating of the liquid crystal which obscures the re-orientation effect in the NMR spectrum. This could be overcome, simply, by using a liquid crystal with a higher clearing temperature, which would be more insensitive to heating. A liquid crystal with a lower viscosity should be re-oriented more easily and, therefore, the use of lower ultrasonic power levels could be studied. Ultrasonic streaming is more easily attainable at lower frequencies, say 20 kHz, because the nodes of the wave exist outside the sample tube, thus giving a pressure gradient within the sample. Attenuation at lower frequencies is reduced, and should enable heating effects to be minimised. Consequently, low acoustic frequency studies of the manipulation of the director orientation is advocated.

The re-orientation of the liquid crystals may be more finely controlled by using standing waves. A standing wave set up in the liquid crystal will give rise to domains of sample experiencing different ultrasonic intensities and, thus, stable orientations. Manipulation of the standing wave, either by changing the direction of propagation or ultrasonic frequency, will change the orientation of the liquid crystal with respect to the magnetic field.

The results of SPADES has shown that the intensity of the NMR signal can be enhanced by rapid stirring of the liquid. The future of the technique lies in its application to nuclei which have very long relaxation times, making their observation difficult, e.g. ^{29}Si. Further work into this technique should concentrate ascertaining the conditions necessary for optimum enhancement for the nucleus under observation. This will include the measurement of the influence of flow

rate/viscosity, spectral parameters/repetition rate and the development of the rotor to give more efficient operation.

BIBLIOGRAPHY

B1: NMR TEXTS

A. Abragam, "Principles of Nuclear Magnetism, Clarendon Press, Oxford, 1961.

J. W. Akitt, "NMR and Chemistry", 3rd Edn., Chapman & Hall, London, 1992.

C. Brevard and P. Granger, "Handbook of High Resolution Multinuclear NMR", Wiley, New York, 1981.

A. E. Derome, "Modern NMR Techniques for Chemistry Research", Pergamon, Oxford, 1987.

J. W. Emsley, J. Feeney, and L. H. Sutcliffe, "High Resolution Nuclear Magnetic Resonance Spectroscopy- Volume One/Two", Pergamon, Oxford, 1965.

R. R. Ernst, G. Bodenhausen, A. Wokaun, "Principles of Nuclear Magnetic Resonance in One and Two Dimensions", Clarendon Press, Oxford, 1987.

E. Fukushima and S. B. Roeder, "Experimental Pulse NMR, A Nuts and Bolts Approach", Addison-Wesley, Reading, Mass. USA, 1981.

C. A. Fyfe, "Solid State NMR for Chemists", C.F.C. Press, Ontario, 1983.

U. Haeberlen, "High Resolution NMR in Solids, Selective Averaging", Suppl. 1, Adv. Magn. Reson., Academic Press, New York, 1976.

R. K. Harris, "Nuclear Magnetic Resonance Spectroscopy", Pitman, London, 1983.

J. W. Hennel and J. Klinowski, "Fundamentals of Nuclear Magnetic Resonance", Longman UK, Essex, England, 1993.

S. W. Homans, "A dictionary of Concepts in NMR", Clarendon Press, Oxford, 1992.

M. Mehring, "High Resolution NMR in Solids", 2nd Edn., Springer-Velag, New York, 1983.

M. Munowitz, "Coherence and NMR", Wiley, New York, 1988.

J. K. M. Sanders and B. K. Hunter, "Modern NMR Spectroscopy- A Guide for Chemists", 2nd Edn., Oxford, 1983.

C. P. Schlicter, "Principles of Magnetic Resonance", 3rd Edn., Springer-Verlag, New York, 1990

B2: ULTRASOUND TEXTS

R. T. Beyer and S. V. Letcher, "Physical Ultrasonics", Academic Press, New York, 1969.

J. Blitz, "Ultrasonics: Methods and Applications", Butterworths, London, 1971.

J. Blitz, "Fundamentals of Ultrasonics, Butterworths, London, 1967

B. Brown and J. E. Goodman, "High Intensity Ultrasonics", Iliffe Books, New Jersey, 1965.

J. R. Frederick, "Ultrasonic Engineering", Wiley, New York, 1965.

G. L. Gooberman, "Ultrasonics; Theory and Application", English University Press, London, 1968.

T. J. Mason, "Chemistry with Ultrasound", Elsevier, Essex, 1990.

W. P. Mason, "Physical Acoustics, Volumes I to XIII", Academic Press, New York, 1965.

G. Price, Ed., "Current Trends in Sonochemistry", The Royal Society of Chemistry, Cambridge, 1992.

K. S. Suslick (Ed.), "Ultrasound -Its Chemical, Physical and Biological Effects", VCH Ltd, New York.

REFERENCES

1 E.R. Andrew, A. Bradbury and R. G. Eades, "Nuclear Magnetic Resonance Spectra from a Crystal rotated at High Speed", Nature, 1958, **182**, 1659.

2 I. J. lowe, "Free Induction Decays of Rotating Solids", Phys. Rev. Lett, 1959, **2**, 285.

3 A. Samoson, E. Lippmaa and A. Pines, "High resolution solid-state NMR. Averaging of second-order effects by means of a double rotor", Mol. Phys., 1988, **65**(4), 1013.
A. Samoson and A. Pines, "Double rotor for solid-state NMR", Rev. Sci. Instrum., 1989, **60**(10), 3239.

4 A. Llor and J. Virlet, "Towards High Resolution NMR of more Nuclei in Solids: Sample Spinning with Time-dependent Spinner Axis Angle", Chem. Phys. Let., 1988, **152**(2.3), 248.

5 J. Homer, P. McKeown, W. R. McWhinnie, S. U. Patel and G. J, Tilestone, "Sonically Induced Narrowing of Solid State Nuclear Magnetic Resonance Spectra: A Possible Alternative to Magic Angle Spinning Nuclear Magnetic Resonance Spectra", J. Chem. Soc., Faraday Trans., 1991, **87**, 2253.

6 J. Homer and M. J. Howard, "Studies on the Origin of Sonically Induced Narrowing of Solid-State Nuclear Magnetic Resonance Spectra", J. Chem. Soc., Faraday Trans., 1993, **89**, 3029.

7 A. Weissler, "Sonochemistry: The Production of Chemical Change with Sound Waves", J. Acoust. Soc. Amer., 1953, **25**, 651.

8 J. C. Rowell, W. D. Phillips, L. R. Melby and M. Panar, "NMR Studies of Some Liquid Crystal Systems", J. Chem. Phys., 1965, **43**, 3442.

W. D. Phillips, J. C. Rowell and L. R. Melby, "Quadrupolar splitting in the Deuterium Magnetic Resonance Spectra of Liquid Crystals", J. Chem. Phys., 1964, **41**, 2551.

9 W. Gerlach amd O. Stern, "Über die Richtungsquantelung im Magnetfeld", Ann. Physiks, 1924, **74**, 673.

10 S.Tolansky, "High resolution spectroscopy", Meuthen, London, 1947.

11 W. Pauli, "Zuschriften und vorläufige Mitteilungen", Naturwisschaften, 1924, **12**, 741.

12 F. Bloch, W. W. Hansen and M. Packard, "Nuclear Induction", Phys. Rev., 1946, **69**, 127.

13 E. M. Purcell, H. C. Torrey and R. V. Pound, "Resonance Absorption by Nuclear Magnetic Moments in Solids", Phys. Rev., 1946, **69**, 37.

14 R. R. Ernst, "Sensitivity Enhancements in Magnetic Resonance", Adv. Mag. Reson., 1966, **2**, 1.

M. P. Klein and G.W. Barton, "Enhancement of Signal-to-Noise Ratio by Continuous Averaging: Application to Magnetic Resonance", Rev. Sci. Instrum., 1963, **34**, 754.

P. Laszlo and P.R. Schleyer, "Ring Size Effect on cis-Olefinic Coupling Constants of Cycloalkenes. Use of ^{13}C Patterns", J. Am. Chem. Soc., 1963, **85**, 2017.

L. C. Allen and L.F. Johnson, "Chemical Applications of Sensitivity Enhancement in Nuclear Magnetic Resonance and Electron Spin Resonance", J. Am. Chem. Soc., 1963, **85**, 2668.

O. Jardetsky, N. G. Wade and J. J. Fisher, "Proton Magnetic Resonance Investigation of Enzyme-Coenzyme Complexes", Nature, 1963, **197**, 183.

R. R. Ernst, "Sensitivity Enhancement in Magnetic Resonance. I. Analysis of the Method of Time Averaging", Rev. Sci. Instrum., 1965, **36**, 1689.

R. R. Ernst and W. A Anderson, "Sensistivity Enhancment in Magnetic Resonance. II. Investigation of the Intermediate Passage Conditions", Rev. Sci. Instrum., 1965, **36**, 1696.

15 T. C. Farrar and E. D. Becker, "Pulse and Fourier transform NMR", Academic Press, New York, 1971.

D. Shaw, "Fourier transform NMR spectroscopy", Elsevier, Amsterdam, 2nd edn., 1984.

M. L. Martin, J.-J. Delpuech and G. J. Martin, "Practical NMR spectroscopy", Heyden, London, 1977.

16 S. R. La Paglia, "Introductory Quantum Chemistry", p. 238, Harper & Row, 1971.

17 F. Bloch, "Nuclear Induction", Phys. Rev., 1946, **70**, 460.

18 R. L. Vold and R. R. Vold, Prog. NMR Spec., Eds. J. W. Emsley, J. Feeney and L. Sutcliffe, Vol. 12, Pergamon Press, New York, 1978.

19 D. M. Grant, C. L. Mayne, F. Liu and T. Xiang, "Spin-lattice Relaxation of Coupled Nuclear Spins with Application to Molecular Motion in Liquids", Chem. Rev., 1991, **91**, 1591.

20 N. Bloembergen, E. M. Purcell and R. V. Pound, "Relaxation Effects in Nuclear Magnetic Resonance Absorption", Phys, Rev., 1948, **73**, 679.

21 R. L. Vold, J. S. Waugh, M. P. Klein and D. E. Phelps, "Measurement of Spin Relaxation in Complex Systems", J. Chem. Phys., 1968, **48**, 3831.

22 R. Freeman and H. D. W. Hill, "Spin-Lattice Relaxation in High Resolution NMR Spectra of Carbon-13", J. Chem. Phys., 1970, **53**, 4103.

23 R. Freeman and H. D. W. Hill, "Fourier Transform Study of NMR Spin-Lattice Relaxation by "Progressive Saturation"", J. Chem. Phys., 1971, **54**, 3367.

24 R. K. Gupta, G. H. Weiss, J. A. Ferretti and E. D. Becker, "A Variable Perturbation Method for Nuclear Spin-Lattice Relaxation Measurements", J. Magn. Reson., 1979, **35**, 301.

25 J. Homer and M. S. Beevers. "Driven-Equilibrium Single–Pulse Observation of T_1 Relaxation. A Re-evaluation of a Rapid "New Method for Determining NMR Spin-Lattice Relaxation Times", Magn. Reson., 1985, **63**, 287.
J. Homer and J. K. Roberts, "Routine Evaluation of M_0 Ratios and T_1 Values from Driven Equilibrium NMR Spectra", J. Magn. Reson, 1990, **89**, 265.

26 K. A. Christensen, D. M. Grant, E. M. Schulman and C. Walling, "Optimal Determination of Relaxation Times of Fourier Transform Nuclear Magnetic Resonance. Determination of Spin-Lattice Relaxation Times in Chemically Polarized Species", J. Phys. Chem., 1974, **78**, 1971.

Y. N. Luzikov, N. M. Sergeyev and M. G. Lerkovitc, "The "Rapid" Modification of the Progressive Saturation Technique" J. Magn. Reson., 1974, **21**,359.

R. K. Gupta, "A New Lookat the Method of Variable Nutation Angle for the Measurement of Spin-Lattice Relaxation Times Using Fourier Transform NMR", J. Magn. Reson., 1977, **25**, 231.

27 H. Y. Carr and E. M. Purcell, "Effects of Diffusion on the Free Precession in Nuclear Magnetic Resonance Experiments", Phys. Rev., 1954, **94**, 630.

28 R. Freeman and H. D. W. Hill, "Fourier Transform Study of NMR Spin-Spin Relaxation", J. Chem. Phys., 1971, **55**, 1985.

29 A. Pines, M. G. Gibby, J. S. Waugh, "Proton-Enhanced Nuclear Induction Spectroscopy. A Method for High Resolution NMR of Dilute Spins in Solids", J. Chem. Phys., 1972, **56**, 1776.
A. Pines, J. S. Waugh, "Quantitative Aspects of Coherent Averaging. Simple Treatment of Resonance Offset Processes in Multiple-Pulse NMR", J. Magn. Reson., 1972, **8**, 354.

30 N. F. Ramsey. "The Internal Diamagnetic Field Correction in Measurements of the Proton Magnetic Moment", Phys. Rev., 1950, **77**, 567, "Magnetic Shielding of Nuclei in Molecules", Phys. Rev. 1950, **78**, 699; "Chemical Effects in Nuclear Magnetic Resonance and in Diamagnetic Susceptibility", Phys. Rev., 1952, **86**, 243.

31 D. E. O'Reilly, 'Chemical Shift Calculation', Prog. NMR. Spec, Vol. 2, Ed. Emsley, Feeney and Sutcliffe, Pergammon Press Ltd, Oxford, 1967.

32 J. I. Musher, 'Theory of the Chemical Shift', Adv. Mag. Res., Ed. J. Waugh, Vol. 2, 1966.

33 J. A. Pople, W. G. Schneider, and H. J. Bernstein, "High Resolution Nuclear Magnetic Resonance Spectroscopy", McGraw-Hill, New York, 1959.

34 J. W. Emsley, J. Feeney and L.H. Sutcliffe, "High Resolution Nuclear Magnetic Resonance Spectroscopy", Vol. 1, Peragamom Press, Oxford, 1965.

35 J. W. Emsley, and L. Philips, "Fluorine Chemical Shift", Prog. NMR Spec., Eds. J. W. Emsley, J. Feeney and L. Sutcliffe, Vol. 7, Pergamon Press, New York, 1971

36 C. Brevard and P. Granger, "Handbook of high resolution multinuclear NMR", part two, Wiley, New York, 1981.

37 M. Karplus, "Contact Electron-Spin Coupling of Nuclear Magnetic Moments", J. Chem. Phys., 1959, **30**, 11.

38 M. Karplus, "Vicinal Proton Coupling in Nuclear Magnetic Resonance", J. Am. Chem. Soc., 1963, **85**, 2870.

39 F. Bloch, A. Siegert, "Magnetic Resonance for Non-Rotating Fields", Phys. Rev., 1940, **57**, 522.

40 N. F. Ramsey, "Resonance Transitions Induced by Perturbation at Two or More Different Frequencies", Phys. Rev., 1955, **100**, 1191.

41 J. Jeener, Ampère International Summer School, Basko Polje, Yugoslavia, 1971.

42 W. P. Aue, E. Bartholdi and R. R. Ernst, "Two-dimensional Spectroscopy. Application to Nuclear magnetic Resonance", J. Chem. Phys., 1976, **64**, 2229.

43 H. Kessler, M. Gehrke, C. Griesinger, "Two-dimensional NMR Spectroscopy: Background and Overview of the Experiments", Angew. Chem. Int. Ed. Engl., 1988, **27**, 490.

44 General introduction: D. D. Traficante, "The nature of the second dimension in 2D NMR", Concepts in Magn. Reson., 1989, **1**,7.

45 A. W. Overhauser, "Polarization of Nuclei in Metals", Phys. Rev. 1953, **91**, 476.
ibid, 1953, **92**, 411.

46 J. H. Noggle and R. E Schirmer, "The Nuclear Overhauser effect-Chemical Applications", Academic Press, 1972.

47 A. Kumar and S. I. Gordon , "Overhauser Studies in Two-Spin Systems, J. Chem. Phys., 1971, **34**(7), 3207.

48 W. Heisenberg, "Uber den anschaulichen Inhalt der quantentheoretischen Kinematik und Mechanik", Z. Phys., 1927, 43, 172.
W. Heisenberg, "The Physical Prinicples of Quantum theory", 1930, New York.
P. W. Atkins, "Quanta: A Handbook of Concepts", 2nd ed.,1991, Oxford Uni. Press, Oxford.

49 G. A. Morris and R. Freeman, "Selective Excitation in Fourier Transform Nuclear Magnetic Resonance", J. Magn Reson.,1978, **29**, 433.

50 D. I. Hoult, "The NMR Receiver: A Description and Analysis of Design", Progr. NMR Spectr., 1978, **12**, 41.

51 R. M. Bracewell, "The Fourier Transform and its applications", 1965, McGraw-Hill, New York.
E. O. Brigham, "The Fast Fourier Transform", Prentice-Hall, London, 1974.

52 R. R. Ernst and W. A Anderson, "Application of Fourier Transform Spectroscopy to Magnetic Resonance", Rev. Sci. Instrum., 1966, **37**, 93.

53 S. A. Smith, W. E. Palke and J. T. Gerig, "The Hamiltonians of NMR: Part 1", Concepts in Magn. reson., 1992, **4**, 107.
S. A. Smith, W. E. Palke and J. T. Gerig, "The Hamiltonians of NMR: Part 2", Concepts in Magn. reson., 1992, **4**, 181.

54 G. E. Pake , "Nuclear Resonance Absorption in Hydrated Crystals: Fine Structure of the Proton Line", J. Chem. Phys., 1948, **16**, 327.

55 F. A. I. Anet and D. J. O`Leary, "The Shielding Tensor, Part 1: Understanding its Symmetry Properties", Concepts in Magn. Reson., 1991, **3**, 193.
F. A. I. Anet and D. J. O`Leary, "The Shielding Tensor, Part 2: Understanding its Strange Effects on Relaxation", Concepts in Magn. Reson., 1992, **4**, 35.

56 U. Haeberlen, " High-resolution NMR in solids: selective averaging", Suppl 1, Adv. Magn. Reson., Academic Press, New York, 1976.

57 J. P. Amoureux, C. Fernandez, P. Granger, "Interpretation of Quadrupolar Powder Spectra: Static and MAS Experiments", Multinuclear Magnetic Resonance in Liquids and Solids-Chemical Applications, p. 409, eds. P. Granger and R. Harris, Kluwer Academic Press, 1990.

58 F. Taulelle, "NMR of Quadrupolar Nuclei in the Solid State", Multinuclear Magnetic Resonance in Liquids and Solids-Chemical Applications, p. 393, eds. P. Granger and R. Harris, Kluwer Academic Press, 1990.

59 A. Samoson and E. Lippma, 'Synchronized Double Rotation NMR Spectroscopy', J. Mag. Res., 1989, **84**, 410.

60 K. T. Mueller, B. Q. Sun, G. C. Chingas, J. W. Zwanziger, T. Terao and A. Pines, "Dynamic-Angle Spinning of Quadrupolar Nuclei", J. Magn. Reson., 190, **86**, 470.

61 A. Pines, M. G. Gibby, J. S. Waugh, "Proton-Enhanced Nuclear Induction Spectroscopy. ^{13}C Chemical Shielding Anisotropy in Some Organic Solids", Chem. Phys. Lett., 1972, **15**, 373.
A. Pines, M. G. Gibby, J. S. Waugh, "Proton-Enhanced NMR of Dilute Spins in Solids", J. Chem. Phys., 1973, **59**, 569.

62 G. A. Morris and R. Freeman, "Enhancement of Nuclear Magnetic Resonance Signals by Polarization Transfer", J. Am. Chem. Soc. 1979, **101**, 760.

63 D. P. Burum and R. R. Ernst, "Net Polarization Transfer via a J-Ordered State for Signal Enhancement of Low-Sensitivity Nuclei", J. Magn. Reson., 1980, **39**, 163.

64 S. R. Hartmann and E. L. Hahn, "Nuclear Double Resonance in the Rotating Frame", Phys. Rev. 1962, **128**, 2042.

65 J. Schaefer, E. O. Stejskal and R. Buchdahl, "High-Resolution Carbon-13 Nuclear magnetic Resonance Study of Some Solid, Glassy Polymers", Macromolecules, 1975, **8**, 291.

66 C. S. Yannoni, "High-Resolution NMR in Solids: The CPMAS Experiment" Acc. Chem. Res., 1982, **15**, 201.

67 Y. Wu, D. Lewis, J. S. Frye, A. R. Palmer and R. A. Wind, "Cross-Polarization Double-Rotation NMR", J. Magn. Reson., 1992, **100**, 425.

68 J. S. Waugh, M. L. Huber, U. Haeberlen, " Approach to High-Resolution NMR in Solids", Phys. Rev. Lett., 1968, 20, 180.

69 P. Mansfield, "Symmetrized Pulse Sequences in High Resolution NMR in Solids", J. Phys. C: Solid State Phys., 1971, **4**, 1444.

70 P. Mansfield, M. J. Orchard, D. C Stalker and K. H. B. Richards, "Symmetrized Multipulse Nuclear Magnetic Resonance Experiments in Solids: Measurement of the Chemical Shift Shielding Tensor in some compounds", Phys. Rev., 1973, **B7**, 90.

71 W. K. Rhim, D. D. Elleman and R. W. Vaughan, "Enhanced Resolution for Solid State NMR", J. Chem. Phys., 1973, **58**, 1772.

72 W. K. Rhim, D. D. Elleman and R. W. Vaughan, "Analysis of Multiple Pulse NMR in Solids", J. Chem. Phys., 1973, **59**, 3740.

73 A.N. Garroway, P. Mansfield and D. C. Stalker, "Limits to Resolution in Multiple-Pulse NMR", Phys. Rev., 1975, B11, 121.

74 W. K. Rhim, D. D. Elleman, L. B. Schreiber and R. W. Vaughan, "Analysis of Multiple Pulse NMR in Solids. II", J. Chem. Phys., 197, **60**, 4595.

75 D. P. Burum and W. K. Rhim, "Analysis of Multiple Pulse NMR in Solids. III", J. Chem. Phys., 1979, **71**, 944.

76 D. P. Burum and W. K. Rhim, "An Improved NMR Technique for Homonuclear Dipolar Decoupling in Solids: Application to polycrystalline ice", J. Chem. Phys., 1979, **70**, 3553.

77 W. K. Rhim, D. P. Burum and D. D. Elleman, "Proton Anisotropic Chemical Shift Spectra in a Single Crystal of Hexagonal Ice", J. Chem. Phys., 1979, **71**, 3139.

78 G. E. Maciel, C. E. Bronnimann and B. L. Hawkins, "High Resolution ^{1}H Nuclear Magnetic Resonance in Solids via CRAMPS", Adv. Magn. Reson., 1990, **14**, 125.

79 U. Haeberlen and J. S. Waugh, "Coherent Averaging Effects in Magnetic Resonance", Phys. Rev., 1968, **175**, 453.

80 B. C. Gerstein, R. G. Pembelton, R. C. Wilson and L. M. Ryan, "High Resolution NMR in Randomly Orientated solids with Homonuclear Dipolar Broadening: Combined Multiple Pulse NMR and Magic Angle Spinning", J. Chem. Phys., 1977, **66**, 361.

81 B. C. Gerstein, C. Chow, R. G. Pembelton and R. C. Wilson, "Utility of Pulse Nuclear Magnetic Resonance in Studying Protons in Coal", J. Phys. Chem., 1977, **81**, 565.

82 R. E. Taylor, R. G. Pembelton, L. M. Ryan and B. C. Gerstiein, "Combined Multiple Pulse NMR and Sample Spinning: Recovery of ^{1}H Chemical Shift Tensors", J. Chem. Phys., 1979, **71**, 4541.

83 L. M. Ryan, R. E. Taylor, A. J. Paff and B. C. Gerstein, "An Experimental Study of Resolution of Proton Chemical Shifts in Solids: Combined Multiple Pulse NMR and Magic Angle Spinning", J. Chem. Phys., 1980, **72**, 508.

84 B. C. Gerstein, "High Resolution NMR in Solids with Strong Homonuclear Dipolar Broadening: Combined Multi-pulse Decoupling and Magic Angle Spinning", Phil. Trans. Roy. Soc. Lond., 1981, **A299**, 521.

85 J. Blitz, "Fundamentals of Ultrasonics", 2nd edn., Butterworth & Co., London, 1967.

86 G. L. Gooberman, "Ultrasonics: Theory and Application", English University Press, London, 1968.

87 W. P. Mason, "Physical Acoustics-Principles and Methods", Vol. 1A-Vol VXIII, Academic Press, New York, 1964.

88 Reproduced from:G. W. C Kaye and T. H. Laby, "Table of Physical and Chemical Constants", 11th edn., Longmans Green, London, 1957.
"Handbook of Chemistry and Physics", Chemical Rubber Company, Cleveland, Ohio.

89 W. P. Mason and H. J. McSkimn, "Energy Losses of Sound Waves in Metals Due to Scattering and Diffusion", J. Appl. Phys., 1948, **19**, 940.

90 P. Curie and J. Currie, Compt. Rend, 1880, **91**, 294.

91 B. Jaffe, R. S Roth and S. Marzullo, "Piezoelectric Properties of Lead-Zirconate Titanate Solid-Solution Ceramics", J. Appl. Phys., 1954, 25, 809.
F. Kulcsar, "Electromechanical Properties of Lead Titanate Zirconate Ceramics with Lead Partially Replaced by Calcium or Strontium", J. Am. Ceram. Soc., 1959, **42**, 49

92 F. A. Firestone, "The Supersonic Reflectoscope, an Instrument for Inspecting the Interior of Solid Parts by Means of Sound Waves", J. Acoust. Soc. Am. 1946, **17**, 287.

93 F. A. Firestone and J. R. Frederick, "Refinements in Supersonic Reflectoscopy. Polarized Sound", J. Acoust. Soc. Am., 1946, **18**, 200.

94 C. L. Frederick and D. C. Worlton, Nondestructive testing, p51, Jan.-Feb., 1962

95 R. A. Shahbender, "Nondestructive Measurement of Tensile and Compressive Stresses", Trans. I.R. E., 1961, **UE-8**, 19.

96 B. Brown and D. Gordon, "Ultrasonic Techniques in Biology and Medicine", Iliffe Books, London, 1967.
J. R. Frederick, "Ultrasonic Engineering", p. 317, Wiley, New York, 1965.

97 W. Le Mars Nyborg, "Physical Acoustics: Principles and Methods", Vol. IIB, p. 265, W. P. Mason Ed., Academic Press, New York, 1965.

98 H. G. Flynn, "Physical Acoustics: Principles and Methods", Vol. IB, p. 58, W. P. Mason Ed., Academic Press, New York, 1965.

99 F. Fox, and K. J. Herzfeld, "Gas Bubbles with Organic Skin as Cavitation Nuclei", J. Acoust. Soc. Am., 1954, **26**, 984.
D. J. Yount, "Skins of Varying Permeability: A Stabilization Mechanism for Gas Cavitation Nuclei", J. Acoust. Soc. Am., 1979, **65**, 1429.
D. J. Yount, "Cavitation Nuclei", J. Acoust. Soc. Am.,1982, **71**, 1473.

100 V. Akulichev, "Hydration of Ions and the Cavitation Resistance of Water", Sov. Phys. Acoust., 1966, **12**, 144.

101 E. N. Haney, K. K. Barnes, A. H. Whitely, W. D. McElroy, D. C. Purse, and K. W. Cooper, J. Cell. Comp. Physical, 1944, **24**, 1.

102 M. J. Straberg, "Onset of Ultrasonic Cavitation in Tap Water", J. Acoust. Soc. Am., 1959, **31**, 163.

103 R. J. Apfel, "The Role of Impurities in Cavitation-Threshold Determination", J. Acoust. Soc. Am., 1970, **48**, 1179.

104 R. J. Winterton, "Nucleation of Boiling and Cavitation", J. Phys. D:Appl. Phys., 1977, **10**, 2041.

105 L. Crum, "Tensile Strength of Water", Nature (London), 1979, **278**, 148.

106 A. A. Atchley, Ph. D Dissertation, The University of Mississippi, Oxford, MS1984.

107 B. E. Noltingk and E. A. Neppiras, "Cavitation produced by Ultrasonics", Proc. Phys. Soc. (London), 1950, **B63**, 674.

108 Lord Raleigh, "The Pressure Developed in a Liquid during the Collapse of a Spherical Cavity", Phil. Mag., Ser. 6, 1917, **34**, 94.

109 B. E. Noltingk and E. A Neppiras, "Cavitation Produced by Ultrasonics: Theoretical Conditions for the Onset of Cavitation", Proc. Phys. Soc. B (Lond.),1951, **64B**, 1032.

110 K. S. Suslick, D. A. Hammerton and R. E. Chine, Jr., "The Sonochemical Hot Spot", J. Am. Chem. Soc., 1986, **108**, 5641.
K. S. Suslick and D. A Hammerton, Proc. Ultrasonics Int. Conf., p. 231, Butterworths, London. 1985.

111 H. Frenzel and H. Schultes, "Luminescenz im Ultraschallbeschickten Wasser. Kurze Mitteilung", Z. Phys. Chem., 1935, **27B(5/6)**, 421.

112 R. E. Verrall and C. M. Sehgal, "Ultrasound. Its Chemical, Physical and Biological Effects", Ed. K. S. Suslick, p. 227, VCH, New York, 1988.

113 M. Kornfeld and L. Suvorov, "On the Destructive Action of Cavitation", J. Appl. Phys.,1944, **15**, 495.

114 C. F. Naudè and A. T. Ellis, "On the Mechanism of Cavitation Damage by Nonhemispherical Cavities Collapsing in Contact With a Solid Boundary", J. Basci. Eng.,1961, **83**, 648.

115 M. S. Plesset and R. B. Chapman, "Collapse of an Initially Spherical Vapour Cavity in the Neighbourhood of a Solid Boundary", J. Fluid Mech., 1971, **47**, 283.

116 G.L. Gooberman, "Ultrasonics Theory and Application" The English Universities Press Ltd, London, 1968, p99-100.

117 J. B. Dysthe, "Force on a Small Inclusion in a Standing Acoustic Wave", J. Sound Vib., 1969, **10**, 157.

118 M. E. Fitzgerald, V. Griffing and J. Sullivan, "Chemical Effects of Ultrasonics-"Hot Spot" Chemistry", J. Chem. Phys., 1956, **25**, 926.

119 E. N. Harvey, "Sonoluminescence and Sonic Chemiluminescense", J. Am. Chem. Soc., 1939, **61**, 2392.

120 V. Griffing and D. Sette, "Luminescence Produced as a Result of Intense Ultrasonic Waves", J. Chem. Phys., 1955, **23**, 503.

121 R. O. Prudhomme and Th. Guilmart, "Photogenese Ultraviolette Par-Irradiation Ultrasonore de L'Eau en Presence des Gaz Rares", J. Chim. Phys. 1957, **54**, 336.

122 O. Lindström and O. Lamm, J. Phys. Colliod. Chem., 1951, **55**, 1139.

123 P. Kruus and T. J. Patraboy, "Initiation of Polymerization with Ultrasound in Methyl Methacrylate", J. Phys. Chem, 1985, **89(15)**, 3379.

124 A. Weissler, "Depolymerisation by Ultrasonic Irradiation: The Role of Cavitation", J. Appl. Phys.. 1950. **21**, 171.

125 S. L. Regen and A. Singh, "Biphasic Sonochemistry. Convient Generation of Dichlorocarbene", J. Org. Chem., 1982, **47**, 1587.

126 T. J. Mason, Private communication.

127 P. K. Chendke and H. S. Fogler, "Sonoluminescence and Sonochemical Reactions of Aqueous Carbon Tetrachloride Solutions", J. Phys. Chem., 1983, **87(8)**, 1362.

128 D. Dennis, "Ultrasonic Initiation of Methyl Methacrylate", Final year project, 1996.

129 S. Glasstone, "Textbook of Physical Chemistry", Macmillan, London, 1960.

130 J. P. Yesinowski, "High Resolution NMR Spectrosopy of Solids and Surface Absorbed Species in Colloidal Suspension: ^{31}P NMR Spectra of Hydroxyappatite and Diphosphonates", J. Am. Chem. Soc., 1981, **103**, 6266.

131 K. Kimura and N. Satoh, "High Resolution Solid State NMR of $^{27}AlF_3$ Particles Observed by a Conventional Fourier-Transform Spectrometer", Chem. Lett. (Jpn), 1989, 271.

132 N. Satoh and K. Kimura, "High Resolution Solid State NMR in Liquids. 2. ^{27}Al NMR Study of AlF_3 Ultrafine Particles", J. Am. Chem. Soc.,1990, **112**, 4688.

133 J. W. Emsley and J. Lindon, "NMR Spectroscopy using Liquid Crystal Solvents", Pergamon, Oxford, 1975.

134 F. M. Leslie, G. R. Luckhurst and H. J. Smith, "Magnetohydrodynamic Effects in the Nematic Phase", Chem. Phys. Lett., 1972, **13**, 368.

135 F. Reinitzer, "Beiträge zur Kenntniss des Cholesterins", Monatsch Chem., 1888, **9**, 421.

136 O. Lehmann, "Über Fliessende Krystalle", Z. Physikal. Chem., 1889, **4**, 462.

137 G. Friedel, "Les État Mésomorphes de La Matiére", Ann. Phys., 1922, **18**, 273.

138 S. Chandrasekhar, "Liquid Crystals", 2nd Edn., Cambridge University, Cambridge, 1992.

APPENDIX 1

AN INTRODUCTION TO HAMILTONIAN AND TENSOR NOTATION

A1.0: INTRODUCTION TO HAMILTONIANS

Many of the nuclear interactions in NMR can be explained in classical terms of the rotating frame. However, some interactions cannot be understood without invoking a quantum mechanical description. In its most elementary form a Hamiltonian, $\mathcal{H}$, is an energy operator that acts on a function as given by the Schrödinger equation,

$$\mathcal{H}.\psi = E.\psi \qquad \text{(A1.1)}$$

In the context of NMR the wavefunction, ψ, is the state of the spin or an ensemble of spins and the Hamiltonian is a perturbation in the energy of the spin state.

The application of Hamiltonians can be seen for a simple case such as the Zeeman interaction. The classical energy of a magnetic moment, μ, in a static magnetic field is given by,

$$E = -\mu.\mathbf{H}_0 \qquad \text{(A1.2)}$$

Equation A1.2 can be rewritten in its quantum mechanical format, by replacing the magnetic moment, μ, with the spin angular momentum vector operator, $\gamma.\hbar.\mathbf{I}$, to yield the Hamiltonian,

$$\mathcal{H}_Z = -\hbar.\gamma.\mathbf{I}.\mathbf{H}_0 \qquad \text{(A1.3)}$$

or,

$$\mathcal{H}_Z = -\hbar.\sum_i \gamma.\mathbf{I}.\mathbf{H}_0 \qquad \text{(A1.4)}$$

for an ensemble of spins.

Similar, although more complex, Hamiltonians can be derived for the other nuclear interactions: $\mathcal{H}_{RF}$: Spin interaction with the external r.f. field, $\mathcal{H}_{CS}$: Chemical shift, $\mathcal{H}_{Q}$: Quadrupolar interaction, $\mathcal{H}_{SR}$: Spin rotation, $\mathcal{H}_{D}$: Dipolar coupling, $\mathcal{H}_{J}$: J-coupling. Some or all of these Hamiltonians may interact with the spin system, thus, the observed NMR signal is described by a total Hamiltonian which is the linear summation of individual Hamiltonian interactions. The reader is referred to an article by Smith, Palke and Gerig[A1] for an introduction to Hamiltonians.

A1.1: TENSOR NOTATION

The tensor is a useful mathematical tool in NMR as it allows the rotation of molecules from one axis to another, describing interactions such as chemical shift[A2] and electric field gradients. A zero rank tensor is a scalar quantity and is invariable to molecular rotation. A vector is a first rank tensor, which defines a particular direction in space, it possesses three components I_x, I_y and I_z, which relate to the unit orthogonal axes as,

$$I=I_x i+I_y j+I_z k \qquad \text{(A1.5)}$$

To describe an object in n dimensional space requires a second rank tensor composed of n^2 components, i.e. for 3 dimensional space a matrix of nine components is required. The use of tensor notation can be seen for the magnetic moment, μ, figure A1.0.

Figure A.1.0: Magnetic moment in the Cartesian frame.

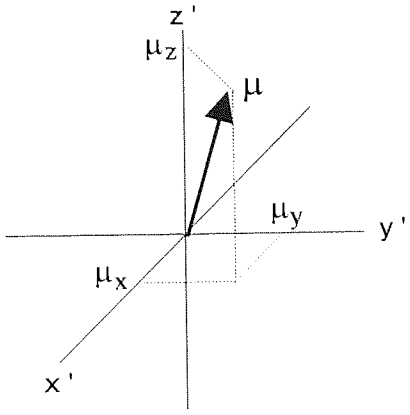

If the external magnetic field, H_0, is aligned with the z-axis then the components of μ are; μ_{xz}, μ_{yz}, μ_{zz}. Similarly, components can be obtained when H_0 is aligned with the x and y axes giving a (3×3) matrix,

$$\begin{pmatrix} \mu_{xx} & \mu_{xy} & \mu_{xz} \\ \mu_{yx} & \mu_{yy} & \mu_{yz} \\ \mu_{zx} & \mu_{zy} & \mu_{zz} \end{pmatrix} \qquad \text{(A1.6)}$$

In NMR, tensors are principally used in describing chemical shifts. The electron density around a nucleus is defined by a shielding constant, σ, experienced by the nucleus. The electron density around the nucleus may be anisotropic and therefore is defined by a second rank tensor,

$$\begin{pmatrix} \sigma_{xx} & \sigma_{xy} & \sigma_{xz} \\ \sigma_{yx} & \sigma_{yy} & \sigma_{yz} \\ \sigma_{zx} & \sigma_{zy} & \sigma_{zz} \end{pmatrix} \qquad \text{(A1.7)}$$

By selection of the appropriate molecular axis the tensor can be converted into the Principle Axis System reducing the number of matrix elements to three components known as the principal axes,

$$\begin{pmatrix} \sigma_{xx} & 0 & 0 \\ 0 & \sigma_{yy} & 0 \\ 0 & 0 & \sigma_{zz} \end{pmatrix} \qquad \text{(A1.8)}$$

where the isotropic shift can be found from 1/3(Tr.{A1.8}).

A1.2: REFERENCES

A1. S. Smith, W. Palke and J. Gerig, "The Hamiltonians of NMR, Part 1", Concepts in Magnetic Resonance, 1992, **4**, 107-144.

S. Smith, W. Palke and J. Gerig, "The Hamiltonians of NMR, Part 2", Concepts in Magnetic Resonance, 1992, **4**, 181-204.

A2. F. Anet and D. O'Leary, "The Shielding tensor, Part 1: Understanding its symmetry properties", Concepts in Magnetic Resonance, 1991, **3**, 193-214.

APPENDIX 2

ACQUISITION PARAMETERS FOR RECORDED SPECTRA

A2.1: ACQUISITION PARAMETERS FOR CHAPTER 7

Table A2.1: Parameters for figure 7.0.

PARAMETER	VALUE
SPECTROMETER	BRUKER AC 300
NUCLEUS	^{27}AL
OBSERVATION FREQUENCY, MHz	78.2
OBSERVATION FREQUENCY OFFSET, kHz	102.631
DATA POINTS	TD=32K, SI=32K
SWEEP WIDTH, Hz	100000
DELAY, μs	8.8
PULSE WIDTH, μs	1
RELAXATION DELAY, s	0.5
NUMBER OF SCANS	400
ACQUISITION TIME, s	0.16384
LINE BROADENING, Hz	10

Table A2.2: Parameters for figure 7.1.

PARAMETER	VALUE
SPECTROMETER	BRUKER AC 300
NUCLEUS	^{27}AL
OBSERVATION FREQUENCY, MHz	78.2
OBSERVATION FREQUENCY OFFSET, kHz	102.631
DATA POINTS	TD=32K, SI=32K
SWEEP WIDTH, Hz	100000
DELAY, μs	8.8
PULSE WIDTH, μS	2
RELAXATION DELAY, s	0.5
NUMBER OF SCANS	400
ACQUISITION TIME, s	0.16384
LINE BROADENING, Hz	10

Table A2.3: Parameters for figure 7.2.

PARAMETER	VALUE
SPECTROMETER	JEOL FX-90Q
NUCLEUS	^{27}AL
OBSERVATION FREQUENCY, MHz	23.3
OBSERVATION FREQUENCY OFFSET, kHz	47.68
DATA POINTS	8192
SWEEP WIDTH, Hz	30030
DELAY, μs	150
PULSE WIDTH, μs	50
RELAXATION DELAY, s	0.1
NUMBER OF SCANS	6872
ACQUISITION TIME, s	0.1363
LINE BROADENING, Hz	0

Table A2..4: Parameters for figure 7.3/4.

PARAMETER	VALUE
SPECTROMETER	JEOL FX-90Q
NUCLEUS	^{27}AL
OBSERVATION FREQUENCY, MHz	23.3
OBSERVATION FREQUENCY OFFSET, kHz	47.68
DATA POINTS	8192
SWEEP WIDTH, Hz	30030
DELAY, μs	150
PULSE WIDTH, μs	50
RELAXATION DELAY, s	0.1
NUMBER OF SCANS	800
ACQUISITION TIME, s	0.1363
LINE BROADENING, Hz	52.5

Table A2.5: Parameters for figure 7.5/6.

PARAMETER	VALUE
SPECTROMETER	BRUKER AC 300
NUCLEUS	^{11}B
OBSERVATION FREQUENCY, MHz	96.29
OBSERVATION FREQUENCY OFFSET, kHz	81.326
DATA POINTS	TD=32K, SI=32K
SWEEP WIDTH, Hz	125000
DELAY, μs	7.5
PULSE WIDTH, μs	3
RELAXATION DELAY, s	1
NUMBER OF SCANS	240
ACQUISITION TIME, s	0.13107
LINE BROADENING, Hz	10

Table A2.6: Parameters for figure 7.7-12.

PARAMETER	VALUE
SPECTROMETER	JEOL FX-90Q
NUCLEUS	^{11}B
OBSERVATION FREQUENCY, MHz	28.7
OBSERVATION FREQUENCY OFFSET, kHz	49.1
DATA POINTS	8192
SWEEP WIDTH, Hz	30030
DELAY, μs	150
PULSE WIDTH, μs	30
RELAXATION DELAY, s	0.1
NUMBER OF SCANS	800
ACQUISITION TIME, s	0.1363
LINE BROADENING, Hz	50

Table A2.7: Parameters for Section 7.1.5.

PARAMETER	VALUE
SPECTROMETER	BRUKER WM 250
NUCLEUS	^{27}AL
OBSERVATION FREQUENCY, MHz	65.143
OBSERVATION FREQUENCY OFFSET, kHz	66.527
DATA POINTS	TD=8 K, SI= 8 K
SWEEP WIDTH, Hz	55555
DELAY, μs	50
PULSE WIDTH, μs	20
RELAXATION DELAY, s	0.75
NUMBER OF SCANS	4000
ACQUISITION TIME, s	0.0737
LINE BROADENING, Hz	200

A2.2: ACQUISITION PARAMETERS FOR CHAPTER 8

Table A2.8: Acquisition parameters for figure 8.7/8.

PARAMETER	VALUE
SPECTROMETER	JEOL FX 90Q
NUCLEUS	^{2}D
OBSERVATION FREQUENCY, MHz	13.70
OBSERVATION FREQUENCY OFFSET, kHz	54.44
DATA POINTS	8192
SWEEP WIDTH, Hz	30030
DELAY, μs	76.2
PULSE WIDTH, μs	22.5
RELAXATION DELAY, s	1
NUMBER OF SCANS	128
ACQUISITION TIME, s	0.1363
LINE BROADENING, Hz	0

Table A2.9: Acquisition parameters for figure 8.10.

PARAMETER	VALUE
SPECTROMETER	BRUKER WM 250
NUCLEUS	^{2}D
OBSERVATION FREQUENCY, MHz	38.37
OBSERVATION FREQUENCY OFFSET, kHz	47.826
DATA POINTS	TD=4K, SI=4K
SWEEP WIDTH, Hz	50000
DELAY, μs	12.5
PULSE WIDTH, μs	10
RELAXATION DELAY, s	0.1
NUMBER OF SCANS	400
ACQUISITION TIME, s	0.0409
LINE BROADENING, Hz	0

Table A2.10: Acquisition parameters for figure 8.12/13.

PARAMETER	VALUE
SPECTROMETER	BRUKER WM 250
NUCLEUS	^{2}D
OBSERVATION FREQUENCY, MHz	38.4095
OBSERVATION FREQUENCY OFFSET, kHz	47.826
DATA POINTS	TD=4K, SI=4K
SWEEP WIDTH, Hz	25000
DELAY, μs	25
PULSE WIDTH, μs	10
RELAXATION DELAY, s	0.1
NUMBER OF SCANS	400
ACQUISITION TIME, s	0.08192
LINE BROADENING, Hz	0

Table A2.11: Acquisition parameters for figure 8.15.

PARAMETER	VALUE
SPECTROMETER	BRUKER WM 250
NUCLEUS	^{2}D
OBSERVATION FREQUENCY, MHz	38.405
OBSERVATION FREQUENCY OFFSET, kHz	47.826
DATA POINTS	TD=4K, SI=4K
SWEEP WIDTH, Hz	50000
DELAY, μs	15
PULSE WIDTH, μs	10
RELAXATION DELAY, s	0.1
NUMBER OF SCANS	100
ACQUISITION TIME, s	0.0409
LINE BROADENING, Hz	0

Table A2.12: Acquisition parameters for figure 8.17.

PARAMETER	VALUE
SPECTROMETER	BRUKER WM 250
NUCLEUS	^{2}D
OBSERVATION FREQUENCY, MHz	38.39
OBSERVATION FREQUENCY OFFSET, kHz	47.447
DATA POINTS	TD=32K, SI=32K
SWEEP WIDTH, Hz	25000
DELAY, μs	25
PULSE WIDTH, μs	20
RELAXATION DELAY, s	0.2
NUMBER OF SCANS	400
ACQUISITION TIME, s	0.65536
LINE BROADENING, Hz	0

A2.3: ACQUISITION PARAMETERS FOR CHAPTER 9

Table A2.13: Acquisition parameters for figure 9.0/1.

PARAMETER	VALUE
SPECTROMETER	BRUKER WM 250
NUCLEUS	^{13}C
OBSERVATION FREQUENCY, MHz	62.90
OBSERVATION FREQUENCY OFFSET, kHz	51.290
DATA POINTS	TD=8K, SI=8K
SWEEP WIDTH, Hz	12500
DELAY, μs	50
PULSE WIDTH, μs	21.3
RELAXATION DELAY, s	1
NUMBER OF SCANS	128
ACQUISITION TIME, s	0.327
LINE BROADENING, Hz	0

Table A2.14: Acquisition parameters for figure 9.2/3.

PARAMETER	VALUE
SPECTROMETER	BRUKER WM 250
NUCLEUS	^{13}C
OBSERVATION FREQUENCY, MHz	62.855
OBSERVATION FREQUENCY OFFSET, kHz	51.290
DATA POINTS	TD=8K, SI=8K
SWEEP WIDTH, Hz	12500
DELAY, μs	50
PULSE WIDTH, μs	20
RELAXATION DELAY, s	10, 5, 1, 0.5, 0.25, 0.1
NUMBER OF SCANS	128
ACQUISITION TIME, s	0.327
LINE BROADENING, Hz	0

Table A2.15: Acquisition parameters for figure 9.7/8.

PARAMETER	VALUE
SPECTROMETER	BRUKER WM 250
NUCLEUS	^{13}C
OBSERVATION FREQUENCY, MHz	62.90
OBSERVATION FREQUENCY OFFSET, KHz	51.200
DATA POINTS	TD=250, 624, 1250, 2500, 6250, SI=8K
SWEEP WIDTH, Hz	12500
DELAY, μs	50
PULSE WIDTH, μs	20
RELAXATION DELAY, s	1
NUMBER OF SCANS	128
ACQUISITION TIME, s	0.01, 0.025, 0.05, 0.1, 0.25
LINE BROADENING, Hz	0

Table A2.16: Acquisition parameters for figure 9.5/6.

PARAMETER	VALUE
SPECTROMETER	BRUKER WM 250
NUCLEUS	^{13}C
OBSERVATION FREQUENCY, MHz	62.855
OBSERVATION FREQUENCY OFFSET, kHz	51.290
DATA POINTS	TD=8K, SI=8K
SWEEP WIDTH, Hz	12500
DELAY, μs	5, 10, 25, 50
PULSE WIDTH, μs	20
RELAXATION DELAY, s	1
NUMBER OF SCANS	128
ACQUISITION TIME, s	0.327
LINE BROADENING, Hz	0

Table A2.17: Acquisition parameters for figure 9.15.

PARAMETER	VALUE
SPECTROMETER	BRUKER WM 250
NUCLEUS	^{13}C
OBSERVATION FREQUENCY, MHz	62.855
OBSERVATION FREQUENCY OFFSET, kHz	51.290
DATA POINTS	TD=250, SI=8K
SWEEP WIDTH, Hz	12500
DELAY, μs	5
PULSE WIDTH, μs	20
RELAXATION DELAY, s	1
NUMBER OF SCANS	128
ACQUISITION TIME, s	0.01
LINE BROADENING, Hz	0

Table A2.18: Acquisition parameters for figure 9.16.

PARAMETER	VALUE
SPECTROMETER	BRUKER WM 250
NUCLEUS	^{13}C
OBSERVATION FREQUENCY, MHz	62.855
OBSERVATION FREQUENCY OFFSET, kHz	51.290
DATA POINTS	TD=8K, SI=8K
SWEEP WIDTH, Hz	8928
DELAY, μs	70
PULSE WIDTH, μs	4
RELAXATION DELAY, s	0
NUMBER OF SCANS	128
ACQUISITION TIME, s	0.458
LINE BROADENING, Hz	0

Table A2.19: Acquisition parameters for figure 9.17/18.

PARAMETER	VALUE
SPECTROMETER	BRUKER WM 250
NUCLEUS	^{13}C
OBSERVATION FREQUENCY, MHz	62.89
OBSERVATION FREQUENCY OFFSET, kHz	51.290
DATA POINTS	TD=8K, SI=8K
SWEEP WIDTH, Hz	12500
DELAY, μs	50
PULSE WIDTH, μs	21
RELAXATION DELAY, s	30O, SEE VD LIST WITH FIGURES
NUMBER OF SCANS	128
ACQUISITION TIME, s	0.327
LINE BROADENING, Hz	0

Table A2.20: Acquisition parameters for figure 9.19.

PARAMETER	VALUE
SPECTROMETER	BRUKER WM 250
NUCLEUS	^{13}C
OBSERVATION FREQUENCY, MHz	62.90
OBSERVATION FREQUENCY OFFSET, kHz	50.811
DATA POINTS	TD=8K, SI=16K
SWEEP WIDTH, Hz	12500
DELAY, μs	50
PULSE WIDTH, μs	19
RELAXATION DELAY, s	60
NUMBER OF SCANS	128
ACQUISITION TIME, s	0.327
LINE BROADENING, Hz	0

Table A2.21: Acquisition parameters for figure 9.20.

PARAMETER	VALUE
SPECTROMETER	BRUKER WM 250
NUCLEUS	^{13}C
OBSERVATION FREQUENCY, MHz	62.90
OBSERVATION FREQUENCY OFFSET, kHz	50.811
DATA POINTS	TD=8K, SI=16K
SWEEP WIDTH, Hz	12500
DELAY, μs	50
PULSE WIDTH, μs	19
RELAXATION DELAY, s	3
NUMBER OF SCANS	128
ACQUISITION TIME, s	0.327
LINE BROADENING, Hz	0

Table A2.22: Acquisition parameters for figure 9.21.

PARAMETER	VALUE
SPECTROMETER	BRUKER WM 250
NUCLEUS	^{13}C
OBSERVATION FREQUENCY, MHz	62.89
OBSERVATION FREQUENCY OFFSET, kHz	50000
DATA POINTS	TD=16K, SI=16K
SWEEP WIDTH, Hz	15625
DELAY, μs	40
PULSE WIDTH, μs	20
RELAXATION DELAY, s	7
NUMBER OF SCANS	128
ACQUISITION TIME, s	0.524
LINE BROADENING, Hz	0

Table A2.23: Acquisition parameters for figure 9.22.

PARAMETER	VALUE
SPECTROMETER	BRUKER WM 250
NUCLEUS	^{13}C
OBSERVATION FREQUENCY, MHz	62.89
OBSERVATION FREQUENCY OFFSET, kHz	50000
DATA POINTS	TD=8K, SI=16K
SWEEP WIDTH, Hz	15625
DELAY, μs	40
PULSE WIDTH, μs	20
RELAXATION DELAY, s	1
NUMBER OF SCANS	128
ACQUISITION TIME, s	0.262
LINE BROADENING, Hz	0

Table A2.24: Acquisition parameters for figure 9.23.

PARAMETER	VALUE
SPECTROMETER	BRUKER WM 250
NUCLEUS	^{13}C
OBSERVATION FREQUENCY, MHz	62.89
OBSERVATION FREQUENCY OFFSET, kHz	50000
DATA POINTS	TD=8K, SI=16K
SWEEP WIDTH, Hz	15625
DELAY, μs	540
PULSE WIDTH, μs	20
RELAXATION DELAY, s	0.1
NUMBER OF SCANS	128
ACQUISITION TIME, s	0.262
LINE BROADENING, Hz	0

APPENDIX 3

YAESU CONTROL PROGRAM

A3.1: COMPUTER CONTROL PROGRAM FOR YAESU CAT SYSTEM

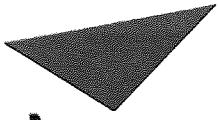

Aston University

Content has been removed for copyright reasons

APPENDIX 4

CHEMICAL STRUCTURE OF LIQUID CRYSTALS

A4.0: CHEMICAL STRUCTURE OF LIQUID CRYSTALS USED IN CHAPTER 8

Figure A.4.0: Chemical structure of the liquid crystal, I35

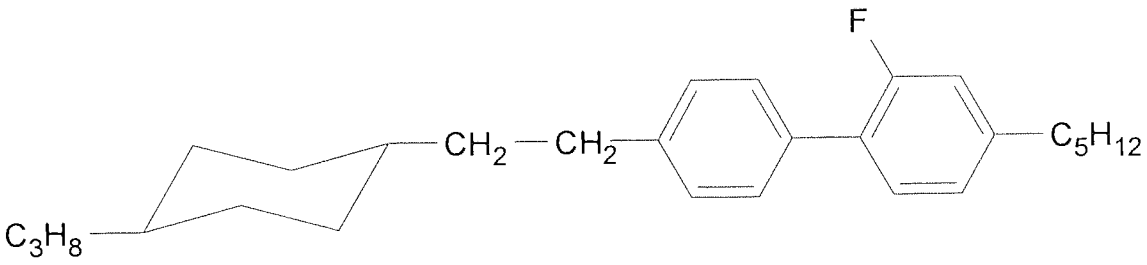

Figure A.4.1 Chemical structure of the liquid crystal mixture, ZLI-1167

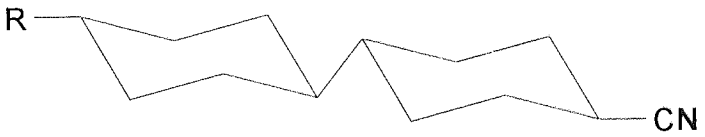

where R= C_3H_8
C_5H_{12}
C_7H_{16}